Ministry of Education and Science of the Russian Federation
Saint Petersburg National Research University of Information Technologies, Mechanics, and Optics

NANOSYSTEMS:

PHYSICS, CHEMISTRY, MATHEMATICS

2022, volume 13(4)

Наносистемы: физика, химия, математика

2022, том 13, № 4

NANOSYSTEMS:

PHYSICS, CHEMISTRY, MATHEMATICS

Address: ITMO University, Kronverkskiy pr., 49, St. Petersburg 197101, Russia.
Phone: +7(812)607-02-54, **Journal site:** http://nanojournal.ifmo.ru/,
E-mail: nanojournal.ifmo@gmail.com

AIM AND SCOPE

The scope of the journal includes all areas of nano-sciences. Papers devoted to basic problems of physics, chemistry, material science and mathematics inspired by nanosystems investigations are welcomed. Both theoretical and experimental works concerning the properties and behavior of nanosystems, problems of its creation and application, mathematical methods of nanosystem studies are considered.

The journal publishes scientific reviews (up to 30 journal pages), research papers (up to 15 pages) and letters (up to 5 pages). All manuscripts are peer-reviewed. Authors are informed about the referee opinion and the Editorial decision.

CONTENT

MATHEMATICS

PHYSICS

CHEMISTRY AND MATERIAL SCIENCE

NANOSYSTEMS:
PHYSICS, CHEMISTRY, MATHEMATICS

Perelmuter M.N. *Nanosystems: Phys. Chem. Math.*, 2022, **13** (4), 356–364.
http://nanojournal.ifmo.ru
DOI 10.17586/2220-8054-2022-13-4-356-364

Original article

Interface cracks bridged by nanofibers

Mikhail N. Perelmuter

Ishlinsky Institute for Problems in Mechanics RAS, Moscow, Russia

perelm@ipmnet.ru

PACS 46.25.Cc, 68.35.Np

ABSTRACT The model of different materials joint with bridged interface crack is considered. It is assumed that between the crack faces there are nanofibers constraining the crack opening. The size of the zone filled with nanofibers (the bridged zone) can be comparable to the whole crack length. The bond tractions depend on the crack opening at the bridged zone according to the prescribed nonlinear bond deformation law. The system of two singular integral-differential equations with Cauchy-type kernel is used for evaluation of bond tractions for the interface crack bridged by nanofibers. A phenomenological description of the bond deformation law in the crack bridged zone is used. Numerical experiments have been performed to analyze the influence of the bilinear bond deformation law parameters, the size of the crack bridged zone and also the magnitude of the external load on the convergence of the numerical iteration solution of the integral-differential equations system.

KEYWORDS bridged crack, nanofibers, nonlinear bonds deformation law, stress state, stress intensity factors.

ACKNOWLEDGEMENTS This work was supported by the Government program (contract AAAA-A17-117021310386-3).

FOR CITATION Perelmuter M.N. Interface cracks bridged by nanofibers. *Nanosystems: Phys. Chem. Math.*, 2022, **13** (4), 356–364.

1. Introduction

Models of a crack with interaction of its faces make it possible to combine the approaches of fracture mechanics and physics of strength in the analysis of crack growth. Zones of the crack faces interaction (fracture process zones) are usually adjacent to the crack tips. In these zones forces applied to the crack faces restrain the crack opening, [1]. There are two main versions of fracture process zone models depending on the stress singularity condition at the crack tip - cohesive and bridged (see reviews [2], [3]). If several physical mechanisms are involved in the processes of materials deformation and rupture then in such case, it is more effective to use the process zone models with the crack tips stresses singularity accounting. Such models (in the terminology of [3], these are bridged crack models) have been studied for cracks in homogeneous materials as two-dimensional problems [4–8] and as axisymmetic problems [9–11]. For interface cracks, the bridged crack model have been extended and developed for two-dimensional case in [12, 13] and for axisymmetic problems in [14].

In fracture mechanics, the crack bridging model is used to analyze fracture toughness and cracks growth assuming the bridged zone destruction as cracks advance. Application of the bridged crack model together with the crack growing criterion [15, 16] allows one to obtain dependencies of materials toughness and strength versus a crack length. The toughening effects of bonds is presented, mathematically, by bonds deformation law. The bonds deformation law for straight nanofibers was considered in [17–19] on the basis of shear-lag model. Straight nanofibers orientations influence on composite fracture toughness was considered in [20,21]. The effects of nanotubes curvature on bonds deformation law were analysed in [22,23]. The fracture toughness of oriented multi-wall carbon-nanotube-reinforced alumina composites was experimentally obtained and it was compared with results obtained by analytical and numerical models [24, 25]. Results confirm that the contribution to toughness from the nanotube bridging induced considerable nanoscale toughening.

In this paper, the interface crack bridged zone model is used with the following assumptions: 1) a zone of weakened bonds between materials is considered as an interfacial crack with distributed nonlinear spring-like bonds (nanofibers) between the crack faces (bridged zone, see Fig. 1); 2) distributed bridging tractions, which are functions of the crack opening, are imposed to the crack faces at the bridged zone, see Fig. 2; 3) materials ahead of the crack tips are considered as linearly-elastic; 4) ahead of crack tips, these materials are deformed together with the infinitely thin adhesion layer without loss of their continuity; 5) the total stress intensity factor (due to the action of the external loading and the bridging tractions) is not zero. Note that the last assumption defines the main difference between cohesive and bridged models. Bonding in the crack bridged zone reduces the stress intensity factors. This effect depends on the bridged zone length and bonds properties, but within the crack bridging model (in contrast to cohesive crack models) tractions are assumed to exist together with a stress singularity at the crack tip.

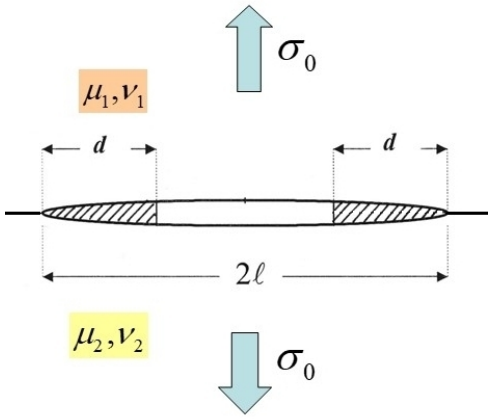

FIG. 1. Crack with two bridged zones at the materials interface

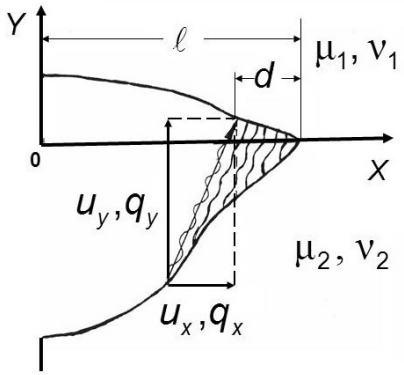

FIG. 2. Components of the crack opening $u_{x,y}$ and bonds tractions $q_{x,y}$ at the bridged zone

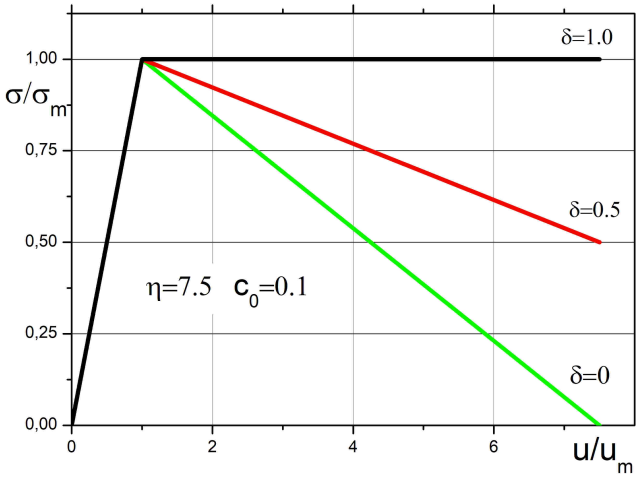

FIG. 3. Bilinear bonds deformation law, $u_m = 10^{-7}m$, $\sigma_m = 50$ MPa, $u_{cr} = \eta u_m$, softening parameter δ variation

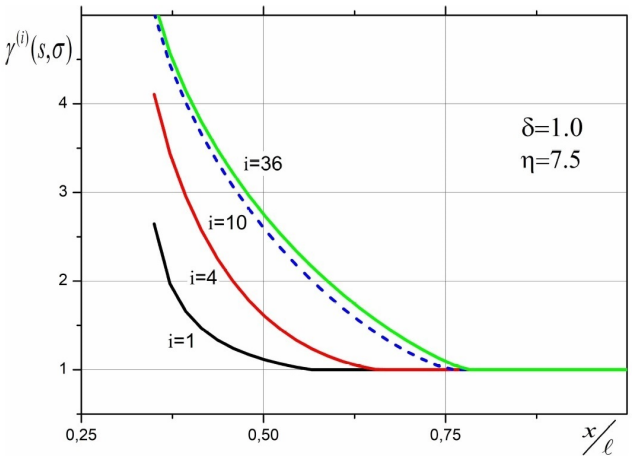

FIG. 4. Relative bond compliance over bridged zone length, $d/\ell = 0.65$, external load - $\sigma_0 = 40$ MPa

2. Statement of the problem

Let us consider the main statements of the interface bridged crack model proposed in [12]. Under external loads in bonds connecting the crack faces in the bridged zone (Fig. 2) tractions $Q(x)$ with normal $q_y(x)$ and tangential $q_x(x)$ components are arisen (even for loads normal to the crack line)

$$Q(x) = q_y(x) - iq_x(x), \quad i^2 = -1, \quad \sigma(x) = \sqrt{q_y^2(x) + q_x^2(x)}, \tag{1}$$

where $q_{y,x}(x)$ are the normal and shear components of the bonds tractions, respectively, $\sigma\,(x)$ is the bond stress vector modulus.

Normal and tangential stresses, numerically equal to $q_y(x)$ and $q_x(x)$, respectively, are applied to the crack faces at the bridged zone.

The crack opening, $u(x)$, at the bridged zones $\ell - d \le |x| < \ell$ is determined as follows

$$u(x) = u_y(x) - i\,u_x(x) = c_b(x,\sigma)(q_y(x) - iq_x(x)), \tag{2}$$

$$c_b(x,\sigma) = \varphi(x,\sigma)\frac{H}{E_b}, \quad u_b(x) = \sqrt{u_y^2(x) + u_x^2(x)}, \tag{3}$$

where $u_{y,x}(x)$ are the projections of the crack opening on the coordinate axes (Fig. 2), $c_b(x,\sigma)$ is the effective compliance of quasi-linear bonds depending on the bond position in the bridged zone and the bonds tension $\sigma(x)$, H is a linear scale related to the thickness of the intermediate layer adjacent to the interface, E_b is the effective elasticity modulus of the bond, $\varphi(x,\sigma)$ is dimensionless function which defines variation of bonds compliance over bridged zone and $u_b(x)$ is the modulus of the crack opening. Accounting the problem linearity, it is possible to write the crack opening $u(x)$ at the

bridged zone as follows

$$u(x) = u_\infty(x) - u_Q(x)\ , \tag{4}$$

where $u_\infty(x)$, $u_Q(x)$ are the crack opening caused by the external load σ_0 and bond tractions $Q(x)$ closing crack faces, respectively.

By using formulae (2)-(4), we can obtain a system of integral-differential equations relative to bonds tractions $q_{x,y}(x)$. Introduce the new variables, $s = x/\ell$, $q_{y,x}(s) = q_{y,x}(x)/\sigma_0$, and differentiate relation (4) with accounting relation (1)-(2) one obtains

$$c_0 \frac{\partial}{\partial s} \varphi(s,\sigma)\ [q_y(s) - i\, q_x(s)] + u'_Q(s) E_b = u'_\infty(s) E_b\ , \quad c_0 = \frac{H}{\ell}, \tag{5}$$

Here the right side of this relation is the given coordinate function and c_0 is the relative bond compliance.

The derivatives in relation (5) are defined as follows: the derivative of the crack opening under the action of homogeneous external loading $u'_\infty(s)$ is determined by the well-known solution presented in [26]; the derivative of the crack opening caused by bonds stress action $u'_Q(s)$ can be obtained starting from the representation for the derivatives of the opening crack under the action of arbitrary static loads on the crack faces. Following [12] and [13], one can obtain the system of two singular integral-differential equations (SIDE) relative to bonds tractions $q_y(s)$ and $q_x(s)$ in the form

$$T_{ij}(s,\sigma)\frac{df_j(s)}{ds} + W_{ij}(s,\sigma) f_j(s) + \varepsilon \int\limits_{1-d/\ell}^{1} G_{ij}(s,\xi) f_j(\xi) d\xi = Z_i(s);\ i,j = 1,2; \tag{6}$$

where $f_j(s)$ is unknown function depending on bond tractions $q_{x,y}(s)$ as follows

$$q_y(s) - i q_x(s) = (f_2(s) - i f_1(s))\sqrt{1-s}\left(\frac{1-s}{1+s}\right)^{-i\beta}, \tag{7}$$

and

$$\beta = \frac{\ln\ \alpha}{2\pi},\ \alpha = \frac{\mu_1 + \mu_2\kappa_1}{\mu_2 + \mu_1\kappa_2},\ \varepsilon = \frac{E_b}{2\pi c_0}\left(\frac{k_1+1}{\mu_1} + \frac{k_2+1}{\mu_2}\right), \tag{8}$$

In relations (8) $\kappa_{1,2} = 3 - 4\nu_{1,2}$ or $\kappa_{1,2} = (3-\nu_{1,2})/(1+\nu_{1,2})$ for plane strain and plane stress, respectively, $\nu_{1,2}$ and $\mu_{1,2}$ are Poisson's ratios and the shear modulus of jointed materials 1 and 2, ε is the main parameter affecting the SIDE solution, it includes the relative stiffness of bonds in the crack bridged zone and the mechanical properties of the both materials.

The singular kernel $G_{ij}(s,\xi)$ and the vector-column $Z_i(s)$ in equation (6) can be written as [13]

$$G_{ij}\,(s,\xi) = \frac{(1-\xi)\sqrt{1+\xi}}{(\xi^2 - s^2)\sqrt{1+s}} \begin{bmatrix} s & -\xi\cdot\Omega\,(s) \\ s\cdot\Omega\,(s) & \xi \end{bmatrix}, \quad \Omega\,(s) = \tan\left(\beta \ln\frac{1-s}{1+s}\right),$$

$$Z_i(s) = \frac{\pi\,\varepsilon}{2\cosh\,(\pi\beta)\sqrt{1+s}} \begin{bmatrix} 2\beta\cdot\,\Omega(s) - s \\ -2\beta - s\cdot\,\Omega(s) \end{bmatrix}.$$

The details of SIDE (6) derivation and the explicit relations for the coefficients of this equation $T_{ij}(s,\sigma)$, $W_{ij}(s,\sigma)$ (which depend on coordinates, properties of materials, function $\varphi(s,\sigma)$ and its derivatives with respect to s) are presented in [13].

3. Bonds deformation curves and numerical solution

To model the stress state in the crack bridged zone, it is convenient to present the nonlinear bond deformation law (the relationship between the crack opening and the bonds tractions) in a relatively simple analytical form, described by the minimum number of parameters, which can be experimentally obtained. As the first step simplification of bonds deformation law, one can rewrite it as follows

$$\sigma(u_b) = \begin{cases} \kappa_b(s) u_b(s), & 0 \le u_b(s) \le u_m \\ \Phi(u_b), & u_m < u_b(s) \le u_{cr}, \end{cases} \tag{9}$$

where the initial part of bonds deformation law is assumed as linear-elastic, it may depend on the bond position along the crack bridged zone ($s = x/\ell$), $\sigma(s)$ and $u_b(s)$ are defined by relations (2)-(3), $\kappa_b(s)$ is the bond stiffness and the slope of the elastic rising segment of the deformation law, u_m is the crack opening corresponding to transition from the linear-elastic to non-linear parts of the bond deformation law. The parameter u_m depends, in particular, on the mechanical and physical characteristics of bonds and the crack length.

For the numerical solution of equations (6), we use the iteration scheme which is similar to the well-known elastic steps method. At each iteration, equations (6) is solved by a collocation scheme with a piecewise-quadratic approximation of the unknown functions, see details in [13]. The method of variable elasticity parameters for solving equations (6) is

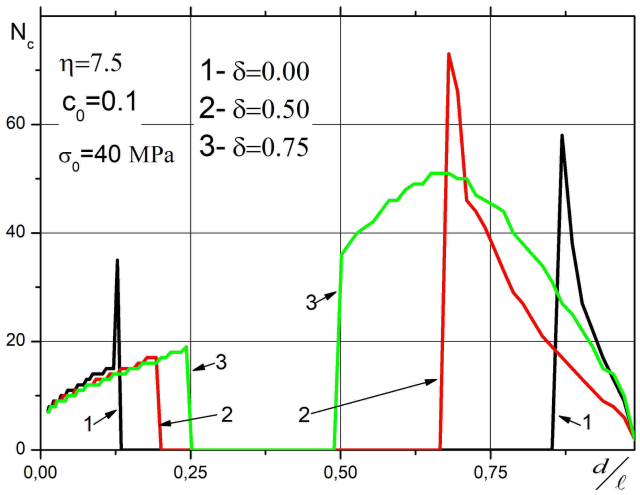

FIG. 5. Number of iterations until solution convergence versus crack bridged zone length, external load – $\sigma_0 = 40$ MPa

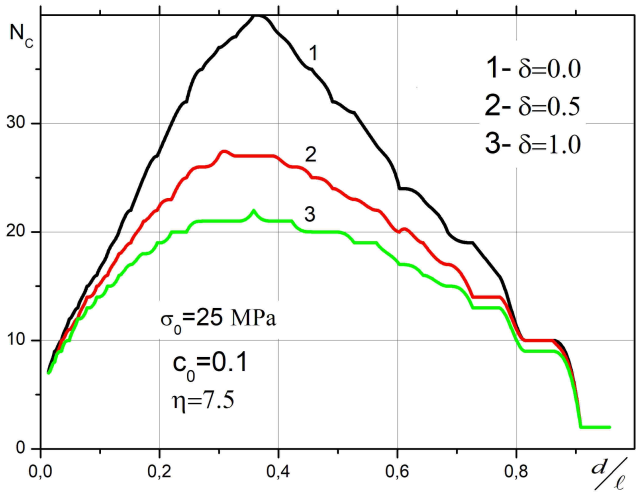

FIG. 6. Number of iterations until solution convergence versus crack bridged zone length, external load – $\sigma_0 = 25$ MPa

realized as the method of the tangential compliance with assumption that nonlinear part of the bond deformation law is given by the explicit relation. The first step of the iteration process consists of solving equations (6) for linear elastic bonds. Subsequent iterations are performed if, on the crack bridged zone part, $u(s) > u_m$. At each iteration, equations (6) are solved for quasi-elastic bonds with an effective compliance that is variable along the crack bridged zone and depends on the magnitude of the tractions vector modulus in the bonds obtained at the previous solution step. The effective compliance is calculated in a similar manner for the determination of the secant modulus in the variable elasticity parameters method. The process of successive approximations terminates when there is little difference in the bonds tractions that are obtained in two successive iterations. In the current version of the computer code, the termination of the solution is performed if the relative difference in two successive iterations is less then $\omega = 10^{-5}$.

The non-linear part of the bond deformation curve can be described as a monotonically decreasing or increasing function, the specific form of which depends on the type and characteristics of the bonds in the crack bridged zone. The decreasing non-linear part of the bond deformation curve corresponds to the weakening of bonds as the crack opening increases. The criterion of the limiting elongation of bonds assumes that bond rupture occurs when the limiting elongation of the bond, u_{cr}, is reached with the bond critical stress, σ_{cr}, corresponding to this bond elongation value. Depending on the type of bonds, the magnitude of σ_{cr} may also be zero. Note that the iteration process also terminates (before convergence is reached) if the crack opening on the bridged zone edge exceeds u_{cr}, which corresponds to the impossibility of static equilibrium of the bridged zone for the crack of given length. Two types of the non-linear polynomial decreasing parts of the bond deformation curve were proposed in [13]. It was assumed that the decreasing part of the bond deformation curve is a power-law function (convex and concave) passing through points with the coordinates (u_m, σ_m) and (u_{cr}, σ_{cr}) in the (u, σ) plane (here $\sigma_m = \kappa_b(s)u_m$ is the maximum stress corresponding to transition to non-linear part of the bond-deformation law). The bilinear law of bonds deformation is widely used as effective simplification of the general nonlinear deformation law [19, 27]. It can be written in our case as

$$\sigma(u_b) = \begin{cases} \kappa_b(s)u_b(s), & 0 \le u_b(s) \le u_m \\ \dfrac{\sigma_m}{(\eta-1)}\left[\left(\eta - \dfrac{u_b(s)}{u_m}\right) + \delta\left(\dfrac{u_b(s)}{u_m} - 1\right)\right], & u_m < u_b(s) \le u_{cr}, \end{cases} \tag{10}$$

where the following notations are used

$$\eta = \frac{u_{cr}}{u_m}, \qquad \delta = \frac{\sigma_{cr}}{\sigma_m}. \tag{11}$$

When $\sigma_{cr} < \sigma_m$ ($\delta < 1$), the second dependence in (10) is decreasing (softening). When $\sigma_{cr} > \sigma_m$, it is the increasing one (linear hardening), and the ideal plasticity condition is satisfied when $\delta = 1$. Relative bond elongation before it breaks is defined by the parameter $\eta > 1$.

4. Convergence of iteration solution and bridged stresses

Consider a crack of length $2\ell = 10^{-3}m$ at the interface of half-planes of different materials (the junction of a metal (elastic modulus $E_1 = 135\,GPa$) and a hard reinforced polymer (elastic modulus $E_2 = 25\,GPa$) and Poisson's ratios of the materials $\nu_1 = \nu_2 = 0.35$) with two bridged zones of equal size, filled with bonds. It is assumed that the bond deformation law is a bilinear diagram. The initial elastic part of this diagram has the bond stiffness constant along of

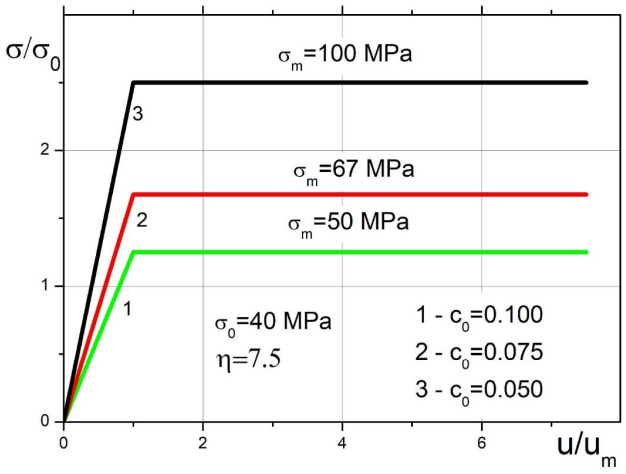

FIG. 7. Bilinear bonds deformation law, perfect plasticity ($\delta = 1$), $u_{cr} = \eta u_m$, variation of initial relative compliance c_0, external load – $\sigma_0 = 40$ MPa

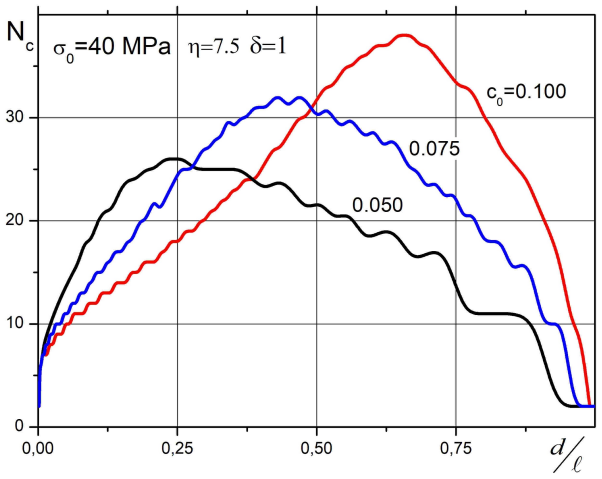

FIG. 8. Number of iterations until solution convergence versus crack bridged zone length, external load – $\sigma_0 = 40$ MPa, variation of initial relative compliance c_0

the bridged zone (see (3)) $\kappa_b = {c_b}^{-1} = E_b/H$, the elastic modulus of nanofibers is $E_b = E_2$ and $\varphi(s,\sigma) = 1$). The crack opening value for transition to the second part of the bond deformation law is assigned as $u_m = 10^{-7}m$. In the calculations, the size of the crack bridged zone is regarded as a free parameter, and the convergence of the iteration process and the stress distributions in the crack bridged zone are analysed for $0 < d \le \ell$.

We will obtain some parameters of the deformation law, expressing them in terms of the relative compliance of bonds c_0. The value of compliance c_b on the elastic part of the deformation diagram for the crack of length $2\ell = 10^{-3}m$ and with the elastic modulus of nanofibers $E_b = 25\,GPa$ can be written as

$$c_b = c_0 \frac{\ell}{E_b} = c_0 \frac{0.5 \cdot 10^{-3}}{25 \cdot 10^9} = 2c_0 \cdot 10^{-8}\text{m/MPa}.$$

According to (9) the maximum elastic stress admissible in bonds is

$$\sigma_m = u_m/c_b = 5/c_0\,\text{MPa}. \tag{12}$$

When $c_0 = 0.1$ (this value of the relative compliance corresponds to elastic deformation of bonds consisting of polymer molecules bundles or nanonfibers), we obtain the values $c_b = 2 \times 10^{-9}$ m/MPa and $\sigma_m = 50$ MPa. These parameters have been used to plot the graphs according to the relation (10) for different dishardening parameters δ (Fig. 3).

To illustrate the iterative solution of the SIDE for $\delta = 1, \eta = 7.5$, some results of calculations at the external load $\sigma_0 = 40$ MPa, and $d/\ell = 0.65$ are presented. The change in the relative bonds compliance along the crack bridged zone $\gamma^{(i)}(s,\sigma)$ is shown in Fig. 4 where

$$\gamma^{(i)}(s,\sigma) = c_b^{(i)}(s,\sigma)\frac{E_b}{H}, \quad s = \frac{x}{\ell}.$$

Here $\gamma^{(1)}(s,\sigma) = 1$ is the initial relative compliance of bonds at the first step of iteration solution. The solution convergence in this example is achieved in $N_c = 36$ iterations. The iterative process converges quite fast and after the 7th-8th iteration the solution parameters change slightly.

Changing the softening parameter in the range $0 \le \delta \le 1$ under constant external load significantly affects on the iteration process convergence.

Due to strong bonds stress concentration in the elastic solution [12], the minimum external load for which non-linear deformation of bonds will occur for $c_0 = 0.1$ is about $\sigma_0 = 11$ MPa [13]. It was numerically revealed that for bilinear dependence under the external load 11 MPa $\le \sigma_0 \le 40$ MPa and $0.9 \le \delta \le 1$, the iterative solution converges at any size of the crack bridged zone, and when parameter δ decreases, regions of solution divergence arise. Iterations number dependencies N_c until the solution convergence versus the crack bridged zone length under the external load $\sigma_0 = 40$ MPa , $\eta = 7.5$ and softening parameter values $\delta = 0.0;\ 0.5;\ 0.75$ is shown in Fig. 5. If $\delta = 0.0$, the divergence zone of the iterative solution occupies more than half of the crack length ($0.13 < d/\ell < 0.87$), for $\delta = 0.50$ the divergence zone is $0.19 < d/\ell < 0.68$ and for $\delta = 0.75$ the divergence zone decreases up to $0.25 < d/\ell < 0.50$. In all these cases of solution divergence, there is no static equilibrium state for the given external load and bonds deformation law. Decreasing the external load allows one to achieve the solution convergence at any values of the parameter δ. For the external load $\sigma_0 = 25$ MPa iterations number dependencies until solution convergence is achieved versus the crack bridged zone length, at variation of softening parameter δ is shown in Fig. 6. The maximum number of iterations depends significantly on the

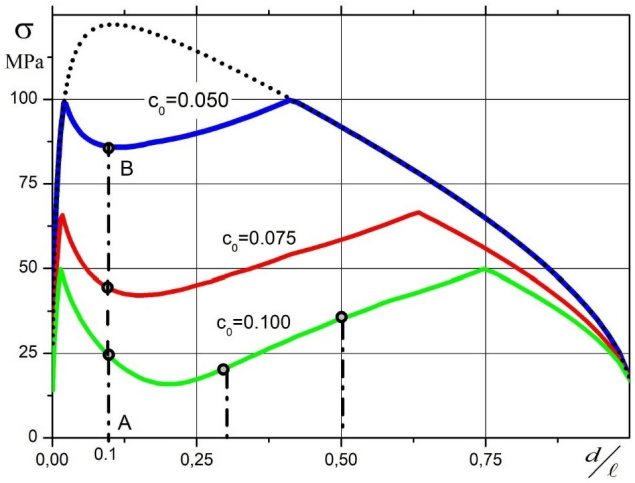

FIG. 9. Traction vector modulus at the crack bridged zone edge vs bridged zone length, $\eta = 2$, $\delta = 0.5$, external load – $\sigma_0 = 17.5$ MPa

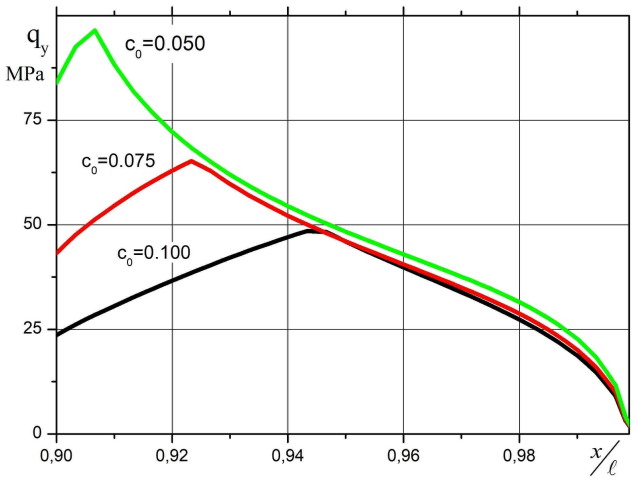

FIG. 10. Normal traction over bridged zone length, $d/\ell = 0.1$, $\eta = 2$, $\delta = 0.5$, external load – $\sigma_0 = 17.5$ MPa

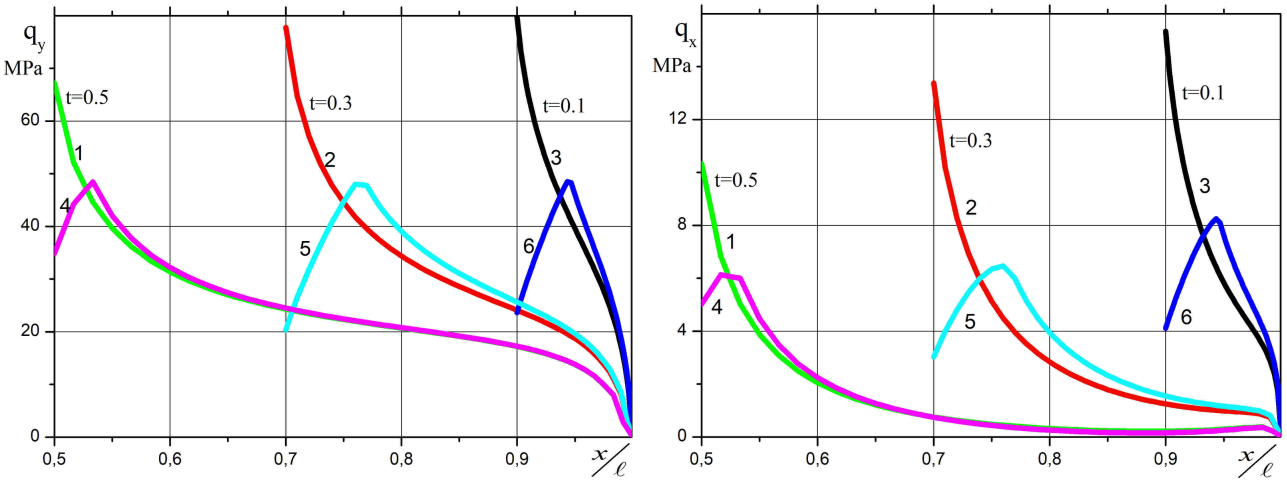

a) **b)**

FIG. 11. Normal **(a)** and shear **(b)** bond traction over bridged zone, $1, 2, 3$ – elastic solution, $4, 5, 6$ – nonlinear solution, $\eta = 2$, $\delta = 0.5$, external load - $\sigma_0 = 17.5$ MPa, $t = d/\ell$

softening parameter, and the position of this maximum keeps when parameter δ changes. The number of iterations for which convergence of the iterative solution process is achieved increases in proportion to the external load value.

Bonds deformation diagrams with different stiffness of the initial elastic part and with the next perfect plasticity part ($\delta = 1$) for the external load $\sigma_0 = 40$ MPa are shown in Fig. 7. As stiffness of the elastic part of this diagram increases then relative compliance of bonds decreases and the maximum stress corresponding to transition to the second part of the diagram increases ($\sigma_m = 67$ MPa and $\sigma_m = 100$ MPa, see (12)).

The maximum number iterations up to the solution convergence reduces with decreasing of bonds relative compliance in view of increasing the stress σ_m. The position of the iteration number maximum shifts towards the small sizes of the crack bridged zone with decreasing of bonds relative compliance (see Fig. 8) because the maximum elastic stress value at the trailing edge of the bridge also shifts to a small zone size, [12].

Decreasing of bonds relative compliance c_0 and keeping $u_m = const$ lead to reduction of crack bridged zone range covered by nonlinear deformation because together with compliance, the crack opening in the bridged zone also decreases in the elastic solution [12]. For relatively big external load, this zone reduction is weak (see Fig. 8), but when the external load decreases, the zone reduction is noticeable. The results for less load shown in Fig. 9–11 were also obtained for different bonds relative compliance but for external load $\sigma_0 = 17.5$ MPa and $\eta = 2$ and $\delta = 0.5$. The dependence of the traction vector module σ at the crack bridged zone edge versus the bridged zone relative size d/ℓ is given in Fig. 9. If the bonds deformation diagram with a dishardening branch is considered then the most significant traction redistribution occurs at the range of the bridged zone sizes d/ℓ close to the position of the bonds traction maximum in linear-elastic

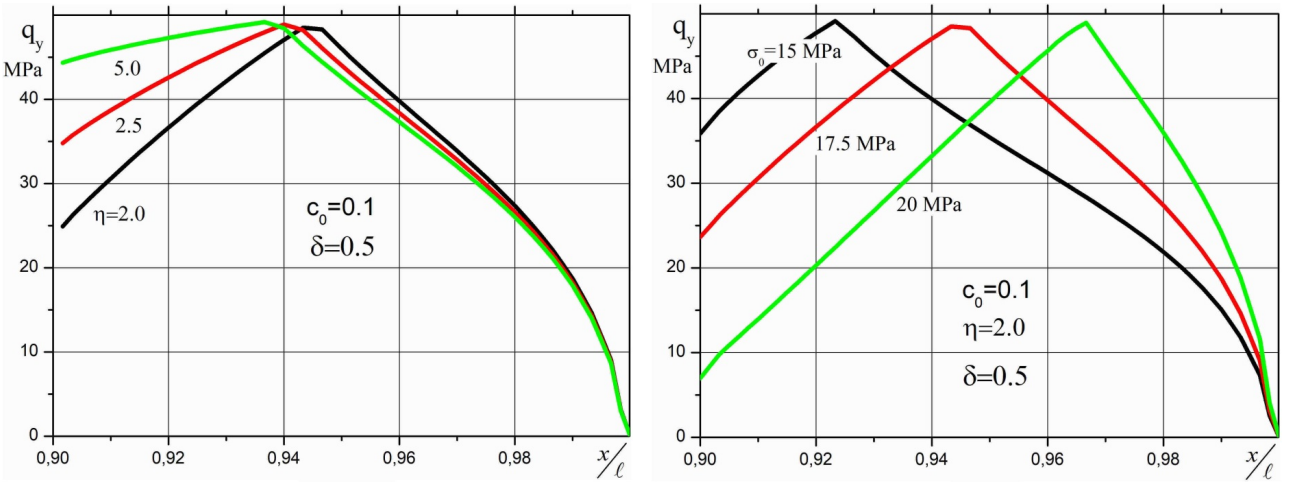

a) **b)**

FIG. 12. Normal bonds tractions over bridged zone, $d/\ell = 0.1$: **(a)** -external load - $\sigma_0 = 17.5$ MPa, variation of parameter η; **(b)** - variation of external load

solution, see the upper line in Fig. 9 which corresponds to linear-elastic solution. In Fig. 9 it can be noticeable seen the decreasing the zone of nonlinear deformation with the decreasing of the relative bond compliance. The effect of the relative bonds compliance variation on the zone of nonlinear deformation size is also illustrated by Fig. 10. At the specified external load ($\sigma_0 = 17.5$ MPa) and at the crack bridged zone length $d/\ell = 0.1$ (the position of this zone size is also marked in Fig. 9, line $A - B$), the size of the bonds nonlinear deformation zone increases if the relative bond compliance c_0 of the linear part of the deformation curve increases.

Distributions of the normal and tangent tractions at the external load $\sigma_0 = 17.5$ MPa, for the bonds deformation parameters of $\eta = 2$, $\delta = 0.5$ and $c_0 = 0.1$ are shown in Fig. 11 for $t = d/\ell = 0.1, 0.3, 0.5$. Stresses at the trailing edge of these bridged zones are shown in Fig. 9 by grey circles. For the given load the range of the crack bridged zones length, in which nonlinear deformation of the bonds is possible is $0.015 \le d/\ell \le 0.75$ (see Fig. 9). As the length of the crack bridged zone increases, the value of elastic stresses in the bonds decreases and, accordingly, a part of the crack bridged zone with nonlinear bonds deformation also decreases.

Changing the parameter $\eta = u_{cr}/u_m$ has a noticeable effect on the distribution of tractions in the region of bonds nonlinear deformation (see Fig. 12a). As $u_{cr}/u_m \to \infty$ than distribution of tractions in the region where $u(x) > u_m$ approaches to uniform $\sigma(x) \to \sigma_m$ since the convergence of iterative process is reached at $u \ll u_{cr}$. Increasing of the external load at fixed length of crack bridged zone and the prescribed bonds deformation curve leads to increasing of bonds nonlinear deformation region (see Fig. 12b).

The stress intensity factors (SIF) for bridged crack depend on the bridged zone length and the parameters of bonds deformation law. Having the distribution of bonds traction over the crack bridged zone, one can calculate the stresses ahead of the crack tip and the SIFs following to [12]:

$$K_{\rm I} + iK_{\rm II} = \lim_{\varrho \to 0} \sqrt{2\pi\varrho}\, \left(\sigma_{yy}(\varrho) + i\sigma_{xy}(\varrho)\right) \left(\frac{\varrho}{2\ell}\right)^{-i\beta}, \tag{13}$$

where $\sigma_{yy}(\varrho)$ and $\sigma_{xy}(\varrho)$ are the stresses ahead the crack tip caused by the external loads and by the bonds traction, ϱ represents the small distance to the crack tip.

The total SIFs due to external load and bonds tractions can be defined as follows

$$K_{\rm I} + iK_{\rm II} = \left(K_{\rm I}^{ext} + K_{\rm I}^{\rm int}(d)\right) + i\left(K_{\rm II}^{ext} + K_{\rm II}^{\rm int}(d)\right),\ K_b = \sqrt{K_I^2 + K_{II}^2}, \tag{14}$$

where $K_{I,II}^{ext}$ and $K_{I,II}^{int}(d)$ are the SIFs caused by the external loads and the bond tractions and K_b is the SIFs modulus.

On the basis of relationships for the stress distribution ahead the interface crack tip under arbitrary loads on the crack faces [28] and using statements (13)-(14), we can obtain the total SIFs for the interface straight bridged crack under the external tension load σ_0 [12]

$$K_{\rm I} + iK_{\rm II} = \sigma_0\sqrt{\pi\ell}\left[(1 + 2i\beta) - \frac{2\cosh(\pi\beta)}{\pi}\int\limits_{1-d/\ell}^{1} \frac{(p_y(\xi) + i\xi p_x(\xi))}{\sqrt{1-\xi^2}}\, d\xi\right], \tag{15}$$

where $p_{x,y}$ are dimensionless amplitudes of bonds traction $q_{x,y}(s)$

$$p_y(\xi) - ip_x(\xi) = (q_y(\xi) - iq_x(\xi))\left(\frac{1-\xi}{1+\xi}\right)^{i\beta}.$$

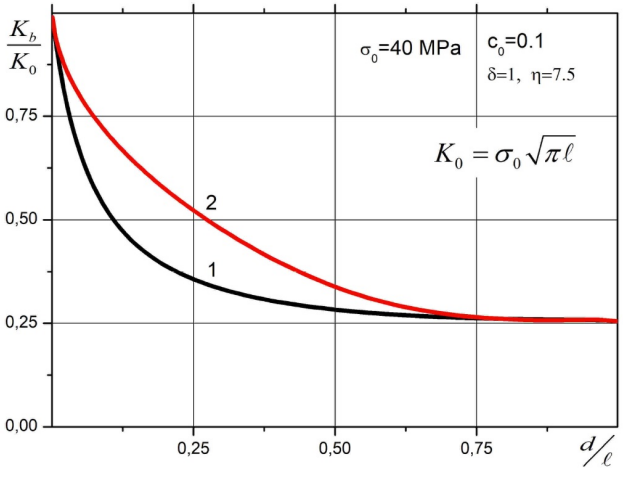

FIG. 13. Relative SIF versus the crack bridged zone length: 1 – linear-elastic bonds; 2 – bilinear bonds deformation law

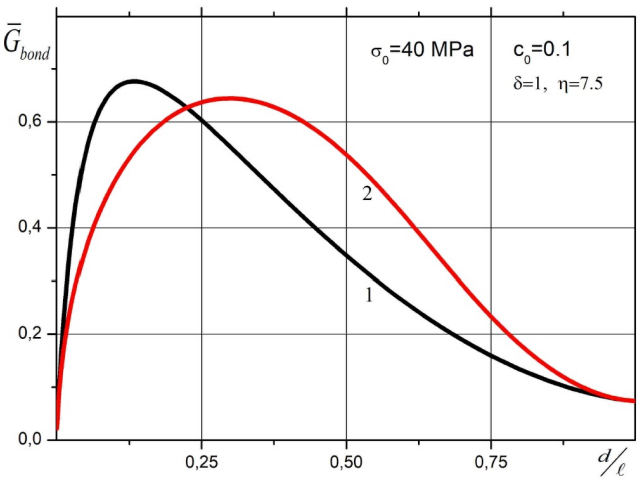

FIG. 14. The rates of deformation energy absorption by bonds: 1 – linear-elastic bonds; 2 – bilinear bonds deformation law

Let's consider the effect of the bond deformation law on the level of the stress intensity factors. Decreasing the softening parameter δ of the bond deformation law leads to reducing of the stress level in the crack bridged zone bonds and, therefore, the SIF increases. Increasing the bond compliance of the linear part bond deformation law leads to nonlinear deformation region enlargement. For example, in Fig. 13, the dependence of the SIF module versus the crack bridged zone length for $\sigma_0 = 40$ MPa and $c_0 = 0.1$ is shown. The nonlinear deformation zone and the degree of softening of the bonds increase with increasing of the bonds compliance.

Two energy characteristics of interfacial bridged cracks are used in bridged cracks growth criterion [15]:

1) the deformation energy release rate associated with the crack tip stress intensity factors (15) is as follows

$$G_{\text{tip}}(d,\ell) = \left(\frac{\kappa_1+1}{\mu_1} + \frac{\kappa_2+1}{\mu_2}\right)\frac{K_b^2}{16\,\cosh^2(\pi\beta)}, \tag{16}$$

2) the rate of the energy absorbtion by bonds associated with the energy necessary to create a unit of new surface of the bridged zone is as follows

$$G_{\text{bond}}(d,\ell) = \int\limits_{\ell-d}^{\ell}\left(\frac{\partial\, u_y(x)}{\partial\,\ell}q_y(u) + \frac{\partial\, u_x(x)}{\partial\,\ell}q_x(u)\right)dx, \quad \bar{G}_{bond} = \frac{G_{bond}\,(d,\ell)}{G_{tip}\,(0,\ell)}, \tag{17}$$

where $\bar{G}_{bond}$ is the dimensionless energy parameter, $G_{tip}(0,\ell)$ is the energy release rate for a crack without bridged zone.

The effect of the bonds deformation law on the bridged crack energy characteristic $\bar{G}_{bond}$ is shown in Fig. 13. For linear-elastic bonds in the crack bridged zone, the rate of energy consumption by bonds reaches a maximum value at a certain size of the bridged zone. Changing the law of bonds deformation results in a change in this energy parameter in the whole non-linear deformation zone, which in this case covers the entire range of the crack bridged zones, as well as a shift in the position of the maximum of this function to larger value of the size of the bridged zone.

5. Conclusion

Parametric description of nonlinear bonds deformation law in the crack bridged zone as the bilinear diagram taking into account sections of softening makes it possible to evaluate effects of basic characteristics of deformation curves on the numerical solution convergence, to investigate tractions distribution over bonds in the crack bridged zone, and also evaluate effect of softening on energy parameters of bridged cracks.

The results obtained can be useful (despite the limited possibility of transferring the solution of non-linear problems to other scales) in the development of methods for solving similar problems for bridged cracks by finite and boundary element methods.

The model of bridged crack at the materials interface allows one to analyze bonds tractions distribution for different laws of bonds deformation, to evaluate the crack limit equilibrium taking into account the kinematic and energy conditions of fracture, see [15]. The model can be used at different fracture scales and allows one to analyse the process of fracture of adhesive compounds and composites from unified point of view, including the stages of defect onset, crack formation and growth at the nano-, micro- and macro-scales.

References

[1] Barenblatt G.I. The mathematical theory of equilibrium cracks in brittle fracture. In H.L. Dryden, Th. von Karman, G. Kuerti, F.H. van den Dungen, and L. Howarth, editors, *Advances in Applied Mechanics*, 1962, **7**, P. 55–129.

[2] Bao G. and Suo Z. Remarks on Crack-Bridging Concepts. *Applied Mechanics Reviews*, 1992, **45**(8), P. 355–366.

[3] Cox B.N. and Marshall D.B. Concepts for bridged cracks in fracture and fatigue. *Acta Metallurgica et Materialia*, 1994, **42**(2), P. 341–363.

[4] Walton J.R. and Weitsman Y. Deformations and stress intensities due to a craze in an extended elastic material. *Journal of Applied Mechanics*, 1984, **51**(1), P. 84–92.

[5] Weitsman Y. Nonlinear analysis of crazes. *ASME. Journal of Applied Mechanics*, 1986, **53**, P. 97–103.

[6] Rose L.R.F. Crack reinforcement by distributed springs. *Journal of the Mechanics and Physics of Solids*, 1987, **35**(4), P. 383–405.

[7] Budiansky B., Amazigo J.C. and Evans A.G. Small-scale crack bridging and the fracture toughness of particulate-reinforced ceramics. *Journal of the Mechanics and Physics of Solids*, 1988, **36**(2), P. 167–187.

[8] Willis J.R. Asymptotic analysis of crack bridging by ductile fibres. *Composites*, 1993, **24**(2), P. 93–97.

[9] Willis J.R. and Movchan N.V. Penny-shaped crack bridged by fibres. *Quarterly of Applied Mathematics*, 1998, **56**(2), P. 327–40.

[10] Grekov M.A. and Morozov N.F. Equilibrium cracks in composites reinforced with unidirectional fibres. *Journal of Applied Mathematics and Mechanics*, 2006, **70**(6), P. 945–955.

[11] Selvadurai A.P.S. Bridged defects in continuously and discretely reinforced solids. *Journal of Engineering Mathematics*, 2015, **95**(1), P. 359–80.

[12] Goldstein R. and Perelmuter M. Modeling of bonding at an interface crack. *International Journal of Fracture*, 1999, **99**, P. 53–79.

[13] Perelmuter M.N. An interface crack with non-linear bonds in a bridged zone. *Journal of Applied Mathematics and Mechanics*, 2011, **75**(1), P. 106–118.

[14] Perelmuter M. Stress analysis of composites with interfacial bridged cracks and damaged zones. *Journal of Physics: Conference Series*, 2022, **2231**, P. 012021–1–012021–7.

[15] Perelmuter M.N. A criterion for the growth of cracks with bonds in the end zone. *Journal of Applied Mathematics and Mechanics*, 2007, **71**(1), P. 137–153.

[16] Perelmuter M.N. Analysis of crack resistance of interfaces between materials. *Mechanics of Solids*, 2020, **55**(4), P. 536–551.

[17] Perelmuter M.N. Mechanical modelling of nanotube-polymer adhesion. *NANOSYSTEMS: PHYSICS, CHEMISTRY, MATHEMATICS*, 2011, **2**(2), P. 119–125.

[18] Wang J., Tong L., and Karihaloo B.L. A bridging law and its application to the analysis of toughness of carbon nanotube-reinforced composites and pull-out of fibres grafted with nanotubes. *Archive of Applied Mechanics*, 2016, **86**(1), P. 361–73.

[19] Hu Y.-G., Ma Y.L., Hu C.P., Lu X.Y. and Gu S.T. Analysis of stress transfer in short fiber-reinforced composites with a partial damage interface by a shear-lag model. *Mechanics of Materials*, 2021, **160**, P. 103966.

[20] Mirjalili V. and Hubert P. Modelling of the carbon nanotube bridging effect on the toughening of polymers and experimental verification. *Composites Science and Technology*, 2010, **70**(10), P. 1537–1543.

[21] Meng Q., Li B., Li T. and Feng X-Q. Effects of nanofiber orientations on the fracture toughness of cellulose nanopaper. *Engineering Fracture Mechanics*, 2018, **194**, P. 350–361.

[22] Chen X., Beyerlein I.J. and Brinson L.C. Bridged crack models for the toughness of composites reinforced with curved nanotubes. *Journal of the Mechanics and Physics of Solids*, 2011, **59**(9), P. 1938–1952.

[23] Budarapu P.R., Kumar S., Prusty B.G., and Paggi M. Stress transfer through the interphase in curved-fiber pullout tests of nanocomposites. *Composites Part B: Engineering*, 2019, **165**, P. 417–434.

[24] Xia Z., Riester L., Curtin W.A., Li H., Sheldon B.W., Liang J., ChangB. and Xu J.M. Direct observation of toughening mechanisms in carbon nanotube ceramic matrix composites. *Acta Materialia*, 2004, **52**(4), P. 931–944.

[25] Xia Z., Curtin W.A. and Sheldon B.W. Fracture toughness of highly ordered carbon nanotube/alumina nanocomposites. *Journal of Engineering Materials and Technology*, 2004, **126**(3), P. 238–244.

[26] England A.H. A crack between dissimilar media. *ASME. Journal of Applied Mechanics*, 1965, **32**(2), P. 400–402.

[27] Alfano G. and Crisfield M.A. Finite element interface models for the delamination analysis of laminated composites: mechanical and computational issues. *International Journal for Numerical Methods in Engineering*, 2001, **50**(7), P. 1701–1736.

[28] Perelmuter M.N. Bridged crack – opening outside of the bridged zone and stresses at the material interface. *Vestnik I. Yakovlev Chuvach State Pedagogical University. Series: Mechanics of a limit state*, 2020, **2**(44), P. 69–77.

Submitted 9 August 2022; revised 17 August 2022; accepted 18 August 2022

Information about the authors:

Mikhail N. Perelmuter – Ishlinsky Institute for Problems in Mechanics RAS, Vernadsky avenue 101-1, Moscow, 119526, Russia; perelm@ipmnet.ru

Conflict of interest: the author declare no conflict of interest.

NANOSYSTEMS:
PHYSICS, CHEMISTRY, MATHEMATICS

Topaev T.N., et al. *Nanosystems: Phys. Chem. Math.*, 2022, **13** (4), 365–371.
http://nanojournal.ifmo.ru
DOI 10.17586/2220-8054-2022-13-4-365-371

Original article

On Keller-Rubinow model for Liesegang structure formation

Timur N. Topaev[a], Anton I. Popov[b], Igor Y. Popov[c]

ITMO University, St. Petersburg, 197101, Russia

[a]topaev-timur@mail.ru, [b]popov239@gmail.com, [c]popov1955@gmail.com

Corresponding author: Anton I. Popov, popov239@gmail.com

ABSTRACT We consider a chemical process, the precipitate of which will be represented by a structure in the form of rings. The study and modeling of this process is relevant, since it becomes possible to form micro- and nanostructures based on this approach. We consider the version of the one-dimensional model of Keller and Rubinow which describes the formation of Liesegang rings due to the Ostwald supersaturation. The dependencies of the results obtained on the initial conditions and the model parameters were studied numerically.

KEYWORDS nanostructures, Liesegang rings, Keller-Rubinow model, chemical reaction modeling.

FOR CITATION Topaev T.N., Popov A.I., Popov I.Y. On Keller-Rubinow model for Liesegang structure formation. *Nanosystems: Phys. Chem. Math.*, 2022, **13** (4), 365–371.

1. Introduction

In 1896, colloid chemist R. E. Liesegang observed a striking regular patterns of reactions with the formation of a precipitate, which are called are formed by bands or Liesegang rings, depending on their shape [1]. The Liesegang phenomenon is a spontaneous pattern formation, which is a periodic distribution of the precipitate discovered in diffusion-limited systems. Over the past century, it has been experimentally attempted to control the periodicity of patterns and structures of precipitates by varying the concentration of the hydrogel or electrolytes, adding organic or inorganic impurities, and applying an electric or pH field [2–7].

These precipitate-forming reactions are briefly described as follows: created electrolyte (e.g., $\mathrm{Pb}\,(\mathrm{NO_3})_2$) at a relatively low concentration Traces are placed in a test tube filled with gel. Then the second is added electrolyte (e.g., KI) in high concentration on top of the gel so that the I-ions diffuse into the gel and react with $\mathrm{Pb}+$ ions, forming created by $\mathrm{PbI2}$. Then layers of $\mathrm{PbI2}$ precipitate appear parallel to the surface diffusion layer. The self-organized structure of Liesegang rings can be attributed to the periodic colloidal structures. Such rings can also be seen on self-organization of bilirubin and protein in cholelithiasis, fungal howling colony on an apple. Self-assembly is the autonomous organization of components into patterns or structures without human intervention. Self-assembling processes are common throughout nature and technology. They involve components from the molecular (crystals) to the planetary (weather systems) scale and many different kinds of interactions [8].

2. Formation of Liesegang rings

The layers of sediment that precipitate in a chemical reaction exhibit several scaling properties. If we denote by X_n the distance from the nth strip to the first one, then it is surprising to observe that $X_{n+1} = \sigma X_n$ for some positive constant σ . This phenomenon is the so-called law of intervals. In addition, it was noticed that there is a positive constant α such that $X_n = \alpha\sqrt{t_n}$, where t_n- is the growth time of the n-th stripe. This relationship is commonly referred to as the law of time. Finally, if $\boldsymbol{w}_n$ denotes the thickness of the nth layer, then it turns out that the ratio w_{n+1}/w_n is approximately constant: this is the so-called width law [9–11]. Fig. 1 shows a sketch of possible configuration; however, this figure does not represent a real experiment but is the result of numerical simulations.

A number of scientific studies have been carried out, both from an experimental and theoretical point of view. Based on the study of these processes, two major theories have been developed.

- The first one is the prenucleation theory, which is based on the ideas of supersaturation: this theory uses the diffusion reaction model proposed by Keller and Rubinow. Numerical calculations clearly show the fulfillment of the width law for one-dimensional Liesegang rings [12–14].
- The second theory is the theory of postnucleation, which is based on the process of maturation of colloidal particles according to Ostwald [15, 16].

Let us consider the existence of discrete precipitates bands that appear in experiments. To do this, we choose a one-dimensional model based on the ideas of Keller and Rubinow. Let a, b and c be the concentrations of the monomers $\mathcal{A}, \mathcal{B}$ and the resulting substance $\mathcal{C}$ during the reaction $\mathcal{A} + \mathcal{B} \to \mathcal{C}$ and let d be the concentration of the substance formed

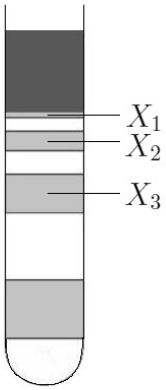

FIG. 1. Liesegang bands in vitro

as a result of precipitation of $\mathcal{C} \to \mathcal{D}$. Then the diffusion reaction process under consideration can be described by the following system:

$$\begin{cases} a_t = D_a a_{xx} - kab, \\ b_t = D_b b_{xx} - kab, \\ c_t = D_c c_{xx} + kab - P(c,d), \\ d_t = P(c,d). \end{cases}$$

Here D_a, D_b and D_c are the diffusion coefficients for A, B and C, respectively. $P(c,d)$ is a precipitate that includes the supersaturation effect. It can be given by the following expression:

$$P(c,d) = \begin{cases} 0 & \text{if } c < C_s \text{ and } d = 0, \\ \lambda\,(c - c^*)^+ & \text{if } c \geq C_s \text{ or } d > 0, \end{cases}$$

where C_s and c^* $(C_s > c^*)$ are the concentrations of supersaturation and saturation, respectively; λ is the settling rate constant $\mathcal{C} \to \mathcal{D}$. The superscript $^+$ denotes the non-negative parts of the corresponding function. We simplify our system under the following assumptions:

(i) The diffusion rate D_b is much less than the diffusion rate D_a,

(ii) The reaction rate k is very fast,

(iii) $c^* = 0$.

Assumption (i) allows us to perform a number of explicit calculations. Without this assumption, we can formally perform similar calculations, but we have no proof of their validity. Assumption (ii) is realistic from the chemical point of view. This leads to a simplification of the system:

$$\begin{cases} a_t = D_a a_{xx} - kab, & 0 < x < \infty,\ t > 0, \\ b_t = -kab, & 0 < x < \infty,\ t > 0, \\ c_t = D_c c_{xx} + kab - P(c,d), & 0 < x < \infty,\ t > 0, \\ d_t = P(c,d), & 0 < x < \infty,\ t > 0. \end{cases}$$

Here we assume that k is very large [10]. Initial and boundary conditions are as follows

$$\begin{cases} a(x,0) = c(x,0) = d(x,0) = 0, \quad b(x,0) = b_0, \quad 0 < x < \infty, \\ a(0,t) = a_0, \quad c_x(0,t) = 0, \quad t > 0, \end{cases}$$

where a_0 and b_0 are positive constants. In experiments, a_0 is much larger than b_0. Let's run numerical simulations where we assume (iii) $c^* > 0$. Note that there have been several precipitation events; these events are characterized by peaks in the function d and the corresponding discontinuities in the spatial derivative of the function c.

Let's start by rewriting the problems taking into account our assumption that $c^* = 0$

$$(\mathrm{P}_k^*) \quad \begin{cases} a_t = D_a a_{xx} - kab, & 0 < x < \infty,\ t > 0, \\ b_t = -kab, & 0 < x < \infty,\ t > 0, \\ c_t = Dc_{xx} + kab - \lambda c \tilde{H}\left((c - C_s)^+ + d\right), & 0 < x < \infty,\ t > 0 \\ d_t = \lambda c \tilde{H}\left((c - C_s)^+ + d\right), & 0 < x < \infty,\ t > 0, \\ a(0,t) = a_0 > 0, & t > 0, \\ c_x(0,t) = 0, & t > 0, \\ a(x,0) = c(x,0) = d(x,0) = 0; \quad b(x,0) = b_0 > 0 & 0 < x < \infty. \end{cases}$$

Here D_c is now replaced by D and $\tilde{H}$ is the Heaviside function.

$$\tilde{H}(y) = \begin{cases} 0 & \text{if } y \le 0, \\ 1 & \text{if } y > 0. \end{cases}$$

The equations for c and d (in the P_k^* problem) were formulated to express the chemical assumption that $d_t = \lambda c$ if $c > C_s$ or if $d > 0$, otherwise $d_t = 0$. The above formulation introduces a non-uniqueness problem, which can be avoided if we choose a different formulation. On the one hand, the equations for c and d are not continuous. It is for this reason that we cannot be sure that the solution is unique, even if $c - C_s \le 0$ is everywhere. The chemical arguments imply that $d(x,t)$ can be positive if and only if its growth was caused by a positive value of $c(x,\tau) - C_s$ for some τ $leqt$. This leads us to find a solution such that $d(x,t) = 0$ if $c(x,\tau) \le C_s$ for all $\tau < t$. Let us then reformulate our problem P_k^* in a slightly different way, more precisely, from the chemical point of view, since this excludes any possibility of spontaneous growth of d. Let's try to assume that c is continuous, then we introduce the function

$$w(x,t) = \int_0^t (c(x,s) - C_s)^+ \, ds.$$

We claim that $w(x,t) > 0$ if and only if $(c(x,t) - C_s)^+ + d(x,t) > 0$. Indeed, let's first assume that $w(\bar{x},\bar{t}) > 0$. Then there exists $t_1 < t_2 \le \bar{t}$ such that $c(x,t) > C_s$ for all $t_1 < t < t_2$. The differential equation for d implies that $d(\bar{x},\bar{t}) > 0$, which in turn means that $(c(\bar{x},\bar{t}) - C_s)^+ + d(\bar{x},\bar{t}) > 0$. Conversely, if $w(x,t) = 0$, then it is clear that $c(x,\tau) \le C_s$ for all $\tau \le t$. Due to the chemical arguments discussed above, we assume that $d(x,t) = 0$. Therefore, it is quite reasonable to replace the argument $(c - C_s)^+ + d$ from $\tilde{H}$ with the new argument w. Note that with such a change in the arguments, any reference to d can be completely excluded from the P_k^* problem. Let's continue consideration of problem P_k^*:

$$(\mathrm{P}_k^*) \begin{cases} a_t = D_a a_{xx} - kab, & 0 < x < \infty,\ t > 0, \\ b_t = -kab, & 0 < x < \infty,\ t > 0, \\ c_t = Dc_{xx} + kab - \lambda c \tilde{H}\left(\int_0^t (c(x,\tau) - C_s)^+ \, d\tau\right), & 0 < x < \infty,\ t > 0, \\ a(0,t) = a_0 > 0, & t > 0, \\ c_x(0,t) = 0, & t > 0, \\ a(x,0) = c(x,0) = 0; \quad b(x,0) = b_0 > 0, & 0 < x < \infty. \end{cases}$$

Let's consider the P_k^* problem for very large values of k, or, in other words, to study its asymptotic behavior as k tends to infinity. In this problem, we will use the notation a_k, b_k, c_k to solve P_k^*. Let's solve a_k and b_k first, then calculate ka_kb_k and use this expression as the given source in the equation for c_k. In particular, we will be interested in the rationale for this approach, since k tends to infinity. The behavior of a_k and b_k was considered in [10, 11]. Namely, it was shown that $a := \lim\limits_{k\to\infty} a_k$ is the solution of the single-phase Stefan problem with the melting boundary $\zeta(t) = \alpha\sqrt{t}$ for some positive constant α.

$$(\mathrm{P}_k) \begin{cases} c_{kt} = Dc_{kxx} + ka_kb_k - \lambda c_k \tilde{H}\left(\int_0^t (c_k(x,\tau) - C_s)^+\right) d\tau\Big), & 0 < x < \infty,\ t > 0, \\ c_{kx}(0,t) = 0, & t > 0, \\ c_k(x,0) = 0, & x > 0. \end{cases}$$

3. Modeling

To simulate these rings, let's try to reproduce the Liesegang phenomenon numerically. To simulate the chemical process described in the previous chapter, we will simulate the process of diffusion of two monomers $\mathcal{A}$, $\mathcal{B}$ and the substance $\mathcal{A}+\mathcal{B}$ obtained in the course of a chemical reaction $\rightarrow \mathcal{C}$. As a result of calculations, we obtain the concentration of the precipitate $\mathcal{D}$, which precipitates from the reaction product. We will model the reactions on the segment $X = [0, 1]$.

We inherit the initial conditions for our substances, as well as the initial conditions of the process. Since the considered chemical reaction is described by differential equations, therefore, the time step δt must be chosen according to the Courant-Friedrichs-Levy criterion, which is necessary for the stability of our model.

Let us consider the process of diffusion of the substance $\mathcal{A}$. The distribution of the substance concentration $\mathcal{A}$ on X is shown in Fig. 2 for two time moments $t_1 = 0, t_2 = 600$ (we use δt as a time unit. The distribution of the $\mathcal{B}$ substance

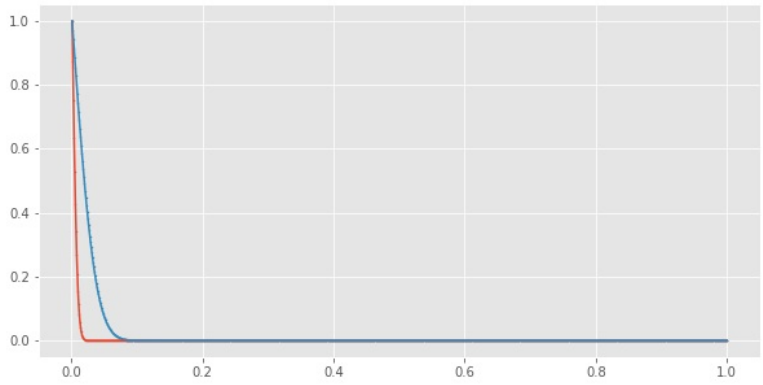

FIG. 2. Graph of dependence of substance concentration $\mathcal{A}$ on X. Where, the red line on the graph is the concentration of substance $\mathcal{A}$ at $t_1 = 0$, and the blue line on the graph shows the concentration of substance $\mathcal{A}$ at $t_2 = 600$ (arbitrary units)

will proceed in a similar way to the spread of the $\mathcal{A}$ substance considered above, only with a different diffusion rate, until these substances react and some product $\mathcal{C}$ is formed. The chemical reaction product $\mathcal{C}$ will also begin to diffuse through the test tube. The distribution of the concentration $\mathcal{C}$ over the test tube on the graph is shown in Fig. 3. As you can see on the graph, the diffusion of $\mathcal{C}$ starts at some point in the tube where the chemical reaction started after the diffusing substances $\mathcal{A}$ and $\mathcal{B}$ entered into a chemical reaction.

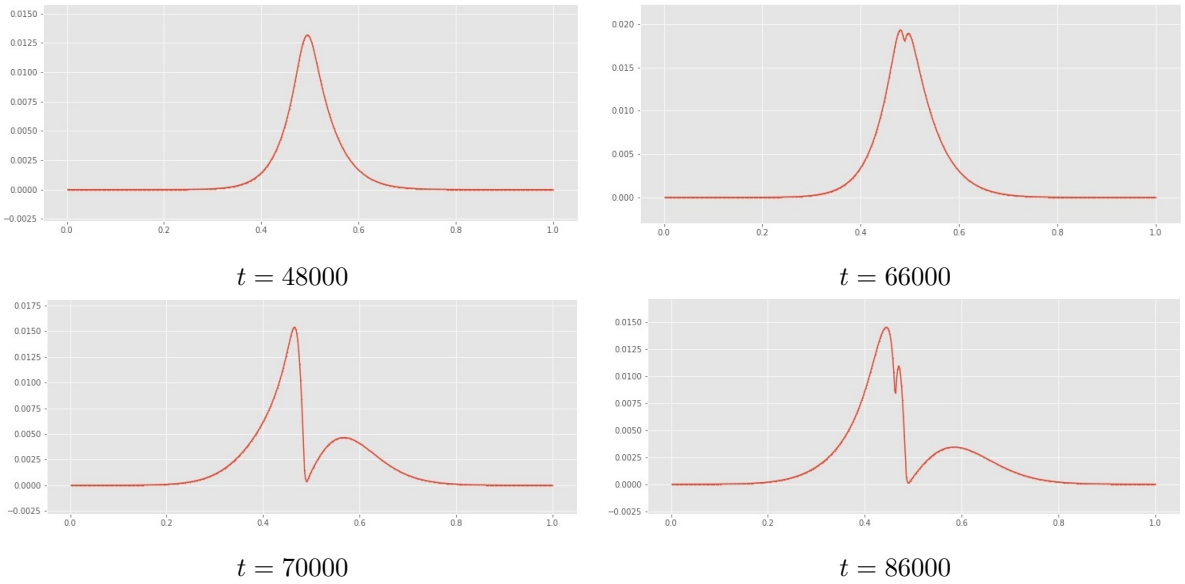

FIG. 3. Plot of $\mathcal{C}$ product concentration versus X over time

We can observe the refraction of the graph of the concentration of the substance $\mathcal{C}$ at some point in time. At this time moment, $\mathcal{C} \rightarrow \mathcal{D}$ will precipitate. We will be interested in the $\mathcal{D}$ precipitate, since rings will form when it is isolated. Let's look at the graphs of the concentration of the substance $\mathcal{D}$, which will fall out over time. It can be noted that the

refraction of the $\mathcal{C}$ concentration graph corresponds to the beginning of $\mathcal{C}$ precipitation. It is at these moments in time that Liesegang rings will appear or grow.

Let's make sure on the graphs that our model will satisfy the law of time and distance, respectively. It is shown in Fig. 4.

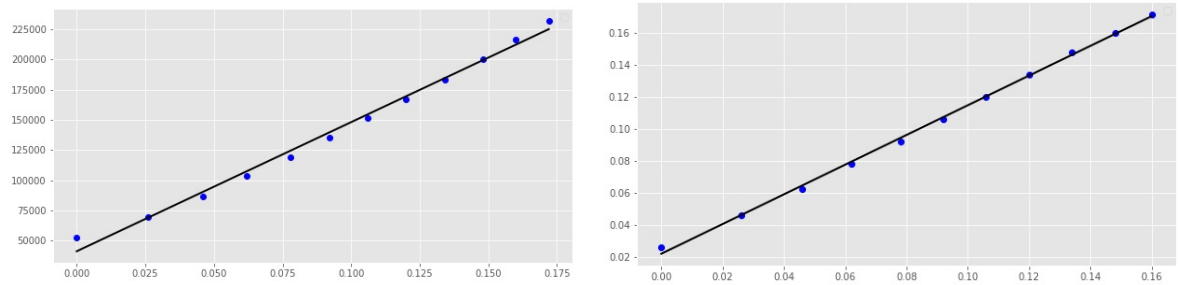

(A) (B)

FIG. 4. (A)Time low. Graph of square root of formation time versus distance between the first and N-th rings. (B)Distance low. Graph of the distance between the first and rings and the first and $(N+1)$-th rings N-th

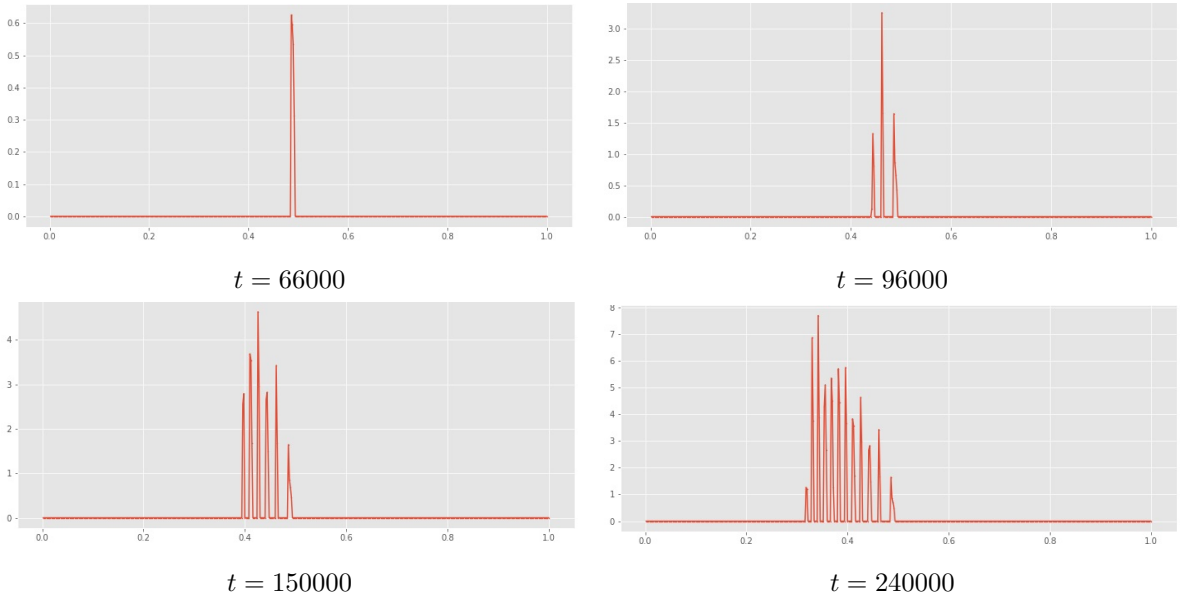

$t = 66000$ $t = 96000$

$t = 150000$ $t = 240000$

FIG. 5. Graph of the distribution of the sediment concentration $\mathcal{D}$ on X over time

Formation of Liesegang bands, i.e. the distribution of the sediment concentration $\mathcal{D}$ on X for different time moments is shown in Fig. 5.

Let us study the dependence of the ring structure on the diffusion rate parameter. The simulation of the chemical process showed that over time, a different amount of $\mathcal{D}$ precipitate appears. The required amount of sediment for further study was obtained at the time moment $t = 260000$ (arbitrary unit). All further simulations were performed with this value of t.

One can observe an interesting behavior of our model when the diffusion rate parameter $\dashv D_a$ changes. When studying the chemical model, we used the tabular value of the parameter $D_a = 4e - 7$. We performed calculations by increasing the value of the parameter D_a. When this parameter was changed, we began to observe a different arrangement of the formed Liesegang rings (see Fig. 6). When the value of this parameter increases to $D_a = 8e - 7$, a shift is observed on the graph of the distribution of the sediment concentration $\mathcal{D}$ on X, the general group of Liesegang rings to the right. It can also be seen that one of the peaks of the distribution of the sediment concentration $\mathcal{D}$ on X budded from the general group of peaks, thereby violating the linearity of the distance law. One can see that the following increase of D_a confirm this tendency. Another interesting peculiarity is that the total number of rings decreased.

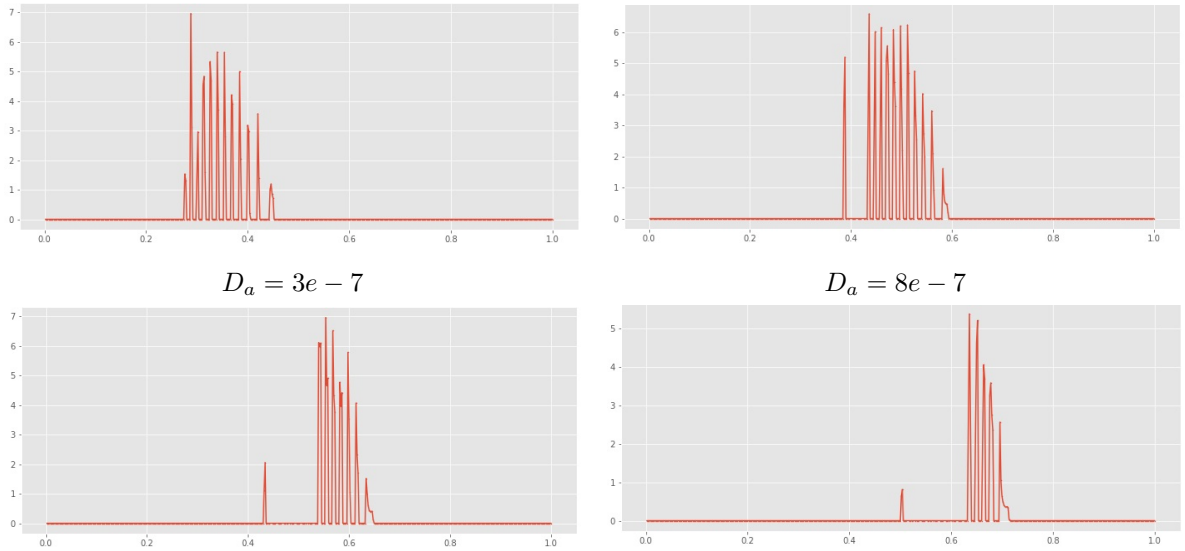

FIG. 6. Graphs of the dependence of the sediment concentration $\mathcal{D}$ on X, for different values of the diffusion rate parameter D_a

4. Conclusion

The aim of this work was to provide a working model simulating the chemical process of growing Liesegang rings. To construct such a model, theoretical provisions were studied, and systems of differential equations were described that characterize the diffusion process. We implemented the one-dimensional model of Keller and Rubinow, used in their analysis of the Ostwald supersaturation theory, to grow Liesegang rings. For numerical analysis, we used the `C++` [19] programming language and the `Armadillo` [17] library for linear algebra and scientific computing. The programming language `Python` [20, 21] and the package for data processing and analysis `Pandas` [18] were used for data analysis. To test this model for correctness, we checked the laws of time and distance. It showed satisfactory results.

The resulting model for simulating the growth of Liesegang rings gives us the opportunity to study the chemical process under various initial conditions and parameters. The beginning of the formation of the reaction product $\mathcal{C}$ is shown on the graph of the distribution of the concentration of $\mathcal{C}$ on X, which corresponds to the beginning of the chemical reaction between substances $\mathcal{A}$ and $\mathcal{B}$. A plot of $\mathcal{C}$ concentration versus X over time shows an interesting behavior, namely its refraction. Also, the product $\mathcal{C}$, in turn, precipitates $\mathcal{C} \to \mathcal{D}$. We have considered in detail the dependence of the formation of the precipitate and the rings themselves, respectively, on the diffusion propagation of $\mathcal{C}$. We managed to understand the dependence of $\mathcal{C}$ on its sediment $\mathcal{D}$. Namely, we learned that the moment of time when the precipitate begins to fall out is equal to the moment of the beginning of refraction of the graph of the dependence of the concentration $\mathcal{C}$ on X. And also that each subsequent refraction of the graph of the distribution of the concentration of $\mathcal{C}$ on X will tell us about the growth of Liesegang rings, or an increase in the number of Liesegang rings.

We also simulated the growth of Liesegang rings for other values of the parameter D_a, which is responsible for the rate of diffusion propagation. When changing the values of this parameter, we observed a shift in the location of the rings. There is a certain relationship between an increase in the value of the parameter D_a and a shift of the Liesegang rings on the graph of the distribution of the concentration $\mathcal{D}$ on X to the right. There is also some budding of one of the rings from the general group of rings.

References

[1] Liesegang R.E. Über einige Eigenschaften von Gallerten. *Naturwiss. Wochenschr.*, 1896, **11**, P. 353–362.
[2] Young Shin Cho, Miyoung Moon, Gabor Hollo, Istvan Lagzi, Sung Ho Yang. Bioinspired Control of Calcium Phosphate Liesegang Patterns Using Anionic Polyelectrolytes. *Langmuir*, 2022, **38**(8), P. 2515–2524.
[3] Eltantawy M.M., Belokon M.A., Belogub E.V., Ledovich O.I., Skorb E.V., Ulasevich S.A. Self-Assembled Liesegang Rings of Hydroxyapatite for Cell Culturing. *Adv. NanoBiomed Res.*, 2021, **1**, P. 200048 10.1002/anbr.202000048.
[4] Morsali M., Khan M.T.A., Ashirov R., Hollo G., Baytekin H.T., Lagzi I., Baytekin B. Mechanical Control of Periodic Precipitation in Stretchable Gels to Retrieve Information on Elastic Deformation and for the Complex Patterning of Matter. *Adv. Mater.*, 2020, **32**, P. 1905779.
[5] Walliser R.M., Boudoire F., Orosz E., Toth R., Braun A., Constable E.C., Racz Z., Lagzi I. Growth of Nanoparticles and Microparticles by Controlled Reaction-Diffusion Processes. *Langmuir*, 2015, **31**, P. 1828–1834.
[6] Lagzi I., Kowalczyk B., Grzybowski B.A. Liesegang Rings Engineered from Charged Nanoparticles. *J. Am. Chem. Soc.*, 2009, **132**, P. 58–60.
[7] Jo M., Cho Y.S., Hollo G., Choi J., Lagzi I., Yang S.H. Spatiotemporal and Microscopic Analysis of Asymmetric Liesegang Bands: Diffusion-Limited Crystallization of Calcium Phosphate in a Hydrogel. *Cryst. Growth Des.*, 2021, **21**, P. 6119–6128.

[8] Whitesides G.M., Grzybowski B. Self-Assembly at All Scales. *Science*, 2002, **295**(5564), P. 2418–2421.
[9] Jablczynski K. Zur Theorie der Liesegangschen Ringe. *Bull. Soc. Chim.* Princeton University Press, 1923, 1592 p.
[10] Hilhorst D., van der Hout R., Peletier L.A. The fast reaction limit for a reaction-diffusion system. *J. Math. Analysis and Appl.*, 1996, **199**, P. 349–373.
[11] Hilhorst D., van der Hout R., Mimura M., Ohnishi I. A Mathematical study of the one-dimensional Keller and Rubinow model for Liesegang bands. *Journal of Statistical Physics*, 2009, **135**, P. 107–132.
[12] Keller J.B., Rubinow S.I. Recurrent precipitation and Liesegang rings. *J. Chem. Phys*, 1981, **74**, P. 5000–5007.
[13] Duley J.M., Fowler A.C., Moyles I.R., O'Brien S.B.G. On the Keller-Rubinow model for Liesegang ring formation. *Proc. R. Soc. A.*, 2017, **473**, P. 20170128.
[14] Ohnishi I. and Mimura M. A mathematical aspect for Liesegang phenomena. Proceeding of Equadiff. Comenius University, Bratislava, Slovakia, July 25–29, 2005. P. 343–352.
[15] Ostwald W. *Zur Theorie der Liesegangschen Ringe*. Princeton University Press, Princeton, NJ, 1925, P. 380–390.
[16] Kai S., Muller. Spatial and temporal macroscopic structures in chemical reaction system: precipitation patterns and interfacial motion. *Sci. Form.*, 1985, **1**, P. 8–38.
[17] Doerr B. and Doerr C. *Armadillo library for linear algebra scientific computing* [Electronic resource], 2016. URL: http://arma.sourceforge.net/docs.html
[18] Doerr B. and Doerr C. Pandas documentation [Electronic resource]. 2020. URL: https://pandas.pydata.org/
[19] Doerr B. and Doerr C. C++ reference [Electronic resource]. 2019. URL: https://en.cppreference.com/w/
[20] Doerr B. and Doerr C. Python Doc [Electronic resource]. 2019. URL: https://docs.python.org/3/
[21] Doerr B. and Doerr C. Jupyter notebook [Electronic resource]. 2019. URL: https://jupyter.org/documentation

Submitted 7 May 2022; revised 15 July 2022; accepted 31 July 2022

Information about the authors:

Timur N. Topaev – ITMO University, Kronverkskiy, 49, St. Petersburg, 197101, Russia; topaev-timur@mail.ru

Anton I. Popov – ITMO University, Kronverkskiy, 49, St. Petersburg, 197101, Russia; popov239@gmail.com

Igor Y. Popov – ITMO University, Kronverkskiy, 49, St. Petersburg, 197101, Russia; popov1955@gmail.com

Conflict of interest: the authors declare no conflict of interest.

NANOSYSTEMS:
PHYSICS, CHEMISTRY, MATHEMATICS

Goncharov R.K., et al. *Nanosystems: Phys. Chem. Math.*, 2022, **13** (4), 372–391.
http://nanojournal.ifmo.ru
DOI 10.17586/2220-8054-2022-13-4-372-391

Original article

Continuous-variable quantum key distribution: security analysis with trusted hardware noise against general attacks

Roman K. Goncharov[a], Alexei D. Kiselev[b], Eduard O. Samsonov[c], Vladimir I. Egorov[d]

ITMO University, Kronverkskiy, 49, St. Petersburg, 197101, Russia

[a]rkgoncharov@itmo.ru, [b]alexei.d.kiselev@gmail.com, [c]eosamsonov@itmo.ru, [d]viegorov@itmo.ru

Corresponding author: R. K. Goncharov, rkgoncharov@itmo.ru

PACS 03.67.-a, 42.50.-p

ABSTRACT In this paper, using the full security framework for continuous-variable quantum key distribution (CV-QKD), we provide a composable security proof for the CV-QKD system in a realistic implementation. We take into account equipment losses and contributions from various components of excess noise and evaluate performance against collective and coherent attacks assuming trusted hardware noise. The calculation showed that the system remains operable at channel losses up to 10.2 dB in the presence of collective attacks and up to 7.5 dB in the presence of coherent ones.

KEYWORDS quantum key distribution, continuous variables, security proof, composability, trusted noise.

ACKNOWLEDGEMENTS The work was done by Leading Research Center "National Center for Quantum Internet" of ITMO University by order of JSCo Russian Railways.

FOR CITATION Goncharov R. K., Kiselev A. D., Samsonov E. O., Egorov V. I. Continuous-variable quantum key distribution: security analysis with trusted hardware noise against general attacks. *Nanosystems: Phys. Chem. Math.*, 2022, **13** (4), 372–391.

1. Introduction

Quantum key distribution (QKD) [1] is a special method of generating a secure key between two parties, Alice and Bob, which will ensure the privacy of transmitted information in the era of the quantum computer. Historically, the first protocols to be presented were discrete variable (DV) ones [2, 3], where information was encoded in the state of a single photon: polarization, phase or time bin. However, over time, continuous-variable (CV) protocols [4–6] have been introduced, which are considered more efficient, high-rate and cost-effective due to the use of homodyne/heterodyne detection systems instead of single photon detectors.

Considering the security of QKD systems, one must take into account that each of them has a finite physical implementation that is not ideal, which opens up opportunities for the eavesdropper, Eve, to carry out a multiple attacks and extract part of the secret key. To prevent this threat, for each protocol, a complex system for assessing the information available to Eve and the acceptable level of errors is being developed.

Currently, a fairly significant amount of work has been presented, covering the topic of security of CV-QKD protocols [7–14]. Of the protocols most suitable for practical implementation, the GG02 protocol [6, 15] stands out, for which the security is proven against coherent (general) attacks, taking into account the finite-key effects. Moreover, models of untrusted and trusted hardware noise are considered [12]. The latter is preferable, since many security levels imply that Eve does not have access to Alice's and Bob's blocks, moreover, accounting for untrusted noise makes the protocol essentially unusable.

Thus, this paper will present a full security proof of CV-QKD on a realistic implementation with trusted hardware noise against general attacks. In Section 2 we describe an optical configuration of the CV-QKD scheme, in Sections 3–5 we give a description of the protocol in the trusted noise scenario and consider a possibility of specific attacks that go beyond general security proof framework. In Section 6 we provide a technique of evaluation and monitoring of experimental parameters and in Section 7 we clarify security analysis and estimate the finite-length secure key generation rate. In Section 8 we discuss the results and draw the appropriate conclusions.

2. Optical CV-QKD scheme configuration

The optical scheme of the described protocol is shown in Fig. 1 and consists of the following blocks:

- Alice block, in which the generation of signal states (Gaussian modulation) and a local oscillator (LO) is carried out, after which, by means of polarization-time multiplexing, they sent to Bob. Gaussian modulation itself can be done in two stages: amplitude modulation with a Rayleigh distribution and phase modulation with a uniform phase distribution; as a result, the complex signal amplitude value will correspond to the Gaussian distribution [16]. It should also be noted that the need for reference signal, which is used in the phase protocols of the DV-QKD [3, 17], is no longer necessary in this case.
- Quantum channel block, which in this work is represented by an optical fiber.
- Bob block, in which demultiplexing and heterodyne detection are carried out.

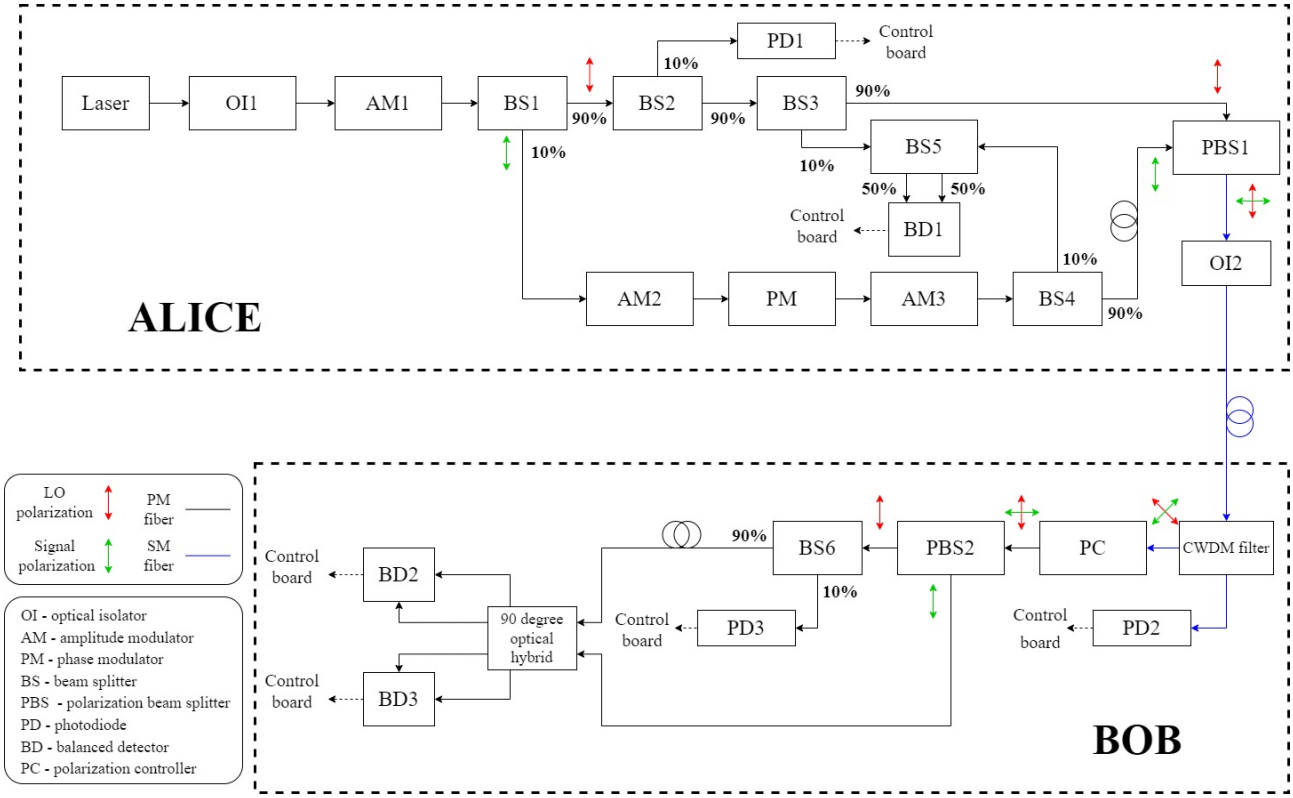

FIG. 1. Scheme of typical setup for CV-QKD with Gaussian modulation and heterodyne detection.

In the considered configuration, Alice uses the same laser to generate LO and signal states modulated according to the Gaussian distribution, which then experience the procedure of polarization-time multiplexing before sending through the quantum channel. Bob then performs a demultiplexing procedure and heterodyne detection. Fig. 1 also shows additional elements for monitoring.

In Alice block, a continuous wave (CW) laser with a central wavelength of 1550 nm and a spectral line width of 100 kHz is used. The width of the spectral line makes it possible to estimate the coherence time, and also affects the amount of phase noise. Coherent detection systems require the use of sources with a narrow spectral line. The Bob block uses a polarization-maintaining optical fiber of the Panda type due to the sensitivity of the optoelectronic components to polarization and implementation polarization multiplexing. The optical isolator OI1 is used in order to avoid backlight due to reflection on the optical scheme elements in the laser module. An amplitude modulator AM1 is used to form identical optical pulses with a repetition rate of 50 MHz and a duration of 3 ns. Laser pulses are then divided by amplitude into two arms using a 10/90 beam splitter BS1: the signal arm (10%) and LO arm (90%).

The second 90/10 beam splitter BS2 in the LO arm is used to separate 10% of the optical pulse power and direct it to the photodiode PD1, which allows one to organize feedback with an amplitude modulator to control the power of LO.

In the signal arm, Gaussian modulation of optical pulses occurs using an amplitude modulator AM2 and a phase modulator PM. Amplitude modulation is realized according to the Rayleigh distribution with a given variance. Phase modulation is implemented according to a uniform distribution in the range from 0 to 2π. The amplitude modulator AM3 is used as a fast attenuator with a wide range of extinction coefficient to set the average number of photons in an optical pulse. Every second pulse in the signal arm is a reference pulse and is not subjected to amplitude and phase modulation on amplitude modulators AM1 and AM2 and phase modulator PM. The modulators are controlled by a digital-to-analog converter (DAC), which is not indicated on Fig. 1.

In the signal and LO arms, 90:10 beam splitters BS3 and BS4 are used to separate part of the signal and LO pulses to control the power and variance (feedback for amplitude modulators AM1 and AM2) using a homodyne detector, which is carried out using 50/50 beam splitter BS5 and balanced detector BD1. For successful balanced detection, it is necessary that the optical paths of the signal and LO are identical.

In order to avoid the interaction of signal pulses and LO before their detection in Bob's side, time-division and polarization multiplexing is used. Time-division multiplexing is implemented by increasing length of the signal arm in Alice's side by an amount corresponding to half the pulse repetition period compared to LO arm. Polarization multiplexing is implemented using a polarization combiner PBS1 with a single-mode (SM) output, to which polarization maintaining fibers of two arms are connected with mutually orthogonal slow optical axes.

A SM optical isolator OI2 is used to prevent backlighting of Alice from the channel output. Alice and Bob are connected through a SM optical fiber of the G.652.D standard with a length of 25 km.

On Bob side, the signal and LO enter the CWDM filter with a central wavelength of 1550 nm. The use of a CWDM filter is due to protection against backlight at a different wavelength from the channel input. The output of the CWDM filter which corresponds to the reflected light is connected with the monitor photodiode PD2, by the signal from which one can analyse the presence or absence of backlights. The output of the CWDM filter which corresponds to the transmitted light, is connected with the input of the polarization controller PC, which is used to compensate for polarization distortions in the SM optical fiber between Alice and Bob. The input of a polarization beam splitter PBS2 is connected to the output of the polarization controller, which is used for polarization demultiplexing of the signal and LO. In the LO arm, there is a delay line for demultiplexing signals in time domain and also a 90:10 beam splitter BS6, which is used to organize the feedback of the polarization controller: a part of LO pulse power (10%) is sent to the photodiode PD3 to determine the optical power. The other output of the 90/10 beam splitter, which corresponds to 90% optical power, is connected to LO input of the 90-degree optical hybrid. In the signal arm, after the output of the polarizing beam splitter PBS2, it is connected to the signal input of the 90-degree optical hybrid. The 90-degree optical hybrid has four outputs: two outputs correspond to the sum and the difference amplitude of the signal field and LO with zero additional relative phase and two outputs correspond to an additional phase equal to 90 degrees. The outputs of the 90-degree optical hybrid are connected to the inputs of two balanced detectors. The signal from the balanced detectors is entered to analog-to-digital converter (ADC), which is not shown in Fig. 1).

3. GG02 protocol features

3.1. Gaussian modulation of coherent states

In the CV-QKD with Gaussian modulation [6,15], Alice prepares coherent states (with a given value of amplitude and phase) with quadrature components q and p which are realizations of two independent and identically distributed random variables $\mathcal{Q}$ and $\mathcal{P}$, which have the same Gaussian distribution with zero mean and given variance

$$\mathcal{Q} \sim \mathcal{P} \sim \mathcal{N}\left(0,\, \tilde{V}_{\mathrm{A}}\right), \tag{1}$$

where $\tilde{V}_{\mathrm{A}}$ is a modulation variance.

Alice prepares a sequence of coherent states $|\alpha_1\rangle, \ldots |\alpha_j\rangle, \ldots, |\alpha_N\rangle$ of the form:

$$|\alpha_j\rangle = |q_j + ip_j\rangle, \text{ for } q_j \in \mathcal{Q},\, p_j \in \mathcal{P}. \tag{2}$$

In this case, the equations for the eigenvalues are satisfied in shot noise units (SNU)

$$\hat{a}|\alpha_j\rangle = \alpha_j|\alpha_j\rangle, \tag{3}$$

$$\frac{1}{2}(\hat{q} + i\hat{p})|\alpha_j\rangle = (q_j + ip_j)|\alpha_j\rangle, \tag{4}$$

where $\hat{a}$ is a creation operator and $\hat{p}$, $\hat{q}$ are a quadrature operators.

The mean photon number in each individual state is estimated as follows

$$\langle n_j\rangle = \langle\alpha_j|\hat{n}|\alpha_j\rangle = |\alpha_j|^2 = q_j^2 + p_j^2. \tag{5}$$

Given that q_j and p_j taken from the distribution in Eq. (1), the mean photon number over the ensemble of states prepared by Alice is

$$\langle n\rangle = \langle\mathcal{Q}^2\rangle + \langle\mathcal{P}^2\rangle = 2\tilde{V}_{\mathrm{A}}. \tag{6}$$

To calculate the variance of the quadrature operator $V(\hat{q}) = \langle \hat{q}^2 \rangle - \langle \hat{q} \rangle^2$, it is necessary to find the averaged values:

$$\langle \hat{q} \rangle = \langle \alpha | \hat{q} | \alpha \rangle = 0, \tag{7}$$

$$\begin{aligned} \langle \hat{q}^2 \rangle &= \langle \alpha | \hat{q}^2 | \alpha \rangle = \langle \alpha | (\hat{a} + \hat{a}^\dagger)^2 | \alpha \rangle = \\ &= \langle \alpha | \hat{a}^2 | \alpha \rangle + \langle \alpha | (\hat{a}^\dagger)^2 | \alpha \rangle + \langle \alpha | \hat{a}\hat{a}^\dagger | \alpha \rangle + \langle \alpha | \hat{a}^\dagger \hat{a} | \alpha \rangle = \\ &= \alpha^2 + (\alpha^*)^2 + \alpha^* \alpha + 1 + \alpha^* \alpha = \\ &= q^2 - p^2 + 2iqp + q^2 - p^2 - 2iqp + 2(q^2 + p^2) + 1 = \\ &= 4q^2 + 1. \end{aligned} \tag{8}$$

Considering that the values q and p are realizations of the random variables $\mathcal{Q}$ and $\mathcal{P}$, respectively, we can write:

$$\langle \hat{q}^2 \rangle = 4\langle \mathcal{Q}^2 \rangle + 1 = 4\tilde{V}_{\mathrm{A}} + 1, \tag{9}$$

$$\langle \hat{p}^2 \rangle = 4\langle \mathcal{P}^2 \rangle + 1 = 4\tilde{V}_{\mathrm{A}} + 1. \tag{10}$$

According to Eqs. (9), one has:

$$V \equiv V(\hat{q}) = V(\hat{p}) \equiv V = 4\tilde{V}_{\mathrm{A}} + 1 \equiv V_{\mathrm{A}} + 1. \tag{11}$$

In Eq. (11), the transition from the variance of random variable corresponding to the quadrature distribution to the variance of quadrature operator is carried out. It should be noted that there is also a shot noise component in SNU (equal to one).

Combining (6) and (11), we can express the average number of photons over the ensemble in terms of the variance of quadrature operator

$$\langle n \rangle = \frac{1}{2}(V - 1) = \frac{1}{2}V_{\mathrm{A}}. \tag{12}$$

After the preparation stage, Alice sends the $|\alpha_j\rangle$ state to the Gaussian quantum channel, after which Bob performs coherent detection and decodes information about the sent state in the case of heterodyne detection or the projection of its quadrature components in the case of homodyne detection. It should be emphasized that in this paper only heterodyne detection is considered.

3.2. Gaussian sequence processing

This subsection briefly describes the stages of classical data post-processing, which means Alice's modulation and Bob's detection results data.

The first step is sifting. Despite sifting is not implied in the case of heterodyne detection (in which the sequence after the distribution session and before error correction can be considered as a sifted key), it is worth mentioning that in CV-QKD with homodyne detection, Alice and Bob choose the bases they use to prepare and measure the states respectively, using independently and identically distributed generated random bits. In these cases, the sifting step eliminates all uncorrelated signals when different bases were used for preparation and measurement. The presence of signal bases is more typical for CV-QKD protocols with discrete modulation, however, in protocols with Gaussian modulation and homodyne detection, sifting means discarding the quadrature not measured by Bob.

The second step is parameter estimation. After transmitting and detecting a sequence of states, legitimate parties compare a random subset of their data. This comparison allows one to estimate the quantum channel parameters: transmittance and excess noise of the channel, from which they can calculate a mutual information I_{AB} and evaluate an information χ available to Eve. If χ is greater than βI_{AB}, where $\beta \in [0,\ 1]$ is the reconciliation efficiency, the protocol is aborted at this point.

If $\beta I_{\mathrm{AB}} > \chi$, users go to the third, information reconciliation step, which is a form of error correction procedure.

The fourth step is confirmation. After the reconciliation procedure, legitimate parties perform a confirmation step using a family of universal hash functions [18] to limit the chance that error correction fails: Alice or Bob chooses one particular hash function with uniform probability and announces its choice over the classical channel. Users apply this hash function to their key to get a hash code. Subsequently, Alice and Bob exchange and compare their hash codes. If the values are different, the keys are considered compromised and the protocol is aborted; if the values are equal, then it is considered that an upper bound on the probability that the keys are not identical has been obtained. This error rate depends on the length of the hash codes and the type of hash functions used.

The fifth and final step is privacy amplification. After successfully passing the confirmation stage, Alice and Bob will have the same bit string with a very high probability. However, Eve has some information about the key, so to reduce the chance that she successfully guesses part of the key to an acceptable value, users perform a privacy amplification protocol by applying a seeded randomness extraction algorithm to their bit strings, which uses a family of 2-universal hash functions.

3.3. Quantum channel description

The Gaussian quantum channel is characterized by the transmittance coefficient (taking into account losses directly in the channel, losses in the equipment and detection efficiency) and noise (on Alice side, in the channel, and on Bob side). The potential advantage of Eve depends on both characteristics. The noise in the channel can be expressed as [1, 13, 19]

$$\Xi_{\text{ch}} = \frac{1 - T_{\text{ch}}}{T_{\text{ch}}} + \xi_{\text{A}}, \tag{13}$$

where T_{ch} is a quantum channel transmittance, ξ_{A} is a excess noise (in SNU).

The excess noise itself includes variances of all noise sources

$$\xi_{\text{A}} = \xi_{\text{modul, A}} + \xi_{\text{Raman, A}} + \xi_{\text{phase, A}} + \cdots, \tag{14}$$

where $\xi_{\text{modul, A}}$ is the modulation noise, $\xi_{\text{Raman, A}}$ is the Raman noise, and $\xi_{\text{phase, A}}$ is the phase noise.

Similarly, the detector noise can be estimated as [1, 13, 14, 19]

$$\Xi_{\text{det}} = \frac{1 - T_{\text{rec}}\eta_{\text{det}}}{T_{\text{rec}}\eta_{\text{det}}} + \frac{v_{\text{el}}}{T_{\text{rec}}\eta_{\text{det}}}, \tag{15}$$

where η_{det} is the balanced detector efficiency, v_{el} is the electronic noise of the balanced detector and T_{rec} is the transmittance coefficient responsible for losses in the receiver module.

For a more convenient notation, it can be written as

$$T_{\text{det}} \equiv T_{\text{rec}}\eta_{\text{det}}. \tag{16}$$

The total noise related to the channel input is then determined by the sum of the channel noise and the detector noise normalized to T_{ch}

$$\Xi = \Xi_{\text{ch}} + \frac{1}{T_{\text{ch}}}\Xi_{\text{det}}. \tag{17}$$

After the signal state passing through a channel with noise and losses, Bob measures the total variance of the quadrature operator as [1, 13, 14, 19]

$$\begin{aligned}
V_{\text{B}} &= V\left(\hat{q}_{\text{B}}\right) = V\left(\hat{p}_{\text{B}}\right) = T_{\text{ch}}T_{\text{det}}(V + \Xi) = \\
&= T_{\text{ch}}T_{\text{det}}\left(V + \frac{1 - T_{\text{ch}}}{T_{\text{ch}}} + \xi_{\text{A}} + \frac{1}{T_{\text{ch}}}\left(\frac{1 - T_{\text{det}}}{T_{\text{det}}} + \frac{v_{\text{el}}}{T_{\text{det}}}\right)\right) = \\
&= T_{\text{ch}}T_{\text{det}}V - T_{\text{ch}}T_{\text{det}} + T_{\text{ch}}T_{\text{rec}}\eta_{\text{det}}\xi_{\text{A}} + 1 + v_{\text{el}} \equiv \\
&\equiv TV - T + T\xi_{\text{A}} + 1 + v_{\text{el}} = \\
&= T(V - 1) + T\xi_{\text{A}} + 1 + v_{\text{el}}.
\end{aligned} \tag{18}$$

Since the parameter v_{el} is the noise variance in SNU and can be considered stochastically independent of other noise sources, it can be considered as another component of the excess noise, i.e. $v_{\text{el}} \equiv \xi_{\text{det}}$, thus

$$T\xi_{\text{A}} + \xi_{\text{det}} = T\left(\xi_{\text{A}} + \frac{1}{T}\xi_{\text{det}}\right) \equiv T\xi_{\text{tot, A}} = \xi_{\text{tot, B}} \equiv \xi, \tag{19}$$

$$V_{\text{B}} = T(V - 1) + 1 + \xi = TV_{\text{A}} + 1 + \xi. \tag{20}$$

3.4. Signal-to-noise ratio and mutual information

The signal-to-noise ratio is expressed as

$$\text{SNR} = \frac{P_{\text{S}}}{P_{\text{N}}}, \tag{21}$$

where P_{S} is the total signal power and P_{N} is the total noise power.

The purposed model makes it possible to separate the signal and noise components in the variance of the quadrature operator observed by Bob

$$V_{\text{B}} = \frac{T}{\mu}V_{\text{A}} + 1 + \frac{\xi}{\mu}, \tag{22}$$

where $\mu \in \{1;\ 2\}$ is the homodyne/heterodyne detection system parameter, respectively.

Thus, the signal-to-noise ratio for the purposed protocol is as follows

$$\text{SNR} = \frac{\frac{1}{\mu}TV_{\text{A}}}{1 + \frac{1}{\mu}\xi}. \tag{23}$$

Mutual information between Alice and Bob in this case is evaluated as [13]

$$I_{\text{AB}} = \frac{\mu}{2}\log_2(1 + \text{SNR}) = \frac{\mu}{2}\log_2\left(1 + \frac{\frac{1}{\mu}TV_{\text{A}}}{1 + \frac{1}{\mu}\xi}\right). \tag{24}$$

As it has been already mentioned, the purposed protocol assumes a heterodyne detection method, i.e. $\mu = 2$. According to Eq. (24), despite the increase in mutual information by a factor of two (two quadratures per message are detected at once, instead of one), the signal-to-noise ratio decreases. Obviously (estimating the rate of increase of logarithmic functions), the advantage of heterodyne detection in terms of estimating mutual information will be observed only at large TV_{A}.

4. Trusted hardware noise. Holevo bound

After variable ρ_{AB} has been removed from the shared state equation, it can be viewed as a pure two-particle state with a common Alice and Bob on one side and Eve on the other. As such, it can be written in terms of the Schmidt decomposition

$$|\Psi_{\mathrm{ABE}}\rangle = \sum_i \sqrt{\lambda_i}\,|\psi_i\rangle_{\mathrm{AB}}\,|\phi_i\rangle_{\mathrm{E}}\,, \tag{25}$$

where λ_j is a real non-negative number.

Taking a partial trace over subsystems gives one

$$\mathrm{Tr}_{\mathrm{E}}\,\rho_{\mathrm{AB}} = \rho_{\mathrm{AB}} = \sum_i \lambda_i |\psi_i\rangle_{\mathrm{AB}}\langle\psi_i|, \tag{26}$$

$$\mathrm{Tr}_{\mathrm{AB}}\,\rho_{\mathrm{AB}} = \rho_{\mathrm{E}} = \sum_i \lambda_i |\phi_i\rangle_{\mathrm{E}}\langle\phi_i|. \tag{27}$$

The von Neumann entropy depends only on the λ_i components, which, due to the Schmidt decomposition, are the same for ρ_{AB} and ρ_{E}. Therefore, the von Neumann entropy of Eve is the same as the entropy shared by Alice and Bob

$$S_{\mathrm{E}} = S_{\mathrm{AB}} = -\sum_i \lambda_i \log_2 \lambda_i. \tag{28}$$

Then, the following transformation is obvious

$$\chi_{\mathrm{E}} = S_{\mathrm{E}} - S_{\mathrm{E|B}} = S_{\mathrm{AB}} - S_{\mathrm{A|B}}. \tag{29}$$

In the trusted noise model [12], the noise coming from the Alice's and Bob's equipment is assumed to be trusted, that is, Eve cannot manipulate it. The same applies to equipment losses. In this context, it is necessary to clarify Eq. (19)

$$\xi = T\xi_{\mathrm{pr}} + T_{\mathrm{det}}\xi_{\mathrm{ch}} + \xi_{\mathrm{rec}}, \tag{30}$$

where ξ_{pr} is the Alice excess noise, ξ_{ch} is the channel excess noise, and ξ_{rec} is the Bob excess noise.

Assuming that the detection devices are well calibrated and reliable, T_{rec} and ξ_{rec} are beyond Eve's influence. Then the covariance matrix describing its von Neumann entropy prior to measurement by Bob is as follows

$$\Sigma_{\mathrm{AB}}^{\text{trusted rec.}} = \begin{pmatrix} V\mathbf{1}_2 & \sqrt{T_{\mathrm{ch}}(V^2-1)}\sigma_z \\ \sqrt{T_{\mathrm{ch}}(V^2-1)}\sigma_z & (T_{\mathrm{ch}}(V-1)+1+\xi_{\mathrm{ch}})\,\mathbf{1}_2 \end{pmatrix}. \tag{31}$$

The matrix itself can be represented in the form

$$\begin{pmatrix} a\mathbf{1}_2 & c\sigma_z \\ c\sigma_z & b\mathbf{1}_2 \end{pmatrix}. \tag{32}$$

The symplectic eigenvalues of this matrix are expressed as

$$v_{1,\,2} = \frac{1}{2}(z \pm (b-a)), \tag{33}$$

where $z = \sqrt{(a+b)^2 - 4c^2}$.

Although in the trusted noise model the quantities T_{rec} and ξ_{rec} do not contribute to S_{E}, though they do affect Alice measurements and, consequently, Eve entropy $S_{\mathrm{E|B}}$.

In the trusted noise scenario, the eavesdropper can only manipulate the state in the channel and carry out purifying in the same place. This means that the state of the system must be viewed through three distinct subsystems in the entanglement base scenario. Let the state "Alice-Bob-Eve" consist of two entangled states and a thermal state, each of which is uniquely determined by its variance: one entangled state $\mathrm{EPR}_{\mathrm{AB}}$ with variance V used for key exchange between Alice and Bob, one entangled state $\mathrm{EPR}_{\mathrm{ch}}$ with variance W_{ch} for modeling noise and loss in the quantum channel and thermal state $\mathrm{Th}_{\mathrm{rec}}$ with variance W_{rec} to simulate the noise and losses of the receiver. The beam splitters, one with T_{ch} transmittance and one with T_{rec} transmittance, mix the initial Bob's entangled state modes with the channel state and

the thermal state modes, respectively. The general state before the action of the beam splitters can be represented by the covariance matrix

$$\Sigma_{\text{tot},\,0} = \text{EPR}_{\text{AB}} \oplus \text{EPR}_{\text{ch}} \oplus \text{Th}_{\text{rec}} = \\ = \begin{pmatrix} V\mathbf{1}_2 & \sqrt{V^2-1}\sigma_z & 0 & 0 & 0 \\ \sqrt{V^2-1}\sigma_z & V\mathbf{1}_2 & 0 & 0 & 0 \\ 0 & 0 & W_{\text{ch}}\mathbf{1}_2 & \sqrt{W_{\text{ch}}^2-1}\sigma_z & 0 \\ 0 & 0 & \sqrt{W_{\text{ch}}^2-1}\sigma_z & W_{\text{ch}}\mathbf{1}_2 & 0 \\ 0 & 0 & 0 & 0 & W_{\text{rec}}\mathbf{1}_2 \end{pmatrix}. \tag{34}$$

It can be noted here that the eavesdropper attack on the quantum channel involves only two entangled states, EPR_{AB} and EPR_{ch}, which guarantees purifying as part of an attack. Unitary equivalence with complete purifying thus makes it easier to express the state on Bob's side: in the general case, it must be represented by another entangled state [14].

The beam splitter in the channel affects Alice's mode and one of the EPR_{ch} state modes; the second beam splitter affects Bob's mode and the thermal state simulating the detection module

$$\text{BS}_{\text{ch}} = \begin{pmatrix} \mathbf{1}_2 & 0 & 0 & 0 & 0 \\ 0 & \sqrt{T_{\text{ch}}}\mathbf{1}_2 & \sqrt{1-T_{\text{ch}}}\mathbf{1}_2 & 0 & 0 \\ 0 & -\sqrt{1-T_{\text{ch}}}\mathbf{1}_2 & \sqrt{T_{\text{ch}}}\mathbf{1}_2 & 0 & 0 \\ 0 & 0 & 0 & \mathbf{1}_2 & 0 \\ 0 & 0 & 0 & 0 & \mathbf{1}_2 \end{pmatrix}, \tag{35}$$

$$\text{BS}_{\text{rec}} = \begin{pmatrix} \mathbf{1}_2 & 0 & 0 & 0 & 0 \\ 0 & \sqrt{T_{\text{det}}}\mathbf{1}_2 & 0 & 0 & \sqrt{1-T_{\text{det}}}\mathbf{1}_2 \\ 0 & 0 & \mathbf{1}_2 & 0 & 0 \\ 0 & 0 & 0 & \mathbf{1}_2 & 0 \\ 0 & -\sqrt{1-T_{\text{det}}}\mathbf{1}_2 & 0 & 0 & \sqrt{T_{\text{det}}}\mathbf{1}_2 \end{pmatrix}. \tag{36}$$

Denoting the sequence of both beam splitters as $\text{BS}_{\text{tot}} = \text{BS}_{\text{rec}}\text{BS}_{\text{ch}}$, the total quantum state is transformed as follows

$$\Sigma_{\text{tot}} = \text{BS}_{\text{tot}}\Sigma_{\text{tot},0}\text{BS}_{\text{tot}}^T. \tag{37}$$

To simplify expressions for the covariance matrix, it should be considered block by block. Thus, the block describing the Alice-Bob subsystem is transformed as follows

$$\Sigma_{\text{AB}} = \begin{pmatrix} V\mathbf{1}_2 & \sqrt{T_{\text{ch}}}\sqrt{T_{\text{det}}}\sqrt{V^2-1}\sigma_z \\ \sqrt{T_{\text{ch}}}\sqrt{T_{\text{det}}}\sqrt{V^2-1}\sigma_z & \begin{pmatrix} T_{\text{ch}}T_{\text{det}}V \\ +(1-T_{\text{ch}})\,T_{\text{det}}W_{\text{ch}} \\ +(1-T_{\text{det}})\,W_{\text{rec}} \end{pmatrix} \end{pmatrix}. \tag{38}$$

Let the variances for entangled states be defined as

$$W_{\text{ch}} = \frac{\xi_{\text{ch}}}{1-T_{\text{ch}}} + 1, \tag{39}$$

$$W_{\text{rec}} = \frac{\xi_{\text{rec}}}{1-T_{\text{det}}} + 1. \tag{40}$$

Then the variance of Bob's quadrature operator is as follows

$$V_{\text{B}} = T_{\text{ch}}T_{\text{det}}(V-1) + 1 + T_{\text{det}}\xi_{\text{ch}} + \xi_{\text{rec}} = \\ = T_{\text{ch}}T_{\text{det}}(V-1) + 1 + \xi_{\text{ch},B} + \xi_{\text{rec}}. \tag{41}$$

The final expression for the Alice-Bob block is

$$\Sigma_{\text{AB}} = \begin{pmatrix} V\mathbf{1}_2 & \sqrt{T}\sqrt{V^2-1}\sigma_z \\ \sqrt{T}\sqrt{V^2-1}\sigma_z & (T(V-1)+1+\xi)\,\mathbf{1}_2 \end{pmatrix}. \tag{42}$$

The Eve block is described by the matrix

$$\Sigma_{\mathrm{E}} = \begin{pmatrix} \left(\left(1-T_{\mathrm{ch}}\right)V + T_{\mathrm{ch}}W_{\mathrm{ch}}\right)\mathbf{1}_2 & \sqrt{T_{\mathrm{ch}}}\sqrt{\mathrm{W}_{\mathrm{ch}}^2-1}\sigma_z \\ \sqrt{T_{\mathrm{ch}}}\sqrt{W_{\mathrm{ch}}^2-1}\sigma_z & W_{\mathrm{ch}}\mathbf{1}_2 \end{pmatrix}. \tag{43}$$

This matrix can be described in the form given by Eq. (32), so its symplectic eigenvalues can be calculated by Eq. (33). It can be verified that the entropy of Eve S_{E} is the same as the entropy shared by Alice and Bob and obtained from their mutual covariance matrix in the trusted receiver noise scenario from Eq. (31), which is expected when Eve purifies the state of Alice and Bob, i.e.

$$S_{\mathrm{E}} \equiv S\left(\Sigma_{\mathrm{E}}\right) = S\left(\Sigma_{\mathrm{AB}}^{\text{trusted rec.}}\right) \equiv S_{\mathrm{AB}}. \tag{44}$$

Now, in order to get $S_{\mathrm{E|B}}$, we have to calculate $\Sigma_{\mathrm{tot|B}}$, i.e. the covariance matrix of the common state of the remaining modes after the projective measurement of the receiver mode. It is convenient to represent Σ_{tot} so that the Alice's mode is located in the last row and column. This can be done by using a permutation matrix, which allows to rearrange the third and fourth rows (columns) down (to the right) when multiplied by Σ_{tot} from the left (right) [14]:

$$P_{3,\,4\to9,\,10} = \begin{pmatrix} \mathbf{1}_2 & 0 & 0 & 0 & 0 \\ 0 & 0 & \mathbf{1}_2 & 0 & 0 \\ 0 & 0 & 0 & \mathbf{1}_2 & 0 \\ 0 & 0 & 0 & 0 & \mathbf{1}_2 \\ 0 & \mathbf{1}_2 & 0 & 0 & 0 \end{pmatrix}, \tag{45}$$

$$\Sigma'_{\mathrm{tot}} = P_{3,4\to9,10}\Sigma_{\mathrm{tot}}P_{3,4\to9,10}^T. \tag{46}$$

Since $P_{3,\,4\to9,\,10}P_{3,\,4\to9,\,10}^T = \mathbf{1}$, the above permutation is a similarity transformation and therefore leaves the eigenvalues of the matrix Σ_{tot} invariant. The covariance matrix itself now looks like this:

$$\Sigma'_{\mathrm{tot}} = \begin{pmatrix} \Sigma_{\mathrm{A,\,ch,\,rec}} & \Sigma_{\mathrm{C}} \\ \Sigma_{\mathrm{C}}^T & \Sigma_{\mathrm{B}} \end{pmatrix}, \tag{47}$$

where $\Sigma_{\mathrm{A,\,ch,\,rec}} \in \mathbb{R}^{8\times8}$ is a matrix describing the Alice's mode and the state of the channel and the detection module, $\Sigma_{\mathrm{B}} \in \mathbb{R}^{2\times2}$ is a matrix describing the Bob's mode, and $\Sigma_C \in \mathbb{R}^{8\times2}$ is a matrix describing quadrature correlations between $\Sigma_{\mathrm{A,\,ch,\,rec}}$ and Σ_{B}.

The $\Sigma_{\mathrm{tot|B}}$ matrix after a projective measurement of the Bob's mode depends on whether it performs homodyne or heterodyne detection.

In the case of heterodyne detection, the remaining modes are projected into the state described by the 8×8 matrix

$$\Sigma_{\mathrm{tot|B}} = \Sigma_{\mathrm{A,\,ch,\,rec}} - \frac{1}{V_{\mathrm{B}}+1}\Sigma_{\mathrm{C}}\Sigma_{\mathrm{C}}^T. \tag{48}$$

Again, there is no need to evaluate the entire covariance matrix. Instead, one can evaluate a block describing the eavesdropper information that is two modes representing the entangled state that was used to model the noise and the channel loss. The block itself is expressed as follows

$$\Sigma_{\mathrm{E|B}} = \frac{1}{V_{\mathrm{B}}+1}\begin{pmatrix} e_1\mathbf{1}_2 & e_2\sigma_z \\ e_2\sigma_z & e_3\mathbf{1}_2 \end{pmatrix}, \tag{49}$$

$$\begin{aligned} e_1 = {} & V\left(\left(1-T_{\mathrm{rec}}\right)W_{\mathrm{rec}} + T_{\mathrm{rec}}W_{\mathrm{ch}} + 1\right) + \\ & + T_{\mathrm{ch}}\left(W_{\mathrm{ch}} - V\right)\left(1 + \left(1-T_{\mathrm{rec}}\right)W_{\mathrm{rec}}\right), \end{aligned} \tag{50}$$

$$e_2 = \sqrt{T_{\mathrm{ch}}\left(W_{\mathrm{ch}}^2-1\right)}\left(T_{\mathrm{rec}}V + \left(1-T_{\mathrm{rec}}\right)W_{\mathrm{rec}} + 1\right), \tag{51}$$

$$e_3 = \left(1-T_{\mathrm{rec}}\right)W_{\mathrm{ch}}W_{\mathrm{rec}} + T_{\mathrm{rec}}T_{\mathrm{ch}}\left(VW_{\mathrm{ch}} - 1\right) + T_{\mathrm{rec}} + W_{\mathrm{ch}}. \tag{52}$$

Considering that the matrix $\Sigma_{\mathrm{E|B}}$ can also be represented in the form of Eq. (32), then the symplectic eigenvalues can also be represented similarly to Eq. (33) as

$$v_{3,\,4} = \frac{z \pm \left(e_3 - e_1\right)}{2\left(V_B+1\right)}, \tag{53}$$

$$z = \sqrt{\left(e_1+e_3\right)^2 - 4e_2^2}. \tag{54}$$

Thus, the necessary values for estimating the Holevo bound in the presence of collective attacks in the trusted receiver noise scenario have been obtained. Further, the model will need to be supplemented taking into account the lack of access of Eve to the noise of Alice in order to consider the full scenario of trusted noise from trusted nodes.

The noise on the Alice side can be composed of the noise from laser power fluctuation and imperfect modulation [13, 20]. Models of such trusted Alice noise for collective attacks are presented in [14, 21–23]. This noise is modeled analogously to the noise of the channel and the detection module using an additional thermal state $\mathrm{Th}_{\mathrm{pr}}$ with variance

$$W_{\mathrm{pr}} = \frac{\xi_{\mathrm{pr}}}{1 - T_{\mathrm{pr}}} + 1, \tag{55}$$

where T_{pr} is the transmittance coefficient of Alice module.

Then the Alice noise measured by Bob will be $\xi_{\mathrm{pr,\,B}} = T_{\mathrm{ch}} T_{\mathrm{rec}} \xi_{\mathrm{pr}}$. The thermal state $\mathrm{Th}_{\mathrm{pr}}$ interacts with Bob's mode through a beam splitter with a transmittance $T_{\mathrm{pr}} \to 1$, since the initial signal power is assumed already at the output of the Alice module. While the limit $T_{\mathrm{pr}} \to 1$ would result in $W_{\mathrm{pr}} \to \infty$, the noise $(1 - T_{\mathrm{pr}})\, W_{\mathrm{pr}} = \xi_{\mathrm{pr}} + 1 - T_{\mathrm{pr}} \to \xi_{\mathrm{pr}}$ of the mode reflected into the channel will be finite and good certain.

The problem can again be reduced to considering only two modes available to Eve, reducing the eigenvalue problem to a second degree polynomial. This allows one to describe the trusted noise of Alice and Bob using simple analytical expressions.

The overall initial state now includes the thermal state responsible for the Alice's noise

$$\Sigma_{\mathrm{tot},0} = \mathrm{EPR}_{\mathrm{AB}} \oplus \mathrm{Th}_{\mathrm{pr}} \oplus \mathrm{EPR}_{\mathrm{ch}} \oplus \mathrm{Th}_{\mathrm{rec}}. \tag{56}$$

Then one should redesignate the sequence of all beam splitters $\mathrm{BS}_{\mathrm{tot}} = \mathrm{BS}_{\mathrm{rec}} \mathrm{BS}_{\mathrm{ch}} \mathrm{BS}_{\mathrm{pr}}$. Then the symplectic transformation, analogous to Eq. (37), will change the block of the covariance matrix related to the eavesdropper as

$$\Sigma_{\mathrm{E}} = \begin{pmatrix} \left((1 - T_{\mathrm{ch}})\,(V + \xi_{\mathrm{pr}}) + T_{\mathrm{ch}} W_{\mathrm{ch}}\right) \mathbf{1}_2 & \sqrt{T_{\mathrm{ch}}} \sqrt{W_{\mathrm{ch}}^2 - 1}\, \sigma_z \\ \sqrt{T_{\mathrm{ch}}} \sqrt{W_{\mathrm{ch}}^2 - 1}\, \sigma_z & W_{\mathrm{ch}} \mathbf{1}_2 \end{pmatrix}. \tag{57}$$

Obviously, the matrices from Eqs. (43) and (57) coincide up to the replacement $V \to V + \xi_{\mathrm{pr}}$. The symplectic eigenvalues v_1 and v_2 (required for calculating S_{E}) are again obtained by Eq. (33). To calculate v_3 and v_4 for $S_{\mathrm{E|B}}$, $\Sigma_{\mathrm{tot|B}}$ must be rearranged according to the modified shared state structure.

Thus, after substitution $T_{\mathrm{pr}} = 1$ and with the accuracy of replacement $V \to V + \xi_{\mathrm{pr}}$, Eve's covariance matrix after heterodyne detection by Bob has the form in accordance with Eq. (49). The symplectic eigenvalues v_3 and v_4 are again obtained by Eqs. (50)–(52).

The advantage of this model is that as equipment losses increase, the Holevo bound decreases faster than mutual information [14].

5. Gaussian quantum channel modeling

The Gaussian quantum channel, as has already been mentioned in this paper, is characterized by two parameters: the transmittance and excess noise. Often CV-QKD papers do not provide clarifications on the components of these characteristics [16, 24, 25]: an analytical assessment has been carried out only for some components.

Modeling the parameters of the Gaussian channel is necessary to obtain the value of the signal-to-noise ratio, which will be maintained at a given distance.

As has already been demonstrated in the previous section, the transmittance is composite, which is why it cannot be estimated in the aggregate, which, for example, was done in [24, 26]. This assumption significantly improves the performance and the amount of allowable losses in the stability analysis but remains incorrect.

So, given that the quantum channel is an optical fiber channel, the transmittance can be estimated in accordance with the well-known expression [27]:

$$T_{\mathrm{ch}} = 10^{-\zeta L/10}, \tag{58}$$

where ζ is the fiber attenuation in dB/km.

The coefficient T_{det} can be obtained from the equipment loss and the detector efficiency as:

$$T_{\mathrm{det}} = \eta_{\mathrm{det}} 10^{-\mathrm{losses}/10}, \tag{59}$$

where losses is the cumulative losses on Alice's equipment.

Here, it should be clarified that T_{det} is the transmittance in the signal arm, T'_{det} is a transmittance in the LO arm. The latter will be necessary for estimating the excess noise. Both coefficients are calculated using Eq. (59) taking into account the fact that losses in both arms are different. For example, the power of LO is expressed as

$$P_{\mathrm{LO}} = T'_{\mathrm{det}} P_{\mathrm{LO,\,A}}, \tag{60}$$

where $P_{\mathrm{LO,\,A}}$ is the power of LO at the output of Alice.

The cumulative losses on the equipment in the Bob module are presented in Table 1.

TABLE 1. Cumulative losses in the signal arm and in the arm of LO obtained from [28–35]

Arm	Name of the optical component	Insertion loss, dB
Signal	FC/APC Connectors	3
	CWDM-filter	0.6
	Polarization controller	0.05
	Polarizing beam splitter	0.6
	90-degree hybrid	3
	All components	7,25
LO	FC/APC Connectors	3,6
	CWDM-filter	0.6
	Polarization controller	0.05
	Polarizing beam splitter	0.6
	Beam splitter 10/90 6	0.85
	90-degree hybrid	3
	All components	8.7

In many theoretical works, the excess noise values are approximated and fixed [14, 25, 36–38]. This is motivated by the fact that in real CV-QKD systems, the excess noise, as well as the transmittance, is estimated from experimental data on the variances of quadrature operators. As far as strictly theoretical works are concerned, the substitution is necessary only for illustrative purposes. However, for a theoretical performance evaluation of the considered CV-QKD system, it is necessary to take into account various noise sources, which will be further carried out in accordance with work [13].

Like the transmittance, excess noise is compound. In this case, the excess noise components are:

- Alice module noises:
  - laser power fluctuations noise;
  - DAC noise;
- channel noises:
  - phase noise;
- Bob module noises:
  - common-mode rejection ratio (CMRR) noise;
  - internal noise of the balanced detector;
  - ADC noise.

Laser power fluctuations noise contains two components, signal and LO ones

$$\xi_{\mathrm{RIN,\,sig}} = V_{\mathrm{A}}\sqrt{\mathrm{RIN}_{\mathrm{sig}} B_{\mathrm{sig}}}, \tag{61}$$

$$\xi_{\mathrm{RIN,\,LO}} = \frac{1}{4}\mathrm{RIN}_{\mathrm{LO}} B_{\mathrm{LO}} V, \tag{62}$$

$$\xi_{\mathrm{RIN}} = \xi_{\mathrm{RIN,\,LO}} + \xi_{\mathrm{RIN,\,sig}}, \tag{63}$$

where $\mathrm{RIN}_{\mathrm{sig}}$ is the relative intensity noise (RIN) of signal, $\mathrm{RIN}_{\mathrm{LO}}$ is the relative intensity noise of LO, B_{sig} is a signal spectrum width, and B_{LO} is the LO spectrum width.

It is important to note that due to the fact that both the signal and LO emit from the same laser, the spectral width and the relative intensity noise for them will be the same [13], i.e. $B_{\mathrm{sig}} = B_{\mathrm{LO}} \equiv B$, $\mathrm{RIN}_{\mathrm{sig}} = \mathrm{RIN}_{\mathrm{LO}} \equiv \mathrm{RIN}$.

The excess noise caused by noise from the modulating voltage side is estimated by the inequality [13]

$$\xi_{\mathrm{DAC}} \leq V_{\mathrm{A}} \left(\pi\alpha \frac{\sqrt{V_{\mathrm{q}}}}{V_\pi} + \frac{1}{2}\pi^2\alpha^2 \frac{V_{\mathrm{q}}}{V_\pi^2} \right)^2, \tag{64}$$

$$V_{\mathrm{q}} = \mathrm{LSB}^2/12 = V_{\mathrm{FS}}^2/(12 \cdot 2^{2N_{\mathrm{res}}(f_{\mathrm{rep}})}). \tag{65}$$

where V_π is the voltage required to reverse the phase by π, α is the DAC gain coefficient, V_{q} is the converter output voltage variance, LSB is the least significant bit, V_{FS} is the full-scale voltage range of the converter, and N_{res} is the DAC resolution.

Coherent quantum signal detection requires a well calibrated phase and frequency relationship between the signal and LO. In addition, the signal initially carries a certain level of phase noise. This phase noise, as well as relative phase shifts,

can be compensated with a strong reference sent by Alice [39–42]. The reference (or pilot) signal carries well-known phase with a fixed phase relation to the original signal pulse. Bob performs heterodyne detection of the reference signal by measuring its quadratures q and p. It can determine the deviation from a fixed and time-constant reference phase. Any of such measured phase shift is used to appropriately correct the measured phase of the quantum signal. The remaining phase noise is then expressed as [13]

$$\xi_{\mathrm{PR}} = \frac{1}{2} V_{\mathrm{A}} \frac{V_{\mathrm{pt}}}{N_{\mathrm{pt}} \langle N_{\mathrm{pt}} \rangle}, \tag{66}$$

where V_{pt} is the variance of the quadrature operator of the reference signal, N_{pt} is the number of the reference signals, $\langle N_{\mathrm{pt}} \rangle$ is the average number of photons in the reference pulse.

It should be noted that in the presented paper, it is assumed that for each signal message there is a reference signal, i.e. the number of reference signals is half of the total number of messages.

It is convenient to express the internal noise of the balanced detector in terms of a characteristic called clearance C, which is defined as the ratio of the total experimental variance of the zero power signal (dispersion shot noise $V_0(\hat{q})$ and electronic noise of dispersion $V_{\mathrm{det}}(\hat{q})$) and variance $V_{\mathrm{det}}(\hat{q})$ caused only by detector electronic noise:

$$C = \frac{V_0(\hat{q}) + V_{\mathrm{det}}(\hat{q})}{V_{\mathrm{det}}(\hat{q})}. \tag{67}$$

The shot noise variance depends linearly on the power of LO, which, however, is limited by the saturation limit of the detector's PIN diodes. Experimentally, the numerator of Eq. (67) can be determined by measuring the quadrature variance of LO when it is mixed with the vacuum inlet. The denominator is the remaining quadrature variance after LO is disconnected from the detector. In SNU by definition $V_0(\hat{q}) = 1$, and the equation becomes as follows

$$C = \frac{1 + V_{\mathrm{det}}(\hat{q})}{V_{\mathrm{det}}(\hat{q})} = \frac{1 + \xi_{\mathrm{det}}}{\xi_{\mathrm{det}}}. \tag{68}$$

Thus, the noise of the balanced detector relative to the clearance, taking into account one/two detectors in homo-/heterodyne detection, respectively, is the following one

$$\xi_{\mathrm{det}} = \mu \frac{1}{C - 1}. \tag{69}$$

An experimental evaluation of ξ_{det} was carried out for the General Photonics OEM Balanced Detector (BPD-003) with the operating frequency band of 200 MHz (see Fig. 2). The choice of the detector was based on the following parameters for the optimal signal-to-noise ratio:

- low noise equivalent power — indicates the possibility of detecting signals with a power comparable to that of shot noise;
- high gain coefficient — allows one to detect low power signals with high attenuation of LO;
- high CMRR — shows the gain quality;
- a wide operating frequency band — allows one to increase the frequency of sending states, which, in accordance with the current technical level, should be about MHz [16, 24, 26]. The established relationship between the excess noise of the detector and its operating frequency band is linear [13], so a too large range can lead to a high level of the internal detector noise.

The dependence of the excess noise of the detector and, as a result, the signal-to-noise ratio on the operating frequency band does not have a minimum due to linearity, however, as can be seen in Fig. 2, the obtained noise level in the considered detector is quite low and corresponds to the level established by [13,24]. So, for example, with the total loss of 13.7 dB (5 dB in the channel and 8.7 dB in the LO arm), $\xi_{\mathrm{det}} = 0.093$ is observed in [13] at operating frequency band of the detector is 250 MHz. In [24], one obtains $\xi_{\mathrm{det}} \sim 10^{-1}$, based on the given data.

According to the obtained dependence of the excess noise of the balanced detector on the input power of LO, one can observe an increase in the contribution of the noise with a decrease in its values. In practice, a decrease in power is associated with an increase in losses. The resulting dependence will be used later in the overall assessment of the total excess noise. The experimental background of the obtained formula is related to the fact that the proposed models do not take into account the full composition of the balanced detector.

A realistic differential amplifier will amplify not only the difference current with a coefficient g, but also to a small extent with a coefficient g_{CM} their average value of the input photocurrents in the subtractive circuit. As a characteristic for estimating such amplification, CMRR [43] is used:

$$\mathrm{CMRR} = \left| \frac{g}{g_{\mathrm{CM}}} \right|. \tag{70}$$

Noise dependent on CMRR is calculated as [13]:

$$\xi_{\mathrm{CMRR}} = \frac{\mu}{4\mathrm{CMRR}^2} \left(\frac{h f V_{\mathrm{A}}^2}{4\tau P_{\mathrm{LO}}} \mathrm{RIN}_{\mathrm{sig}} B_{\mathrm{sig}} + \frac{\tau}{hf} P_{\mathrm{LO}} \mathrm{RIN}_{\mathrm{LO}} B_{\mathrm{LO}} \right), \tag{71}$$

where P_{LO} is a LO power, τ is the pulse duration, f is the optical frequency and h is Planck's constant.

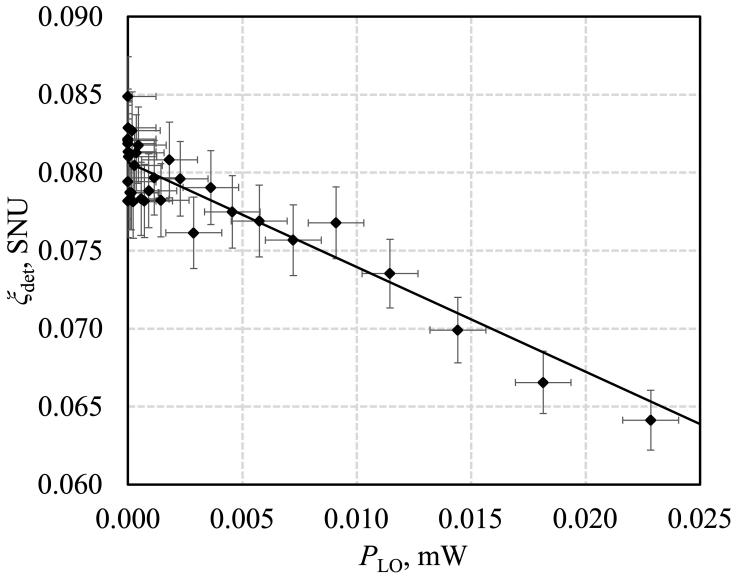

FIG. 2. Dependence of the excess noise of the balanced detector on the input power of LO for General Photonics OEM Balanced Detector (BPD-003).

The incoming signal pulse will be received and amplified by Bob's balanced detector, where the output voltage will be proportional to the measured quadrature. However, if the output voltage is quantized by DAC, it will introduce additional error into the measured signal, thereby contributing to excess noise as [13]:

$$\xi_{\text{ADC}} = \mu \frac{\tau V_{\text{q}}}{hf\ \text{g}^2 \rho^2 P_{\text{LO}}}, \tag{72}$$

where g is the gain coefficient of the electrical circuit of the balanced detector and ρ is the photodiode responsivity.

It should be noted that in Eqs. (64) and (72) the output voltage variance of DAC and ADC are equal, because they are selected with the same scope and resolution.

The calculation of the components of the total excess noise was carried out in accordance with the parameters specified in Table 2. The substantiation of the variance of the quadrature operator is given below in Sec. 6.1. It is important that in the considered case of transmitted LO (see Fig. 1), the power of the LO, as well as the signal power, depends significantly on the losses on equipment and in the channel, which must be taken into account in assessing the excess noise related to the receiver.

6. Evaluation and monitoring of experimental parameters

This subsection describes the procedure for assessing, optimizing and monitoring the key parameters of the CV-QKD. Since the selection of parameters directly affects the secure key generation rate, it is necessary to introduce a boundary with respect to which the calculation will be carried out.

In the general case, the secure key generation rate K is determined by

$$K = f_{\text{sym}} \cdot r, \tag{73}$$

where f_{sym} is the repetition rate and r is the secure key fraction.

The asymptotic secure key generation rate in terms of a message with ideal post-processing for the CV-QKD system in the case of collective attacks is given by the Devetak-Winter bound [45] as

$$r_{\text{coll}}^{\text{asympt}} \geqslant I_{\text{AB}} - \chi. \tag{74}$$

Given the non-ideal reverse reconciliation, the bound can be refined as

$$r_{\text{coll}}^{\text{asympt}} \geqslant (1 - \text{FER})\,(\beta I_{\text{AB}} - \chi_{\text{EB}})\,, \tag{75}$$

where $\text{FER} \in [0,\ 1]$ is the frame error rate (FER).

The quantities I_{AB} and χ_{EB} are respectively obtained by Eqs. (24) and (29). The dependence of these quantities on losses in the quantum channel is shown in Fig. 3.

It can be seen that the Holevo bound does not exceed the mutual information at large distances, thereby keeping the secure key generation rate positive (see Fig. 4). Such an assessment poorly reflects reality, because with an infinite number of messages, and, hence, with an infinite sample for estimating the parameters and an infinite number of reference signals, the excess noise in the channel is very small. At the same time, the excess noise and losses on the Bob side are still large.

TABLE 2. Parameters used in modeling excess noise obtained from Refs. [13,44]

Parameter	Description	Value	Units
V_{A}	Alice's modulation variance	6.77	SNU
RIN	RIN	$10^{-14.5}$	Hz^{-1}
B	laser spectrum width	10^4	Hz
V_π	voltage required to reverse the phase by π	5	V
α	DAC gain	8	a.u.
V_{q}	variance of output voltage of converter	$1.94{\cdot}10^{-11}$	V
V_{FS}	full-scale voltage range of DAC	1	V
N_{res}	DAC resolution	16	bit
V_{pt}	variance of pilot signal	1.2	SNU
n_{pt}	number of pilot signals	$3 \cdot 10^8$	–
$\langle N_{\mathrm{pt}} \rangle$	mean photon number in pilot puls	600	–
μ	homo-/heterodyning parameter	2	–
$P_{\mathrm{LO},\,A}$	Alice's output LO power	$2{\cdot}10^{-3}$	W
T_{det}	transmittance of signal arm	$10^{-0,745}$	a.u.
T'_{det}	transmittance of LO arm	$10^{-0,89}$	a.u.
τ	pulse duration	$3{\cdot}10^{-9}$	s
f	optical frequency	$1.934 \cdot 10^{14}$	Hz
h	Planck's constant	$6.63{\cdot}10^{-34}$	J·s
g	balanced detector's gain	10^5	V/A
ρ	photodiode responsivity	0.85	A/W
CMRR	CMRR	30	dB

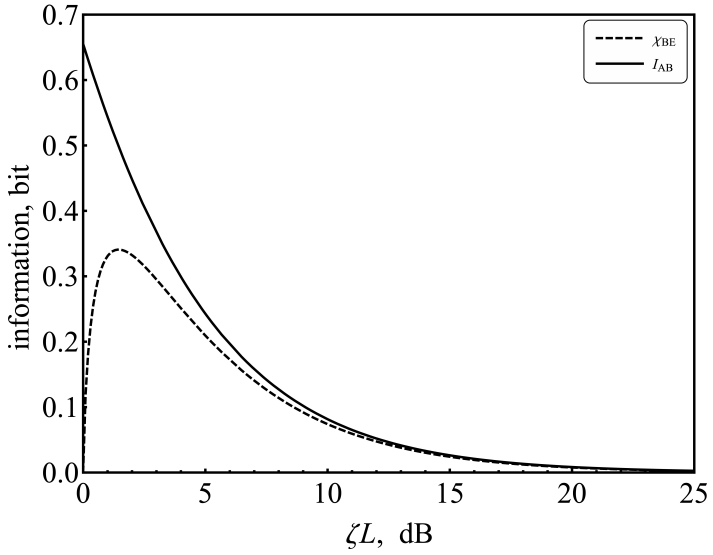

FIG. 3. Mutual information I_{AB} and the Holevo bound χ_{BE} versus losses in the quantum channel.

Limitations on the quantum channel length, as, for example, in [14], are due to the fact that the excess noise model uses not analytical expressions, but approximate fixed values. It can also be noted that when using error correction codes over an alphabet of size q, each symbol of the code corresponds to $\log_2 q$ bits, and for a given code rate R, which is selected based on the channel parameters, one can write [13]:

$$R \log_2 q = \beta I_{\mathrm{AB}}. \tag{76}$$

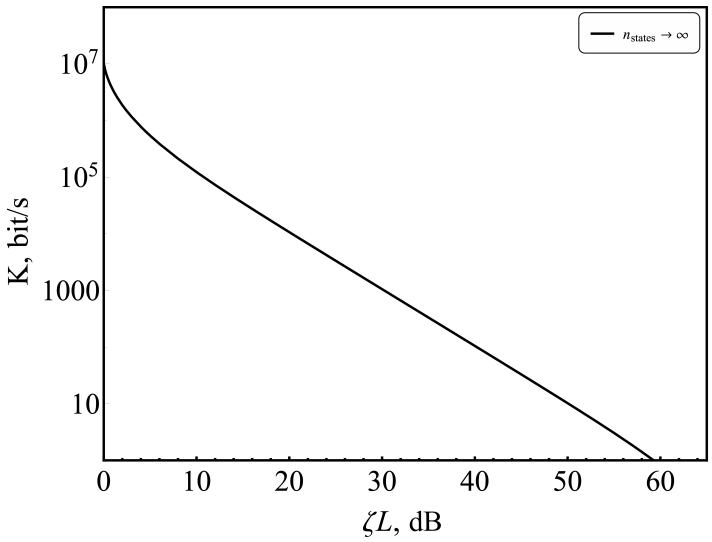

FIG. 4. Dependence of the secure key generation rate in the asymptotic limit on losses in the quantum channel considering the presence of collective attacks.

6.1. Mean photon number optimization

Obviously, an increase in the variance of Alice's quadrature operator V_{A}, which specifies the average number of photons over an ensemble of states (see Eq. (12)), will lead to a proportional increase in the signal-to-noise ratio (see Eq. (21)). That is, an increase in the average number of photons in the signal will give better discrimination of the Gaussian states up to the limits provided by the detector. However, it must be taken into account that in this case, Eve will also receive more information. In this regard, it is necessary to estimate the value of V_{A} by maximizing the value of the secure key fraction r at the target distance.

Thus, with a target loss in the quantum channel of 5 dB and the efficiency of the reconciliation procedure $\beta = 0.95$, the optimal value V_{A} is 6.77 SNU, which is obtained by maximizing the adjusted value of r from Eq. (99). It is important to note that this parameter is significantly affected by the total number of states n_{states}, which, in turn, determines the limit for the number of reference signals.

6.2. Parameter estimation

The Bob measurement data does not initially correspond to the Gaussian quantum information terminology. For this reason, it is necessary to introduce a conversion coefficient ϕ, expressed in V^2/SNU, which converts the original data to SNU. To keep track of possible changes to the calibration parameters, this procedure should be repeated during the key exchange step. Instead of the variance of the quadrature operator, Bob measures the voltage variance (see Eq. (22))

$$V(U) = \phi V\left(\hat{q}_{\mathrm{B}}\right). \tag{77}$$

Alice and Bob randomly jointly select n_{pe} from n_{states} distributed signals and publicly disclose the corresponding μn_{pe} value pairs. Under the collective Gaussian attack assumption, these pairs are independent and equally distributed Gaussian variables. In accordance with the maximum likelihood method, the following estimate can be obtained from the sample

$$V(U) = \langle U^2 \rangle - \langle U \rangle^2 = \frac{1}{\mu n_{\mathrm{pe}}} \sum_{i=1}^{\mu n_{\mathrm{pe}}} U_i^2 - \left(\frac{1}{\mu n_{\mathrm{pe}}} \sum_{i=1}^{\mu n_{\mathrm{pe}}} U_i \right)^2, \tag{78}$$

where U_i is a measured voltage value.

Approximately the parameter ϕ can be estimated as

$$\phi \approx P_{\mathrm{LO}} \rho^2 g^2 B_{\mathrm{BD}} h f, \tag{79}$$

where B_{BD} is an operating frequency of the balanced detector.

However, the coefficient ϕ must be determined experimentally more precisely. To do this, Bob disables the signal input ($TV_{\mathrm{A}} = \xi_{\mathrm{ch}} = 0$) and, instead, measures the quadratures of the vacuum state. Then, the variance of the Bob quadrature operator is as follows

$$V(\hat{q}_B) = 1 + \frac{\xi_{\mathrm{rec}}}{\mu}, \tag{80}$$

$$V(U) = \phi + \phi\frac{\xi_{\mathrm{rec}}}{\mu} \equiv \phi + N_{\mathrm{rec}}. \tag{81}$$

It should be noted that ϕ is linearly directly proportional to the LO power, while the detector noise is inversely proportional, as shown in Eq. (72) and as can be seen from Fig. 2 (the analytical formula for the detector noise is presented in [13]). Therefore, the product of two is constant with respect to P_{LO}

$$\phi \propto P_{\mathrm{LO}}, \tag{82}$$

$$\xi_{\mathrm{rec}} \propto \frac{1}{P_{\mathrm{LO}}}, \tag{83}$$

$$\frac{\partial N_{\mathrm{rec}}}{\partial P_{\mathrm{LO}}} = \frac{\partial(\phi\xi_{\mathrm{rec}})}{\partial P_{\mathrm{LO}}} = 0. \tag{84}$$

Thus, in the case of $P_{\mathrm{LO}} = 0$, the coefficient ϕ will become zero, but N_{rec} will remain unchanged, since it does not depend on the LO power. Therefore, when not only the signal but also the LO input are disabled, Eq. (81) becomes

$$V(U) = N_{\mathrm{rec}}. \tag{85}$$

Now, for a given voltage dispersion $V(U)$, obtained with a given non-zero LO power, we can write the final formula for ϕ:

$$\phi = V(U) - N_{\mathrm{rec}}. \tag{86}$$

The quantity ϕ is the quadratic measure of the voltage of exactly one SNU, still assuming that only the vacuum input is measured, i.e. $TV_{\mathrm{A}} = 0$. For subsequent parameter estimation, Bob divides his measured voltages representing q and p by $\sqrt{\phi}$ and any calculated voltage variance by ϕ, so that all his data will be represented in SNU system.

6.3. Confidence intervals

Depending on the chosen security model (trusted or untrusted noise), when estimating the parameters, it is necessary to set certain confidence intervals. Since the noise of the equipment is assumed to be trusted in the model under consideration, the total transmittance for Bob (in Eq. (60)) must be estimated in terms of the best case, while the transmittance and the excess noise of the channel — in terms of the worst.

As have already been mentioned, Alice and Bob have a sample of μn_{pe} independent and equally distributed pairs $\{x_i,\, y_i\}_{i=1}^{\mu n_{\mathrm{pe}}}$, where x_i and y_i are Gaussian variables, which are related by the ratio of the channel with additive white Gaussian noise:

$$y = \sqrt{T}x + \mathcal{N}(0,\, \xi). \tag{87}$$

For pairs of values, estimates of the transmittance and the excess noise are determined:

$$\hat{T} = \frac{\sum_{i=1}^{\mu n_{\mathrm{pe}}} x_i y_i}{\sum_{i=1}^{\mu n_{\mathrm{pe}}} x_i^2}, \tag{88}$$

$$\hat{\xi} = \frac{1}{\mu n_{\mathrm{pe}}} \sum_{i=1}^{\mu n_{\mathrm{pe}}} (y_i - \hat{T}x_i). \tag{89}$$

It should be taken into account that corrections must be introduced, depending on the belonging of the noise for a correct assessment of the mutual information and the Holevo bound. At the same time, the channel model with additive noise is preserved. The corrections themselves are expressed as [38]:

$$\mathrm{Corr}_{\xi,\,j} = w\sqrt{\mathrm{Var}(\hat{T}_j^{1/2})} = w\frac{\xi_j + \mu}{\sqrt{2\mu n_{\mathrm{pe}}}}, \tag{90}$$

$$\mathrm{Corr}_{T,\,j} = w\sqrt{\mathrm{Var}(\hat{\xi}_j)} = 2w\sqrt{\frac{2T_j^2 + T_j(\xi_j + \mu)/V_{\mathrm{A}}}{\mu n_{\mathrm{pe}}}}, \tag{91}$$

where w is the confidence factor, m is the number of signals for parameter estimation and j is the parameter that defines belonging to Alice/channel/Bob.

Such approximations are correct up to $O(n_{\mathrm{pe}}^{-1})$. The expression $\mathrm{Var}(\hat{T}^{1/2})$ can be further approximated for large n_{pe}, so a more optimistic estimate can be written

$$\mathrm{Corr}_{T,\,j} = 2w\xi_j/V_{\mathrm{A}}\sqrt{T_j/(\mu n_{\mathrm{pe}})}. \tag{92}$$

However, the estimate from Eq. (91) will be used for performance analysis.

Thus, it is necessary to carry out the replacement as follows

$$T'_{\mathrm{det}} \longrightarrow T'_{\mathrm{det}} + \mathrm{Corr}_{T,\,\mathrm{full}}, \tag{93}$$

$$T_{\mathrm{ch}} \longrightarrow T_{\mathrm{ch}} - \mathrm{Corr}_{T,\,\mathrm{ch}}, \tag{94}$$

$$\xi_{\mathrm{ch}} \longrightarrow \xi_{\mathrm{ch}} + \mathrm{Corr}_{\xi,\,\mathrm{ch}}\,. \tag{95}$$

Each of these estimates limits the corresponding actual value to within the error probability $\varepsilon_{\mathrm{pe}}$, if denote

$$w = \frac{\sqrt{2}}{\mathrm{erf}\,(1-2\varepsilon_{\mathrm{pe}})} \approx \sqrt{2\ln(1/\varepsilon_{\mathrm{pe}})}. \tag{96}$$

Approximation in Eq. (96) is allowed for small $\varepsilon_{\mathrm{pe}} \leq 10^{-17}$.

7. Estimating the finite-length secure key generation rate

After parameter estimation, each initial sequence of n_{states} dimensions goes into n symbols to be processed into the final key using error correction and privacy amplification procedures. For each information block, errors are successfully corrected with a probability of $1 - \mathrm{FER}$. The value of this probability depends on the signal-to-noise ratio, the target reconciliation efficiency β, and the ε-criteria correctness $\varepsilon_{\mathrm{cor}}$. The latter limits the probability that local bit strings of Alice and Bob are different after error correction and successful execution of the validation procedure.

On average, $n(1-\mathrm{FER})$ signals from the information block remain for the privacy amplification procedure. This final step is implemented with the ε-security parameter $\varepsilon_{\mathrm{sec}}$, which limits the trace distance between the final key and the ideal key, which has no correlation with the eavesdropper. In the QKD paradigm, it is necessary to take into account the pessimistic assessment of information distributed among users. In this case, not Shannon entropies, but smoothed Renyi min-entropies are used, which are reduced to the former through the asymptotic equipartition property [46]. The smoothness determines the allowable error fluctuations. In turn, ε-security is technically decomposed as:

$$\varepsilon_{\mathrm{sec}} = \varepsilon_{\mathrm{s}} + \varepsilon_{\mathrm{h}}, \tag{97}$$

where ε_{s} is the min-entropy smoothing parameter and ε_{h} is the parameter that determines the match of hash codes after privacy amplification procedure.

All declared ε-security parameters are set small (for example, $2^{-33} \approx 10^{-10}$) and form a general security criteria

$$\varepsilon = 2(1-\mathrm{FER})\varepsilon_{\mathrm{pe}} + \varepsilon_{\mathrm{cor}} + \varepsilon_{\mathrm{sec}}. \tag{98}$$

7.1. Satisfying the composability criteria of CV-QKD protocol in the presence of collective attacks

Taking into account the finiteness of the keys and the requirement that the protocol under consideration be composable in the presence of collective attacks, the boundary from Eq. (75) is refined, and the secure key generation rate in terms of the message is expressed as [7, 8, 37, 38]

$$r_{\mathrm{coll}}^{\mathrm{finite}} \geqslant \frac{n(1-\mathrm{FER})}{n_{\mathrm{states}}}\left(\beta I_{\mathrm{AB}}(w) - \chi_{\mathrm{EB}}(w) - \frac{\Delta_{\mathrm{AEP}}}{\sqrt{n}} + \frac{\Theta}{n}\right), \tag{99}$$

$$\Delta_{\mathrm{AEP}} = 4\log_2(2\sqrt{d}+1)\sqrt{\log_2\left(\frac{18}{(1-\mathrm{FER})^2\varepsilon_{\mathrm{s}}^4}\right)}, \tag{100}$$

$$\Theta = \log_2\left[(1-\mathrm{FER})\left(1-\varepsilon_{\mathrm{s}}^2/3\right)\right] + 2\log_2\sqrt{2}\varepsilon_{\mathrm{h}}, \tag{101}$$

where n is the number of characters left to process the final key, n_{states} is the number of states, Δ_{AEP} is the correction according to asymptotic equipartition property [46], Θ is the correction coefficient that combines hash mismatch accounting after privacy amplification procedure according to Lemma 2 of [47] and a leak on the error correction procedure [37, 38], d is the size of the effective alphabet after the final digitization of the continuous variables of Alice and Bob and ε_j is the security parameter.

To improve performance, Δ_{AEP} can be refined as [38, 48]

$$\Delta_{\mathrm{AEP}} = 4\log_2(\sqrt{d}+2)\sqrt{\log_2\left(\frac{18}{(1-\mathrm{FER})^2\varepsilon_{\mathrm{s}}^4}\right)}. \tag{102}$$

The value of n, in turn, is obtained from n_{states} as follows

$$n = n_{\mathrm{states}} - (n_{\mathrm{pt}} + n_{\mathrm{pe}}), \tag{103}$$

where n_{pt} is the number of reference signals and n_{pe} is the number of signals given for parameter estimation.

7.2. Security of CV-QKD protocol against coherent attacks

So far, the security of the CV-QKD protocol with the Gaussian modulation in the presence of Gaussian collective attacks has been substantiated. The level of security for a protocol with heterodyne detection can be extended to security against coherent attacks using the mathematical apparatus from [49].

Let the protocol $\mathcal{P}$, which uses coherent states as information carriers, be ε-secure with a secure key generation rate of finite length $r_{\text{coll}}^{\text{finite}}$ in the presence of collective Gaussian attacks, and $\mathcal{P}$ can be symmetrized with respect to the representation of the group of unitary matrices in the Fock space. This symmetrization is equivalent to applying an identical random orthogonal matrix to the classical continuous variables [49], which is certainly possible for a protocol that implies heterodyne detection. The symmetrized protocol can be denoted as $\tilde{\mathcal{P}}$.

Then it can be assumed that users jointly perform the so-called energy tests on the sample $n_{\text{et}} = f_{\text{et}} n$ from random inputs for some coefficient $f_{\text{et}} < 1$. In each test, the parties measure the local average of the number of photons, which can be extrapolated from the data, and calculate the average over the n_{et} tests. If these averages exceed the specified thresholds (d_{A} for Alice and d_{B} for Bob), the protocol is aborted. Setting $d_{\text{A}} \geqslant V_{\text{A}}/2 + O(n_{\text{et}})$ guarantees almost successful passing of the test with probability $p_{\text{et}} \approx 1$ in typical scenarios, where the signals are attenuated and the noise is not too high, at large values of n_{et} [37]. Also, for a channel with losses and sufficiently small excess noise, the average number of photons reaches Bob, which is clearly less than in the state prepared by Alice, which means that the successful value for d_{B} can be chosen to be d_{A}, i.e. relies $d_{\text{A}} = d_{\text{B}} \equiv d_{\text{et}}$.

Thus, the parties are moving to the symmetrized $\tilde{\mathcal{P}}$ protocol, which will now use $\tilde{n} = n_{\text{states}} - n_{\text{coh}}$ signals to generate secret quantum keys, where $n_{\text{coh}} \equiv n_{\text{pt}} + n_{\text{pe}} + n_{\text{et}}$.

Moreover, additional privacy amplification is required, reducing the output key string by [37, 38, 49] Φ_n

$$\Phi_n = 2\left[\log_2 \binom{K_n + 4}{4}\right], \tag{104}$$

$$K_n = \max\left\{1, 2\tilde{n} d_{\text{et}} \frac{1 + 2\sqrt{\vartheta} + 2\vartheta}{1 - 2\sqrt{\vartheta / f_{\text{et}}}}\right\}, \tag{105}$$

$$\vartheta = (2\tilde{n})^{-1} \ln(8/\varepsilon). \tag{106}$$

Assuming that the original protocol has ε security criteria against collective Gaussian attacks, otherwise the security criteria for the symmetrized protocol against coherent attacks goes to [49]

$$\varepsilon' = K_n^4 \varepsilon / 50. \tag{107}$$

It should be noted that a very strict limitation on ε-parameters is implied. In particular, this means that ε_{pe} must be sufficiently small (for example, 10^{-43}, as suggested by [25, 37]), and the corresponding coefficient confidence w must be calculated using Eq. (96).

Given the changed length of the input sequence and the change in the security criteria, Eq. (99) is rewritten as

$$r_{\text{coh}}^{\text{finite}} \geqslant \frac{\tilde{n}(1 - \text{FER})}{n_{\text{states}}} \left(\beta I_{\text{AB}}(w) - \chi_{\text{EB}}(w) - \frac{\Delta_{\text{AEP}}}{\sqrt{n}} + \frac{\Theta - \Phi_n}{n}\right). \tag{108}$$

7.3. Analysis of the potential performance of CV-QKD system

The dependence of the finite-length secure key generation rate in the presence of collective and coherent attacks on losses in the quantum channel is shown in Fig. 5. The corresponding parameters are presented in the Tables 2 and 3. A significant contribution to the performance of any system CV-QKD is made by the number of states, while increasing this parameter imposes a limit on the computing resource. In the case under consideration, this value was estimated from the calculation of memory characteristics and information processing speed, i.e. the number of states was chosen as large as possible to fully record information about them in high-speed memory of the type DDR. It is supposed to use the Kria K26 computing module from Xilinx with a memory of 4 GB, of which 2 GB is allocated for data. With further increase in the number of states, information will need to be recorded in a larger, but low-speed memory, using which, the final rate of generation of the secret quantum key will be lower. For this reason, there is a limitation on the amount of recorded information about states in memory caused by the use of high-speed memory.

The marginal losses in the quantum channel in CV-QKD in the presence of collective attacks are 10.2 dB, in the presence of coherent — 7.5 dB.

Ensuring the security of the CV-QKD protocol with Gaussian modulation against coherent attacks, in turn, requires not only a significant limitation on security criteria, but also an increase in the number of messages to maintain the proper performance level.

According to the collective attack security criteria set in p. 7.1 (see also Table 3), the number of states is $6 \cdot 10^8$. Each quantum signal pulse is followed by a reference pulse in such a way that the total number of quantum signal pulses and reference pulses is $6 \cdot 10^8$ for each block. For each quantum message, the random number generator generates 32 bits: 16 bits each to determine the value of each of the quadratures.

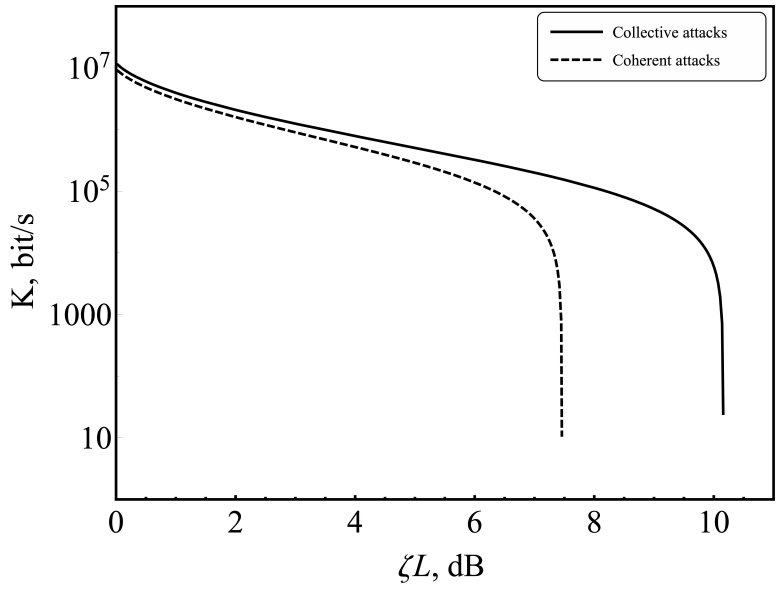

FIG. 5. Dependence of the secure key generation rate of finite length in the presence of collective and coherent attacks on losses in the quantum channel.

TABLE 3. Parameters used to evaluate the performance of the CV-QKD system. Security parameters are selected in accordance with the works [25, 36–38]

Parameter	Description	Value (collective attacks)	Value (coherent attacks)	Units
n_{states}	number of states	$6 \cdot 10^8$	$6 \cdot 10^8$	–
β	reconciliation efficiency	0.95	0.95	a.u.
FER	frame error rate	0.03	0.03	a.u.
d	size of the effective alphabet	10^4	10^4	bit
n_{pe}	number of signals for parameter estimation	$6 \cdot 10^7$	$6 \cdot 10^7$	–
f_{et}	fraction os states for energy tests	0.2	0	a.u.
w	confidence	6.34	14.07	a.u.
ε_{s}	smoothness parameter	10^{-10}	10^{-43}	a.u.
ε_{h}	parameter that determines hash code match	10^{-10}	10^{-43}	a.u.
ε	general security parameter	$5.6 \cdot 10^{-9}$	$1.3 \cdot 10^{-9}$	a.u.

Alice in the process of generating the message writes the package number without taking into account the reference pulses, using 27 bits for this (5 bits are laid down for redundancy to align the word to 4 bytes), as well as a 4-byte number obtained using a software random number generator implemented on the basis of the FPGA Alice module. Bob detects both quadratures of each message received from the channel. Given that half of the states are reference pulses and two quadrature values are recorded for each state, legitimate users within each block write down information about $6 \cdot 10^8$ quantum state quadrature values. During detection, Bob writes the number of the message (which accounts for 4 bytes) and 4 bytes of information about the two registered values of quadratures of quantum messages to high-speed DDR memory, as well as 4 bytes of information about the two registered values of the quadratures of the reference pulses.

Information about the registered reference pulse quadratures is used to compensate for the phase shift of quantum messages as a result of transmission over a quantum channel, after which this information is deleted from memory. Every ten states, Bob randomly selects one to be used for channel characterization (for the parameter estimation procedure). For the remaining messages, insignificant bits are discarded in the part containing information about quadratures, as a result

of which eight bits remain out of 32 bits of information. On average, each package has 5.3 bytes of information. The time taken for detection and storage is 12 seconds.

To evaluate the channel, states are disclosed for which insignificant bits have not been discarded. After that, errors are corrected using multi-level encoding and multi-stage decoding [50–52]. During error correction, three of the four bits are revealed, thereby reducing the bit sequence to a length of $5.4 \cdot 10^8$ bits.

After the error correction is completed, universal hashing is used to exhaustively verify that all Alice and Bob sequences are the same (confirmation procedure). Hashing of the key with corrected errors is performed both in Alice's and Bob's blocks. As a result of hashing, users still have hash codes on their hands. Bob sends the received hash code to Alice. She then compares the values of two hash codes: the one calculated in her block and the one received from Bob. The result of the comparison is then transmitted to him. If the values do not match, then the processing of this sifted key stops without generating a secret key. The key that has not passed the confirmation procedure is erased from memory on both sides.

A 2-universal hash function is used at the privacy amplification step. The input is a key with corrected errors. The corrected key is loaded in blocks. The ratio of the length of the output sequence after privacy amplification procedure to the length of the input sequence is 1:66.

Since the post-processing of the sequence is faster than writing information to memory during detection, these processes can be performed in parallel.

8. Conclusion

In this paper, we have carried out a theoretical analysis of the performance of the realistic CV-QKD system. Our estimates show that performance can be maintained with losses as low as 10 dB in the most common assumption of collective attacks. In the presence of coherent attacks, there is a noticeable drop in allowable losses (down to 7 dB), and at the same time, tougher security criteria must be taken into account, which are still quite difficult to satisfy in practice. Further work will be focused on creating an experimental setup in accordance with what is described in the article and evaluating the performance of a real system.

References

[1] Pirandola S., Andersen U.L., Banchi L., Berta M., Bunandar D., Colbeck R., Englund D., Gehring T., Lupo C., Ottaviani C., Pereira J.L., Razavi M., Shamsul Shaari J., Tomamichel M., Usenko V.C., Vallone G., Villoresi P., and Wallden P., Advances in quantum cryptography. *Advances in Optics and Photonics*, 2020, **12**, P. 1012.

[2] Bennett C.H., Brassard G., Quantum cryptography: Public key distribution and coin tossing. *Theoretical Computer Science*, 2014, **560**(12), P. 7–11.

[3] Bennett C.H., Brassard G., Mermin N.D., Quantum cryptography without Bell's theorem. *Physical Review Letters*, 1992, **68**(2), P. 557–559. .

[4] Ralph T.C., Continuous variable quantum cryptography. *Phys. Rev. A*, 1999, **61**(1), P. 010303.

[5] Cerf N.J., Lévy M., Assche G.V., Quantum distribution of Gaussian keys using squeezed states. *Physical Review A*, 2001, **63**(4), P. 052311.

[6] Grosshans F., Van Assche G., Wenger J., Brouri R., Cerf N.J., Grangier P., Quantum key distribution using gaussian-modulated coherent states. *Nature*, 2003, **421**(1), P. 238–241.

[7] Leverrier A., Grosshans F., Grangier P., Finite-size analysis of a continuous-variable quantum key distribution. *Physical Review A*, 2010, **81**(6), P. 062343.

[8] Leverrier A., Composable Security Proof for Continuous-Variable Quantum Key Distribution with Coherent States. *Physical Review Letters*, 2015, **114**(2), P. 070501.

[9] Ghorai S.,Grangier P.,Diamanti E., and Leverrier A., Asymptotic Security of Continuous-Variable Quantum Key Distribution with a Discrete Modulation. *Physical Review X*, 2019, **9**(6), P. 021059.

[10] Lin J., Upadhyaya T., Lütkenhaus N., Asymptotic Security Analysis of Discrete-Modulated Continuous-Variable Quantum Key Distribution. *Phys. Rev. X*, 2019, **9**(12).

[11] Denys A., Brown P., Leverrier A., Explicit asymptotic secret key rate of continuous-variable quantum key distribution with an arbitrary modulation. *Quantum*, 2021, **5**(9), P. 540.

[12] Usenko V., Filip R., Trusted Noise in Continuous-Variable Quantum Key Distribution: A Threat and a Defense. *Entropy*, 2016, **18**(1), P. 20. .

[13] Laudenbach F., Pacher C., Fung C.-H. F., Poppe A., Peev M., Schrenk B., Hentschel M., Walther P., and Hübel H., Continuous-Variable Quantum Key Distribution with Gaussian Modulation-The Theory of Practical Implementations. *Advanced Quantum Technologies*, 2018, **1**(8), P. 1800011.

[14] Laudenbach F., Pacher C., Analysis of the Trusted-Device Scenario in Continuous-Variable Quantum Key Distribution. *Advanced Quantum Technologies*, 2019, 2(11), P. 1900055.

[15] Weedbrook C., Lance A.M., Bowen W.P., Symul T., Ralph T.C., Lam P.K., Quantum Cryptography Without Switching. *Physical Review Letters*, 2004, **93**(10), P. 170504.

[16] Huang D., Huang P., Lin D., and Zeng G., Long-distance continuous-variable quantum key distribution by controlling excess noise. *Scientific Reports*, 2016, **6**(5), P. 19201.

[17] Bennett C.H., Quantum cryptography using any two nonorthogonal states. *Physical Review Letters*, 1992, **68**(5), P. 3121–3124.

[18] Carter J., Wegman M.N., Universal classes of hash functions. *Journal of Computer and System Sciences*, 1979, **18**(4), P. 143–154.

[19] Scarani V., Bechmann-Pasquinucci H., Cerf N.J., Du M.\ifmmode \checks\else š\fiek, N. Lütkenhaus, and M. Peev, The security of practical quantum key distribution. *Reviews of Modern Physics*, 2009, **81**(9), P. 1301–1350.

[20] Jouguet P., Kunz-Jacques S., Diamanti E., and Leverrier A., Analysis of imperfections in practical continuous-variable quantum key distribution, *Physical Review A*, 2012, **86**(9), P. 032309.

[21] Filip R., Continuous-variable quantum key distribution with noisy coherent states. *Physical Review A*, 2008, **77**(2), P. 22310.

[22] Usenko V.C., Filip R., Feasibility of continuous-variable quantum key distribution with noisy coherent states. *Physical Review A*, 2010, **81**(2), P. 022318.

[23] Jacobsen C., Gehring T., and Andersen U., Continuous Variable Quantum Key Distribution with a Noisy Laser. *Entropy*, 2015, **17**(7), P. 4654–4663.

[24] Zhang Y., Chen Z., Pirandola S., Wang X., Zhou C., Chu B., Zhao Y., Xu B., Yu S., and Guo H., Long-Distance Continuous-Variable Quantum Key Distribution over 202.81 km of Fiber, *Physical Review Letters*, 2020, **125**(6), P. 010502.
[25] Hosseinidehaj N., Lance A.M., Symul T., Walk N., and Ralph T.C., Finite-size effects in continuous-variable quantum key distribution with Gaussian postselection. *Physical Review A*, 2020, **101**(5), P. 052335.
[26] Jouguet P., Kunz-Jacques S., Leverrier A., Grangier P., and Diamanti E., Experimental demonstration of long-distance continuous-variable quantum key distribution. *Nature Photonics*, 2013, **7**(5), P. 378–381.
[27] Agrawal G.P., *Fiber-optic communication systems*, vol. 222. John Wiley & Sons, 2012.
[28] Polarization Insensitive Isolator (ISO) http://www.lightcomm.com/product/view/typeid/235/id/268.html.
[29] Polarization Maintaining Fused Standard Coupler (PMC) http://www.lightcomm.com/home/product/view/typeid/189/id/206.html.
[30] Intensity Modulators https://photonics.ixblue.com/store/lithium-niobate-electro-optic-modulator/intensity-modulators.
[31] Phase Modulators https://photonics.ixblue.com/store/lithium-niobate-electro-optic-modulator/phase-modulators.
[32] Polarization Beam Combiner/Splitter (PBC/PBS) http://www.lightcomm.com/product/view/typeid/190/id/212.html.
[33] 90-Degree Optical Hybrid http://www.optoplex.com/Optical_Hybrid.htm.
[34] Polarization Maintaining Isolator (PMISO) http://www.lightcomm.com/product/view/typeid/190/id/211.html.
[35] HIGH SPEED POLARIZATION CONTROLLER-SCRAMBLER (OEM VERSION) https://www.ozoptics.com/ALLNEW_PDF/DTS0143.pdf.
[36] Hosseinidehaj N., Walk N., and Ralph T.C., Optimal realistic attacks in continuous-variable quantum key distribution. *Physical Review A*, 2019, **99**(5), P. 1–11.
[37] Pirandola S., Limits and security of free-space quantum communications. *Physical Review Research*, 2021, **3**(3), P. 013279.
[38] Pirandola S., Composable security for continuous variable quantum key distribution: Trust levels and practical key rates in wired and wireless networks. *Physical Review Research*, 2021, **3**(10), P. 043014.
[39] Qi B., Lougovski P., Pooser R., Grice W., and Bobrek M., Generating the Local Oscillator "Locally" in Continuous-Variable Quantum Key Distribution Based on Coherent Detection. *Physical Review X*, 2015, **5**(10), P. 041009.
[40] Soh D.B., Brif C., Coles P.J., Lütkenhaus N., Camacho R.M., Urayama J., and Sarovar M., Self-referenced continuous-variable quantum key distribution protocol. *Physical Review X*, 2015, **5**(4), P. 1–15.
[41] Kleis S., Rueckmann M., and Schaeffer C.G., Continuous variable quantum key distribution with a real local oscillator using simultaneous pilot signals. *Optics Letters*, 2017, **42**(4), P. 1588.
[42] Laudenbach F., Schrenk B., Pacher C., Hentschel M., Fung C.-H.F., Karinou F., Poppe A., Peev M., and Hübel H., Pilot-assisted intradyne reception for high-speed continuous-variable quantum key distribution with true local oscillator. *Quantum*, 2019, **3**(10), P. 193.
[43] Szynowski J., CMRR analysis of instrumentation amplifiers. *Electronics Letters*, 1983, **19**(14), P. 547.
[44] Tang X., Kumar R., Ren S., Wonfor A., Penty R., and White I., Performance of continuous variable quantum key distribution system at different detector bandwidth. *Optics Communications*, 2020, **471**(9), P. 126034.
[45] Devetak I. and Winter A., Distillation of secret key and entanglement from quantum states, *Proceedings of the Royal Society A: Mathematical, Physical and Engineering Sciences*, 2005, **461**(1), P. 207–235.
[46] Tomamichel M., Colbeck R., and Renner R., A fully quantum asymptotic equipartition property. *IEEE Transactions on information theory*, 2009, **55**(12), P. 5840–5847.
[47] Tomamichel M., Schaffner C., Smith A., and Renner R., Leftover Hashing Against Quantum Side Information. *IEEE Transactions on Information Theory*, 2011, **57**(8), P. 5524–5535.
[48] Tomamichel M., *Quantum Information Processing with Finite Resources*. Cham: Springer International Publishing, 2016.
[49] Leverrier A., Security of Continuous-Variable Quantum Key Distribution via a Gaussian de Finetti Reduction. *Physical Review Letters*, 2017, **118**(5), P. 200501.
[50] Van Assche G., Cardinal J., and Cerf N., Reconciliation of a Quantum-Distributed Gaussian Key. *IEEE Transactions on Information Theory*, 2004, **50**(2), P. 394–400.
[51] Mani H., *Error Reconciliation Protocols for Continuous-Variable Quantum Key Distribution*. PhD thesis, Technical University of Denmark, 2021.
[52] Wen X., Li Q., Mao H., Wen X., and Chen N., Rotation Based Slice Error Correction Protocol for Continuous-variable Quantum Key Distribution and its Implementation with Polar Codes. *arXiv preprint arXiv:2106.06206*, 2021, **6**, P. 1–17.

Submitted 30 May 2022; revised 16 June 2022; accepted 17 June 2022

Information about the authors:

Roman K. Goncharov – ITMO University, Kronverkskiy, 49, St. Petersburg, 197101, Russia; rkgoncharov@itmo.ru

Alexei D. Kiselev – ITMO University, Kronverkskiy, 49, St. Petersburg, 197101, Russia; alexei.d.kiselev@gmail.com

Eduard O. Samsonov – ITMO University, Kronverkskiy, 49, St. Petersburg, 197101, Russia; eosamsonov@itmo.ru

Vladimir I. Egorov – ITMO University, Kronverkskiy, 49, St. Petersburg, 197101, Russia; viegorov@itmo.ru

Conflict of interest: the authors declare no conflict of interest.

NANOSYSTEMS:
PHYSICS, CHEMISTRY, MATHEMATICS

Adam I.A., et al. *Nanosystems: Phys. Chem. Math.*, 2022, **13** (4), 392–403.
http://nanojournal.ifmo.ru
DOI 10.17586/2220-8054-2022-13-4-392-403

Original article

Comparison of Gaussian and vortex beams in free-space QKD with phase encoding in turbulent atmosphere

Iurii A. Adam[a], Daniil A. Yashin[b], Daria A. Kargina[c], Boris A. Nasedkin[d]

ITMO University, St. Petersburg, 197101, Russia

[a]adam_yura@mail.ru, [b]dayashin@itmo.ru, [c]dakargina17@gmail.com, [d]b.nasedkin@bk.ru

Corresponding author: Iurii A. Adam, adam_yura@mail.ru

PACS 03.67.Dd, 42.25.Dd

ABSTRACT At present, free-space QKD systems are being actively researched and developed. The main limitation of these systems remains the strong influence of atmospheric turbulence and weather conditions on the propagating Gaussian beam. In turn, a number of works have shown that vortex beams are more stable in a turbulent atmosphere. Thus, in this work, the use of vortex beams in the free-space QKD system with phase encoding under the condition of a turbulent atmosphere and their comparison with Gaussian beams are studied. The possibility of phase modulation preservation with additional modulation and demodulation of the vortex beam is also investigated.

KEYWORDS quantum key distribution, vortex beam, atmospheric turbulence, free-space, phase encoding, fork-grating

ACKNOWLEDGEMENTS The study is funded by RPMA grant of School of Physics and Engineering of ITMO University. The authors of this work express their gratitude to Aleksey Viktorovich Chernykh from ITMO University for his support and discussions during the experiment, to Artur Mukhamadiev for his help with illustration preparation and to the Centre for Reprography at the Russian National Library for the production of the fork-gratings.

FOR CITATION Adam I.A., Yashin D.A., Kargina D.A., Nasedkin B.A. Comparison of Gaussian and vortex beams in free-space QKD with phase encoding in turbulent atmosphere. *Nanosystems: Phys. Chem. Math.*, 2022, **13** (4), 392–403.

1. Introduction

Quantum key distribution (QKD) is a new direction in communication technology. QKD establishes the secure connection between two parties (usually called Alice and Bob), where the reliability of purposed channel is provided by the laws of quantum mechanics, the most important of which is no-cloning theorem [1]. In the long run, QKD provides safer connection than common cryptosystems based on the complexity of calculating mathematical functions.

The first proposed protocol was BB84 [2], where the secret key was generated by using two orthogonal photon polarization bases. Since that time, many protocols and experimental schemes were investigated to improve the parameters of QKD systems and expand the possibilities of their applications [3]. In particular, free-space QKD has been actively developed due to its flexibility and mobility which can be used in mobile devices [4], satellite communication [5] and Internet of Things (IoT) [6]. Despite its advantages, free-space QKD has not been widely used in commercial systems compared to optical fiber ones. The main limitation of these systems is the deviation of the Gaussian beam from the original direction of propagation resulting from atmosphere turbulence and weather conditions. To solve this problem, telescopic systems with a large entrance aperture or special correction systems are currently used, which increase the complexity, weight and cost of QKD systems.

As an alternative method of beam deviation compensation, optical vortices can be used, which, according to a number of studies [7, 8], are more stable in a turbulent atmosphere. Optical vortices, or optical radiation with orbital angular momentum (OAM), have a spatial singularity at their center, where the phase remains indeterminate, and along the inner edges of the beam varies from 0 to 2π [9]. The number of these transitions corresponds to the topological charge of the vortex. At present, vortex beams have already been studied in QKD systems, in particular, as bases for encoding information [10] and for multiplexing a channel with respect to the orbital momentum [11]. However, no comparison has been made between the propagation of Gaussian and vortex beams in a free-space QKD with turbulent atmosphere and their influence on the parameters of such systems. Also, no experimental studies have been carried out on the phase modulation preservation with additional modulation and demodulation of the vortex beam, which is necessary for the effective integration of the atmospheric channel with the optical fiber. These questions will be explored in this article.

2. Theory

2.1. Beam Propagation

Analytical expression for the electric field of Laguerre-Gaussian modes, well-known example of vortex beams shown in Fig. 1, is given in the form [12]:

$$u(r,\phi,z) = E_0 \left(\sqrt{2}\frac{r}{w(z)}\right)^l L_p^l \left(2\frac{r^2}{w(z)^2}\right) \frac{w_0}{w(z)} \exp\left[-i\varphi_{pl}(z)\right] \exp\left[i\frac{k}{2q(z)}r^2\right] \exp(il\phi), \tag{1}$$

where L_p^l is the Laguerre polynomial corresponding to the given mode, $q(z)$ is the complex beam parameter, $w(z)$ is the beam radius, w_0 is the waist radius, $\varphi_{pl}(z) = (2p + l + 1)\tan^{-1}(z/z_0))$ is the Gouy phase shift, $z_0 = \pi w_0^2/\lambda$ is the Rayleigh length, $k = 2\pi/\lambda$ is the wave number, λ is the radiation wavelength, r is the radial coordinate of the cylindrical coordinate system. Indices p and l denote radial and azimuth numbers of the mode respectively (the latter is also called the topological charge). Using expression (1), one can obtain the desired distributions, as well as the beam intensity profiles. Since the Gaussian beam is the Laguerre - Gaussian zero mode, one can obtain an analytical expression for the Gaussian beam by setting $l = 0, p = 0$ in (1).

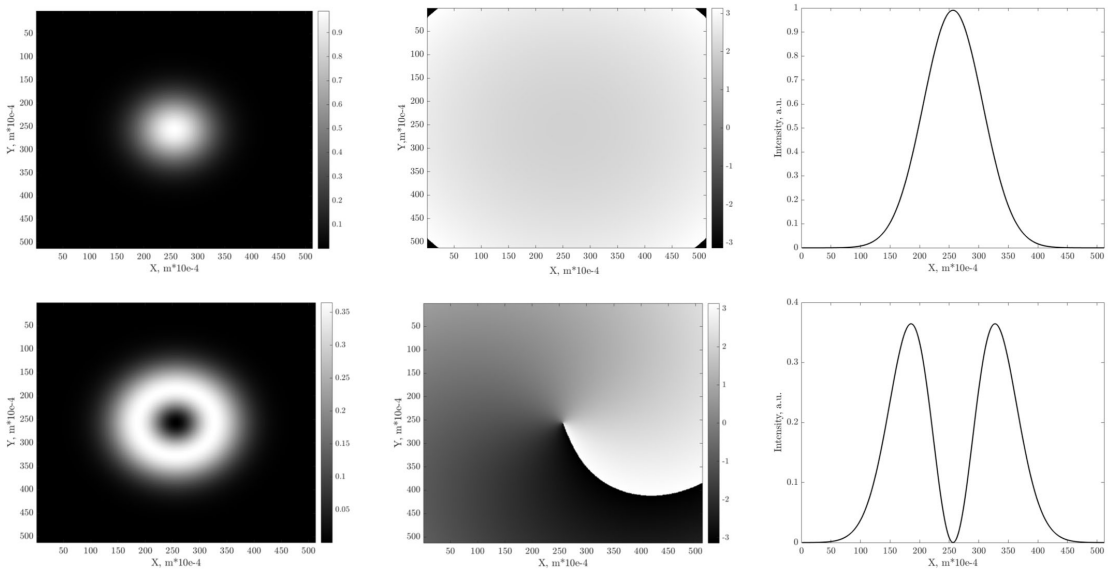

FIG. 1. Laguerre-Gaussian modes. Columns show intensity distributions, phase fronts and beam profiles of Gaussian beam (Top) and Laguerre-Gaussian first mode (Bottom)

Modeling of free space vortex beams propagation is made by using multiple random phase screens method [13], general scheme of which is shown in Fig. 2. In this method, the simulation of turbulence is carried out by placing on the propagation path many thin phase screens, dividing this path into a certain number of segments, on each of which the medium can be considered homogeneous. Thickness is a key point, since in the phase screen approximation, its effect extends only to the radiation phase, the amplitude does not change. The propagation of radiation in a segment of a homogeneous medium can be described by using the calculation of diffraction by the Rayleigh-Sommerfeld method:

$$U_2(x,y) = \frac{z}{j\lambda} \iint_\Sigma U_1(\xi,\eta) \frac{\exp(jkr_{12})}{r_{12}^2} d\xi d\eta, \tag{2}$$

where z is the distance between the centers of the source and receiver planes, r_{12} is the distance between the source and the observation points, ξ, η are the integration variables, Σ is the source area.

Expression (2), in the general case, is a superposition integral, but for planar geometry, in which the source and receiver planes are parallel, it becomes a convolution-type integral

$$U_2(x,y) = \iint U_1(\xi,\eta) h(x-\xi, y-\eta) d\xi d\eta \tag{3}$$

Applying the convolution theorem, we obtain from (3):

$$U_2(x,y) = \mathfrak{J}^{-1}\left\{\mathfrak{J}\left\{U_1(x,y)\right\} H\left(f_X, f_Y\right)\right\}, \tag{4}$$

where the transfer function H is as follows:

$$H\left(f_X, f_Y\right) = e^{jkz} \exp\left[-j\pi\lambda z\left(f_X^2 + f_Y^2\right)\right] \tag{5}$$

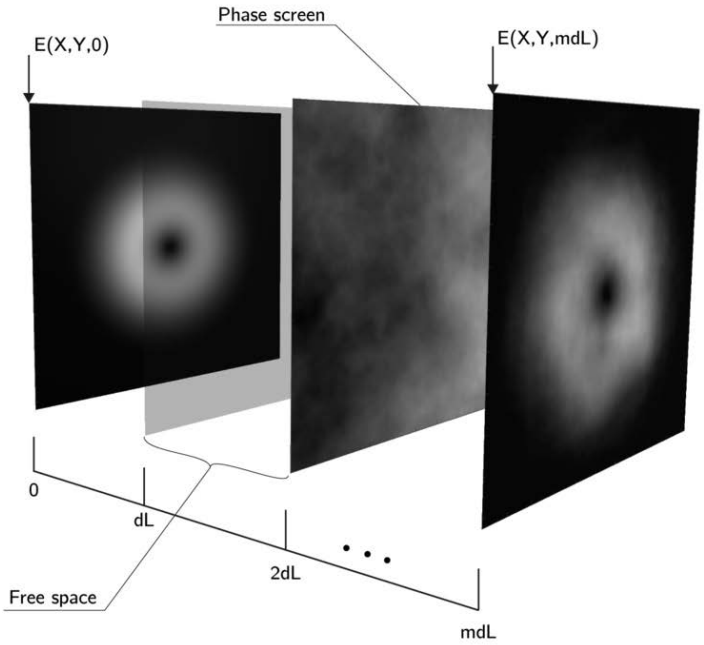

FIG. 2. Scheme of the method of many phase screens for modeling the propagation of radiation in a randomly inhomogeneous medium

2.2. Turbulence and scattering effects

After passing through the homogeneous section of the channel, the beam passes through the phase screen. The effect of the phase screen on the radiation is reduced to the usual multiplication by the exponential term:

$$U_{\text{in}}\ (x, y, z_+) = U_{\text{in}}\ (x, y, z_-) \cdot \exp[i \cdot \varphi(x, y).] \tag{6}$$

The z_+ and z_- coordinates correspond to the field after and before passing through the screen, respectively. Here $\varphi(x, y)$ is the spatial distribution of the random phase, which is a characteristic of some spectrum of the random phase. In this work, the von Karman-type power spectrum of the random phase was used [14]:

$$\Phi(\boldsymbol{\kappa}) = \frac{C(\alpha) r_C^{-\alpha}}{\left(\kappa^2 + \kappa_0^2\right)^{1+\alpha/2}} \exp\left(-\frac{\kappa^2}{\kappa_m^2}\right), \tag{7}$$

$$C(\alpha) = \frac{\alpha 2^{\alpha-2}\Gamma(1+\alpha/2)}{\pi\Gamma(1-\alpha/2)},$$

where $\kappa_0 = 2\pi/L_0$, $\kappa_m = 2\pi/l_0$, $1 < \alpha < 2$, $\Gamma(1 \pm \alpha/2)$ is the Euler Gamma-function, L_0 is the outer scale of turbulence, l_0 is the inner scale of turbulence, r_C is the atmosphere coherence length.

The radiation power loss in the communication channel can be described by the Bouguer - Lambert - Beer law:

$$I(\lambda, z) = I_0(a) \exp\left(-z\alpha_{ext}(\lambda)\right), \tag{8}$$

where $\alpha_{ext}(\lambda)$ is the extinction coefficient. This coefficient consists of two components - the attenuation coefficients due to absorption and scattering:

$$\alpha_{ext}(\lambda) = \alpha_{abs}(\lambda) + \alpha_{scatt}(\lambda)$$

Taking into account the wavelength range in which the system is modeled (the telecommunications range (λ = 1500 nm)), the atmospheric absorption coefficient can be neglected, since its contribution to the total attenuation coefficient is insignificantly small [15].

As for the scattering coefficient, it is the sum of the coefficients of the Rayleigh scattering and the Mie scattering. It is known from theory that the energy loss due to Rayleigh scattering is inversely proportional to the fourth power of the wavelength:

$$\sigma_{\text{s}} = \frac{2\pi^5}{3}\frac{d^6}{\lambda^4}\left(\frac{n^2-1}{n^2+2}\right)^2, \tag{9}$$

where d is the diameter of the molecule, n is the refractive index of the medium, and λ is the radiation wavelength. Given this fact, for the telecommunications wavelength range, the molecular scattering coefficient can be neglected.

Mie scattering occurs on particles whose size is of the order of the radiation wavelength. Typical size of the components of atmospheric aerosols varies greatly and ranges from 10^{-9} m to 10^{-5} m. Since the estimation of the Mie

scattering coefficient requires knowledge of the concentration and distribution of particles, which is an experimentally difficult problem. There are models that describe aerosol conditions depending on the meteorological or local characteristics of the environment. Thus, the signal attenuation caused by Mie scattering can be estimated using the dependence of the attenuation coefficient on the visibility range of objects through the atmosphere [15, 16].

$$\alpha_{scatt}(\lambda) = \frac{3.91}{V}\left(\frac{\lambda}{550}\right)^{-\delta}, \tag{10}$$

$$\delta = \begin{cases} 1.6, & V > 50 \text{ km}; \\ 1.3, & 6 \text{ km} < V < 50 \text{ km}; \\ 0.585\, V^{1/3}, & V < 6 \text{ km}. \end{cases} \tag{11}$$

2.3. Random phase screen generation procedure

We use trigonometric representation of random phase simulation algorithm:

$$\psi(\mathbf{r}) = \sum_{n=1}^{N} a_n \exp\left(i\mathbf{k}_n \cdot \mathbf{r}\right), \quad \varphi_1(\mathbf{r}) = \mathrm{Re}[\psi(\mathbf{r})], \quad \varphi_2(\mathbf{r}) = \mathrm{Im}[\psi(\mathbf{r})], \tag{12}$$

where $\psi(r)$ is the complex phase, $r(x, y)$ is the point at which the phase is calculated, a_n are the random complex spectral amplitudes, $k_n(p_n, q_n)$ are the wave vectors of the individual spectral components, N is the number of spectral components used to represent the complex phase. The method for generating phase screens is based on the discrete Fourier transform of the phase [14]:

$$\psi_{DFT}(j\Delta x, l\Delta x) = \sum_{m,n=-N_{DFT}/2}^{N_{DFT}/2-1} a_{m,n} \exp\left(\frac{2i\pi}{N_{DFT}}(mj + nl)\right), \tag{13}$$

where $\Delta x = L/N_{DFT}$, $\Delta k = 2\pi/L$. The structural function of such phase has the form:

$$D_{DFT}(j\Delta x, l\Delta x) = 2(\Delta k)^2 \sum_{m,n=-N_{DFT}/2}^{N_{DFT}/2-1} \Phi(m\Delta k, n\Delta k)\left[1 - \exp\left(\frac{2i\pi}{N_{DFT}}(mj + nl)\right)\right], \tag{14}$$

where $\Phi(m\Delta k, n\Delta k)$ is the spatial phase spectrum corresponding to the chosen von Karman turbulence model. An example of a generated phase screen is shown in Fig. 3.

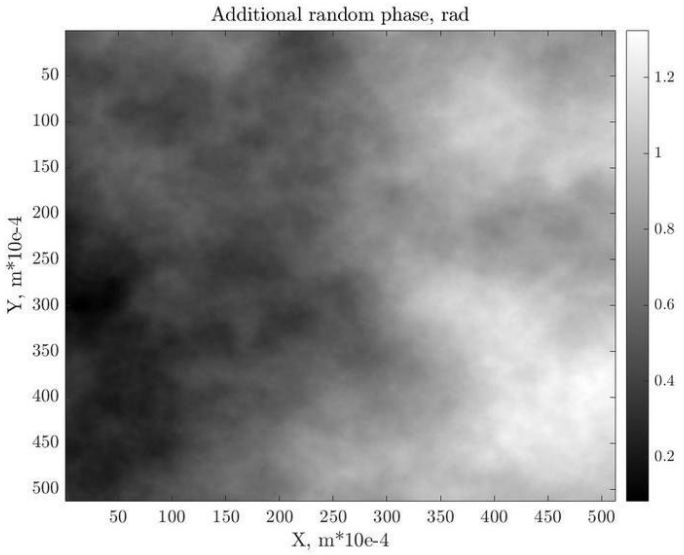

FIG. 3. An example of a generated random phase screen according to the selected turbulence spectrum

2.4. QKD system parameters estimation

As the object of study the subcarrier wave quantum key distribution (SCW QKD) system were chosen [17], the free-space implementation of which is described in [15]. The study of the parameters of this system, as well as their description, are detailed in [18].

It is worth noting that the propagation of quantum signals from the sender to the receiver is considered in the approximation of the classical description. In this article we do not consider the quantum effects such as quantum entanglement, quadrature and photon number squeezing, precisely described in [19, 20]. This approximation was made on the basis of the fact that the protocol used in the SCW QKD system is based on the use of attenuated laser pulses - coherent states (obeying Poisson statistics), which are not strictly single-photon states (constituting the Fock basis).

One of the main values, characterizing a QKD system is the secret key generation rate:

$$K\left(\mu_0, m, L\right) = \frac{1-G}{2T}\left[1 - h\left(\frac{E}{1-G}\right) - h\left(\frac{1}{2}\left(1 - e^{-\mu_0(1-J_0(2m))}\right)\right)\right], \tag{15}$$

where

$$E = \frac{1}{2}P_{det}(0, \pi + \Delta\varphi), \tag{16}$$

$$1 - E - G = \frac{1}{2}P_{det}(0, \Delta\varphi), \tag{17}$$

$$h(Q) = -Q\log_2 Q - (1-Q)\log_2(1-Q), \tag{18}$$

$$Loss = 10\log(\frac{P_{in}}{P_{out}}), \tag{19}$$

$m = \sqrt{m_A^2 + m_B^2 + 2m_A m_B \cos\left(\varphi_A - \varphi_B\right)}$ is the modulation index of the system, where m_A, m_B are modulation indices in Alice's and Bob's modules respectively, $h(Q)$ is the binary Shannon entropy, T is the pulse duration, μ_0 is the average number of photons at the input of Alice's modulator, L is the length of the communication channel, P_{in} is the power at the source plane, P_{out} is the power at the detector plane. The value $P_{det}(0, \pi + \Delta\phi)$ or $P_{det}(0, \Delta\phi)$ in (16), (17) represents the probability of detecting a photon in the recipient block

$$P_{det}\left(\varphi_A, \varphi_B\right) = \left(\eta_D \frac{n_{ph}\left(\varphi_A, \varphi_B\right)}{T} + \gamma_{dark}\right)\Delta t, \tag{20}$$

where φ_A, φ_B are the phase delays introduced in the modulators of Alice and Bob, respectively, η_D is the quantum efficiency of the detector used, γ_{dark} is the frequency of dark counts, Δt is the detector gating time. The average number of photons arriving at Bob's detector in time T:

$$n_{ph}\left(\varphi_A, \varphi_B\right) = \mu_0 \eta(L) \eta_B \left(1 - (1-\vartheta)\left|J_0\left(m\right)\right|^2\right), \tag{21}$$

where η_B is the loss in the Bob's module, ϑ is the coefficient that takes into account the imperfection of spectral filtering in the recipient block, J_0 is the Bessel function of the first kind.

Another equally important characteristic is the quantum bit error rate (QBER):

$$Q(L) = \frac{E}{1-G}. \tag{22}$$

QBER represents the ratio of a negative outcome probability - an error of detection, to the probability of obtaining any outcome.

3. Numerical results

3.1. Beam propagation

Modeling the process of radiation propagation in a turbulent atmosphere contains several stages. At the initial stage, it is necessary to obtain intensity distributions, phases, as well as intensity profiles of both beams in the source plane - at the exit from the Alice's module. In this work, the process of generation of vortex radiation is not considered, and the simulation of its direct propagation begins after the vortex beam has already been obtained. Modeling of Gaussian beam is carried out with the use of the following parameters: λ = 1500 nm; ω_0 =1 cm ; z_0 = 20 m; $l = 0$, $p = 0$. Parameters for vortex beam are λ = 1500 nm; ω_0 =1 cm ; z_0 = 20 m; $l = 1$, $p = 0$. Results of the first stage are shown in Fig. 1.

Further, having the input characteristics of the beams, it is necessary to carry out the procedure for their propagation over a given distance. At the input of the propagation channel, just behind the input plane, a random phase screen is placed, generated by an algorithm based on the discrete Fourier transform of a random phase, mentioned above and described in detail in [14]. A random phase screen affects the phase front of the original beam, distorting it. We numerically investigated two cases: r_C = 1 m; r_C = 0.1 m. The shorter coherence length corresponds to a stronger turbulence. Other chosen parameters of the atmosphere are: l_0 = 1 cm; L_0 = 10 m; $\alpha = \frac{5}{3}$; V = 20 km. Total channel length on this stage was L = 1000 m, the propagation results of which are shown in Fig. 4. Distance between the phase screens

ΔL is chosen to be 100 m, (i.e. 11 phase screens are used), as it is typical distance for this kind of simulation [21]. Aperture of the receiving telescope is D_{det}^{G} = 0.17 m for the Gaussian beam and D_{det}^{V} = 0.20 m for the vortex beam. Aperture diameters remain constant for all the propagation distances. The difference between aperture diameters of the receiving telescopes is dictated by the fact that the studied beams have different cross-sectional areas for equal waist radii. Since the purpose of this study is to compare the considered beams under the same conditions, we chose apertures of the receiving telescopes that would provide the same ratio of the cross-sectional areas of the beams and the areas of the detectors (receiving telescopes). Fig. 4 shows the case, where the beam, propagating through a turbulent atmosphere, undergoes shape distortions, as well as phase front distortions. This distortion is the stronger, the shorter the atmosphere coherence length is. Also, it can be seen that with an increase of turbulence strength, the shift of the beam center relative to the given axis of its propagation becomes more obvious, this phenomenon is called beam wandering. These "wanders", depicted in Fig. 5, lead to geometric losses of radiation, since the beam goes beyond the boundaries of the aperture of the receiving telescopic device. Table 1 shows the average values of the shifts and root-mean-square deviations of the shifts of both beams as they propagate through the turbulent channel at distance L = 1000 m. To perform this assessment, 30 independent simulations were carried out.

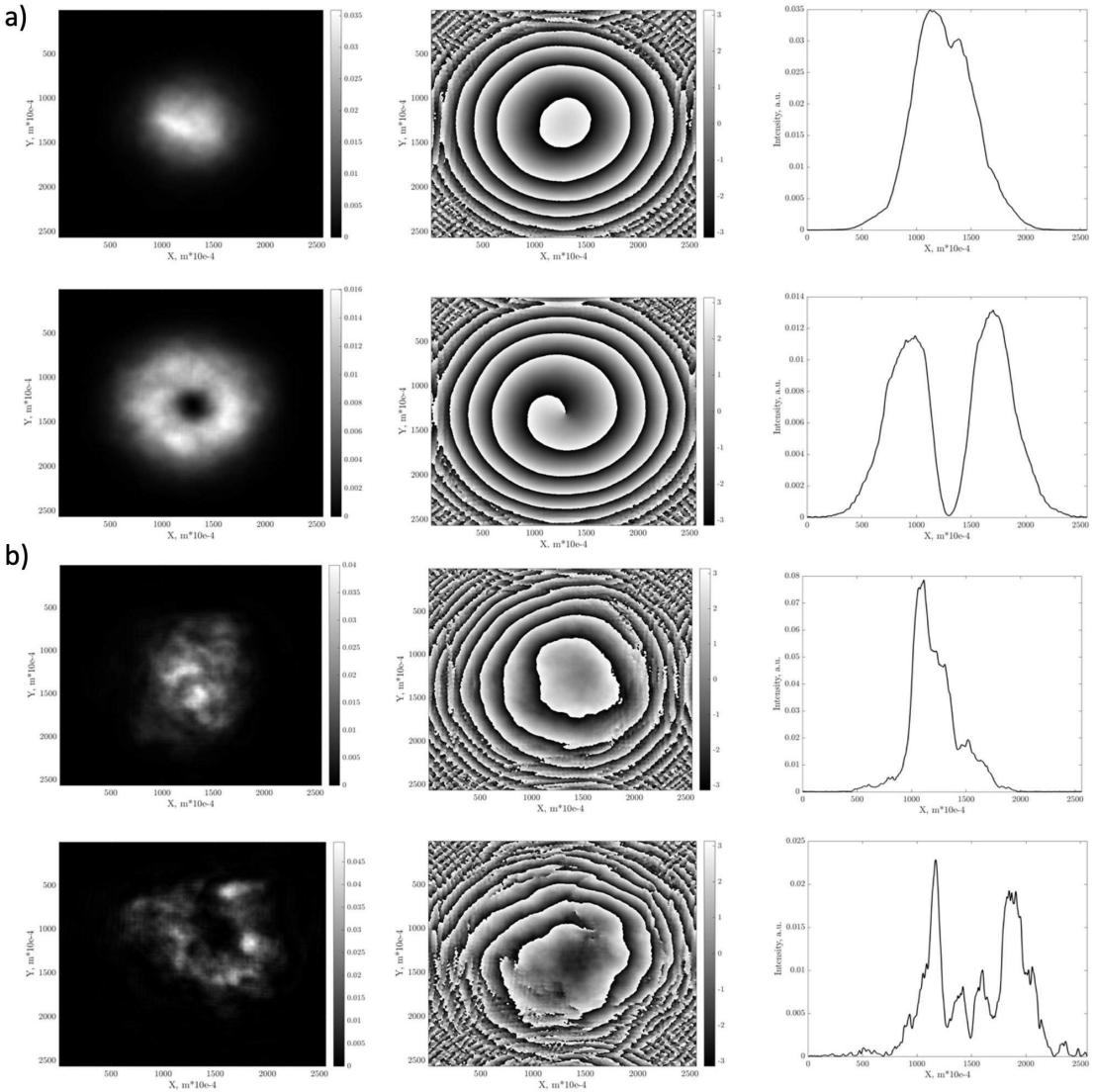

FIG. 4. Intensity distribution, phase distribution and intensity profile in the detector plane of Gaussian beam and vortex beam at the distance L = 1000 m from the source plane in case of a) r_C = 1 m; b) $r_C = 0.1$ m

The achieved values can serve as a measure of beam stability during propagation in a turbulent atmosphere. It is shown that the vortex beam experiences a smaller average deviation compared to the Gaussian beam under turbulence conditions, and the values of the standard deviation of the shift indicate that the area of the region within which the vortex beam will be located is less than for the Gaussian beam. The loss of optical radiation power that beams experience

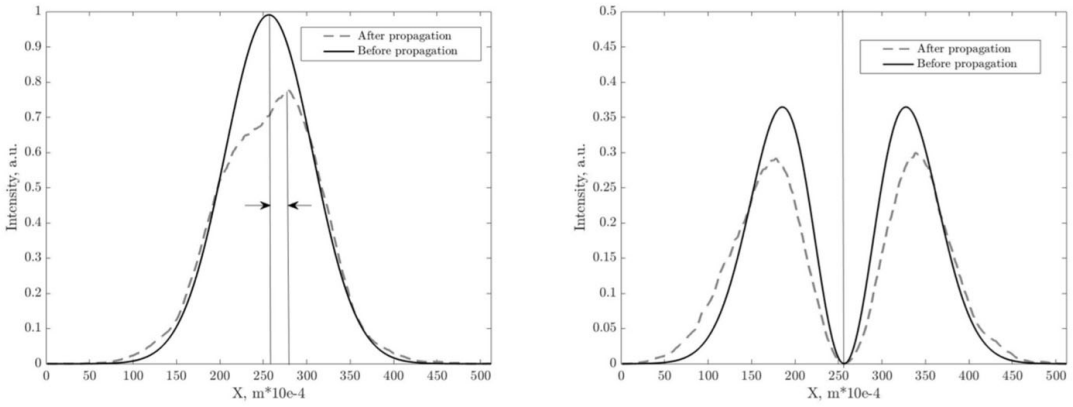

FIG. 5. Shift of beams' centers due to turbulence

TABLE 1. The results of the study of the shift of the centers of the Gaussian and the vortex beams during propagation through a turbulent atmosphere at distance L = 1000 m

	r_C, m	Average shift, mm	RMS shift deviation, mm
Gaussian Beam	1	8.5	±6.5
Vortex Beam	1	3.3	±1.2
Gaussian Beam	0.1	47.5	±25.6
Vortex Beam	0.1	19.2	±12.0

when propagating in a turbulent communication channel can be calculated from the knowledge of the beam intensity distributions in the source and detector planes. In this paper, the power is calculated using the Simpson's method. Optical loss in dB can be calculated using formula (19). The obtained value of losses contains the contribution caused by the influence of Mie scattering, this contribution can be calculated using formulas (11), (12). When calculating losses due to Mie scattering, the parameters for atmospheric visibility V = 20 km were used. A comparison of the radiation loss in the communication channel for Gaussian and vortex beams is shown in Fig. 6. The graphs show that the vortex beams experience lower losses in the communication channel for given values of the atmospheric coherence length. The average loss at the distance L = 1000 m with r_C = 0.1 m for the vortex beam is by 0.2 dB less than for the Gaussian beam.

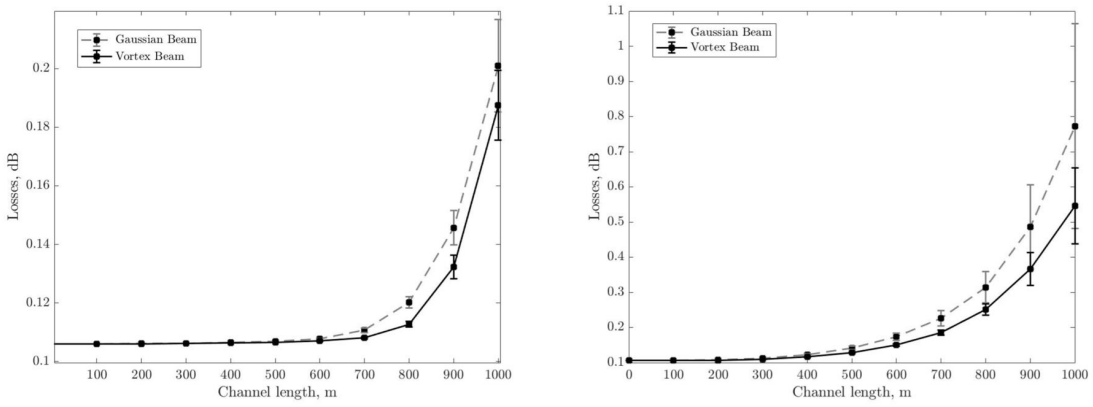

FIG. 6. Dependence of radiation losses in an atmospheric communication channel on its length for $r_C = 1$ m (Left) and $r_C = 0.1$ m (Right)

3.2. QKD parameters

Using the obtained values of losses in the communication channel, we can calculate the average number of photons arriving at Bob's detector (21), the probability of detecting a photon in the receiver unit (20), as well as the key generation

rate (15) - (18) and QBER (22). When calculating the characteristics of the QKD system, the following parameters were used [18]: T = 10 ns ,υ_S = 100 MHz, m = 0.319, μ_0 = 4, $\Delta\phi = 5^\circ$, $\eta_B = 10^{-0.64}$, $\vartheta = 10^{-3}$, γ_{dark} = 20 Hz, η_D = 0.2. The results of numerical calculation of the key generation rate and the quantum bit error rate for r_C = 1 m and r_C = 0.1 m are shown in Fig. 7, 8, respectively.

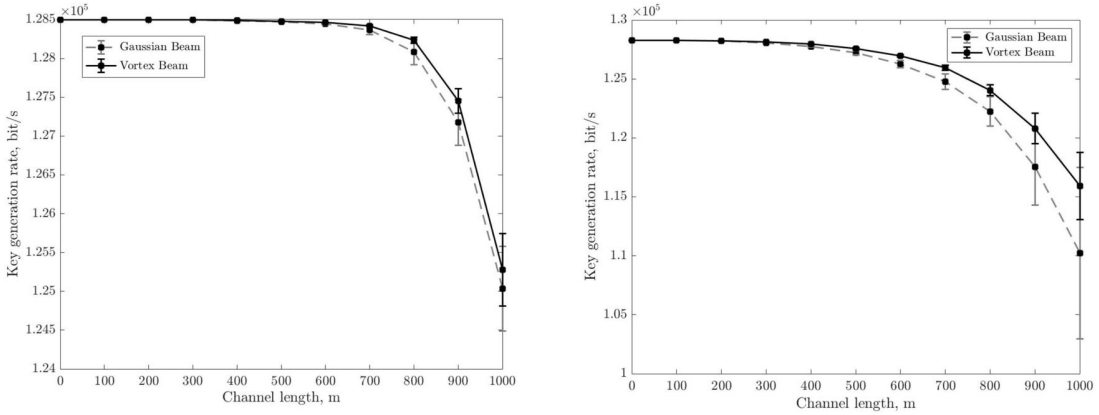

FIG. 7. Dependence of key generation rate in an atmospheric communication channel on its length for r_C = 1 m (Left), r_C = 0.1 m (Right)

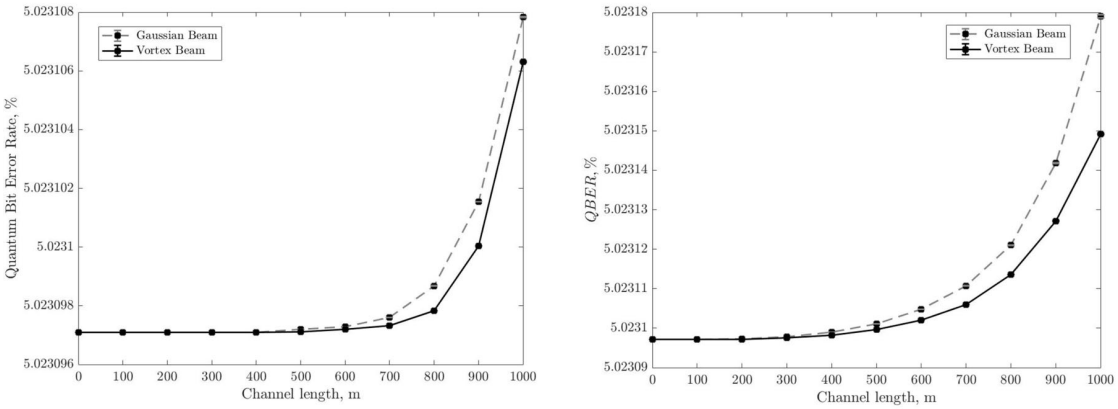

FIG. 8. Dependence of QBER in an atmospheric communication channel on its length for r_C = 1 m (Left), r_C = 0.1 m (Right)

These results are in good agreement with the beam wandering and the channel losses estimates. Since the key generation rate and QBER are related to the losses in the communication channel, it is natural that there is a slight advantage with respect to these parameters as well. For r_C = 1 m, the numerical curves for the key generation rate and QBER are almost indistinguishable: the difference of mean values for given beams is small and the standard deviation values are nearly equal, despite the fact that the vortex beam shows slightly better results. However, more significant advantage can be seen for r_C = 0.1 m. The average key generation rate for the vortex beam is about 5% higher than for the Gaussian beam at L = 1000 m and its standard deviation is noticeably less. Numerical results for QBER, however, shows less difference between the Gaussian and the vortex beams, but may be more significant at longer distances, which requires further studies.

4. Experiment

To study the possibility of phase modulation preservation during the transition from the Gaussian to the vortex beam and vice versa in the QKD system with phase coding, an experimental setup was implemented. The purposed scheme is a classic Mach-Zehnder interferometer, in one of the arms of which modulation and demodulation of the vortex beam were performed. It is important to clarify that the proposed scheme is not a full-fledged QKD system, but it only imitates the process of phase coding in the classical approximation, however, the results obtained in this work will also be valid for a full-fledged quantum communications system.

Currently, to generate vortex beams, the following methods are used: spiral phase plate [22], fork-grating [23] and spatial light modulators (SLM) [24]. In this work, the method of fork-grating was used as the most accessible and inexpensive one. Fork-grating is a diffraction grating in the middle of which a spatial dislocation is located. Mathematically it can be obtained as an interference pattern of a vortex beam and an inclined plane wave. In order to use such gratings in an experimental setup, the pictures with required fork-gratings obtained by mathematical modeling were printed in high resolution and then transferred to a 35 mm film using the reprography method. As a result of the interaction of a Gaussian beam with such fork-gratings, vortex beams are generated in side diffraction orders, the topological charge of which coincides with the order number. Demodulation of the vortex beam in this case is provided by using a second symmetrical fork-grating rotated by 180 degrees, which makes it possible to obtain a Gaussian beam in the same diffraction order as the vortex beam on the first fork-grating. The profiles of the obtained beams is illustrated in Fig. 9. The results obtained confirm the modulation and demodulation of the vortex beam; nevertheless, the resulting demodulated Gaussian beam has residual vortex components, which can be explained by the non-ideal alignment and broadening of the singularity of the vortex beam during propagation, which leads to its incomplete compensation on the second fork-grating.

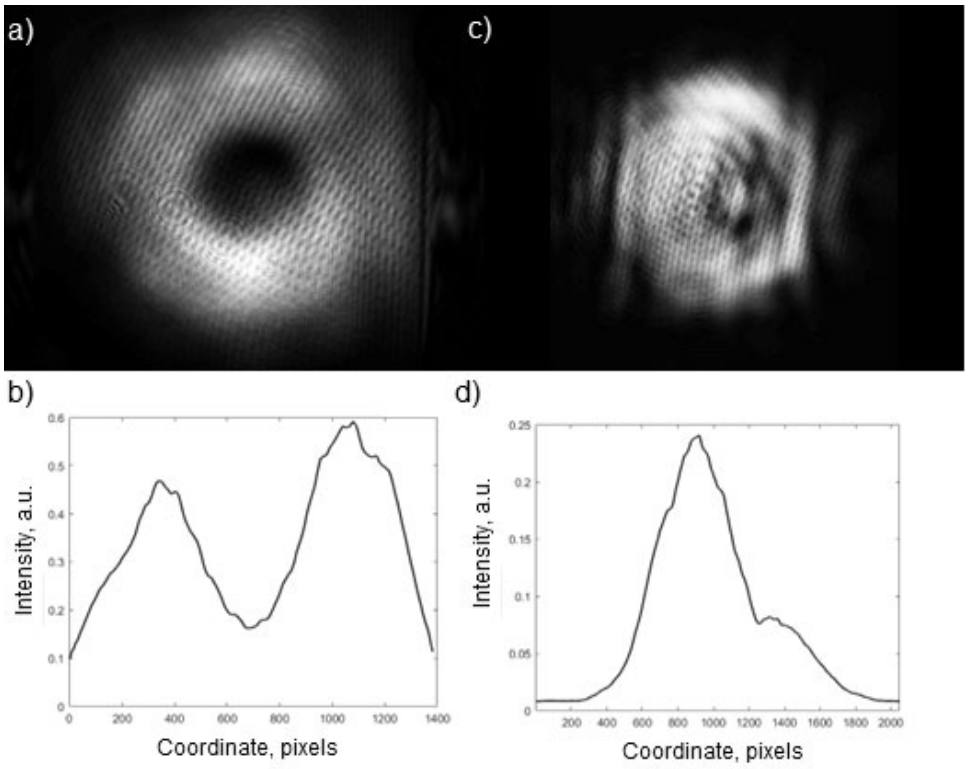

FIG. 9. (a) Profile of a vortex beam modulated on the fork-grating; (b) cross section of the modulated vortex beam; (c) profile of the Gaussian beam demodulated on the fork-grating; (d) cross section of the demodulated Gaussian beam

In the purposed scheme shown in Fig. 10, the He-Ne laser module (LM) with the wavelength of 633 nm were used. This wavelength has already been used in several works on free-space QKD [4, 25, 26] due to the simplification of the alignment process. The optical radiation was directed to the beamsplitter (BS1), after which the first laser beam entered the phase modulator (PM), where it acquired a delay of 0 or π radians, and the second laser beam by the mirror (M1) was directed to beamsplitter (BS2) on the exit of interferometer. Next, the first beam went through the described above process of modulation and demodulation of the optical vortex on two fork-gratings (FG1 and FG2). The distance between these gratings was 42 cm and the first-order diffraction angle was 1.8 degrees. As a result, the obtained demodulated Gaussian beam by the mirror (M2) was directed to beamsplitter (BS2) on the exit of interferometer, where it interfered with the second beam. The interference pattern was recorded using camera (C) placed at one of the outputs of the beamsplitter (BS2). The intensity profiles of the obtained interference patterns at different values of the phase delay, which were additionally averaged over 60 frames to compensate the phase fluctuations in the interferometer, are shown in Fig. 11. From the obtained results, it can be seen that the value of the introduced phase delay is equivalently reflected in the recorded interference pattern. As a result, it can be concluded that the process of modulation and demodulation of the optical vortex does not affect the process of phase encoding and can be used in the QKD systems with phase encoding.

It is necessary to make important remarks on the obtained experimental results. Firstly, in this work there is a certain discrepancy between the theoretical model and the experimental scheme. It lies in the fact that Laguerre-Gaussian modes were used to describe the vortex field in the mathematical model, while in the experimental scheme the vortex beams

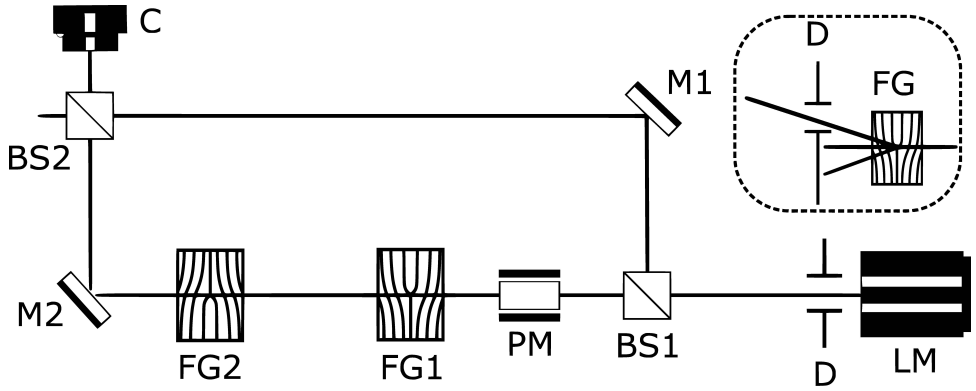

FIG. 10. Mach-Zehnder interferometer on demodulated vortex beam; (in the dotted frame) selection of the first order diffraction on fork-grating

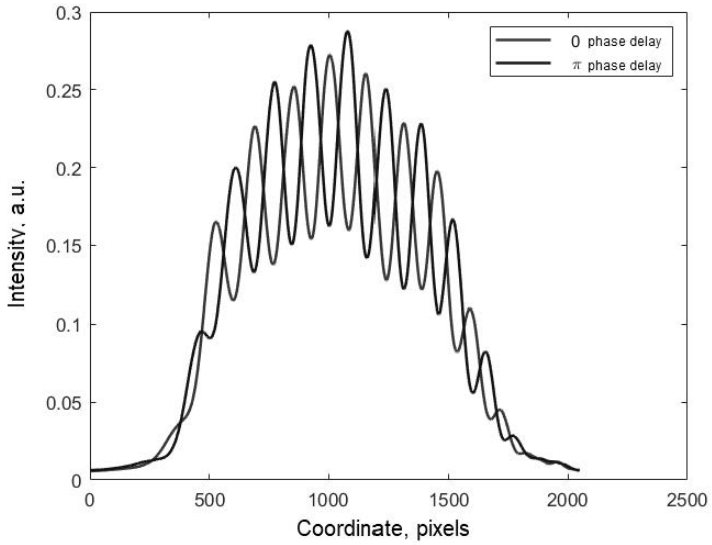

FIG. 11. Cross section of the interference pattern at a phase delay of 0 and π radians, averaged over 60 frames

were modulated on fork-gratings, which, in fact, is described by the Kummer beams [27]. However, this discrepancy is not crucial and does not affect the obtained results, since the theoretical model considers the parameters of the SCW QKD system, and the experimental scheme considers the possibility of the phase encoding preservation, which does not correlate with each other. Secondly, by using a fork-grating in the SCW QKD, the diffraction angles of the carrier and subcarrier waves will differ by 10^{-4} degrees. This will result in their spatial displacement by 1.7 mm at a distance of 1 km, which is comparable to the atmospheric turbulences deviation in the theoretical model. This problem, like the first one, can be solved by using SLM as a method of generating vortex beams, which will allow one to compensate diffraction angle deviation of the carrier and subcarrier waves, as well as to implement Laguerre-Gaussian modes in the experimental scheme to correlate the theoretical model and experiment.

5. Conclusion

Thus, in this work the possibility of using vortex beams in the free-space QKD system and its comparison with the Gaussian beam were studied as well as the phase encoding preservation possibility. The authors of this paper would like to once again emphasize the theoretical nature of the research and the presented results. For further practical use, additional researches are needed.

A mathematical model of radiation propagation in the form of Gaussian and vortex beams in a turbulent atmosphere is demonstrated and a comparative estimate of the amount of beam wandering is carried out. The radiation power losses were also calculated, including the geometric losses arising due to the deviation of beams from given propagation axis, as well as the losses introduced by the Mie scattering. In addition, based on the calculated values of radiation power losses in the atmospheric communication channel, the parameters of SCW QKD system were estimated using the considered beams. Taking into consideration the obtained values of the average shift and standard deviation of the shift for both beams, we

can conclude that the vortex beam is, indeed, less prone to turbulence wandering in the communication channel. Obtained results also show that the vortex beam is a more favorable information carrier due to lower losses in the communication channel in comparison with the Gaussian beam. Finally, SCW QKD system parameters estimate points that using of vortex beams gives one better results compared to Gaussian beams as well.

In turn, the experimental results confirm the possibility of the phase encoding preservation in the process of modulation and demodulation of the vortex beam. It was shown that the fork-grating method has a number of limitations for its application in the SCW QKD system, in particular, the discrepancy between the theoretical model and experiment, diffraction angle deviation of carrier and subcarrier waves, and large additional losses on the receiver side due to the fork-grating method low efficiency. As an alternative, the use of the SLM method has been proposed.

Despite the approximations that were mentioned in Section 2, it can be argued that the use of vortex modulation in SCW QKD system is reasonable, since the comparison of the behavior of the studied beams during propagation in a turbulent atmosphere was carried out under the same conditions. However, the model presented in this paper needs further development. In the future, it is planned to move to a dynamic turbulence model that takes into account the temporal variability of atmospheric parameters, as well as modeling the direct process of vortex modulation. Also, the usage of the vortex beam in practical SCW QKD system is planned.

References

[1] Wootters W.K., Zurek W.H., The no-cloning theorem, *Physics Today*, 2009, 62(2), P. 76–77.

[2] Bennett C.H., Brassard G., Quantum cryptography: public key distribution and coin tossing. *Proceedings of the International Conference on Computers, Systems and Signal Processing*, 1984, **1**, P. 175–179.

[3] Pirandola S., Andersen U.L., Banchi L., Berta M., Bunandar D., Colbeck R., Englund D., Gehring T., Lupo C., Ottaviani C., Pereira J.L., Razavi M., Shamsul Shaari J., Tomamichel M., Usenko V.C., Vallone G., Villoresi P., and Wallden P., Advances in quantum cryptography. *Advances in Optics and Photonics*, 2020, **12**(4), P. 1012.

[4] Bourgoin J.-P.,. Higgins B.L, Gigov N., Holloway C., Pugh C.J., Kaiser S., Cranmer M., and Jennewein T., Free-space quantum key distribution to a moving receiver. *Optics Express*, 2015, **23**(26), P. 33437.

[5] Liao S.K., Cai W.Q., Liu W.Y., Zhang L., Li Y., Ren J.G., Yin J., Shen Q., Cao Y., Li Z.P., Li F.Z., Chen X.W., Sun L.H., Jia J.J., Wu J.C., Jiang X.J., Wang J.F., Huang Y.M., Wang Q., Zhou Y.L., Deng L., Xi T., Ma L., Hu T., Zhang Q., Chen Y.A., Liu N.L., Wang X.B., Zhu Z.C., Lu C.Y., Shu R., Peng C.Z., Wang J.Y., and Pan J.W., Satellite-to-ground quantum key distribution. *Nature*, 2017, **549**(7670), P. 43–47.

[6] Al-Mohammed H.A. and Yaacoub E., On the Use of Quantum Communications for Securing IoT Devices in the 6G Era. *2021 IEEE International Conference on Communications Workshops, ICC Workshops 2021 - Proceedings*, 2021.

[7] Zhou Y., Zhao J., Braverman B., Pang K., Zhang R., Willner A.E., Shi Z., and Boyd R.W., Multiprobe Time Reversal for High-Fidelity Vortex-Mode-Division Multiplexing over a Turbulent Free-Space Link. *Physical Review Applied*, 2021, **15**(3), P. 1.

[8] Aksenov V.P. and Pogutsa C.E., Fluctuations of the orbital angular momentum of a laser beam, carrying an optical vortex, in the turbulent atmosphere. *Quantum Electronics*, 2008, **38**(4), P. 343.

[9] Shen Y., Wang X., Xie Z., Min C., Fu X., Liu Q., Gong M., and Yuan X., Optical vortices 30 years on: OAM manipulation from topological charge to multiple singularities. *Light: Science and Applications*, 2019, **8**(1).

[10] Sit A., Fickler R., Alsaiari F., Bouchard F., Larocque H., Gregg P., Yan L., Boyd R.W., Ramachandran S., and Karimi E., Quantum cryptography with structured photons through a vortex fiber. *Optics Letters*, 2018, **43**(17), P. 4108.

[11] Qu Z. and Djordjevic I.B., High-speed free-space optical continuous-variable quantum key distribution enabled by three-dimensional multiplexing. *Optics Express*, 2017, **25**(7), P. 7919.

[12] Soskin M. and Vasnetsov M., Singular optics. *Progress in optics*, 2001, **42**(4), P. 219–276.

[13] Liu Y., Zhang K., Chen Z., and Pu J., Scintillation index of double vortex beams in turbulent atmosphere. *Optik*, 2019, **181**(November), P. 571–574.

[14] Charnotskii M., Four methods for generation of turbulent phase screens: comparison, 2019, no. November.

[15] Kynev S.M., Chistyakov V.V., Smirnov S.V., Volkova K.P., Egorov V.I., and Gleim A.V., Free-space subcarrier wave quantum communication. *Journal of Physics: Conference Series*, 2017, **917**(5).

[16] Kim I.I., McArthur B., and Korevaar E.J., Comparison of laser beam propagation at 785 nm and 1550 nm in fog and haze for optical wireless communications. *Optical Wireless Communications III*, P. 26–37.

[17] Gleim A., Egorov V., Nazarov Y.V., Smirnov S., Chistyakov V., Banni O.k, Anisimov A., Kynev S., Ivanova A., Collins R., *et al.*, Secure polarization-independent subcarrier quantum key distribution in optical fiber channel using bb84 protocol with a strong reference. *Optics express*, 2016, **24**(3), P. 2619–2633.

[18] Miroshnichenko G.P., Kozubov A.V., Gaidash A.A., Gleim A.V., and Horoshko D.B., Security of subcarrier wave quantum key distribution against the collective beam-splitting attack. *Optics Express*, 2018, **26**, P. 11292.

[19] Vasylyev D.Y., Semenov A., and Vogel W., Toward global quantum communication: beam wandering preserves nonclassicality. *Physical review letters*, 2012, **108**(22), P. 220501.

[20] Faleeva M. and Popov I., Entanglement transmission through turbulent atmosphere for modes of gaussian beam. *Quantum Information Processing*, 2020, **19**(2), P. 1–9.

[21] Cheng W., Haus J.W., and Zhan Q., Propagation of vector vortex beams through a turbulent atmosphere. *Optics express*, 2009, **17**(20), P. 17829–17836.

[22] Hui X., Zheng S., Hu Y., Xu C., Jin X., Chi H., and Zhang X., Ultralow reflectivity spiral phase plate for generation of millimeter-wave OAM beam. *IEEE Antennas and Wireless Propagation Letters*, 2015, **14**, P. 966–969.

[23] Karahroudi M.K., Parmoon B., Qasemi M., Mobashery A., and Saghafifar H., Generation of perfect optical vortices using a Bessel–Gaussian beam diffracted by curved fork grating. *Applied Optics*, 2017, **56**(21), P. 5817.

[24] Pradhan P., Sharma M., and Ung B., Generation of perfect cylindrical vector beams with complete control over the ring width and ring diameter. *IEEE Photonics Journal*, 2018, **10**(1), P. 1–10.

[25] Conrad A., Isaac S., Cochran R., Sanchez D., Wilens B., Gutha A., Rezaei T. , Gauthier D.J. and Kwiat P., Drone-based quantum key distribution: QKD. *Proc. SPIE, Free-Space Laser Communications XXXIII*, 2021, 11678, 116780X.

[26] Hill A.D., Chapman J., Herndon K., Chopp C., Gauthier D.J., and Kwiat P., Drone-based quantum key distribution. *Urbana*, 2017, **51**, P 61801–63003.

[27] Bekshaev A.Y., Karamoch A., Vasnetsov M., Pas' ko V., and Soskin M., Structure of optical vortices produced by holographic gratings with "fork" geometry: Kummer beams. *arXiv preprint arXiv:0906.2619*, 2009.

Submitted 1 June 2022; revised 29 June 2022; accepted 30 June 2022

Information about the authors:

Iurii A. Adam – ITMO University, Kronverkskiy, 49, St. Petersburg, 197101, Russia; adam_yura@mail.ru

Daniil A. Yashin – ITMO University, Kronverkskiy, 49, St. Petersburg, 197101, Russia; dayashin@itmo.ru

Daria A. Kargina – ITMO University, Kronverkskiy, 49, St. Petersburg, 197101, Russia; dakargina17@gmail.com

Boris A. Nasedkin – ITMO University, Kronverkskiy, 49, St. Petersburg, 197101, Russia; b.nasedkin@bk.ru

Conflict of interest: the authors declare no conflict of interest.

NANOSYSTEMS:
PHYSICS, CHEMISTRY, MATHEMATICS

Kameneva S.V., et al. *Nanosystems: Phys. Chem. Math.*, 2022, **13** (4), 404–413.
http://nanojournal.ifmo.ru
DOI 10.17586/2220-8054-2022-13-4-404-413

Original article

Photochromic aerogels based on cellulose and chitosan modified with WO_3 nanoparticles

Svetlana V. Kameneva[1,a], Matvei A. Popkov[1,2,b], Ilya V. Tronev[1,3,c], Sergey Yu. Kottsov[1,2,d], Madina M. Sozarukova[1,e], Vladimir K. Ivanov[1,f]

[1]Kurnakov Institute of General and Inorganic Chemistry of the Russian Academy of Sciences, Moscow, Russia
[2]Lomonosov Moscow State University, Moscow, Russia
[3]HSE University, Moscow, Russia

[a]kamenevasvetlanav@gmail.com, [b]popkovma2001@mail.ru, [c]ivtronev@edu.hse.ru,
[d]sergey12-17@yandex.ru, [e]s_madinam@bk.ru, [f]van@igic.ras.ru

Corresponding author: S. V. Kameneva, kamenevasvetlanav@gmail.com

PACS 68.65.k, 81.20.n

ABSTRACT In this work, we report the first synthesis of photochromic aerogels and films based on TEMPO-oxidized cellulose and chitosan modified with tungsten trioxide nanoparticles. The blue coloring of aerogels based on WO_3-modified biopolymers under UV light occurs due to the reduction of W^{+6} to W^{+5}. The coloration of films of the same composition occurs due to the reduction of W^{+6} to W^{+5} and W^{+4}. The photochromic properties of aerogels and films are reversible; oxidation by atmospheric oxygen leads to bleaching of materials. At that, films become colorless within a few days while aerogels with a high specific surface area (200 m^2/g) become colorless within several minutes. The antioxidant properties of the WO_3 sol and the WO_3/TEMPO-oxidized cellulose/chitosan composite were studied by luminol-activated chemiluminescence method. The antioxidant capacity of WO_3/TEMPO-oxidized cellulose/chitosan gel is 1.5 times higher than that of the commercially available antioxidant mexidol.

KEYWORDS Aerogel, hybrid materials, nanocomposite, biopolymers, cellulose, chitosan, tungsten oxide, photochromic material, antioxidant.

ACKNOWLEDGEMENTS S.V. Kameneva thanks the Council for Grants of the President of the Russian Federation for supporting the study (SP-4398.2021.4).

FOR CITATION Kameneva S.V., Popkov M.A., Tronev I.V., Kottsov S.Yu., Sozarukova M.M., Ivanov V.K. Photochromic aerogels based on cellulose and chitosan modified with WO_3 nanoparticles. *Nanosystems: Phys. Chem. Math.*, 2022, **13** (4), 404–413.

1. Introduction

Cellulose and chitosan are biopolymers that easily undergo chemical modifications, including the introduction of functional groups and cross-linking with other polymers [1–4]. These biopolymers form aqueous dispersions, flexible films, gels and aerogels, effectively adsorb metal cations and inorganic nanoparticles due to the formation of hydrogen and coordination bonds [5, 6]. These qualities make cellulose and chitosan convenient matrices for creating hybrid materials modified with inorganic nanoparticles. Aerogels based on chemically modified cellulose have great potential for application in medicine as moisture-absorbing dressings, biocompatible scaffolds for tissue engineering, in drug delivery systems and can also act as carriers of catalysts, adsorbents, etc. [1, 7–12]. Recently, a work devoted to the creation of a photochromic aerogel based on cellulose modified with an avobenzone derivative was published [13].

Nanosized tungsten trioxide is a semiconductor material with unique photochromic, electrochromic and photocatalytic properties. WO_3 effectively absorbs UV and visible radiation, while the material turns blue due to the reduction of W^{+6} to W^{+5} and W^{+4}. Oxidation of W^{+4} and W^{+5} and bleaching of the material can occur by the atmospheric oxygen. The coordination of some organic ligands containing hydroxyl or amino groups to the surface of WO_3 nanoparticles can increase the rate of the photochromic reaction, increase the color intensity and allow one to repeat the coloration–discoloration cycle [14–16]. Coloration of WO_3 can also occur in a reducing atmosphere which its application as a gas sensor is based on [17–19].

Practically significant property of tungsten trioxide is its antibacterial activity. WO_3/hydroxyethylcellulose membranes have been shown to promote wound healing, possess an anti-inflammatory effect and also demonstrate antibacterial activity against both Gram-positive and Gram-negative bacteria [20]. Under the action of UV radiation, the antibacterial properties of tungsten trioxide stabilized with polyvinylpyrrolidone are significantly enhanced due to its photocatalytic effect, which leads to the destruction of the bacterial cell wall n [21]. WO_3 nanoparticles are toxic in some cases and for

their biomedical applications polymer coatings are used. For example, the toxicity of WO_3 to human cells (human dermal fibroblast cell line) was successfully reduced by its immobilization in a hydroxyethyl cellulose matrix n [20]. Prospects for the biomedical application of nanomaterials based on tungsten trioxide actualize the problem of analyzing their redox activity in relation to various species involved in free radical homeostasis n [22–24], including hydrogen peroxide, being one of the important reactive oxygen species (ROS) n [25, 26].

Up to date the investigations of photochromic properties of hybrid materials based on cellulose modified with WO_3 nanoparticles have been reported only in a few works [14, 15, 27]. In this study, we propose for the first time a synthetic procedure which allows one to obtain aerogels based on TEMPO-oxidized cellulose and chitosan modified with WO_3 nanoparticles. The morphological, hydrophilic, photochromic and antioxidant properties of such aerogels have been studied. The resulting aerogels appear to be promising materials for the development of absorbent wound dressings with antibacterial and antioxidant effects, as well as for the design of UV radiation visualizers and gas sensors.

2. Materials and methods

2.1. Reagents

The following reagents were used in the study: sodium tungstate $Na_2WO_4{\cdot}2H_2O$ (Rushim), TEMPO 2,2,6,6-tetramethylpiperidine-1-oxyl (99%, NIOC SB RAS), sodium hypochlorite NaClO 19% (PCG), sodium bromide NaBr (Lavernalab), filtering paper (blue ribbon), hydrochloric acid HCl 36% (Chimmed), sodium hydroxide NaOH (Chimmed), cation exchange resin, hydrogen peroxide 30% (Chimmed), luminol 97% (Aldrich), potassium dihydrogen phosphate (for cell cultures, Aldrich), polyvinylpyrrolidone (10000, Aldrich), mexidol (6-methyl-2-ethyl-3-hydroxypyridine succinate, Pharmasoft).

2.2. Synthesis of WO_3 nanoparticles

200 ml of cation exchange resin in a protonated form was placed in a separating funnel. A 0.005 M solution of Na_2WO_4 was slowly added to the funnel, maintaining the rate of outflow of the solution from the funnel within 1–2 drops per second. At the outlet of the funnel, a solution of unstable tungstic acid ($WO_2{\cdot}H_2O$) with a pH of about 3 was collected. 1.33 g of PVP was added to 50 ml of the resulting solution and heated to 90°C for two hours with stirring. The WO_3 sol concentration was determined gravimetrically.

2.3. TEMPO-oxidation of cellulose

4.00 g of finely cut filter paper (blue ribbon) was placed in 250 ml of 5 M HCl solution and stirred at 80°C for 40 minutes. The resulting cellulose dispersion was then poured into 1.5 L of cold distilled water to stop the hydrolysis. The resulting nanocrystalline cellulose was washed with distilled water until pH 6. The resulting mixture was kept for 40 minutes in an ultrasonic bath at a temperature not exceeding 18°C to obtain a homogeneous dispersion. The concentration of nanocrystalline cellulose in the dispersion was about 3%.

Weighed portions of TEMPO (0.064 g) and NaBr (0.400 g) were placed in a 1 L beaker, 200 ml of distilled water was added and the mixture was stirred until complete dissolution. The nanocrystalline cellulose dispersion was then added and stirred for additional 10 minutes, followed by addition of 25 ml of 11.9% NaClO with constant stirring. Oxidation reaction was carried out with regular dropwise addition of 0.3 M NaOH from a burette, maintaining pH within 10.5–11 range. After the pH remained constant for 30 minutes, 0.5 M HCl was added to pH 6.5–7 and the mixture was stirred for 15 minutes. The resulting pulp was washed with distilled water and centrifuged. Then ultrasonic dispersion was carried out for 40 min at 15–20°C. The concentration of TEMPO-oxidized cellulose was determined gravimetrically.

The yield of the oxidation reaction was found by conductometric titration. The concentration of carboxyl groups was 600–800 mmol per g of cellulose, the degree of carboxylation was about 10%.

2.4. Synthesis of hybrid aerogels and films

A solution of chitosan was added to the TEMPO-oxidized cellulose dispersion, while stirring in an ultrasonic bath. Then a solution of $WO_3{\cdot}H_2O$ was added dropwise until a homogeneous mixture was formed. To obtain the films, the resulting dispersion was placed in Petri dishes and dried at room temperature. The concentrations were chosen so that the molar ratio of the formula units of tungsten oxide (WO_3), chitosan ($C_6H_{11}O_5N$) and cellulose ($C_6H_{12}O_6$) in the composite (W–CC) was 1/2/8.

To obtain aerogels, the dispersion was left for 7 days for the formation of hydrogels and aging. The obtained hydrogels were placed in isopropanol to replace the solvent, isopropanol was changed daily for 5 days.

Similarly, composites of chitosan and TEMPO-oxidized cellulose without tungsten oxide (CC) were obtained.

The sample was dried in an installation consisting of a Supercritical 24 high-pressure pump (SSI, USA), a 50-mL steel reactor and a back pressure regulator BPR (Go Regulator, Waters, USA). The sample was washed for 3 h with supercritical CO_2 at 50°C and 148 atm. Then, within 30–40 minutes the pressure in the heated autoclave was gradually reduced to atmospheric pressure. As a result, monolithic aerogels were obtained.

2.5. Characterization methods

Scanning electron microscopy (SEM) images were obtained on a Carl Zeiss NVision 40 electron microscope at an accelerating voltage of 3 kV; the samples were preliminarily deposited with a carbon coating. Elemental analysis and element distribution maps were obtained using an X-Max Oxford Instruments detector (UK) at an accelerating voltage of 20 kV with a cobalt standard.

X-ray diffraction data (XRD) was measured on a Bruker D8 Advance diffractometer using CuKa radiation in the 2θ range from 5° to 80°.

Vibrational spectra were recorded on an INFRALUM FT-08 FTIR spectrometer in the range from 400 to 4000 cm^{-1} with a 4 cm^{-1} resolution.

UV visible reflectance spectra and coloration kinetics of composites were obtained on an Ocean Optics QE65000 spectrometer in the range of 250–1000 nm with a resolution of 1 nm using an HPX-2000 xenon lamp.

The hydrodynamic radius and ζ-potential were measured using a Photocor Compact Z analyzer with a thermally stabilized 638 nm semiconductor laser.

The specific surface area of films and aerogels (S_{BET}) was measured by low-temperature nitrogen adsorption on an ATX-06 analyzer (Katakon, Russia). Before the analysis, samples were degassed for 2 hours at 80°C in vacuum. The specific surface area for the samples was calculated by the Brunauer-Emmett-Teller (BET) method in the range of nitrogen partial pressures of 0.05–0.25. The calculation of the pore size distribution was calculated from the nitrogen desorption isotherm by the Barrett-Joyner-Halend (BJM) method in the range of nitrogen partial pressures of 0.05–0.97.

The antioxidant properties of the samples were analyzed by luminol-activated chemiluminescence using a 12-channel "Lum-1200" chemiluminometer (DISoft). The ROS generating system contained hydrogen peroxide and luminol was used as a chemiluminescent probe. The technique of chemiluminescence analysis is described in detail in [28]. The required amounts of luminol (50 μM) and H_2O_2 (980 μM) were added to cuvettes with phosphate buffer solution (100 mM, pH 7.4), the total volume of the system was 1.000 ml. The signal was recorded at 37°C. After reaching the maximum intensity of chemiluminescence, aliquots of the studied samples were added to the cuvettes. Simultaneously the luminescence was recorded for the control sample and samples with different concentrations of the studied compositions (W–CC with WO_3 concentrations from 50 to 1000 μM; WO_3 with concentrations from 50 to 300 μM; the commercially available antioxidant mexidol with concentrations from 30 to 110 μM). The integral intensity was chosen as an analytical signal, i.e., the area under the chemiluminescent curve for a selected time interval, which is proportional to concentration of free radicals.

3. Results and discussion

3.1. Formation of the gels

Biopolymer-based composite gels were obtained by gradually adding a solution of chitosan to the aqueous dispersion of cellulose. Since the viscosity of chitosan solution is sufficiently high, the chitosan drops slowly dissolved in the volume of the cellulose dispersion. An immediate gel formation was observed at the boundary of chitosan droplets with dispersion. To obtain a homogeneous material, a mixture of chitosan and cellulose was homogenized in an ultrasonic bath for 10 minutes under vigorous stirring. Then, a sol of WO_3 nanoparticles was added to the gel and redispersed in an ultrasonic bath.

Immediately after homogenization the gels did not retain their shape and deformed under the action of gravity. For further gelation and aging, they were transferred into plastic containers and stored in the dark for 5–7 days at room temperature.

The formation of biopolymer gels at the first stage occurs due to ionic interactions between cellulose and chitosan. TEMPO-oxidized cellulose is a polyanion due to partial dissociation of carboxyl groups; the ζ-potential of nanocrystalline cellulose particles obtained in this work is -30 mV. The amino groups of chitosan are partially protonated in the presence of hydrochloric acid, which leads to the formation of a polycationic biopolymer. It is noteworthy that WO_3 nanoparticles with negative ζ-potential of about -20 mV are reliably immobilized on polycationic chitosan molecules.

Apparently, the interaction of cationic groups of cellulose and anionic groups of chitosan is not strong enough to produce a gel that retains its shape. During gel aging, new hydrogen bonds between O–H groups of biopolymers are gradually formed which leads to the formation of a stronger network. As a result, after several days of aging the gel ceases to deform under the action of gravity when the container is tilted.

Drying freshly prepared WO_3–CC and CC gels at room temperature and atmospheric pressure results in the formation of transparent flexible films.

After aging, the WO_3–CC and CC gels were subjected to a solvent change to isopropanol and then dried in supercritical CO_2 at a pressure of 150 atm and a temperature of 50°C. As a result, monolithic opaque aerogels were obtained (Fig. 1). At the same time, no shrinkage of the materials occurred during the solvent replacement and drying.

3.2. Characterization of hybrid materials

The CC and W–CC films are composed of rod-shaped cellulose nanoparticles tightly adjacent to each other (Fig. 1A). The porous structure of CC and WO_3–CC aerogels is formed by a disordered network of cellulose nanoparticles (Fig. 1B). According to previously published data [27], the size of WO_3 nanoparticles obtained by ion exchange from sodium tungstate is about 2 nm. Prepared WO_3 nanoparticles cannot be studied by SEM. However, the EDX analysis confirmed the uniform distribution of tungsten in both the W–CC film and the W–CC aerogel (Fig. 1C,D). The specific surface area of CC and W–CC aerogels is about 200 m^2/g. The W–CC hybrid aerogel contains both mesopores with a diameter of 5 and 10–30 nm and macropores (Fig. 2). The geometric density of aerogels CC and W–CC is about 0.04 g/cm^3.

During the development of materials for biomedical applications, it is important to study the ability of the material to absorb water. In this work, to study the absorption capacity, samples of materials of known weight were immersed in distilled water for 30 minutes, after which the weight of the samples with absorbed water was measured. Films obtained by drying a chitosan solution at room temperature completely dissolve in water within a few minutes. In turn, TEMPO-oxidized cellulose films remain intact and practically do not swell, absorbing about 2 g of water per 1 g of film. Composite films of TEMPO-oxidized cellulose and chitosan (CC) and W–CC hybrid films swell in water, absorbing about 8 g of water per 1 g of material. In this case, the films increase in volume but retain their integrity. Swelling occurs due to hydration of chitosan molecules while integrity is maintained due to electrostatic binding of polycationic chitosan molecules with polyanionic cellulose molecules. Aerogels CC and W–CC absorb about 20 g of water per 1 g of material. The volume of aerogels does not change after absorbing water because the water molecules fill the existing pores in the material.

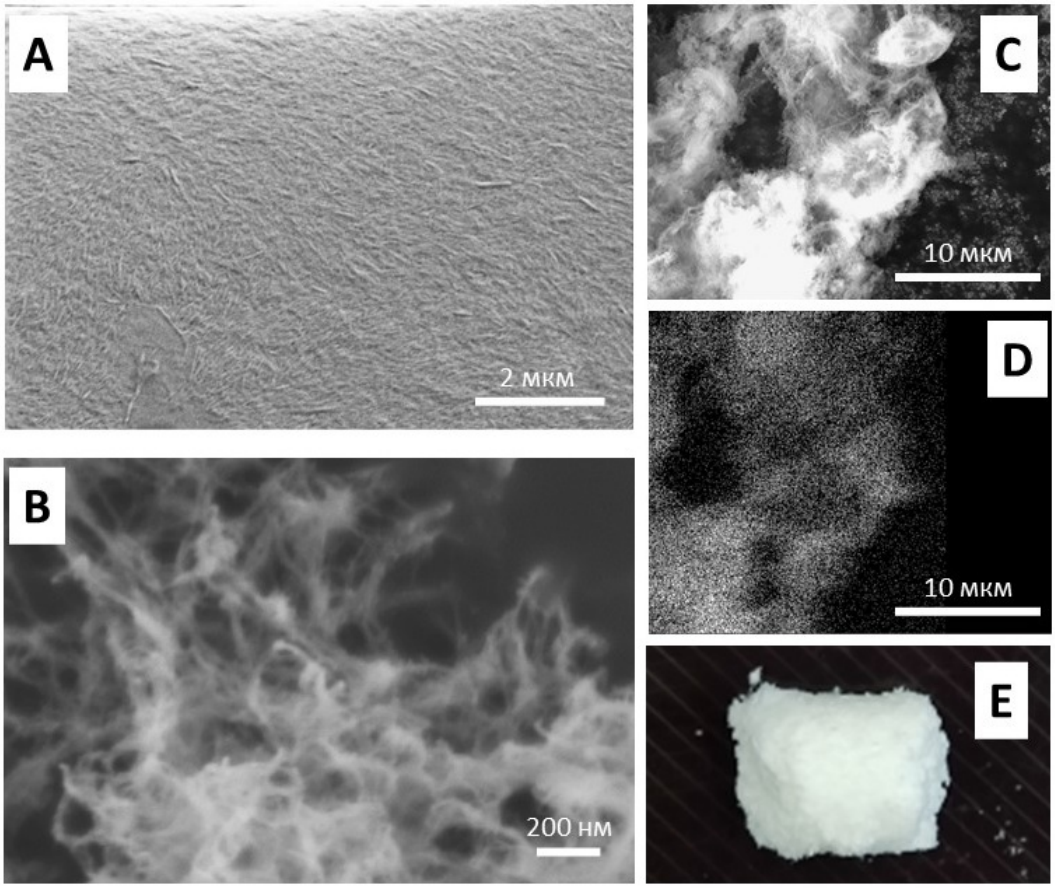

FIG. 1. SEM images of W–CC film (A) and W–CC aerogel (B) at an accelerating voltage of 3 kV; micrograph of W–CC aerogel (C) and distribution of W (D) according to EDX data at an accelerating voltage of 20 kV; the image of W–CC aerogel (E)

The IR spectra of the CC and W–CC composites contain absorption bands which belong to cellulose and chitosan molecules (Fig. 3A). The absorption bands of O–H stretching vibrations of cellulose and chitosan overlap with the absorption band of N–H stretching vibrations of chitosan, forming a wide band in the region of 3100–3500 cm^{-1}. Bands corresponding to stretching and bending vibrations of C–H are observed in the regions of 2900 cm^{-1} and 1200–1500 cm^{-1}, respectively. The absorption bands in the region of 900–1200 cm^{-1} refer to skeletal vibrations of biopolymers. The absorption bands in the region of 1550–1700 cm^{-1} refer to the bending vibrations of O-H in the molecules of both biopolymers and the NH_2 group of chitosan. The shoulder at 1730 cm^{-1} refers to the vibrations of the carboxyl group of

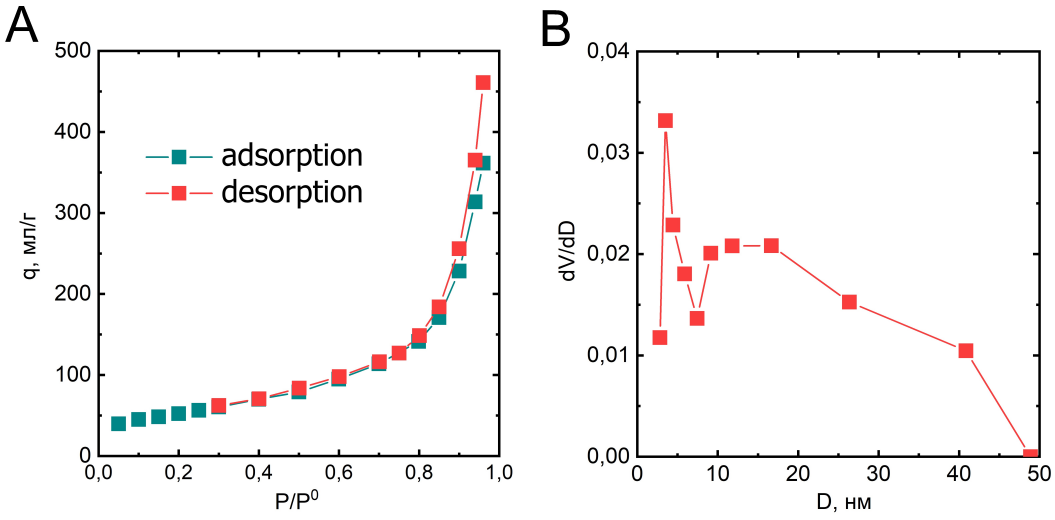

FIG. 2. Nitrogen adsorption and desorption isotherms (A) for W–CC aerogel and pore size distribution (B)

TEMPO-oxidized cellulose. In addition to the absorption bands of cellulose and chitosan, the W–CC spectrum contains absorption bands of W=O and O–W–O at 963 and 805 cm^{-1}, respectively (Fig. 3B).

Particles of TEMPO-oxidized cellulose contain crystalline regions with the Iβ structural type, which follows from the appearance of peaks at angles of 16° (110) and 23° (200) in the XRD patterns of the composites (Fig. 3C). The size of the crystalline regions is about 3 nm, as estimated from the Scherrer formula. Nanoparticles of WO_3 have an amorphous structure; in XRD of the W–CC composite the tungsten oxide corresponds to a wide halo at small angles.

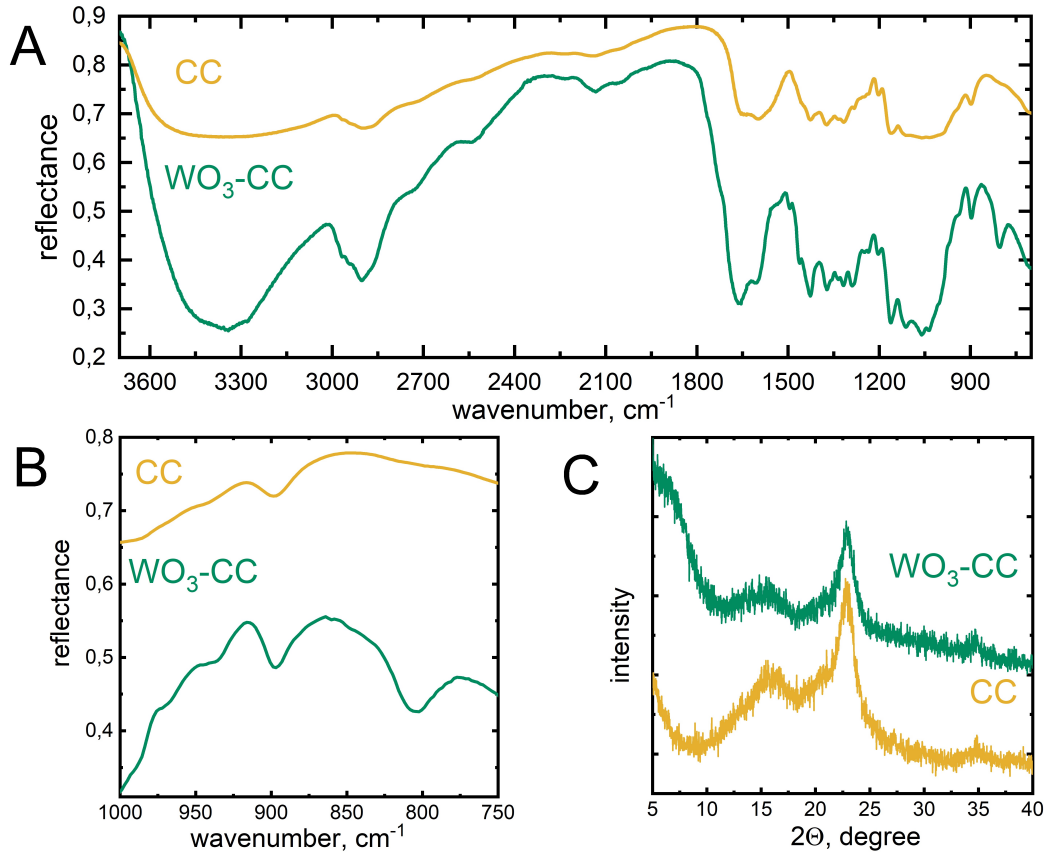

FIG. 3. IR spectra of W–CC and CC aerogels (A and B); XRD pattern of W–CC and CC aerogels (C)

3.3. Photochromic properties

The absorption edge in the UV region of hybrid films and aerogels is located at about 390 nm. The band gap of semiconducting WO_3 nanoparticles in aerogels and W–CC films determined from the data of UV-Vis spectroscopy is about 3.2 eV. Both films and aerogels containing WO_3 exhibited reversible photochromic properties. Under the action of UV radiation, the films were colored in an intense blue color and aerogels were colored in light blue. The absorption of radiation with an energy exceeding the band gap initiates the transition of electrons to the conduction band of the semiconductor oxide and then the delocalized electron is able to reduce metal ions [15]. The mechanism of photochromic reactions is associated with the reduction of W^{+6} in nanodispersed tungsten oxide to lower oxidation states – W^{+5} and W^{+4}. The UV-Vis spectra of blue films and W–CC aerogels (Fig. 4A) contain absorption bands in the visible region related to W^{+5} (770 nm) and W^{+4} (630 nm) ions [29]. The coloration kinetics of films and aerogels were studied using a xenon lamp as a source of both UV radiation initiating photochromic reaction and probing irradiation of the spectrometer. During the irradiation of W–CC aerogels the intensity of the absorption band at 770 nm increases rapidly, the absorption band at 630 nm appears with an induction period of about 2 minutes (Fig. 4B). Thus, successive reduction processes $W^{+6} \rightarrow W^{+5} \rightarrow W^{+4}$ occur in the aerogel under the action of UV radiation. When the W–CC film is irradiated, at the initial stage the absorption bands at 770 and 630 nm simultaneously grow (Fig. 4B). After 3 minutes the growth rate of the 700 nm band intensity decreases, while the intensity of the band at 630 nm continues to increase almost linearly. Evidently, the reduction rate $W^{+5} \rightarrow W^{+4}$ in the film is higher than in the aerogel.

The in-dark bleaching of UV-irradiated aerogels and films is associated with the oxidation of tungsten ions by atmospheric oxygen. The discoloration kinetics of the materials was measured using a halogen lamp as the spectrometer light source to minimize the effects of UV radiation on the samples. The rate of discoloration for aerogels is much higher than for the films (Fig. 4C). The aerogels became colorless within minutes, while the films became colorless after 5 days. The higher bleaching rate of the W–CC aerogel in comparison with the film is associated with higher availability of the reaction centers of WO_3 nanoparticles to oxygen molecules, since the surface area of the aerogel is several orders of magnitude higher than the surface area of the film.

3.4. Antioxidant properties

Hydrogen peroxide and free radicals formed during its decomposition are presented in significant amounts among metabolites in the process of wound healing [30]. Despite the important role of hydrogen peroxide as a cytotoxic component, at present, special attention is paid to its functioning as a signaling molecule, as well as its participation in the regulation of transcription factors [31–33].

If the metabolism is disturbed in damaged tissues an excess of free radicals occurs, which provokes oxidative stress and prevents wound healing. In this case, treatment should include the use of antioxidants – substances that irreversibly react with free radicals. Another way to deal with the oxidative stress is to use enzymes that catalyze the decomposition of hydrogen peroxide into oxygen and water (for example, catalase). The disadvantage of this approach is the high cost of enzyme preparations manufacture. It has been shown recently that inorganic nanomaterials, for example, nanoparticles of cerium dioxide [34] and hematite (α-Fe_2O_3) [35] can exhibit catalase-like activity [36]. The synthesis and investigation of new inorganic analogues of enzymes, nanozymes can contribute to the problem of fighting the oxidative stress during treatment of various diseases.

The antioxidant properties of the W–CC composite were studied by luminol-activated chemiluminescence. The experiment was carried out under conditions close to physiological (37°C, pH 7.4). The molecular ROS generating system consisted of hydrogen peroxide and a luminol chemiluminescent probe. The oxidation of luminol upon interaction with radicals is accompanied by luminescence, the intensity of which is recorded by a chemiluminometer. In the presence of compounds with antioxidant properties the luminescence intensity decreases since competing reactions involving radicals occur in the system.

At the first stage, the effect of tungsten trioxide sol on chemiluminescence in the luminol-H_2O_2 system was studied. The WO_3 sol without a stabilizer increases the luminescence intensity by several times compared to the control therefore it exhibits prooxidant properties (Fig. 5A,B). When analyzing the PVP solution, a significant suppression of luminescence was observed (76±1% and 68±1% of the control with the addition of 25 and 50 μl of PVP, respectively) (Fig. 5B). The data obtained probably indicate the antioxidant properties of this stabilizer. Stabilization of the WO_3 sol with polyvinylpyrrolidone suppresses the prooxidant activity of tungsten oxide, the integrated luminescence intensities in the presence of WO_3–PVP and in the control sample are almost equal (Fig. 5B). Thus, the application of PVP as a stabilizer is desirable in cases where the prooxidant activity of WO_3 nanoparticles can have a negative effect.

The W–CC composite significantly suppresses luminescence in the H_2O_2/luminol system (Fig. 5C). The shape of the kinetic curve (chemiluminogram) characterizes the rate of reaction of the antioxidant with radicals and the duration of its action. In the case of W–CC, incomplete suppression of luminescence was observed, i.e., the W–CC composite is not a strong antioxidant. At the same time, W–CC is a long-acting antioxidant; it suppresses luminescence for a long time; no increase in luminescence intensity was observed on the chemiluminogram during the entire time of the experiment.

For a semi-quantitative evaluation of the antioxidant properties of the W–CC composite the antioxidant capacities of this composite, the PVP-stabilized WO_3 sol and the pharmaceutical antioxidant mexidol were measured. Antioxidant

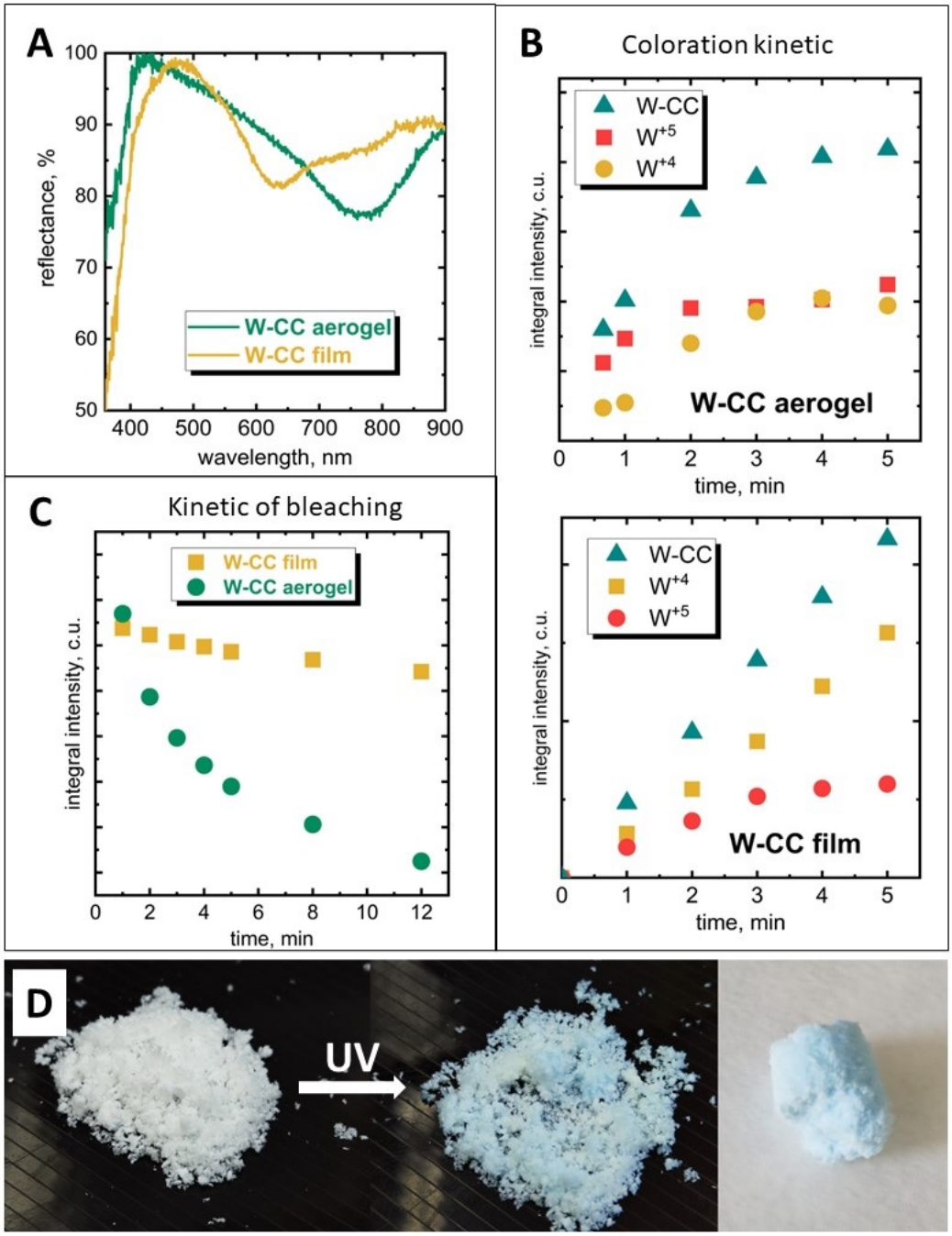

FIG. 4. UV-vis spectra of W–CC aerogel and film (A); coloration kinetics of the aerogel and the W–CC film (B): the integral intensities of absorption bands with peaks at 630 nm (W^{+4}) and 770 nm (W^{+5}), and total integral intensity (W–CC); bleaching kinetics of aerogel and W–CC film (C), total integral intensity of absorption bands at 630 and 770 nm; the image of W–CC aerogel before and after UV irradiation (D)

capacity (AC) is a numerical value proportional to the total amount of free radicals intercepted by a compound of a certain concentration. Antioxidant capacity is calculated as the difference between the areas under the kinetic curves (chemiluminograms) of the control sample and the investigated sample [37]. The antioxidant capacity of the test compound is usually expressed in AC units of one of the standard antioxidants. For this study a pharmaceutical antioxidant mexidol was chosen as the standard.

The antioxidant capacities of W–CC and WO_3 sol at low concentrations are somewhat higher than the antioxidant capacity of mexidol (Fig. 5D). The non-linear nature of the concentration dependence of W–CC antioxidant capacity is probably associated with a large number of various reaction centers on the surface of the composite and a complex mechanism for scavenging of hydroxyl radicals. Based on the experimental data, one can conclude that the antioxidant capacity of the W–CC composite at a concentration of 50 μM is 1.2 mexidol units, the antioxidant capacity of the WO_3 sol at a concentration of 50 μM is 1.5 mexidol units.

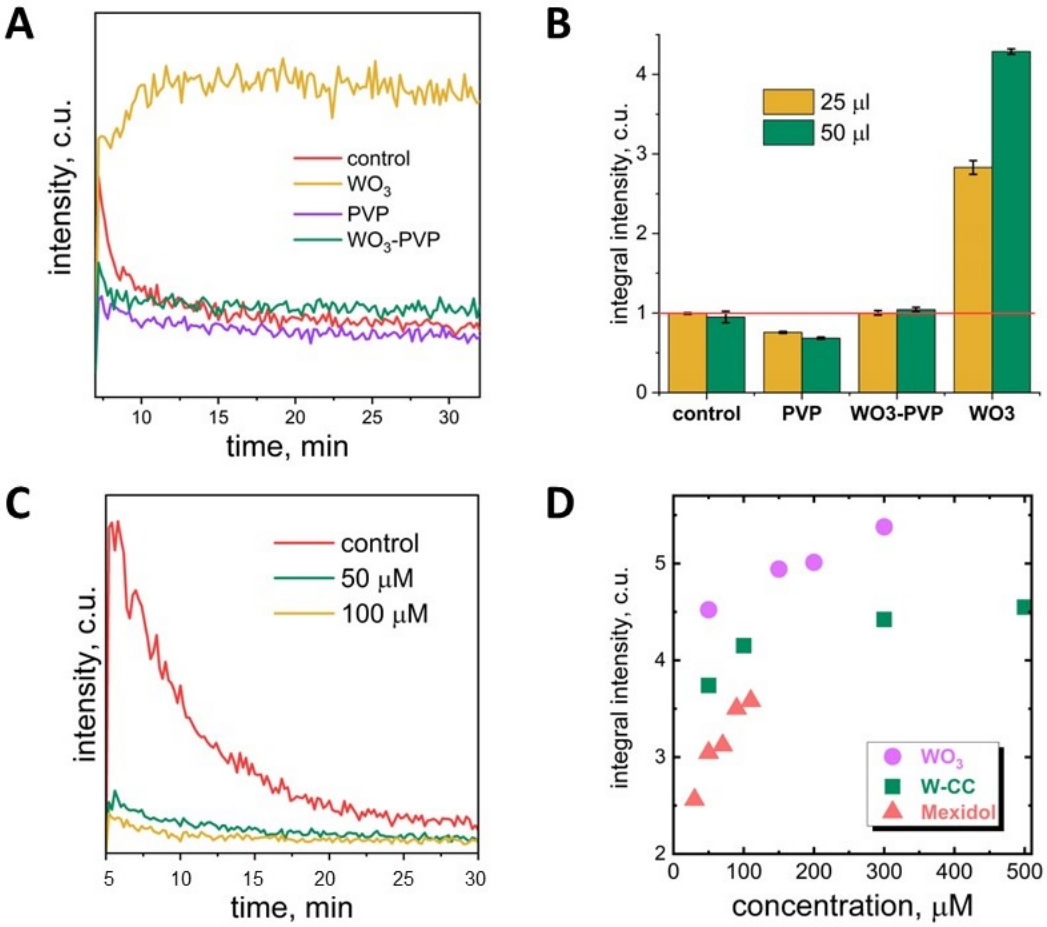

FIG. 5. Chemiluminogram of PVP, WO_3–PVP sol and uncoated WO_3 sol (A); histogram of the integral intensity of chemiluminescence curves of the control sample and samples of PVP, WO_3–PVP sol and uncoated WO_3 sol with concentrations of 25 and 50 μM (B); chemiluminogram of W–CC composite (C); antioxidant capacity of the WO_3–PVP sol, the W–CC composite and the standard antioxidant mexidol (D)

4. Summary

The photochromic hybrid aerogels and films based on TEMPO-oxidized cellulose and chitosan modified with ultrasmall (2 nm) tungsten trioxide nanoparticles were synthesized for the first time.

The synthesized hybrid aerogels and films have reversible photochromic properties. Under the action of UV radiation the materials turn blue within a few minutes as a result of the reduction of tungsten cations in WO_3 nanoparticles. In this case, in films W^{+6} is predominantly reduced to W^{+4}, while in the UV-Vis spectra of aerogels an intense W^{+5} absorption band was observed. Under the action of atmospheric oxygen in the dark the hybrid materials decolorize. The decoloration rate of aerogels is much higher than that of films due to the larger surface area (200 m^2/g) compared to films. The decoloration of the aerogel occurs within a few minutes, while the film decolorizes within five days. Due to

high decoloration rate, photochromic aerogel is a promising material for application in cyclic processes, for example, as a photocatalyst or a gas sensor.

The hybrid films and aerogels based on biopolymers modified with tungsten trioxide demonstrate antioxidant properties comparable to the pharmaceutical antioxidant drug mexidol. The antioxidant capacity of the W–CC composite is 1.2 units of mexidol at a concentration of 50 μM, the antioxidant capacity of the WO_3 sol is 1.5 units of mexidol at a concentration of 50 μM. Due to the use of polyanionic TEMPO-oxidized cellulose and polycationic chitosan as an organic matrix, hybrid films and aerogels retain their integrity when swollen in water. W–CC films absorb up to 8 g of water, while W–CC aerogels absorb up to 20 g of water per 1 g of material. Electrostatic binding of negatively charged WO_3 nanoparticles with a polycation (protonated chitosan) provides immobilization of inorganic particles in a biopolymer matrix. Thus, the synthesized hybrid materials have prospects for application as absorbent wound dressings with antioxidant properties.

References

[1] Budtova T. Cellulose II aerogels: a review. *Cellulose*, 2019, **26**(1), P. 81–121.

[2] Habibi Y., Lucia L.A., and Rojas O.J. Cellulose Nanocrystals: Chemistry, Self-Assembly, and Applications. *Chem. Rev.*, 2010, **110**, P. 3479–3500.

[3] Ganesan K. et al. Review on the production of polysaccharide aerogel particles. *Materials* (Basel)., 2018, **11**(11), P. 1–37.

[4] Abdul Khalil H.P., et al. A review on chitosan-cellulose blends and nanocellulose reinforced chitosan biocomposites: Properties and their applications. *Carbohydr. Polym.*, 2016, **150**, P. 216–226.

[5] William D., Connell O., Birkinshaw C., Francis T., and Dwyer O. Heavy metal adsorbents prepared from the modification of cellulose: A review. 2008, **99**, P. 6709–6724.

[6] Kaushik M. and Moores A. Review: Nanocelluloses as versatile supports for metal nanoparticles and their applications in catalysis. *Green Chem.*, 2016, **18**(3), P. 622–637.

[7] García-González C.A., Alnaief M., and Smirnova I. Polysaccharide-based aerogels—Promising biodegradable carriers for drug delivery systems. *Carbohydr. Polym.*, 2011, **86**(4), P. 1425–1438.

[8] Pircher N., et al. Preparation and Reinforcement of Dual-Porous Biocompatible Cellulose Scaffolds for Tissue Engineering. *Macromol. Mater. Eng.*, 2015, **300**(9), P. 911–924.

[9] Françon H., et al. Ambient-Dried, 3D-Printable and Electrically Conducting Cellulose Nanofiber Aerogels by Inclusion of Functional Polymers. *Adv. Funct. Mater.*, 2020, **30**(12), P. 1909383.

[10] Li Z., et al. Excellent reusable chitosan/cellulose aerogel as an oil and organic solvent absorbent. *Carbohydr. Polym.*, 2018, **191**, P. 183–190.

[11] Li V.C.F., Mulyadi A., Dunn C.K., Deng Y., and Qi H.J. Direct Ink Write 3D Printed Cellulose Nanofiber Aerogel Structures with Highly Deformable, Shape Recoverable, and Functionalizable Properties. *ACS Sustain. Chem. Eng.*, 2018, **6**(2), P. 2011–2022.

[12] Schestakow M., Muench F., Reimuth C., Ratke L., and Ensinger W. Electroless synthesis of cellulose-metal aerogel composites. *Appl. Phys. Lett.*, 2016, **108**(21), P. 213108, May.

[13] Li M. and Fu S. Photochromic holo-cellulose wood-based aerogel grafted azobenzene derivative by SI-ATRP. *Carbohydr. Polym.*, 2021, **259**, P. 117736.

[14] Yamazaki S., Ishida H., Shimizu D., and Adachi K. Photochromic Properties of Tungsten Oxide/Methylcellulose Composite Film Containing Dispersing Agents. *ACS Appl. Mater. Interfaces*, 2015, **7**(47), P. 26326–26332.

[15] Adachi K., et al. Kinetic characteristics of enhanced photochromism in tungsten oxide nanocolloid adsorbed on cellulose substrates, studied by total internal reflection Raman spectroscopy. *RSC Adv.*, 2012, **2**(5), P. 2128–2136.

[16] Zhang Q., Wang R., Lu Y., Wu Y., Yuan J., and Liu J. Highly Efficient Photochromic Tungsten Oxide@PNIPAM Composite Spheres with a Fast Response. *ACS Appl. Mater. Interfaces*, 2021, **13**(3), P. 4220–4229.

[17] Dong C., Zhao R., Yao L., Ran Y., Zhang X., and Wang Y. A review on WO_3 based gas sensors: Morphology control and enhanced sensing properties. *J. Alloys Compd.*, 2020, **820**, P. 153194.

[18] Guo X.Z., Kang Y.F., Yang T.L., and Wang S.R. Low-temperature NO_2 sensors based on polythiophene/WO_3 organic-inorganic hybrids. *Trans. Nonferrous Met. Soc.* China (English Ed.), 2012, **22**(2) P. 380–385.

[19] Yu H., et al. Colloidal synthesis of tungsten oxide quantum dots for sensitive and selective H_2S gas detection. *Sensors Actuators, B Chem.*, 2017, **248**, P. 1029–1036.

[20] El Fawal G.F., Abu-Serie M.M., Hassan M.A., and Elnouby M.S. Hydroxyethyl cellulose hydrogel for wound dressing: Fabrication, characterization and in vitro evaluation. *Int. J. Biol. Macromol.*, 2018, **111**, P. 649–659.

[21] Popov A.L., et al. Photo-induced toxicity of tungsten oxide photochromic nanoparticles. *J. Photochem. Photobiol. B Biol.*, 2018, **178**, P. 395–403.

[22] D'Autréaux B. and Toledano M.B. ROS as signalling molecules: mechanisms that generate specificity in ROS homeostasis. *Nat. Rev. Mol. Cell Biol.*, 2007, **8**(10), P. 813–824.

[23] Ciccarese F., Raimondi V., Sharova E., Silic-Benussi M., and Ciminale V. Nanoparticles as Tools to Target Redox Homeostasis in Cancer Cells. *Antioxidants*, 2020, **9**(3), P. 211.

[24] Kwon S., Ko H., You D.G., Kataoka K., and Park J.H. Nanomedicines for Reactive Oxygen Species Mediated Approach: An Emerging Paradigm for Cancer Treatment. *Acc. Chem. Res.*, 2019, **52**(7), P. 1771–1782.

[25] Di Marzo N., Chisci E., and Giovannoni R. The Role of Hydrogen Peroxide in Redox-Dependent Signaling: Homeostatic and Pathological Responses in Mammalian Cells. *Cells*, 2018, **7**(10), P. 156.

[26] Costa T.J., et al. The homeostatic role of hydrogen peroxide, superoxide anion and nitric oxide in the vasculature. *Free Radic. Biol. Med.*, 2021, **162**, P. 615–635.

[27] Evdokimova O.L., et al. Highly reversible photochromism in composite WO_3/nanocellulose films. *Cellulose*, 2019, **26**, P. 9095–9105.

[28] Sozarukova M.M., Proskurnina E.V., and Ivanov V.K. Prooxidant potential of ceo2 nanoparticles towards hydrogen peroxide. *Nanosyst. Physics, Chem. Math.*, 2021, **12**(3), P. 283–290.

[29] Fayad A.M., Ouis M.A., El Batal F.H., and El Batal H.A. Shielding Behavior of Gamma-Irradiated MoO_3 or WO_3-Doped Lead Phosphate Glasses Assessed by Optical and FT Infrared Absorption Spectral Measurements. *Silicon*, 2018, **10**, P. 1873–1879.

[30] Loo A.E.K., et al. Effects of Hydrogen Peroxide on Wound Healing in Mice in Relation to Oxidative Damage. *PLoS One*, 2012, **7**(11), P. e49215.

[31] Stone J.R. and Yang S. Hydrogen Peroxide: A Signaling Messenger. *Antioxid. Redox Signal.*, 2006, **8**(3–4), 243–270.

[32] Di Marzo N., Chisci E., and Giovannoni R. The Role of Hydrogen Peroxide in Redox-Dependent Signaling: Homeostatic and Pathological Responses in Mammalian Cells. *Cells*, 2018, **7**(10), P. 156.

[33] Lismont C., Revenco I., and Fransen M. Peroxisomal Hydrogen Peroxide Metabolism and Signaling in Health and Disease. *International Journal of Molecular Sciences*, 2019, **20**(15), P. 3673.

[34] Pirmohamed T., et al. Nanoceria exhibit redox state-dependent catalase mimetic activity. *Chem. Commun.*, 2010, **46**(16), P. 2736–2738.

[35] Hu M., Korschelt K., Daniel P., Landfester K., Tremel W., and Bannwarth M.B. Fibrous Nanozyme Dressings with Catalase-Like Activity for H_2O_2 Reduction To Promote Wound Healing. *ACS Appl. Mater. Interfaces*, 2017, **9**(43), P. 38024–38031.

[36] Wei H. and Wang E. Nanomaterials with enzyme-like characteristics (nanozymes): next-generation artificial enzymes. *Chem. Soc. Rev.*, 2013, **42**(14), P. 6060–6093.

[37] Sozarukova M.M., Shestakova M.A., Teplonogova M.A., Izmailov D.Y., Proskurnina E.V., and Ivanov V.K. Quantification of Free Radical Scavenging Properties and SOD-Like Activity of Cerium Dioxide Nanoparticles in Biochemical Models. *Russ. J. Inorg. Chem.*, 2020, **65**(4), P. 597–605.

Submitted 5 May 2022; accepted 15 June 2022

Information about the authors:

Svetlana V. Kameneva – Kurnakov Institute of General and Inorganic Chemistry of the Russian Academy of Sciences, Leninsky Prospekt, 31, Moscow, 119991, Russia; kamenevasvetlanav@gmail.com

Matvei A. Popkov – Kurnakov Institute of General and Inorganic Chemistry of the Russian Academy of Sciences, Leninsky Prospekt, 31, Moscow, 119991, Russia; Lomonosov Moscow State University, Leninskye gory, 1, Moscow, 119991, Russia; popkovma2001@mail.ru

Ilya V. Tronev – Kurnakov Institute of General and Inorganic Chemistry of the Russian Academy of Sciences, Leninsky Prospekt, 31, Moscow, 119991, Russia; HSE University, Myasnitskaya, 20, Moscow, 101000, Russia; ivtronev@edu.hse.ru

Sergey Yu. Kottsov – Kurnakov Institute of General and Inorganic Chemistry of the Russian Academy of Sciences, Leninsky Prospekt, 31, Moscow, 119991, Russia; Lomonosov Moscow State University, Leninskye gory, 1, Moscow, 119991, Russia; sergey12-17@yandex.ru

Madina M. Sozarukova – Kurnakov Institute of General and Inorganic Chemistry of the Russian Academy of Sciences, Leninsky Prospekt, 31, Moscow, 119991, Russia; s_madinam@bk.ru

Vladimir K. Ivanov – Kurnakov Institute of General and Inorganic Chemistry of the Russian Academy of Sciences, Leninsky Prospekt, 31, Moscow, 119991, Russia; van@igic.ras.ru

Conflict of interest: the authors declare no conflict of interest.

NANOSYSTEMS:
PHYSICS, CHEMISTRY, MATHEMATICS

Original article

Khamova T.V., Shilova O.A., et al. *Nanosystems: Phys. Chem. Math.*, 2022, **13** (4), 414–429.
http://nanojournal.ifmo.ru
DOI 10.17586/2220-8054-2022-13-4-414-429

Study of the structure and bioactivity of powdered iron oxides synthesized by sol-gel method

Tamara V. Khamova[1,a], Olga A. Shilova[1,b], Yulia E. Gorshkova[2,c], Natalia V. Tsvigun[3,d], Oleg V. Gerashchenko[4,e], Alexander E. Baranchikov[5,f], Olga R. Udalova[6,g], Anna S. Zhuravleva[6,h], Gaiane G. Panova[6,i], Gennady P. Kopitsa[1,4,k]

[1]Institute of Silicate Chemistry of Russian Academy of Sciences, St. Petersburg, Russia

[2]Joint Institute for Nuclear Research, Dubna, Moscow Region, Russia

[3]Institute of Crystallography Federal R&D Center "Crystallography and Photonics" of the Russian Academy of Sciences, Moscow, Russia

[4]Petersburg Nuclear Physics Institute named by B. P. Konstantinov of National Research Centre Kurchatov Institute, Gatchina, Leningrad Region, Russia

[5]Kurnakov Institute of General and Inorganic Chemistry of the Russian Academy of Sciences, Moscow, Russia

[6]Agrophysical Research Institute, St. Petersburg, Russia

[a]tamarakhamova@gmail.com, [b]olgashilova@bk.ru, [c]Yulia.Gorshkova@jinr.ru, [d]n_tsvigun@mail.ru, [e]gerashchenko_ov@pnpi.nrcki.ru, [f]a.baranchikov@yandex.ru, [g]udal59@inbox.ru, [h]zhuravlan@gmail.com, [i]gaiane@inbox.ru, [k]kopitsa_gp@pnpi.nrcki.ru

Corresponding author: Tamara V. Khamova, tamarakhamova@gmail.com

PACS 61.10.Eq, 61.12.Ex

ABSTRACT Magnetite (Fe_3O_4) and maghemite with an admixture of hematite (γ-Fe_2O_3/α-Fe_2O_3) powders are synthesized via sol-gel process and characterized using XRD, SEM, low temperature nitrogen adsorption, small-angle X-ray scattering (SAXS) and small-angle polarized neutron scattering (SAPNS). The synthesized γ-Fe_2O_3/α-Fe_2O_3 and Fe_3O_4 samples are found to be porous systems featuring with a three-level hierarchically organized structure with different intrinsic scales and aggregation types for each of the structural levels. For both materials, the intrinsic size of the highest level exceeds 70 nm, and magnetic structure involves superparamagnetic particles with a characteristic radius of magnetic-nuclear cross-correlations $R_{MN} \approx 3$ nm. The biological activity of γ-Fe_2O_3/α-Fe_2O_3 and Fe_3O_4 aqueous suspensions in certain concentrations in respect to seed treatment, growth and productivity of plants was studied using the example of spring barley variety Leningradsky under adjustable favorable conditions and physical modeling of stress effects (irradiation with high-intensity UV-B radiation, soil moisture deficiency).

KEYWORDS sol-gel synthesis, iron oxides, mesostructure, magnetic structure, seed presowing treatment

ACKNOWLEDGEMENTS The XRD measurements were performed using the equipment of the Shared Research Center FSRC "Crystallography and Photonics" RAS and were supported by the Russian Ministry of Education and Science. The SEM measurements were performed using shared experimental facilities supported by IGIC RAS state assignment. SAPNS measurements were performed using the equipment of the Jülich Centre for Neutron Science, Forschungszentrum Jülich GmbH, Outstation at MLZ, Garching, Germany. This work was supported by the Ministry of Science and Higher Education of the Russian Federation as part of the IChS RAS state assignment (project 0081-2022-0006) and as part of the Agrophysical Research Institute state assignment No. FGEG-2022-0005.

FOR CITATION Khamova T.V., Shilova O.A., Gorshkova Yu.E., Tsvigun N.V., Gerashchenko O.V., Baranchikov A.E., Udalova O.R., Zhuravleva A.S., Panova G.G., Kopitsa G.P. Study of the structure and bioactivity of powdered iron oxides synthesized by sol-gel method. *Nanosystems: Phys. Chem. Math.*, 2022, **13** (4), 414–429.

1. Introduction

Magnetic nanoparticles of iron oxides attract a permanent interest of researchers due to a wide range of applications in various fields, including magnetic resonance imaging, memory devices, sensors, spintronics, magnetic targeted drug delivery, biomedicine, and environment decontamination [1–5]. Recently, iron oxide nanoparticles have become of particular interest for crop production due to a positive effect on the growth, development, and productivity of agricultural

plants [6–15]. However, this effect can be ambiguous depending on a certain type of plant cultures, crystalline modification of iron oxides, their particle size and concentration in the preparation used to treat plants, as well as the type of plant culture. Therefore, a thorough study of the influence of iron oxides composition, structure, size and concentration on the development of various plant cultures is an essential practically important goal.

Various synthesis methods are used to obtain iron oxide powders: chemical precipitation, mechanochemical method, emulsion method, hydrothermal method, and sol-gel method [16–23]. Each of the above methods has its own advantages and disadvantages. The advantages of the sol-gel method include the simplicity and low cost of the technological process, the high chemical homogeneity of the materials obtained, low temperature of the synthesis and possibility for the adjustment of the target properties of the resulting materials.

The structure of nanosized magnetic powders, including iron oxides, is commonly characterized using XRD, SEM, TEM low-temperature nitrogen adsorption techniques. However, these methods provide the information only about the structural organization on the atomic level. Magnetic properties of such systems are usually studied by such methods as measuring magnetization of samples depending on the applied magnetic field. Such techniques do not allow any data about the structure and characteristic dimensions of the magnetic phases in the studied materials. These parameters can be determined using small-angle polarized neutron scattering (SAPNS) [24,25] affording measurements of magnetic-nuclear interference scattering [26–29].

In our earlier studies, a positive effect of presowing seed treatment, as well as foliar treatment of plants with suspensions of iron oxide nanoparticles synthesized by chemical precipitation, on the germination of seeds, morphometric indicators of growth and their biochemical performances of plants was revealed [30]. This paper repots the continuation of this research in respect to study of the composition and structure of iron oxide powders synthesized by the sol-gel method and effect of their use on the efficiency of pre-sowing seed treatment of spring barley (Leningradsky variety) at the early stages of its development and eventually upon the productivity when growing plants under controlled favorable and stressful conditions.

2. Synthesis and characterization techniques

Magnetite and maghemite were prepared and characterized in this study. Magnetite nanoparticles were synthesized via sol-gel procedure using iron nitrate ($Fe(NO_3)_3 \cdot 9H_2O$) and ethylene glycol ($C_2H_4(OH)_2$), with drying the prepared gel in vacuum. To prepare the sol, 0.1 mol iron nitrate was dissolved in 50 mL ethylene glycol followed by mixing thus obtained solution using a magnetic stirrer at 40 °C within 2 hours. Then the obtained sol was then kept at 80 °C in an oven for approximately 30 min until a brown gel was formed. The resulting gel was aged and then dried at 120 °C for 4 hours. After drying, the xerogel was subjected to vacuum heat treatment at 300 °C for 2 hours. As a result, a consolidated product was obtained and subsequently crumbled into a black powder upon mechanical impact. To prepare maghemite nanoparticles, the resulting black powder was heated in air in an oven at 300 °C for 2 hours. As a result, a red-brown powder was obtained. The synthesis of magnetite nanoparticles was performed according to a similar procedure. The prepared black powder was heated in air in an oven at 300 °C for 2 hours to yield a red-brown target powdered product.

The structure of the prepared iron oxide powders was studied using the following techniques. The phase composition and crystal structure of the powders were characterized by powder X-ray diffraction (XRD) using a Rigaku Miniflex 600 diffractometer. The lattice parameters were calculated by the least squares method using the PDWin software package. The microstructure of the samples was analyzed using a Carl Zeiss NVision 40 high resolution scanning electron microscope (SEM) with an Oxford Instruments X-MAX detector (80 mm^2) at the accelerating voltage of 1 kV.

The texture characteristics of the powders were analyzed by low-temperature nitrogen adsorption using a Quantachrome Nova 1200e analyzer. Before measurements, the samples were degassed at 100 °C in vacuum for 15 – 16 h. The specific surface area of the samples (S_{sp}) was determined using the Brunauer–Emmett–Teller model by 7 points in the range of nitrogen partial pressures $P/P_0 = 0.07 \div 0.25$. The specific pore volume was measured at nitrogen partial pressure $P/P_0 = 0.995$. The pore size distribution was calculated by analyzing the desorption branches of full adsorption-desorption isotherms (in the range of nitrogen partial pressures $0.01 \ldots 0.99$) using the Barrett–Joyner–Halenda (BDH) model.

The structure of iron oxide powders was studied at the mesoscopic scale by SAXS method. SAXS measurements were carried out using the Xeuss 3.0 SAXS/WAXS System (Joint Institute for Nuclear Research, Dubna, Russia) operating in point geometry, and using a GeniX3D microfocus generator of X-ray radiation with Mo$K\alpha$ ($\lambda = 0.071069$ nm), operating in the 30 W/30 μm mode. The spectrometer was equipped with a moving detector Eiger2 R 1M with a sensitive area of 77.1×79.7 mm^2 (pixel size 75 μm). The measurements using two distances from the sample to detector (400 and 4500 mm) enabled the determination of the of X-ray scattering intensity $I(q)$ in the range of momentum transfer of $0.05 < q < 6$ nm^{-1} ($q = (4\pi/\lambda)\sin(\theta/2)$, where λ is the incident X-ray wavelength and θ is the scattering angle).

For the studied iron oxide powders, the measurements were carried out in vacuum at room temperature. To obtain the differential small angle scattering cross section $d\Sigma(q)/d\Omega$ in absolute units, we used a conventional procedure for normalization of the scattering cross section of amorphous carbon (Glassy Carbon), which gives a plateau with an intensity of 3.805 cm^{-1} upon scattering at small angles in the region of $0.1 < q < 0.9$ nm^{-1}. This value is almost 250 times greater than the corresponding value for water H_2O, thus offering a more accurate value of the intensity in absolute terms.

The magnetization of iron oxide powders was measured using the induction method. An ampoule wound round with a measuring inductance coil was placed in a uniform sinusoidal alternating magnetic field with a frequency of 50 Hz generated by a Helmholtz coil. The induced voltage measurements were carried out for the ampoule without a sample and with the sample placed in the ampoule. The specific magnetization was calculated from the difference between these data.

The magnetic structure of iron oxide powders was studied using a small-angle polarized neutron scattering (SAPNS), including the measurement of magnetic-nuclear interference. SAPNS measurements were carried out using a small-angle diffractometer KWS-1 (FRM-II reactor, Garching, Germany) operating in a mode close to point geometry. The measurements were performed using a beam of polarized neutrons with the initial polarization $P_0 \cong 0.95$ and wavelength $\lambda = 0.5$ nm with $\Delta\lambda/\lambda = 0.1$. The sample-detector distance SD = 8 m made it possible to measure the intensity of neutron scattering in the range of transmitted pulses $0.08 < q < 1$ nm^{-1}. The scattered neutrons were recorded by a two-dimensional scintillation position-sensitive detector based on ^{6}Li (128×128 cells with a spatial resolution of 5×5 mm^2).

The studied iron oxide powders were placed in a 1 mm thick quartz cell. The measurements were carried out in a "zero" field H close to zero value, and an external magnetic field $\boldsymbol{H} = 1T$ applied in the horizontal direction rectangular to the incident neutron beam. In the experiment, the dependence of the intensity of scattered neutrons upon the transferred momentum q was measured for neutron polarization P_0 directed parallel $I^+(q, P_0^+)$ and antiparallel $I^-(q, P_0^-)$ to the external magnetic field. The initial spectra were corrected using the standard procedure [31], taking into account the scattering by the installation armature and quartz cell, as well as the laboratory hall background.

To separate the isotropic and anisotropic scattering components, the intensity was radially averaged in the vicinity of the angles $\alpha = 0$ and $\pi/2$ in the detector plane (with the averaging sector $\pm 2\ ^\circ$), corresponding to the directions along and across the applied magnetic field $\boldsymbol{H}$. This averaging results were inserted in the following system of equations:

$$I^+(q,0) = I^+_{\parallel}(q) = \left\langle F_N^2 \right\rangle, \tag{1a}$$

$$I^+(q,\frac{\pi}{2}) = I^+_{\perp}(q) = \left\langle F_N^2(q) \right\rangle + \left\langle F_M^2(q) \right\rangle - 2P \left\langle F_N(q) F_M(q) \right\rangle, \tag{1b}$$

$$I^-(q,0) = I^-_{\parallel}(q) = \left\langle F_N^2 \right\rangle, \tag{1c}$$

$$I^-(q,\frac{\pi}{2}) = I^-_{\perp}(q) = \left\langle F_N^2(q) \right\rangle + \left\langle F_M^2(q) \right\rangle + 2P\varepsilon \left\langle F_N(q) F_M(q) \right\rangle. \tag{1d}$$

Based on the experimental data, this system was resolved to determine the nuclear $\left\langle F_N^2(q) \right\rangle$, magnetic $\left\langle F_M^2(q) \right\rangle$ and interference $\langle F_N(q) F_M(q) \rangle$ contributions to the overall scattering intensity $I(q) = (I^+(q, P_0^+) + I^-(q, P_0^-))/2$.

Assuming that nuclear scattering is independent on the external magnetic field $\boldsymbol{H}$, the magnetic contribution to the scattering intensity in the case of "zero" field was determined as:

$$\left\langle F_M^2(q) \right\rangle_{\boldsymbol{H}\approx 0} = \frac{3}{2} \cdot (I_{\boldsymbol{H}\approx 0}(q) - \left\langle F_N^2 \right\rangle_{\boldsymbol{H}=1T}). \tag{2}$$

To derive the absolute values, the obtained scattering intensities were normalized to the incoherent scattering cross section of plexiglass, taking into account the detector efficiency [31] and bulk density ρ_b for each of the samples. The preliminary processing of the obtained data was carried out using QtiKWS software program [32].

The study of the iron oxide powders biological activity involved the determination of the effect of their treatment with aqueous suspensions of a test plant crop seeds upon the germination energy, seed germination and biometric indicators of seedling growth, as well as on the plant productivity when they are grown in intensive artificial light culture under favorable controlled and under the stress factors action (soil moisture deficiency, high-intensity UV-B radiation). The object of the study was spring barley of the Leningradsky variety from the collection of the N. I. Vavilov All-Russian Institute of Plant Genetic Resources (VIR). The seed treatment was carried out with aqueous suspensions of iron oxide powders at concentrations of 0.01 and 0.001 mg per 1 liter of water according to the procedure [30]. The seeds treated with distilled water were used as reference samples. Germination of seeds and determination of their germination energy were carried out according to the Russian Standard GOST 12038–84. On the 3rd day after soaking, the energy of seed germination was assessed, on the 7th day – their germination, and the length of the sprouts and roots was also measured. Each variant of the experiment was performed for 400 seeds. The studies were carried out in accordance with the rules of the International Seed Testing Association (ISTA).

To study the effect of presowing seed treatment on the production process, the seeds were sown in 3 L plastic vessels filled with 3 kg of soddy-podzolic sandy loamy soil (A arable layer) fertilized at the rate of kg of active substance per 1 ha – N90P90K90. The plants were grown in special plants growing light equipment with a usable area of 1.5 m^2 developed at the Agrophysical Research Institute [33]. The equipment are equipped with lifting light blocks involving DNaZ-400 lamps as light sources. The duration of the light period was 14 hours, the irradiance of plants was 85 – 90 W/m^2 in the photosynthetically active radiation range; the temperature was maintained within the limits of $+22 \ldots 24\ ^\circ$C during the day and $+18 \cdots + 20\ ^\circ$C at night, the relative air humidity was 65 ± 5 %. The oxidative stress conditions in plants in the tubing phase of their development was achieved by a single irradiation with high-intensity UV-B radiation at a dose of

20.0 kJ/m^2; LE-30 lamps (Russia) with a spectral range of 280 – 380 nm and an intensity maximum at $\lambda = 320$ nm were used as the source of UV-B radiation. Physical modeling of soil moisture deficiency was performed during the period of development (tillering – budding) by maintaining soil moisture in some vessels at a level of 25 – 30 % of the total moisture capacity for 21 days, after which the level of soil moisture in these options was increased to the level in the reference samples (60 – 65 % of the total moisture capacity). The plants grown from seeds treated with distilled water on soil with a favorable moisture level of 60 – 65 % of the total moisture capacity and unexposed to UV-B radiation were used as control samples. The stage of plants development at the time of harvesting was full maturation. Every variant of the experiment involved 24 plants, number of vegetation experiments – 2.

3. Results and discussion

3.1. Characterization of the composition and structure of the synthesized powders

XRD profiles of the synthesized iron oxide powders (Fig. 1) demonstrate broad diffraction peaks suggesting that the synthesized samples are poorly crystallized. This conclusion is further confirmed by SEM data (Fig. 2) indicating a porous poorly crystallized aggregated structure of the studied materials.

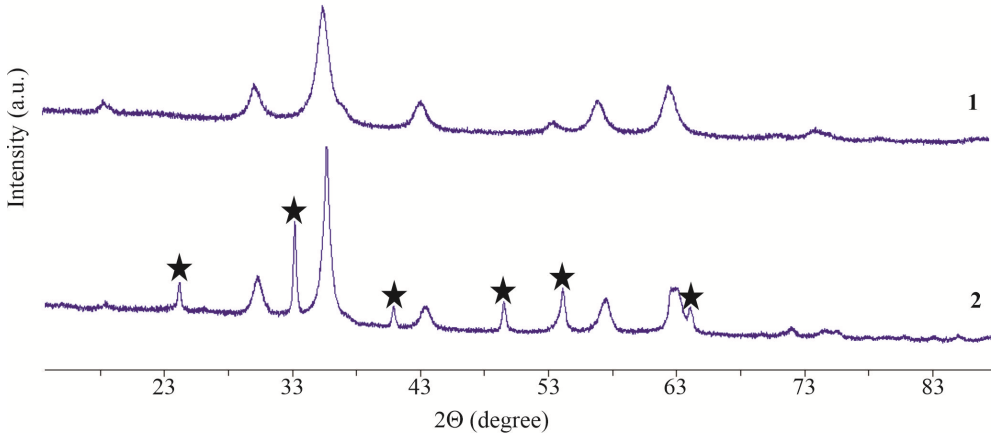

FIG. 1. XRD profiles of the synthesized iron oxide powders: 1 – Fe_3O_4; 2 – γ-Fe_2O_3/α-Fe_2O_3 (asterisks correspond to hematite phase)

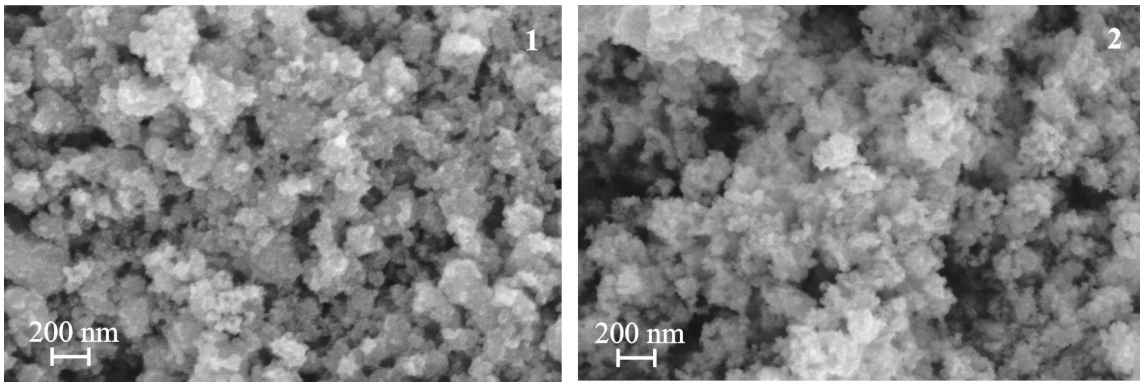

FIG. 2. SEM images of the synthesized iron oxide powders: 1 – Fe_3O_4; 2 – γ-Fe_2O_3/α-Fe_2O_3

Since magnetite and maghemite have almost the same crystal lattice structure with almost coinciding positions of diffraction peaks, in order to distinguish between them, the unit cell parameters were calculated (Table 1).

According to Table 1, the cell parameters of the black iron oxide powder are close to the reference values for magnetite (Fe_3O_4), while the cell parameters of the red-brown powder are closer to those for maghemite (γ-Fe_2O_3). In addition, peaks relating to the hematite phase (α-Fe_2O_3) are observed in the diffraction pattern of the red-brown powder. Thus, the data obtained suggest that the powders synthesized by sol-gel method are iron oxide in the forms of magnetite (Fe_3O_4) and maghemite with an admixture of hematite (γ-Fe_2O_3/α-Fe_2O_3).

The full nitrogen adsorption-desorption isotherms for the synthesized iron oxide powders are shown inn Fig. 3(a,c). The presence of capillary-condensation hysteresis makes it possible to attribute these isotherms to type IV according to the IUPAC classification, which is typical for mesoporous materials containing pores with a diameter of 2 – 50 nm. As

TABLE 1. Unit cell parameters and D_{CSR} estimation for the synthesized iron oxide powders in comparison with reference data

Synthesized samples	Powder color	D_{CSR}, nm	Unit cell parameters, Å	
			Reference	Calculated
Fe_3O_4	Black	8	8.396 – 8.397	8.402(3)
γ-Fe_2O_3/α-Fe_2O_3	Red-brown	11.6	8.336 – 8.339	8.352(4)

can be seen from these figures, the shape of the hysteresis loops for the synthesized samples is close to the H2 type, suggesting the presence of bottle-shaped mesopores in them. In addition, the closing of hysteresis loops for both samples at values of relative pressure P/P_0 less than 0.3 (Fig. 3(a)) indicates the presence of a significant amount of micropores. The results of the obtained isotherms analysis using BET and BDH models are presented in Fig. 3(b,d) and Table 2.

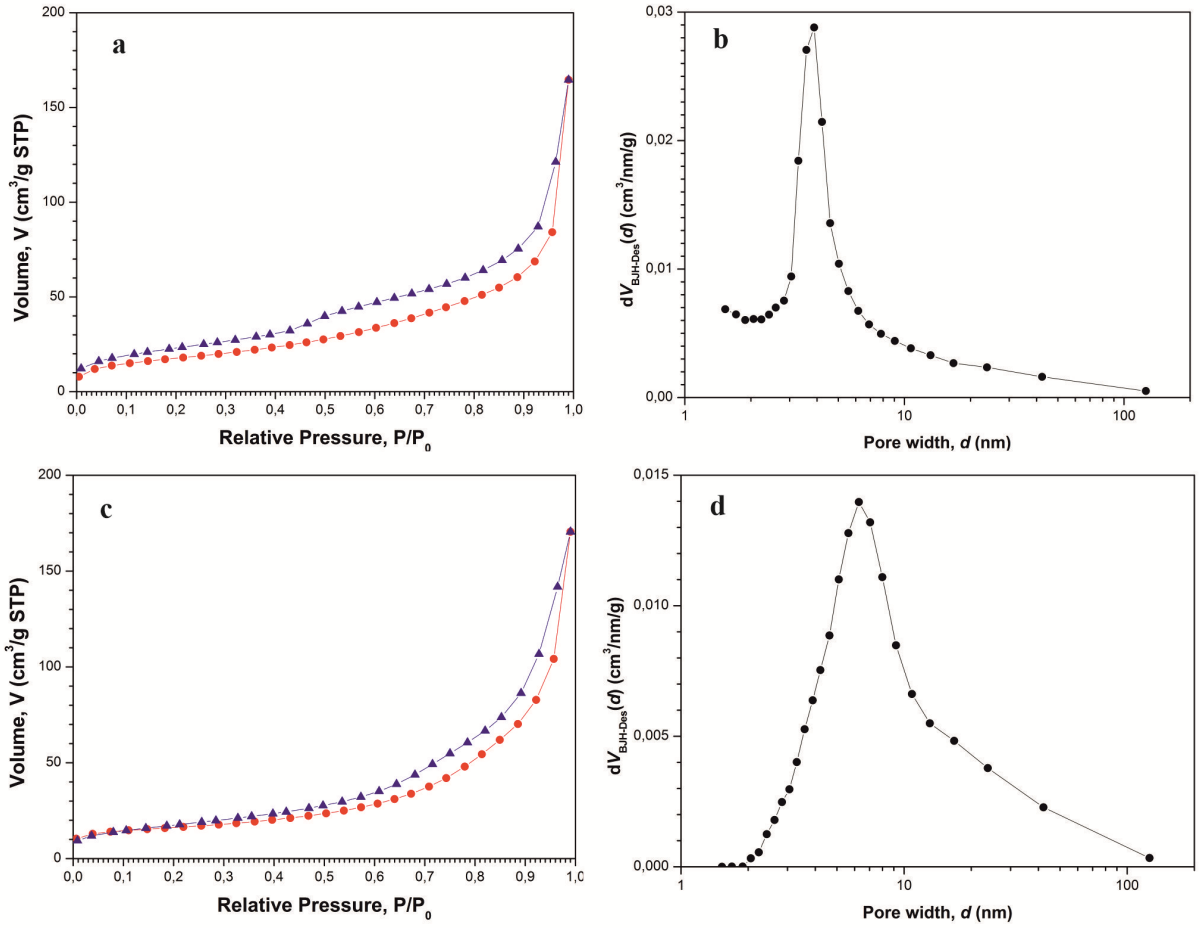

FIG. 3. Full nitrogen adsorption-desorption isotherms (a, c) and pore size distributions (b, d) based on the isotherms processing using the Barrett–Joyner–Halenda (BDH) model for the synthesized Fe_3O_4 (a, c) and γ-Fe_2O_3/α-Fe_2O_3 (b, d)

As shown in Table 2, the synthesized Fe_3O_4 and γ-Fe_2O_3/α-Fe_2O_3 powders have a well-developed surface, similar values of the specific surface area ($S_{BET} \approx 64$ and 58 m^2/g, respectively) and the same quite large specific pore volume ($V_{P/P_0 \to 0.99} = 0.26$ cm^3/g). In addition, for the synthesized Fe_3O_4, a normal (almost symmetrical) pore size distribution is observed with the maximum at $d_p \approx 4$ nm, while γ-Fe_2O_3/α-Fe_2O_3 features with a lognormal distribution of pore $dV(D)$ with the maximum at $d_p \approx 6$ nm.

To obtain more complete information about the supramolecular structure organization of the (size and shape of inhomogeneities, type of their aggregation) in the studied iron oxide powders, SAXS method affording the mesostructure characterization for various materials in the scale range from 1 to 100 nm. A double logarithmic scale plot for the experimental data on the differential macroscopic cross section $d\Sigma(q)/d\Omega$ of small-angle X-ray scattering versus the transferred

TABLE 2. Textural parameters (specific surface area S_{BET}; specific pore volume V_{sp}; average pore diameter, d_p) of the synthesized iron oxide powders determined from the analysis of full nitrogen adsorption-desorption isotherms using BET and BDH models

Powdered iron oxides	S_{BET}, m^2/g	$V_{P/P_0 \cong 0.995}$, cm^3/g	d_p, nm BDH (des.)
Fe_3O_4	63.5 ± 1.2	0.26	3.9
γ-Fe_2O_3/α-Fe_2O_3	57.5 ± 0.6	0.26	6.3

momentum q for the studied Fe_3O_4 and γ-Fe_2O_3/α-Fe_2O_3 powders is shown in Fig. 4. These data clearly indicate that the scattering on γ-Fe_2O_3/α-Fe_2O_3 sample is significantly higher compared with Fe_3O_4 in the entire range of q values, suggesting its lower nuclear density homogeneity on the mesoscopic scale (1... 100 nm).

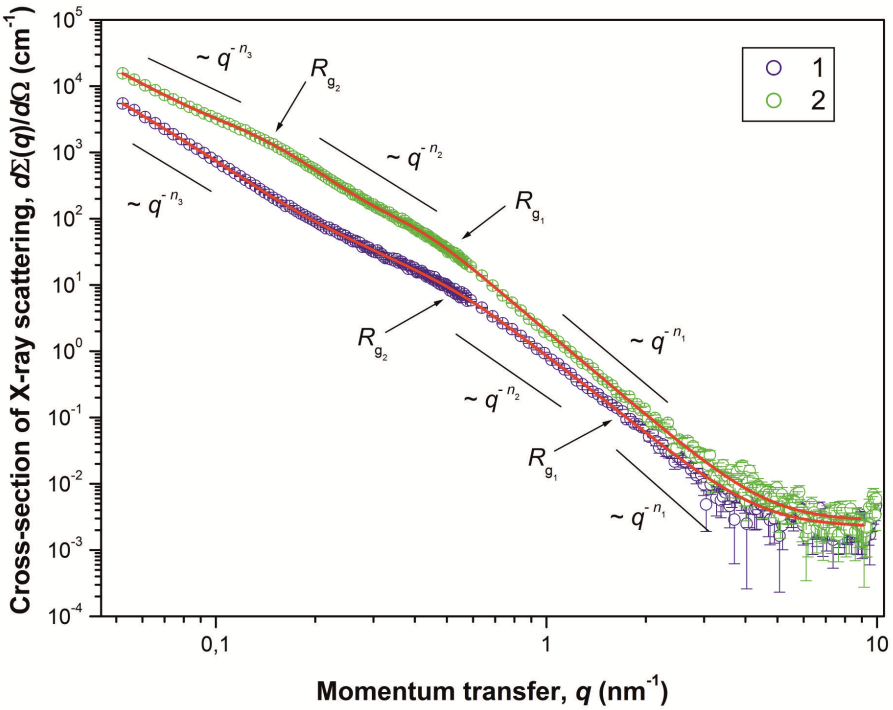

FIG. 4. Differential SAXS cross-section $d\Sigma(q)/d\Omega$ from iron oxide samples Fe_3O_4 (1) and γ-Fe_2O_3/α-Fe_2O_3 (2). Solid lines correspond to the experimental data fits according to the equation (4)

A common feature for both samples under study is the presence on the corresponding scattering curves of three ranges in terms of the transferred momentum q, where the behavior of the scattering cross section $d\Sigma(q)/d\Omega$ follows the power laws $q^{-\Delta}$ with different values $\Delta = n_1$, n_2 and n_3, respectively. In the intermediate regions, near the crossover points q_c (transition points between different scattering modes), the SAXS scattering cross section $d\Sigma(q)/d\Omega$ is satisfactorily described by an exponential dependence (Guinier mode). Thus, the scattering pattern observed for the synthesized iron oxide powders is typical of scattering on three-level hierarchical porous structures [34–36], with different characteristic scales and aggregation types for each of the levels. Moreover, the convex shape of the $d\Sigma(q)/d\Omega$ ($n_1 > n_2 > n_3$) curves clearly indicates that the inhomogeneities of the subsequent structural level with larger in characteristic size R_c are formed from smaller inhomogeneities of the previous structural level, i.e. $R_{c3} > R_{c2} > R_{c1}$. The estimates of the characteristic size R_c for inhomogeneities at each structural level, corresponding to the upper limit of self-similarity for fractal systems, can be obtained from the analysis of scattering in the Guinier mode near the crossover points q_c from the relations $R_c = \sqrt{(5/3)} \cdot R_g$ (in the case of spherical particles with an almost smooth surface [37]) and $R_c = [(D+2)/D]^{1/2} \cdot R_g$ (in the case of fractal objects [38]), where R_g is the gyration radius of the scattering inhomogeneity and D is the fractal dimension. It should be noted that the R_c estimate obtained from the analysis in the Guinier mode corresponds to the maximum size of the scattering inhomogeneities of this type, i.e. always corresponds to the upper estimate.

Scattering from the first (smaller scale) of these structural levels, observed for Fe_3O_4 at $q > 1.5$ nm^{-1} and at $q > 0.5$ nm^{-1} for γ-Fe_2O_3/α-Fe_2O_3 is described by the power dependence q^{-n1}. The power factor n_1 determined from the slope of linear parts in the experimental plots curves $d\Sigma(q)/d\Omega$ in a double logarithmic scale are 4.02 ± 0.04 for

Fe_3O_4 and 4.04 ± 0.04 for γ-Fe_2O_3/α-Fe_2O_3, respectively. This means that both samples feature with scattering by inhomogeneities with almost smooth boundaries $D_{S1} = 2.02 \pm 0.04$ and 2.04 ± 0.04 ($n = 4$ according to the Porod law [39]) in the X-ray wavelength range of the used in this experiment ($\lambda_{\mathrm{MoK}\alpha} = 0.071$ nm).

Scattering from the second structural level, observed for the Fe_3O_4 and γ-Fe_2O_3/α-Fe_2O_3 samples in the ranges $0.5 < q < 1.4$ nm^{-1} and $0.15 < q < 0.4$ nm^{-1} is described by the power dependence q^{-n2} with the power factor $n_2 = 3.42 \pm 0.04$ and 2.69 ± 0.04, respectively. Thus, in the case of Fe_3O_4, scattering takes place at inhomogeneities (clusters) with a highly developed fractal phase interface (solid phase – pore) [40] with the dimension defined as $D_{S2} = 6 - n_2 = 2.58 \pm 0.02$, while for oxide γ-Fe_2O_3/α-Fe_2O_3 the power factor $1 < n_2 < 3$ corresponds to scattering by objects (clusters) with mass-fractal aggregation of inhomogeneities [41] with the fractal dimension $D_{M2} = n_2 = 2.69 \pm 0.04$.

The lower limit of self-resemblance for surface-fractal (Fe_3O_4) and mass-fractal (γ-Fe_2O_3/α-Fe_2O_3) clusters of a given structural level is determined by the characteristic size R_{c1} of inhomogeneities of the 1st structural level. An estimate of the upper limit of self-resemblance R_{c2} for fractal clusters of the 2nd structural level, in both cases, was obtained from the analysis of scattering in the Guinier mode in the ranges $0.3 < q < 0.5$ nm^{-1} for Fe_3O_4 sample and $0.1 < q < 0.15$ nm^{-1} for γ-Fe_2O_3/α-Fe_2O_3 (see Table 3).

TABLE 3. Mesostructure parameters of the synthesized iron oxide powders obtained from SAXS data analysis

Parameters	Synthesized iron oxides	
	γ-Fe_2O_3/α-Fe_2O_3	Fe_3O_4
3rd structural level		
R_{c3}, nm	> 70	
B_3, cm^{-1}nm^{-n3}	18 ± 4	0.56 ± 0.05
$D_{M3} = n_3$	2.25 ± 0.02	—
$D_{S3} = 6 - n_3$	—	2.87 ± 0.02
2nd structural level		
G_2, cm^{2}g^{-1}	2700 ± 500	31 ± 2
$R_{c2} = [(D_{S2,M2} + 2)/D_{S2,M2}]^{1/2} \cdot R_{g2}$, nm	18.0 ± 2	5.5 ± 0.5
B_2, cm^{-1}nm^{-n2}	7.2 ± 1.1	1.1 ± 0.3
$D_{M2} = n_2$	2.69 ± 0.04	—
$D_{S2} = 6 - n_2$	—	2.58 ± 0.04
$Z = [(R_{g2})^2/(R_{g1})^2]^{D/2}$	24	15
1st structural level		
G_1, cm^{-1}	95 ± 22	1.8 ± 0.2
$R_{c1} = \sqrt{(5/3)} \cdot R_{g1}$, nm	5.4 ± 0.6	1.9 ± 0.2
B_1, cm^{-1}nm^{-n1}	1.9 ± 0.06	0.88 ± 0.08
n_1	4.04 ± 0.04	4.02 ± 0.04
$I_{inc} \cdot 10^3$, cm^{-1}	2.5 ± 0.2	2.3 ± 0.2

Note: G_1 and G_2 are Guinier prefactors for the 1st and 2nd structural levels; B_1, B_2 and B_3 are power prefactors for the 1st, 2nd and 3rd structural levels; R_{c1} and R_{c2} are characteristic sizes of inhomogeneities at the 1st and 2nd structural levels; D_{S2} (D_{M2}) and D_{S3} (D_{M3}) are fractal dimensions of surface-fractal (mass-fractal) clusters of the 2nd structural level and aggregates of the 3rd structural level, Z is the degree of primary particles aggregation in a fractal cluster.

Scattering from the third (the largest size) structural level, observed for the Fe_3O_4 and γ-Fe_2O_3/α-Fe_2O_3 samples in the ranges $q < 0.3$ nm^{-1} and $q < 0.9$ nm^{-1} is described by the power dependence $q - n_3$ with the power factors $n_3 = 3.13 \pm 0.02$ and 2.25 ± 0.02, respectively. Therefore, in the case of Fe_3O_4, scattering takes place on inhomogeneities (aggregates) with a highly developed fractal phase interface with the dimension $D_{S3} = 6 - n_3 = 2.87 \pm 0.02$, while

the power factor for γ-Fe_2O_3/α-Fe_2O_3 corresponds to scattering by objects (aggregates) with mass fractal aggregation of inhomogeneities and fractal dimension $D_{M3} = n_3 = 2.25 \pm 0.02$. The lower limit of self-resemblance for fractal aggregates of a given structural level is determined by the characteristic size R_{c2} of fractal clusters of the second structural level. The absence of deviations of the scattering cross section $d\Sigma(q)/d\Omega$ values from the power law $q - n_3$ at low transferred moments q for both samples indicates that the upper limit of self-similarity of mass fractal aggregates R_{c3} of the third structural level in the both cases significantly exceeds the maximum size that can be determined using the applied technique. Nevertheless, according to the expression $R_{\max} \approx 3.5/q_{\min}$ [40], this size can be estimated on the level $R_{c3} > 70$ nm.

Thus, the observed SAXS pattern for the synthesized iron oxides clearly indicates three types of scattering inhomogeneities significantly differing in their characteristic scale. For a general analysis of the observed scattering, we used an integrated exponential-power equation, taking into account the presence of several structural levels in the scattering system [42]:

$$\frac{d\Sigma(q)}{d\Omega} = \sum_{i=1}^{2}\left[G_i \exp\left(-\frac{q^2R_{gi}^2}{3}\right) + B_i \exp\left(-\frac{q^2R_{g(i-1)}^2}{3}\right)\left(\frac{(\mathrm{erf}(qR_{gi}/\sqrt{6}))^3}{q}\right)^{n_i}\right] + I_{inc}. \quad (3)$$

The summation according to (3) is performed for the number of structural levels. In the most general case, expression (3) determines the presence of four free parameters for each structural level, including the Guinier prefactor G_i, the gyration radius R_{gi}, the power prefactor B_i and the power factor n_i. The parameter I_{inc} is a q-independent constant determined by incoherent scattering.

To obtain the final results according to the equation (3), the experimental dependences of the differential SAXS scattering cross section $d\Sigma(q)/d\Omega$ were processed using the least squares method (LSM) in the entire range under study. The results of this analysis are presented in Fig. 4 and Table 3.

The integrated analysis of SEM data, low-temperature nitrogen adsorption, and SAXS indicates that γ-Fe_2O_3/α-Fe_2O_3 and Fe_3O_4 samples synthesized via the sol-gel technology are porous systems with a three-level hierarchical organization of the structure with different characteristic scales and aggregation types for each of the structural levels, and the characteristic size R_{c3} for the largest third level in both cases exceeds 70 nm. Thus, the first structural level of γ-Fe_2O_3/α-Fe_2O_3 powder consists of almost smooth particles with the characteristic size $R_{c1} \approx 5$ nm, which at the second structural level aggregate into mass fractal clusters with the dimension $D_{M2} = 2.69$ and the upper limit of self-resemblance similarity $R_{c2} \approx 18$ nm, from which mass-fractal aggregates with dimension $D_{M3} = 2.25$ are formed at the third structural level. In turn, the Fe_3O_4 powder at the first structural level also consists of small particles ($R_{c1} \approx 2$ nm) with an almost smooth surface, which at the second structural level aggregate into surface fractal clusters with the dimension of $D_{S2} = 2.58$ and the upper self-resemblance boundary $R_{c2} \approx 6$ nm, from which surface fractal aggregates with the dimension $D_{S3} = 2.87$ are formed at the third structural level.

The magnetization $\boldsymbol{M}$ measured by the induction method for the synthesized Fe_3O_4 and γ-Fe_2O_3/α-Fe_2O_3 powders depending on the applied magnetic field $\boldsymbol{H}$ is shown in Fig. 5. These data indicate almost linear dependences without a hysteresis, suggesting these powders to be soft magnetic materials. However, in the range of applied magnetic fields $\boldsymbol{H}$, the saturation of magnetization $\boldsymbol{M}$ in the studied superparamagnetic nanoparticles was not achieved.

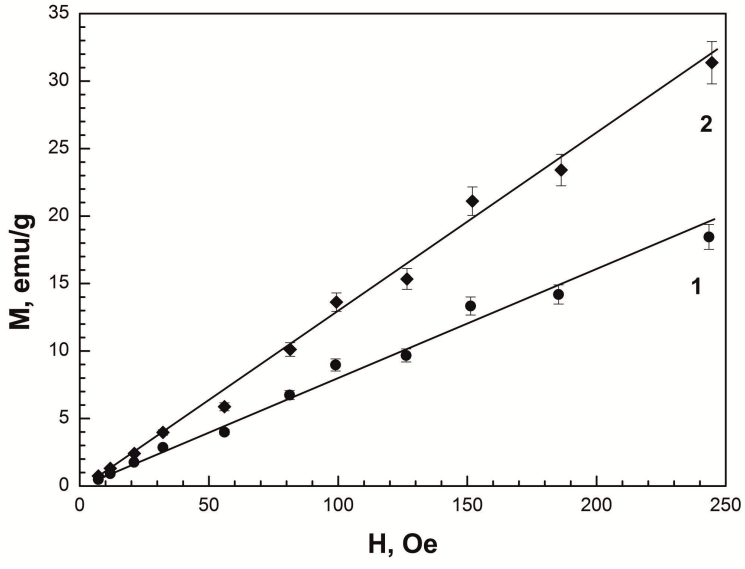

FIG. 5. Magnetization M of Fe_3O_4 (1) and γ-Fe_2O_3/α-Fe_2O_3 (2) as function of the applied magnetic field $\boldsymbol{H}$

The magnetic structure, i.e. spatial distribution and nature of spin correlations in the studied powders of iron oxides, was studied using SAPNS method. Two-dimensional intensities of scattering by iron oxide powders obtained for two polarization states of the neutron beam $I^-(q,\alpha)$ and $I^+(q,\alpha)$ when measured in "zero" ($\boldsymbol{H} \approx 0$) and horizontal magnetic fields ($\boldsymbol{H} = 1T$), respectively, as well as their difference $\Delta I_{MN}(q,\alpha) = I^-(q,\alpha) - I^+(q,\alpha)$ (magnetic-nuclear interference term) during measurements in an external magnetic field. As can be seen from Fig. 6, for the spectra measured in a magnetic field $\boldsymbol{H} = 1T$, the observed scattering pattern is anisotropic with a significant change in the aspect ratios for the two polarization states. The difference signal $\Delta I_{MN}(q,\alpha)$, where all background contributions are self-subtracted, shows an angular dependence on α, with an insignificant intensity along the direction of the applied magnetic field $\boldsymbol{H}$.

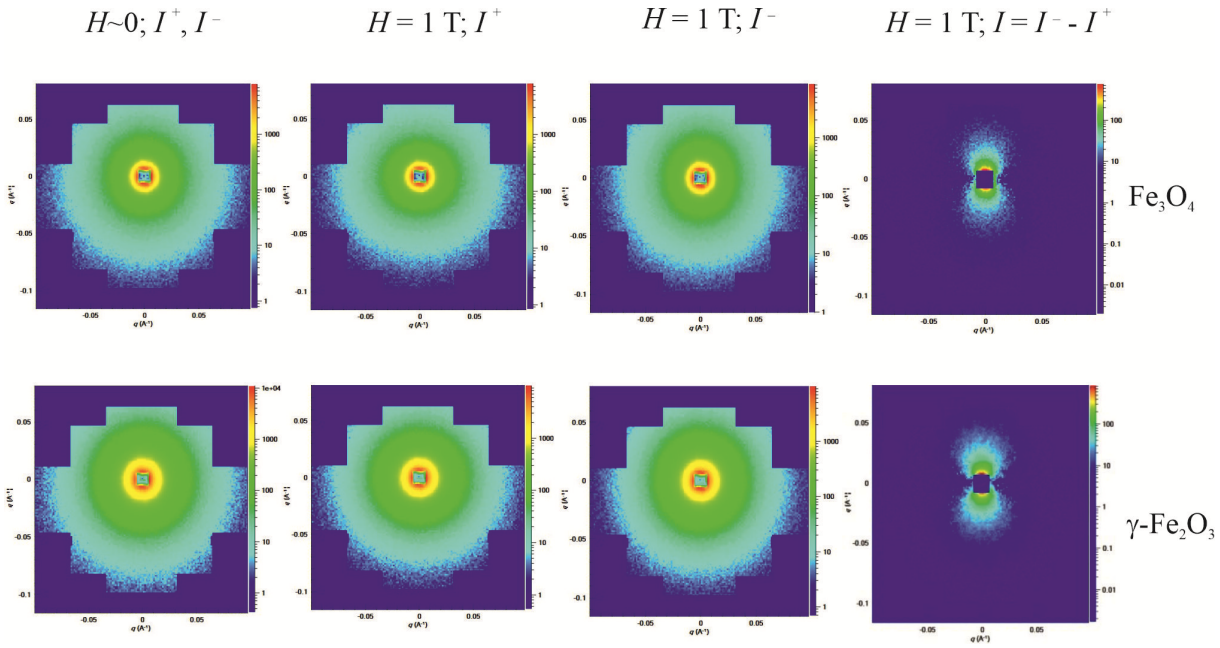

FIG. 6. Experimental two-dimensional intensities of scattering for two polarization states of the incident neutron beam and their difference $\Delta I_{MN}(q,\alpha) = I^-(q,\alpha) - I^+(q,\alpha)$ (magnetic-nuclear interference term) obtained for the synthesized iron oxide powders at measurements in external magnetic field $\boldsymbol{H} = 1T$. The square in the center of the detector is the trace from the beam absorber (beamstop)

The separated nuclear $\langle F_N^2(q)\rangle$, magnetic $\langle F_M^2(q)\rangle_{\mathbf{H}=1T}$ and interference $\langle F_N(q)F_M(q)\rangle_{\mathbf{H}=1T}$ contributions to the scattering are shown in Fig. 7. The comparison of these data indicates that for all the iron oxide samples the nuclear contribution $\langle F_N^2(q)\rangle$ exceeds the magnetic contribution $\langle F_M^2(q)\rangle_{\mathbf{H}=1T}$ by almost an order of magnitude.

3.1.1. Nuclear SAPNS.. The scattering behavior observed for the nuclear component $d\Sigma N(q)/d\Omega$ SANS (Fig. 7) is similar to that revealed for the studied iron oxides using SAXS techniques (Fig. 4) within the used range of transferred momentum $0.08 < q < 1$ nm^{-1}. For γ-Fe_2O_3/α-Fe_2O_3 (Fig. 7(b)), the $d\Sigma N(q)/d\Omega$ plot also features with three q ranges with the nuclear SANS $d\Sigma N(q)/d\Omega$ component following power laws $q^{-\Delta}$ with different power factors $\Delta = n_1, n_2$, and n_3, respectively. In the case of Fe_3O_4 (Fig. 7(a)) only two q regions with different power laws are found for the nuclear component of $d\Sigma N(q)/d\Omega$. This difference is determined by the fact that in the performed experiments $q_{\max} = 1$ nm^{-1}, while in SAXS measurements, scattering from the particles of the first structural level was detected at $q > 1.5$ nm^{-1}. Thus, the analysis of nuclear SANS for the synthesized Fe_3O_4 (Fig. 7(a)) and γ-Fe_2O_3/α-Fe_2O_3 (Fig. 7(b)) samples also involved the integrated exponential-power expression (3) taking into account several structural levels in the scattering system.

To obtain the final results, equation (3) was reduced in couple with the setup resolution function and processed according to the least square method. Thus, obtained data are summarized in Fig. 7 and Table 4.

As shown in Table 4, the atomic supramolecular structure parameters of the synthesized samples based on SANS data are in full agreement with the results obtained from the analysis of SAXS data (Table 3).

3.1.2. SAPNS magnetic scattering $d\Sigma M(q)/d\Omega$ ($\boldsymbol{H} = 1T$). For superparamagnetic nanoparticles, upon saturation of the magnetization, magnetic scattering becomes completely anisotropic, while nuclear scattering remains isotropic. As can be seen from Fig. 7, the magnetic scattering cross section $d\Sigma M(q)/d\Omega$, isolated from the total SAPNS, in the direction $\alpha = \pi/2$, perpendicular to the applied magnetic field $\boldsymbol{H} = 1T$, for iron oxide powders synthesized by the sol-gel technology is small (not more than 10 %) in comparison with nuclear scattering $d\Sigma N(q)/d\Omega$ and is statistically resolvable only in the region of small $q < 0.15$ nm^{-1}, which corresponds to scattering by large-scale magnetic fluctuations appeared to upon the achievement of magnetization saturation.

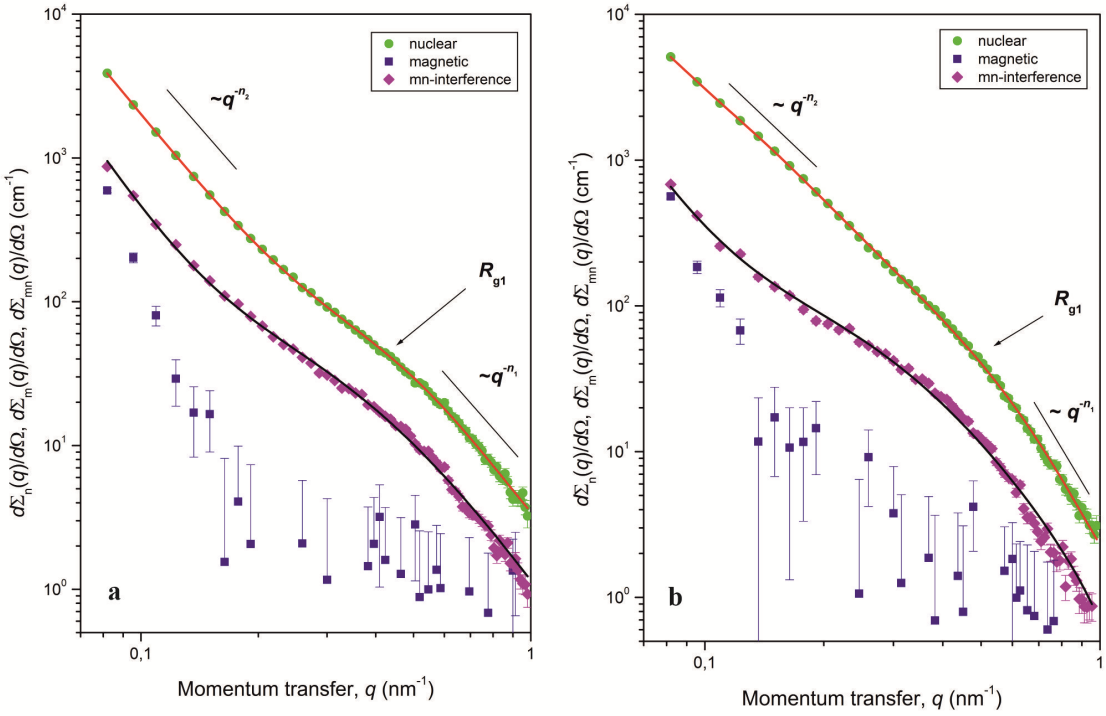

FIG. 7. Nuclear $d\Sigma N(q)/d\Omega$ (◯), magnetic $d\Sigma M(q)/d\Omega$ (□) and magnetic-nuclear interference $d\Sigma_{MN}(q)/d\Omega$ (◊) SAXS cross-dections for Fe_3O_4 (a) and γ-Fe_2O_3/α-Fe_2O_3 (b) samples as function of the transferred momentum q. The data are based on the teo-dimentional spectra (Fig. 6) measured in the magnetic field $\boldsymbol{H} = 1T$. Solid lines correspond to the experimental data fits according to equations (3) and (4)

TABLE 4. Mesostructure parameters of the synthesized iron oxide powders obtained from the analysis of SAPNS cross-section $d\Sigma N(q)/d\Omega$ nuclear component

Parameters	Synthesized iron oxides	
	γ-Fe_2O_3/α-Fe_2O_3	Fe_3O_4
3rd structural level		
R_{c3}, nm	> 45	
$D_{M3} = n_3$	2.35 ± 0.02	—
$D_{S3} = 6 - n_3$	—	2.82 ± 0.02
2nd structural level		
$R_{c2} = [(D_{S2,M2} + 2)/D_{S2,M2}]^{1/2} \cdot R_{g2}$, nm	16 ± 3	5.1 ± 0.5
$D_{M2} = n_2$	2.74 ± 0.04	—
$D_{S2} = 6 - n_2$	—	2.46 ± 0.06
1st structural level		
$R_{c1} = \sqrt{(5/3)} \cdot R_{g1}$, nm	5.9 ± 0.8	—
n_1	4.00 ± 0.05	—

In this regard, the quantitative analysis of the observed magnetic scattering $d\Sigma M(q)/d\Omega$ for the synthesized powders of iron oxides is practically impossible. However, this problem can be addressed by the analysis of the interference contribution $d\Sigma_{MN}(q)/d\Omega$ to the overall SAPNS, that is equal to the magnetic scattering amplitude multiplied by the nuclear scattering amplitude, i.e. corresponding to the first (not to the second, as in the case of measuring the magnetic scattering intensity) power of the magnetic scattering amplitude, that determines an increased sensitivity of this method.

3.1.3. SAPNS magnetic-nuclear cross-section $d\Sigma_{MN}(q)/d\Omega$ ($\boldsymbol{H} = 1T$). The analysis of magnetic-nuclear interference scattering $d\Sigma_{MN}(q)/d\Omega$ contribution into the overall SAPNS obtained in the $\alpha = \pi/2$ direction (orthogonal to the applied magnetic field $\boldsymbol{H} = 1T$) shown in Fig. 7 suggests that the magnetic-nuclear interference scattering $d\Sigma_{MN}(q)/d\Omega$ for both γ-Fe_2O_3/α-Fe_2O_3 and Fe_3O_4 is well fitted by the following equation:

$$\frac{d\Sigma_{MN}(q)}{d\Omega} = \frac{A_2}{q^4} + \frac{A_1}{(q^2 + \kappa_{MN}^2)^2}, \tag{4}$$

where A_1 and A_2 are free parameters, and $\kappa_{MN} = 1/R_{MN}$ is the reverse correlation radius of the magnetic-nuclear contrasting (and, consequently, scattering) region. The first term in the equation (4) ($\sim q^{-4}$) corresponds to the scattering on large-scale spin density fluctuations, and the second term is a squared Lorentzian corresponding to scattering on a spin correlator $\langle S_i, S_j \rangle$ exponentially decreasing with distance r in the coordinate representation:

$$\langle S_i S_j \rangle \propto \exp(-\frac{r}{R_{MN}}). \tag{5}$$

To obtain the final results, the expression (4) was combined with the setup resolution function and processed by the least squares method. The processing results are shown in Fig. 7 and Table 5.

TABLE 5. Correlation radii R_{MN} of the magnetic-nuclear interference scattering for the synthesized iron oxide samples, based on the analysis of the magnetic-nuclear interference component of the SAPNS cross-section $d\Sigma N(q)/d\Omega$

Synthesized iron oxides	R_{MN} (nm)
γ-Fe_2O_3/α-Fe_2O_3	3.2 ± 0.4
Fe_3O_4	2.7 ± 0.3

According to the data in Table 5, the characteristic sizes R_{MN} of the magnetic-nuclear cross-correlations, obtained from the analysis of SAPNS results, are smaller than the characteristic sizes R_c of the nuclear inhomogeneities presented in Tables 3 and 4. However, in this case, the characteristic size R_{MN} corresponds to the average size of magnetic-nuclear cross-correlations, instead of its upper limit, as in the case of the characteristic size R_c of nuclear inhomogeneities in the expressions used in the analysis of $d\Sigma N(q)/d\Omega$.

3.1.4. SANS magnetic cross-section $d\Sigma M(q)/d\Omega$ ($\boldsymbol{H} \approx 0T$). Assuming that the nuclear scattering is isotropic and independent on the applied magnetic field, we determined the magnetic contribution $\left\langle F_M^2(q) \right\rangle_{\mathbf{H} \approx 0}$ into the overall SANS intensity in the case of "zero" field ($\boldsymbol{H} \approx 0T$). The corresponding cross-sections $d\Sigma M(q)/d\Omega$ of the magnetic scattering for the studied samples are shown in Fig. 8.

According to Fig. 8, a statistically resolvable magnetic scattering $d\Sigma M(q)/d\Omega$ is observed for γ-Fe_2O_3/α-Fe_2O_3, while in the case of the synthesized Fe_3O_4, a quantitative analysis is almost impossible. However, the presence of a blurry peak with $q_{\max} \approx 0.4$ nm^{-1} at the $d\Sigma M(q)/d\Omega$ plot for this sample (Fig. 8(a)) suggests the presence of magnetic inhomogeneities structured according to a short-range order with the radius of interparticle magnetic correlations $\xi_M = 2\pi/q_{\max} \approx 16$ nm. The magnetic scattering at small q values ($q < 0.2$ nm^{-1}) is probably determined by scattering on large-scale magnetic fluctuations.

A similar blurred peak with $q_{\max} \approx 0.25$ nm^{-1} is observed at $d\Sigma M(q)/d\Omega$ plot for the synthesized γ-Fe_2O_3/α-Fe_2O_3. The magnetic scattering of this samples was analyzed using the expression:

$$\frac{d\Sigma_{M(q)}}{d\Omega} = \frac{A_2}{q^4} + \frac{A_1}{\left((q - q_{\max})^2 + \kappa_M^2\right)^2}, \tag{6}$$

where A_1 and A_2 are free parameters, and $\kappa_M = 1/R_M$ is the reverse correlation radius of magnetic inhomogeneities. The second term in equation (6) corresponds to the scattering on magnetic inhomogeneities structured according to a short-range order with the radius of interparticle magnetic correlations $\xi_M = 2\pi/q_{\max} \approx 25$ nm.

To obtain the final results, expression (6) was combined with the setup resolution function and processed by the least squares method. The processing results are shown in Fig. 8 and Table 6.

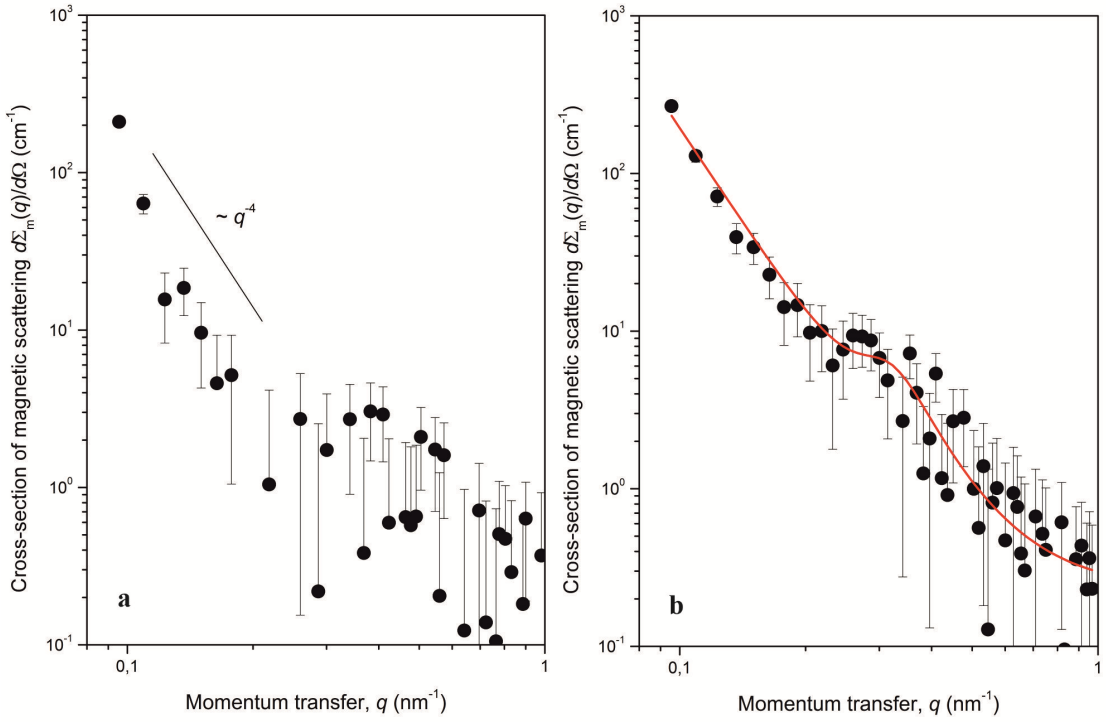

FIG. 8. SANS magnetic cross-sections $d\Sigma M(q)/d\Omega$ in the "zero" field ($\boldsymbol{H} \approx 0$) for the synthesized iron oxides Fe_3O_4 (a) and γ-Fe_2O_3/α-Fe_2O_3 (b) as function of the transferred momentum q. The solid line corresponds to the experimental data fit according to the equation (6)

TABLE 6. Correlation radii R_M of magnetic scattering and interparticle magnetic correlations ξ_M of the synthesized iron oxides, based on the analysis of SANS $d\Sigma M(q)/d\Omega$ cross-section in the "zero" field ($\boldsymbol{H} \approx 0T$)

Synthesized iron oxides	$\xi_M = 2\pi/q_{\max}$ (nm)	R_M (nm)
γ-Fe_2O_3/α-Fe_2O_3	25	4.1 ± 0.9
Fe_3O_4	16	—

3.2. Study of bioactive performances of the synthesized powders

The obtained data concerning to the effect of presowing treatment of spring barley seeds with aqueous suspensions of the synthesized Fe_3O_4 and γ-Fe_2O_3/α-Fe_2O_3 powders on germination performances and biometric indicators of sprout growth are summarized in Table 7. These data show that the treatment of seeds with suspensions of γ-Fe_2O_3/α-Fe_2O_3 or Fe_3O_4 in the previously selected concentrations of 0.01 and 0.001 mg/L does not have a significant effect on their germination and root length of seedlings compared with the control samples. However, the length of seedling sprouts tends to increase or significantly change in values after seed treatment with suspensions of γ-Fe_2O_3/α-Fe_2O_3 in the concentration 0.001 mg/L or Fe_3O_4 in the concentrations of 0.001 and 0.01 mg/L, with the most pronounced effect observed in the case of using a 0.001 mg/L suspension of Fe_3O_4. A slight trend should be also noted towards a decrease in the height of sprouts after seed treatment with suspensions of the tested substances at a higher concentration of 0.01 mg/L.

The revealed tendency to stimulate the growth of spring barley plants at the early stages of development after the treatment of their seeds with aqueous suspensions of the tested substances persisted throughout the ontogeny of plants and, ultimately, resulted in a significant increase in the productivity indicator – the number of productive stems on the plant under favorable growing conditions (Table 8). Noteworthy, the considered effect of seed treatment with aqueous suspensions of iron oxides was not observed in respect of the grain productivity of spring barley, since the values of grain productivity indicators, including the number of seeds and their weight on the plant do not differ significantly from those in the control seeds. Moreover, there is a pronounced trend towards a significant decrease in these indicators of barley grain productivity relative to the control in the case of seed treatment with aqueous suspensions of Fe_3O_4.

The study of the effect of seed treatment on the resistance of plants to the stress factors indicated in Table 8 in the most vulnerable periods of the plants development revealed differences effectiveness of the tested iron oxide additives under different stress conditions.

TABLE 7. Effect of barley seeds (Leningradsky variety) treatment with iron oxide suspensions upon the germination performances and biometric indicators of seedlings growth

Seeds treatment variants	Germination energy		Germination, %		Sprout length		Root length	
	%	% of the reference samples	%	% of the reference samples	cm	% of the reference samples	%	% of the reference samples
Control (treatment with distilled water)	96	100	98	100	8.7±0.6	100	8.6±0.5	100
0.01 mg/l γ-Fe_2O_3/α-Fe_2O_3	88	92	96	98	8.8±0.7	101	8.2±0.5	95
0.001 mg/l γ-Fe_2O_3/α-Fe_2O_3	93	97	95	97	9.3±0.6	107	7.9±0.4	92
0.01 mg/l Fe_3O_4	93	97	97	99	9.2±0.6	106	8.3±0.4	97
0.001 mg/l Fe_3O_4	92	96	95	97	10.1±0.6*	116*	8.6±0.4	100

Note: * the value significantly differs from the control at the 5 % significance level

TABLE 8. Effect of barley seeds (Leningradsky variety) treatment with iron oxide suspensions upon the plants productivity at growing under controlled favorable conditions, after the effect of with UV-B radiation (dose 20.0 kJ/m^2) and soil moisture deficiency (25 – 30 % of the total moisture capacity)

Seeds treatment variants	Number of productive stems, pieces / % of the control	Number of seeds from one plant, pieces / % of the control	Weight of the seeds from one plant, g / % of the control
No stress			
Control (treatment with distilled water)	3.1±0.3 / 100	70.0±5.2 / 100	2.52±0.22 / 100
0.01 mg/l γ-Fe_2O_3/α-Fe_2O_3	4.7±0.6 / 152*	72.0±5.6 / 103	2.60±0.20 / 103
0.01 mg/l Fe_3O_4	3.6±0.4 / 116	60.0±4.2 / 86*	2.22±0.19 / 88
UV-B radiation			
Control (treatment with distilled water)	4.7±0.6 / 152*	58.0±4.8 / 83*	2.10±0.18 / 83*
0.01 mg/l γ-Fe_2O_3/α-Fe_2O_3	4.9±0.7 / 158*	64.3±5.2 / 92	2.36±0.16 / 94
0.01 mg/l Fe_3O_4	3.9±0.5 / 126*	54.0±4.3 / 77*	2.00±0.17 / 79*
Soil moisture deficiency			
Control (treatment with distilled water)	2.2±0.5 / 71*	40.0±3.9 / 57*	1.40±0.14 / 56*
0.01 mg/l γ-Fe_2O_3/α-Fe_2O_3	1.0±0.2 / 32*	44.0±4.2 / 63*	1.60±0.15 / 63*
0.01 mg/l Fe_3O_4	2.7±0.6 / -87	50.0±4.9 / 71*	1.90±0.16 / 75*

Note: * the value significantly differs from the control not stress at the 5 % significance level

Thus, when irradiated with high-intensity UV-B radiation, a significant positive effect on plant productivity is observed in case of seeds treatment with aqueous suspensions of γ-Fe_2O_3/α-Fe_2O_3, providing the target plant performances on the same level or exceeding those for the control samples unaffected by the stress, whereas the control stressed plants, and especially plants treated with an aqueous suspension of Fe_3O_4, reduced the grain productivity by 17 and 21 – 23 %, respectively (Table 8). Under conditions of soil moisture deficiency, seed treatment with tested iron oxide additives showed a positive effect, with a trend to a significantly increased grain productivity of plants relative to stressed reference seeds. Generally, the seed treatment with Fe_3O_4 aqueous suspensions turned out to be more effective in increasing plant resistance to the stressors compared to the treatment with γ-Fe_2O_3/α-Fe_2O_3, apparently due to the formation of a larger number of productive stems and seeds (by 270 and 14 %, respectively).

Thus, aqueous suspensions of the synthesized iron oxides in the concentrations of 0.001 and 0.01 mg/L demonstrate a pronounced biological activity at presowing treatment of spring barley, in respect of stimulating the plants growth at the early stages of their development and increasing the number of productive stems under favorable conditions for the vital activity of plants. However, during the cultivation of spring barley under stressful conditions in the most vulnerable periods of plant development, significant differences were revealed in the effectiveness of the influence of the tested iron oxide additives on the plant resistance, depending on the acting stressor. The treatment of seeds with a suspension of γ-Fe_2O_3/α-Fe_2O_3 in the concentration of 0.01 mg/L provided an effective protection from a negative impact of high-intensity UV-B radiation upon the plant productivity remaining on the same level as for the reference plants tested under favorable conditions. In respect of protection from soil moisture deficiency, treatment with 0.01 mg/L Fe_3O_4 suspension was found to be more effective against the reduction of the productivity indicators.

4. Conclusion

Powdered iron oxides prepared via sol-gel method are studied using a number of characterization techniques, including XRD, SEM, low temperature nitrogen adsorption, small angle X-ray (SAXS) and polarized neutron scattering (SAPNS). The synthesized γ-Fe_2O_3/α-Fe_2O_3 and Fe_3O_4 samples are defined as porous systems with a three-level hierarchical structural organization featuring with different characteristic scales and aggregation types for each of the structural levels. The characteristic size R_{c3} for the largest scale third level in both cases exceeds 70 nm. In γ-Fe_2O_3/α-Fe_2O_3 powder, the first structural level consists of almost smooth particles with the characteristic size $R_{c1} \approx 5$ nm, aggregating at the second structural level into mass fractal clusters with the dimension $D_{M2} = 2.69$ and the upper limit of self-resemblance $R_{c2} \approx 18$ nm, in turn, forming mass fractal aggregates with the dimension $D_{M3} = 2.25$ at the third structural level. In Fe_3O_4 powder, the first structural level also consists of small particles ($R_{c1} \approx 2$ nm) with an almost smooth surface, aggregating at the second structural level into surface-fractal clusters with a dimension of $D_{S2} = 2.58$ and an upper self-resemblance boundary $R_{c2} \approx 6$ nm, forming surface fractal aggregates with the dimension $D_{S3} = 2.87$ at the third structural level.

A detailed analysis of the SAPNS data revealed that the magnetic structure of Fe_3O_4 and γ-Fe_2O_3/α-Fe_2O_3 powders synthesized via sol-gel process consists of superparamagnetic particles with a characteristic radius of magnetic-nuclear cross-correlations $R_{MN} \approx 3$ nm. Moreover, short-range spin correlations are also observed between these superparamagnetic particles with the interparticle magnetic correlation radii $\xi_M \approx 16$ and 25 nm for Fe_3O_4 and γ-Fe_2O_3/α-Fe_2O_3, respectively.

A relationship is revealed between the crystallographic modification and biological activity of the synthesized iron oxide powders towards the seeds of spring barley of the Leningradsky variety. Although the presowing treatment of seeds with Fe_3O_4 and γ-Fe_2O_3/α-Fe_2O_3 suspensions does not affect their germination and the length of roots and sprouts, it stimulates the other plants growth indicators and affects the plants productivity in different ways depending on their growing conditions. Particularly, γ-Fe_2O_3/α-Fe_2O_3 suspension demonstrated a higher efficiency in respect of the productivity and resistance of spring barley plants under favorable conditions and under stressful exposure to UV-B radiation, while the suspension of Fe_3O_4 is more effective under stressful conditions in terms of moisture content in the soil.

References

[1] Samrot A.V., Sahithya C. Sai, et al. A review on synthesis, characterization and potential biological applications of superparamagnetic iron oxide nanoparticles. *Current Research in Green and Sustainable Chemistry*, 2021, **4**, 100042.

[2] Song C., Sun W., Xiao Yu., Shi X. Ultrasmall iron oxide nanoparticles: synthesis, surface modification, assembly, and biomedical applications. *Drug Discovery Today*, 2019, **24** (3), P. 835–844.

[3] Bhateria R., Singh R. A review on nanotechnological application of magnetic iron oxides for heavy metal removal. *J. of Water Process Engineering*, 2019, **31**, 100845.

[4] Sheikholeslami Z., Yousefi Kebria D., Qaderi F. Application of γ-Fe_2O_3 nanoparticles for pollution removal from water with visible light. *J. of Molecular Liquids*, 2020, **299**, 112118.

[5] Wang W., Li F., et al. M2 macrophage-targeted iron oxide nanoparticles for magnetic resonance image-guided magnetic hyperthermia therapy. *J. of Materials Science & Technology*, 2021, **81**, P. 77–87.

[6] Li M., Zhang P., et al. Physiological impacts of zero valent iron, Fe_3O_4 and Fe_2O_3 nanoparticles in rice plants and their potential as Fe fertilizers. *Environmental Pollution*, 2021, **269**, 116134.

[7] Pariona N., Martínez A.I., Hernandez-Flores H., Clark-Tapia R. Effect of magnetite nanoparticles on the germination and early growth of Quercus macdougallii. *Science of The Total Environment*, 2017, **575**, P. 869–875.

[8] Li J., Hu J., et al. Uptake, translocation and physiological effects of magnetic iron oxide (γ-Fe_2O_3) nanoparticles in corn (Zea mays L.). *Chemosphere*, 2016, **159**, P. 326–334.
[9] Iannone M.F., Groppa M.D., et al. Impact of magnetite iron oxide nanoparticles on wheat (Triticum aestivum L.) development: Evaluation of oxidative damage. *Environmental and Experimental Botany*, 2016, **131**, P. 77–88.
[10] Tombuloglu H., Slimani Y., et al. Uptake and translocation of magnetite (Fe_3O_4) nanoparticles and its impact on photosynthetic genes in barley (Hordeum vulgare L.). *Chemosphere*, 2019, **226**, P. 110–122.
[11] Yan L., Li P., et al. Physiological and metabolic responses of maize (Zea mays) plants to Fe_3O_4 nanoparticles. *Science of the Total Environment*, 2020, **718**, 137400.
[12] Ding Y., Bai X., et al. Toxicological responses of Fe_3O_4 nanoparticles on Eichhornia crassipes and associated plant transportation. *Science of the Total Environment*, 2019, **671**, P. 558–567.
[13] Wang Y., Wang S., et al. The impacts of γ-Fe_2O_3 and Fe_3O_4 nanoparticles on the physiology and fruit quality of muskmelon (Cucumis melo) plants. *Environmental Pollution*, 2019, **249**, P. 1011–1018.
[14] Cai L., Jia H., et al. Foliar exposure of Fe_3O_4 nanoparticles on Nicotiana benthamiana: Evidence for nanoparticles uptake, plant growth promoter and defense response elicitor against plant virus. *J. of Hazardous Materials*, 2020, **393**, 122415.
[15] Konate A., Wang Y., et al. Comparative effects of nano and bulk-Fe_3O_4 on the growth of cucumber (Cucumis sativus). *Ecotoxicology and Environmental Safety*, 2018, **165**, P. 547–554.
[16] Nisticò R. A synthetic guide toward the tailored production of magnetic iron oxide nanoparticles. *Boletín de la Sociedad Española de Cerámica y Vidrio*, 2021, **60** (1), P. 29–40.
[17] Lastovina T.A., Budnyk A.P., Kubrin S.P., Soldatov A.V. Microwave-assisted synthesis of ultra-small iron oxide nanoparticles for biomedicine. *Mendeleev Communications*, 2018, **28** (2), P. 167–169.
[18] Calderón P.A., Pablo B., et al. Magnetic iron oxides nanoparticles obtained by mechanochemical reactions from different solid precursors. *J. of Alloys and Compounds*, 2021, **860**, 157892.
[19] Bhavani P., Rajababu C.H., et al. Synthesis of high saturation magnetic iron oxide nanomaterials via low temperature hydrothermal method. *J. of Magnetism and Magnetic Materials*, 2017, **426**, P. 459–466.
[20] Jafari Eskandari M., Hasanzadeh I. Size-controlled synthesis of Fe_3O_4 magnetic nanoparticles via an alternating magnetic field and ultrasonic-assisted chemical co-precipitation. *Materials Science and Engineering: B*, 2021, **266**, 115050.
[21] Koizumi H., Azhar Uddin Md, Kato Y. Effect of ultrasonic irradiation on γ-Fe_2O_3 formation by co-precipitation method with Fe^{3+} salt and alkaline solution. *Inorganic Chemistry Communications*, 2021, **124**, 108400.
[22] Xu J., Yang H., et al. Preparation and magnetic properties of magnetite nanoparticles by sol-gel method. *J. of Magnetism and Magnetic Materials*, 2007, **309** (2), P. 307–311.
[23] Hasanpour A., Niyaifar M., Asan M., Amighian J. Synthesis and characterization of Fe_3O_4 and ZnO nanocomposites by the sol-gel method. *J. of Magnetism and Magnetic Materials*, 2013, **334**, P. 41–44.
[24] Okorokov A.I., Grigor'ev S.V., et al. New magnetic phenomena and polarized neutrons. *Surf. Investigation. X-ray, Synchrotron Neutron Techniq*, 2007, **1**, P. 542–555.
[25] Muhlbauer S., Honecker D., et al. Magnetic small-angle neutron scattering. *Reviews of Modern Physics*, 2019, **91**, 015004.
[26] Runov V., Glattli H., et al. Small-angle polarized neutron scattering in $Sm_{1-x}Sr_xMnO_3$ ($x < 0.5$) perovskite. *Physica B*, 2000, **276–278**, P. 795–796.
[27] Bergenti I., Deriu A., et al. Small angle polarised neutron scattering investigation of magnetic nanoparticles. *J. of Magnetism and Magnetic Materials*, 2003, **262** (1), P. 60–63.
[28] Runov V.V., Bugrov A.N., et al. Mesostructure of Composite Materials Based on Segmented Poly(Urethane Imide) Containing Ferrite Nanoparticles. *Rus. J. of Inorganic Chemistry*, 2021, **66**, P. 225–236.
[29] Runov V.V., Bugrov A.N., et al. Magnetic Neutron Scattering in Reduced Graphene Oxide. *JETP Letters*, 2021, **113**, P. 384–388.
[30] Shilova O., Panova G., et al. Aqueous Chemical Co-Precipitation of Iron Oxide Magnetic Nanoparticles for Use in Agricultural Technologies. *Letters in Applied NanoBioScience*, 2021, **10** (2), P. 2215–2239.
[31] Wignall G.T., Bates F.S. Absolute calibration of small-angle neutron scattering data. *J. Appl. Crystallogr.*, 1987, **20**, P. 28–40.
[32] Jülich Centre for Neutron Science, QtiKWS 2019, URL: www.qtisas.com.
[33] Panova G.G., Chernousov I.N., et al. Scientific basis for large year-round yields of high-quality crop products under artificial lighting. *Russian Agricultural Sciences*, 2015, **41**, P. 335–339.
[34] Beaucage G., Ulibarri T.A., Black E.P., Schaefer D.W. In Mark J., et al. (eds) *Multiple Size Scale Structures in Silica–Siloxane Composites Studied by Small-Angle Scattering*. American Chemical Society, Washington, 1995.
[35] Štěpánek M., Matějíček P, et al. Polyelectrolyte–Surfactant Complexes Formed by Poly[3,5-bis(trimethylammoniummethyl)4-hydroxystyrene iodide]-block-poly(ethylene oxide) and Sodium Dodecyl Sulfate in Aqueous Solutions. *Langmuir*, 2011, **27** (9), P. 5275–5281.
[36] Khamova T.V., Kopitsa G.P., et al. The Structure and Properties of TiO_2 Nanopowders_for Use in Agricultural Technologies. *Biointerface Research in Applied Chemistry*, 2021, 11 (4), P. 12285–12300.
[37] Guinier A., Fournet G. *Small-angle scattering of X-rays*. John Wiley and Sons, Inc, New York, 1955.
[38] Oh C., Sorensen C.M. The Effect of Overlap between Monomers on the Determination of Fractal Cluster Morphology. *J. Colloid Interface Sci.*, 1997, **193** (1), P. 17–25.
[39] Porod G. Die Röntgenkleinwinkelstreuung von dichtgepackten kolloiden Systemen. *Kolloid-Zeitschrift*, 1952, **125**, P. 51–57.
[40] Bale H.D., Schmidt P.W. Small-Angle X-Ray-Scattering Investigation of Submicroscopic Porosity with Fractal Properties. *Phys. Rev. Lett.*, 1984, **53**, 596.
[41] Teixeira J. In: Stanley HE, Ostrowsky N. (eds) Experimental methods for studying fractal aggregates. Springer, Dordrecht, 1986.
[42] Beaucage G. Approximations Leading to a Unified Exponential / Power-Law Approach to Small-Angle Scattering. *J. Appl. Crystallogr.*, 1995, **28**, P. 717–728.

Submitted 18 May 2022; revised 20 May 2022; accepted 30 July 2022

Information about the authors:

Tamara V. Khamova – Institute of Silicate Chemistry of Russian Academy of Sciences, emb. Makarova, 2, St. Petersburg, 199034, Russia; ORCID 0000-0003-4302-3520; tamarakhamova@gmail.com

Olga A. Shilova – Institute of Silicate Chemistry of Russian Academy of Sciences, emb. Makarova, 2, St. Petersburg, 199034, Russia; ORCID 0000-0002-3856-9054; olgashilova@bk.ru

Yulia E. Gorshkova – Joint Institute for Nuclear Research, St. Joliot-Curie, 6, Dubna, Moscow Region, 141980, Russia; ORCID 0000-0002-5016-1553; Yulia.Gorshkova@jinr.ru

Natalia V. Tsvigun – Institute of Crystallography Federal R&D Center "Crystallography and Photonics" of the Russian Academy of Sciences, Leninsky pr., 59, Moscow, 119333, Russia; ORCID 0000-0003-2028-8067; n_tsvigun@mail.ru

Oleg V. Gerashchenko – Petersburg Nuclear Physics Institute named by B. P. Konstantinov of National Research Centre Kurchatov Institute, Orlova roshcha, 1, Gatchina, Leningrad Region, 188300, Russia; ORCID 0000-0003-1951-4805; gerashchenko_ov@pnpi.nrcki.ru

Alexander E. Baranchikov – Kurnakov Institute of General and Inorganic Chemistry of the Russian Academy of Sciences, Leninsky pr., 31, Moscow, 119991, Russia; ORCID 0000-0002-2378-7446; a.baranchikov@yandex.ru

Olga R. Udalova – Agrophysical Research Institute, Grazhdansky pr., 14, St. Petersburg, 195220, Russia; ORCID 0000-0003-3521-0254; udal59@inbox.ru

Anna S. Zhuravleva – Agrophysical Research Institute, Grazhdansky pr., 14, St. Petersburg, 195220, Russia; ORCID 0000-0002-6367-0728; zhuravlan@gmail.com

Gaiane G. Panova – Agrophysical Research Institute, Grazhdansky pr., 14, St. Petersburg, 195220, Russia; ORCID 0000-0002-1132-9915; gaiane@inbox.ru

Gennady P. Kopitsa – Institute of Silicate Chemistry of Russian Academy of Sciences, emb. Makarova, 2, St. Petersburg, 199034, Russia; Petersburg Nuclear Physics Institute named by B. P. Konstantinov of National Research Centre Kurchatov Institute, Orlova roshcha, 1, Gatchina, Leningrad Region, 188300, Russia; ORCID 0000-0002-0525-2480; kopitsa_gp@pnpi.nrcki.ru

Conflict of interest: the authors declare no conflict of interest.

NANOSYSTEMS:
PHYSICS, CHEMISTRY, MATHEMATICS

Mariyal S.R., Nedunchezhian G., et al. *Nanosystems: Phys. Chem. Math.*, 2022, **13** (4), 430–437.
http://nanojournal.ifmo.ru
DOI 10.17586/2220-8054-2022-13-4-430-437

Original article

Photocatalytic activity of Hibiscus leaf extract mediated ZnO nanoparticles by hydrothermal method

S. Roselin Mariyal[1], G. Nedunchezhian[3], D. Benny Anburaj[1], S. Joshua Gnanamuthu[2]

[1]P. G. and Research Department of Physics, D.G. Govt Arts College (Affiliated to Bharathidasan University), Mayiladuthurai, India

[2]P. G. and Research Department of Physics, TBML College (Affiliated to Bharathidasan University), Porayar, India

[3]P. G. and Research Department of Physics Thiru. Vi. Ka. Govt Arts College (Affiliated to Bharathidasan University), Thiruvarur, India

Corresponding author: S. Joshua Gnanamuthu, joshuagnanamuthu@gmail.com

ABSTRACT *Hibiscus* leaf extract mediated ZnO nanoparticles have been prepared through a hydrothermal method and the effects of extract doping on the structural, optical and electronic properties of ZnO NPs were studied. The photocatalytic oxidation of methylene blue dye under visible light irradiation was used to determine the photocatalytic performance of the prepared nanoparticles. The extracted ZnO nanoparticles (R_3) exhibited the lowest band gap and the highest photocatalytic activity for the methylene blue dye. The photocatalytic performance of the (R_3) prepared ZnO nanoparticles was stable after the nanoparticles were reused five times for the oxidation of methylene blue dye.

KEYWORDS Photocatalysis, hydrothermal method

FOR CITATION Mariyal S.R., Nedunchezhian G., Anburaj D.B., Gnanamuthu S.J. Photocatalytic activity of Hibiscus leaf extract mediated ZnO nanoparticles by hydrothermal method. *Nanosystems: Phys. Chem. Math.*, 2022, **13** (4), 430–437.

1. Introduction

Synthetic dyes used in the textile and dye industries account for a large proportion of pollutants in wastewater. Most of the organic dyes used are difficult to degrade, resulting in irreversible damage to the environment [1]. Although many efficient approaches have been applied to manage this problem, including membrane separation, adsorption, coagulation and microbial degradation [2], these methods have many disadvantages, such as generation of secondary pollution, refractory degradation products and high costs, all of which lead to great limitation in practical application [3–5]. Recently, photocatalytic degradation of organic dyes using semiconductors has attracted great attention [6]. This refers to the process in which organic compounds are gradually oxidized into inorganic compounds or even H_2O and CO_2 under the synergistic effects of light and photocatalysis.

ZnO is one of the most suitable catalysts in many industries given its inexpensive, non-toxic, efficient and anti-corrosion properties [7]. Nevertheless, it still has some disadvantages with respect to photocatalysis. For example, it has a narrow response range, low quantum efficiency, and its photogenerated electron-hole pairs are easy to recombine. The photocatalytic performance can be greatly affected by the particle size, morphology and concentration [8, 9]. As such, it is possible to modify these ZnO properties to enhance its photocatalytic efficiency. Doping ZnO with rare-earth ions is an attractive strategy to improve its photocatalytic activity by modifying its surface morphology [10, 11].

ZnO NPs can be synthesized by various chemical and physical routes including the hydrothermal method, the sol-gel method, the laser ablation method, the sonochemical technique, the mechanochemical method and the microwave technique [10–14]. However, some of these methods require high pressure and high temperature, while others require inert atmosphere and toxic chemicals [15]. In addition, these routes include complex and expensive synthesis and purification processes making them less preferable.

Recently, a biological synthesis of ZnO NPs via micro-organisms and plant extracts has been developed as an alternative to chemical and physical routes due to its cost effectiveness, simple handling, nontoxicity and eco-friendly nature [16, 17]. Therefore, in this work, we study the effects of different concentrations of the extract of the *Hibiscus sabdariffa* leaves in the green synthesis of ZnO NPs, as well as the characterization of the obtained material and its application in the photocatalytic degradation of methylene blue (MB).

2. Experimental details

2.1. Synthesis of ZnO nanoparticles

Hibiscus leaves were collected from College campus, (TBML College is located at: Porayar, Tranquebar (Tk), Nagapattinam (Dt), Tamilnadu, Porayar, Tamil Nadu, S. India Latitude: 11.0268187, Longitude: 79.8327422) washed and cut into pieces. It was boiled in distilled water for around an hour to get brown coloured leaf extract. The extract was filtered and preserved in the refrigerator. For the synthesis of zinc nanoparticles, 25 ml of leaf extracts was taken into a 250 ml beaker and boiled the extracts for 15 min at 60 – 80 °C using thermal control magnetic stirrer. 5 g of zinc nitrate was added to the solution when solution reached the temperature 60 °C. The mixture was then boiled until it reduced the Zn^{2+} ions and produced deep yellow coloured paste. Then the yellow paste was taken in a ceramic crucible and heated in furnace at four different temperatures 300, 400, 500 and 600 °C for 2 h. After cooling the crucible a light yellow coloured powder was obtained and this was carefully collected and stored in a zipper packet and used and saved for characterization. Whitish powder of ZnO nanoparticles formed in the crucible was removed from the furnace and crushed into a fine powder by using pestle and mortar.

2.2. Characterization

The materials were characterized and studied by different techniques. X-Ray Diffraction (XRD) was used to understand the crystal structure of the samples. Fourier-Transform Infrared Spectroscopy (FTIR) was used to study the functional groups present in the samples. Scanning Electron Microscopy (SEM) was used to study their morphology. Lastly, Ultra Violet-to-Visible spectroscopy (UV-Vis) for the study of the band gap of the samples, as well as the catalytic activity during the MB degradation.

2.3. Photocatalytic activity

The photocatalytic degradation activity of methylene blue (MB) dye solution was evaluated by the synthesized ZnO NPs. All the experiments were performed in the presence of sun light. Prior to the experiment, a suspension was arranged by adding 10 mg of synthesized ZnO NPs for different temperatures denoted as R_1 for 300 °C, R_2 for 400 °C, R_3 for 500 °C and R_4 for 600 °C. For each samples mixed with 100 ml of methylene blue (MB) dye solution in a 250 ml beaker placed on a magnetic stirrer at sunlight. Later, the mixture solution was kept in the dark for 10 min to set up the adsorption equilibrium. 5 ml reaction mixtures were taken at regular time interval (15 min) and centrifuged the solution for measurement. The absorption spectrum of the suspension mixture was measured periodically using an UV-visible spectrophotometer monitoring its absorption peak around 554 nm. The percentage of dye degradation was calculated using the following formula:

$$\frac{C_0 - C_t}{C_0} \cdot 100\ \%,$$

where C_0 is the initial concentration of methylene blue, and C_t is the concentration of the dye at different time intervals.

3. Results and discussion

3.1. XRD analysis of ZnO nanoparticles

Figure 1 shows the XRD patterns of synthesized ZnO NPs. It reflects that all the diffraction peaks of ZnO NPs match with the standard Zn ONPs data. The X-ray diffraction patterns of the green synthesis NPs show different diffraction peaks at the 2θ values of 32.11, 34.76, 36.59, 47.85, 56.91 and 63.16 °; indexed to the (100), (002), (101), (102), (110) and (103) planes, respectively. These correspond to the hexagonal structure of the Wurtzite crystalline phase that is characteristic for ZnO NPs (JCPDS: 36-1451). For the diffraction pattern of the R_3 sample, rigid and narrow diffraction peaks are observed, indicating that it has a good crystalline structure. However, in the diffraction patterns of the samples R_1, R_2 and R_4 a decrease in the intensity and a widening of the diffraction peaks are observed, which is attributed to the decrease in the size of the crystals.

The crystal size can be calculated using the Debye–Scherrer formula [18]:

$$D = \frac{K\lambda}{\beta \cos\theta},$$

where D is the average size of the crystals, K is a dimensionless value (it is a constant approximately equal to 0.9), λ is the X-ray wavelength, β is the full width at half-maximum peak intensity (FWHM), and θ is the Bragg angle. The sizes of the crystals calculated from the XRD diffractograms were 38.33, 36.24, 28.01 and 32.12 nm for R_1, R_2, R_3 and R_4, respectively. These results indicate that the annealing temperature strongly influenced the crystallinity and the size of the crystals.

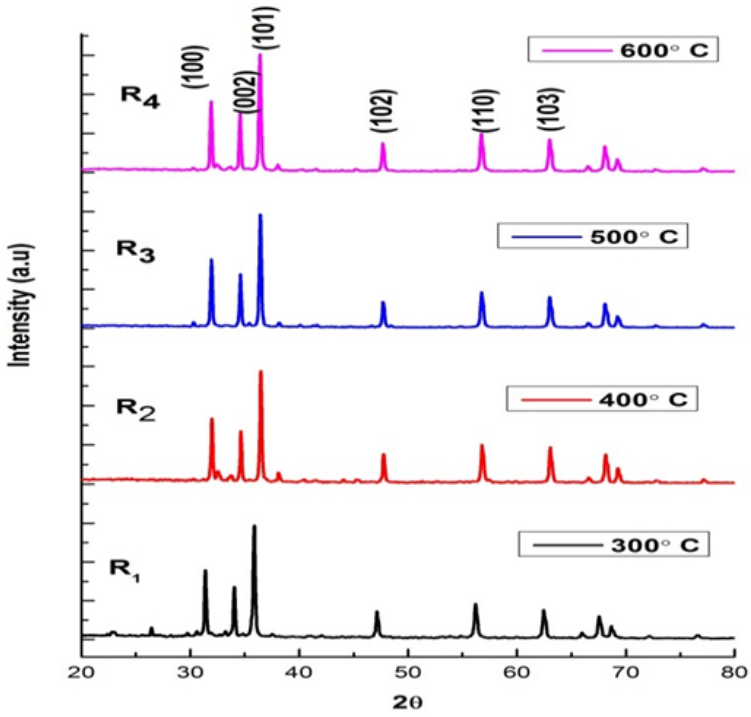

FIG. 1. XRD patterns of synthesized ZnO NPs

3.2. FTIR analysis

FTIR is an important tool to understand the functional groups and the relation between metal particles and biomolecules. The FTIR spectrums of *Hibiscus* leaf extract and synthesized ZnO NPs are shown in Fig. 2. The FTIR absorbance at 3408 cm^{-1} reveals the presence of O–H stretching vibration, a peak at 2927 cm^{-1} is due to C–H stretching vibration. It reveals that there are vibrational wavenumbers 865, 1105, 1495, 2926 and 3445 cm^{-1}, corresponding to CH, C–OH, CH_2–OCH_3/CH_2–CH_3 and OH functional groups which are presented in the *hibiscus* extract in ZnO nanoparticles. The peak at 1614 cm^{-1} results from the stretching bands of C=O functional groups. Metal oxides generally give absorption in fingerprint region, i.e. below 1000 cm^{-1} arising from inter-atomic vibrations. The FTIR spectrum of the main absorption band is due to Zn–O stretching of ZnO in the range of 552 – 417 cm^{-1}. From the FTIR result the soluble elements presented in *hibiscus* extract could have acted as capping agent preventing the aggregate of nanoparticles in solution and laying a relevant role in their extracellular synthesis and shaping [19]. In addition to the absorption bands of the biomolecules used as reduction and stabilization (capping agents), the absorption peak at 440 cm^{-1} indicates the presence of ZnO NPs.

3.3. Morphological studies

The morphological structure and size of the ZnO NPs are analyzed by scanning electron microscopy (SEM). The SEM image of prepared ZnO NPs is shown in Fig. 3(a–d). The nanoparticles are mostly spherical in shape. SEM image of ZnO reveals that the sizes of the spherical nanoparticles are in the range of 20 – 50 nm.

The EDX spectrum of ZnO NPs shows peaks corresponding to Zinc and Oxygen. The atomic percentages of ZnO NPs are found to be 52.69 and 47.31 % respectively as shown in Fig. 4.

3.4. Diffuse reflectance spectroscopy

Diffuse Reflectance Spectrum (DRS) of the synthesized ZnO nanoparticles were recorded at room temperature in the wavelength range of 190 – 900 nm. Kubelka–Munk (K–M (or) $F(R)$) formula [19] was used to determine the band gap of the materials. $F(R)$ was derived from the relation $F(R) = (1-R)^2/2R$, where R is the reflection of the particles which is proportional to the extinction coefficient (α). Modified Kubelka–Munk formula can be derived by multiplying $F(R)$ by $h\nu$ where h is the Planck constant ($6.626 \cdot 10^{34}$ Joules) and ν is the light frequency (s^{-1}) associated with electronic transition. Plotting the value of $(F(R)h\nu)^2$ as a function of $h\nu$ one can find the direct band gap of ZnO nanoparticles. In the present work optical band gap of ZnO nanoparticles prepared from *Hibiscus* extract R_1, R_2, R_3 and R_4 is 3.24, 3.21, 3.28 and 3.22 eV respectively (Fig. 5(a, b)).

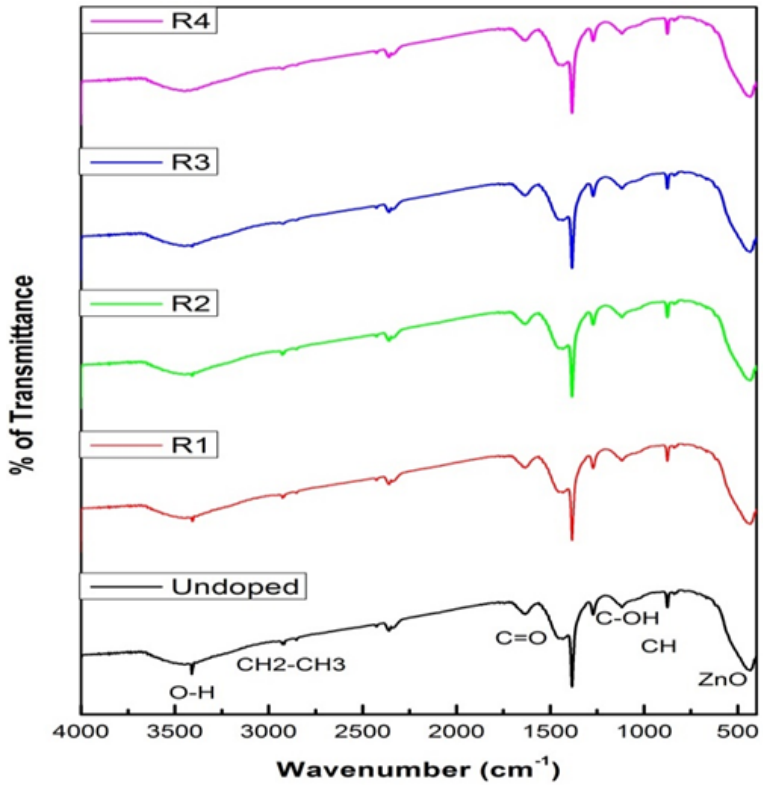

FIG. 2. FTIR spectrum of leaf extracted ZnO

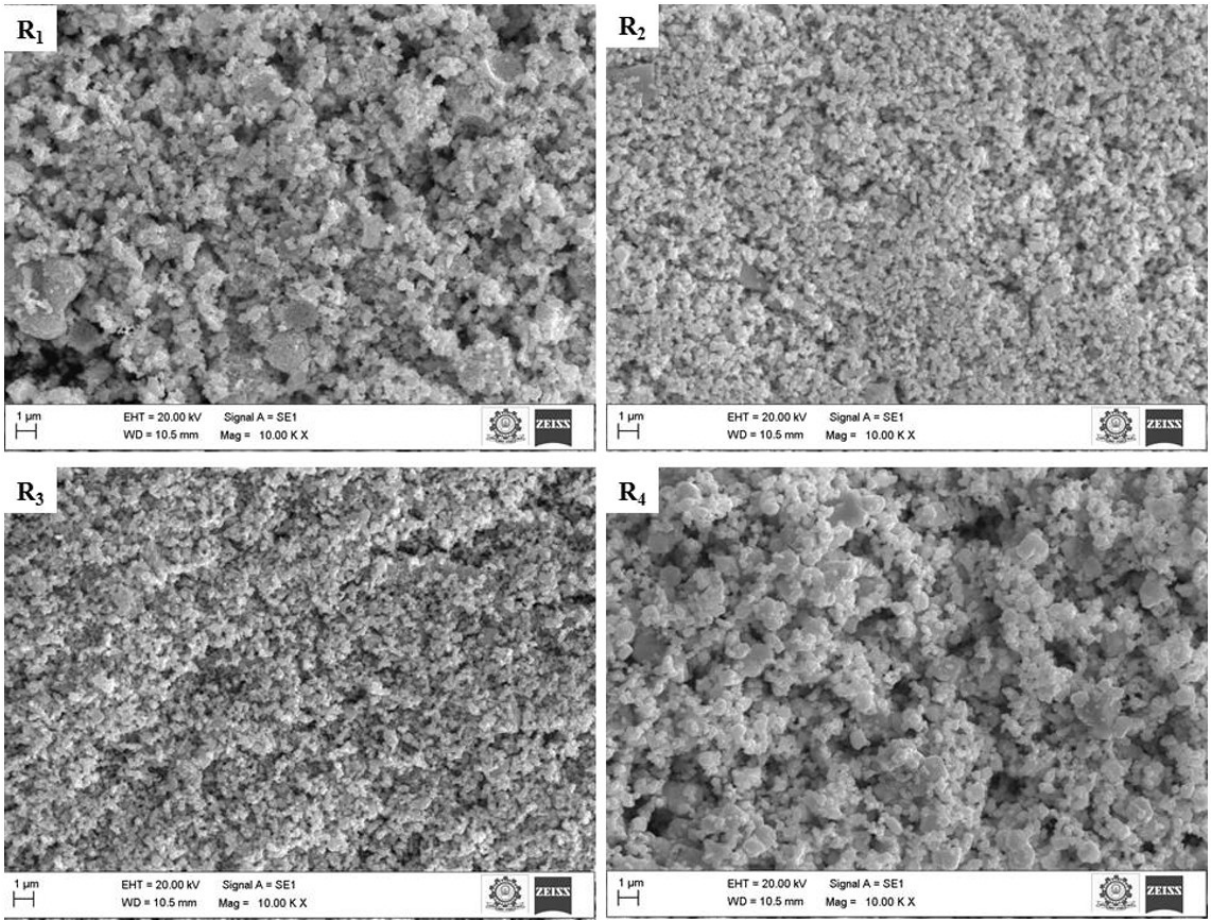

FIG. 3. The SEM image of prepared ZnO NPs

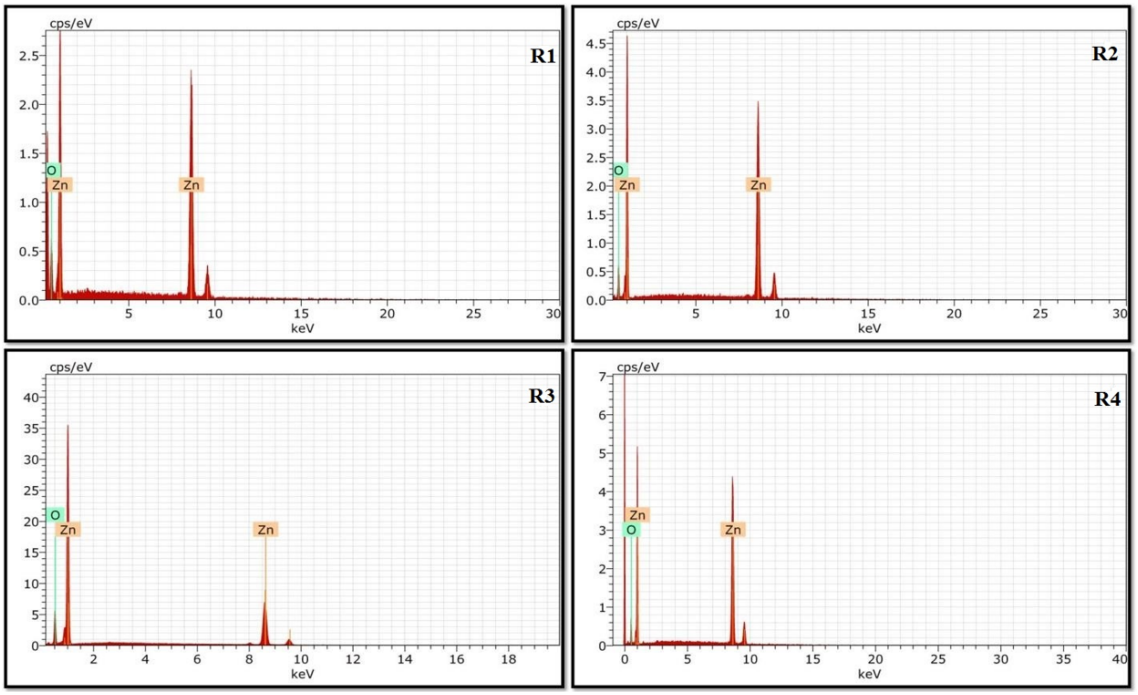

FIG. 4. The EDAX analysis of prepared ZnO NPs

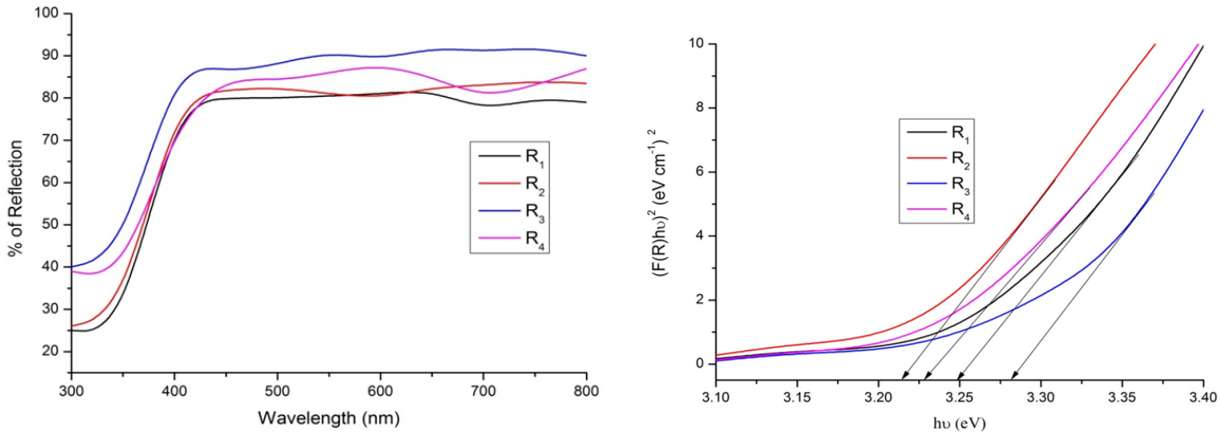

(a) (b)

FIG. 5. DRS of ZnO (a), TAUC plot of *hibiscus* leaf mediated ZnO NPs (b)

3.5. Photocatalytic activity

The photocatalytic dye degradation process 0.5 g of synthesized ZnO nanoparticles was added with 5 ppm of 100 ml of Methylene Blue (MB) solution. Initially MB dye absorption spectrum was recorded in the 190 – 1100 nm range using Shimadzu, UV-2600 spectrophotometer. Further, this solution was continuously stirred for 30 min to analyse adsorption and desorption equilibrium between catalyst and MB under dark condition. The stable aqueous dye solution was stirred and exposed under the sun light irradiation for 30 min. Then the experiment was carried out in the interval of 30 min and the UV-Vis absorption spectrum was recorded. Thus, the experiment was carried out for the total period of 120 min (one cycle) and the absorption spectrum was recorded at the interval of every 30 min. At the end of each cycle the dye solution was centrifuged to separate the ZnO nanoparticles and they were used without further treatment for next cycles.

ZnO nanoparticles synthesized from the Hibiscus extract solution of various annealed temperature (R_1, R_2, R_3 and R_4) were used in the degradation experiment of MB and the results of ZnO nanoparticles in the degradation of MB dye with respect to time (0 to 120 min) are shown in Fig. 6. The characteristic absorption peak of MB at 554 nm was chosen to monitor the photocatalytic degradation process. The degradation of MB dye is 57, 68, 94 and 73 % due to the ZnO nanoparticles prepared at R_1, R_2, R_3 and R_4 respectively as shown in Fig. 6(a–d). The degradation activity of ZnO

catalyst obtained from the precursor solution R_3 is relatively high when compared to the degradation activity of ZnO catalyst prepared from the other samples. It is shown in Fig. 7.

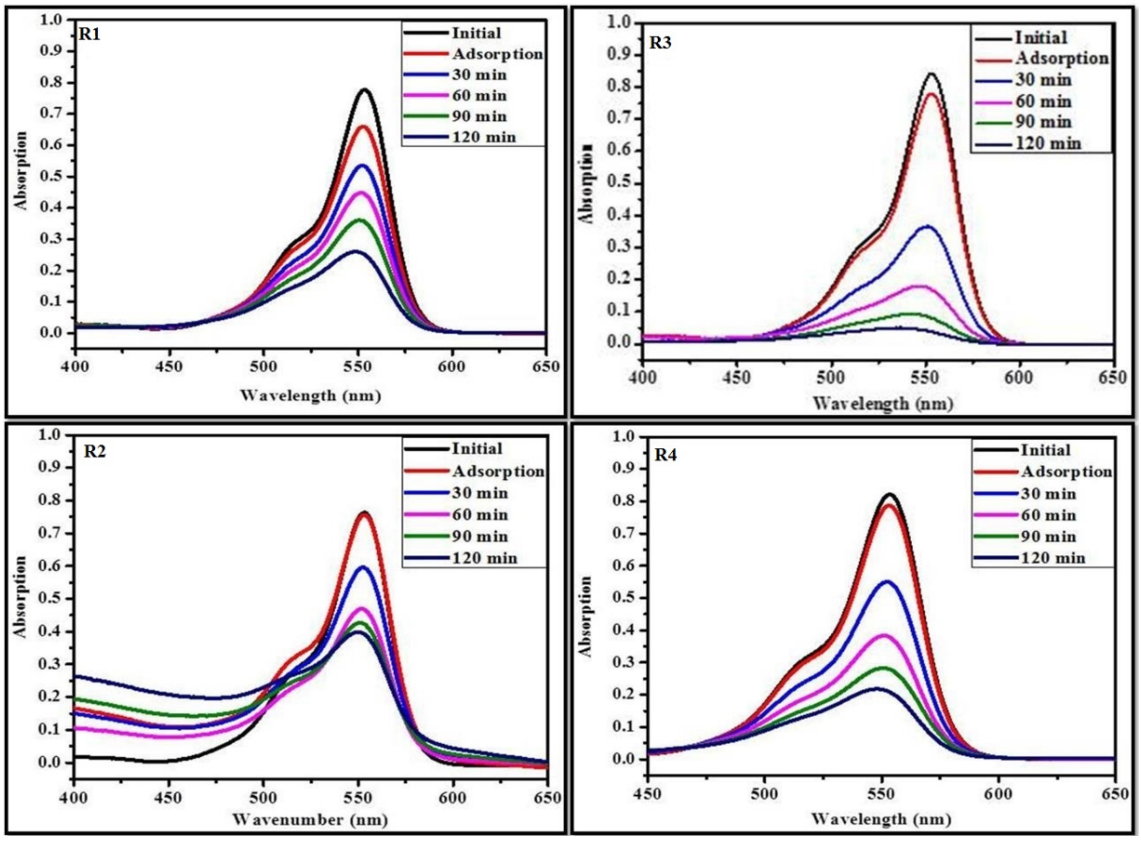

FIG. 6. Degradation effect of *hibiscus* leaf mediated ZnO NPs

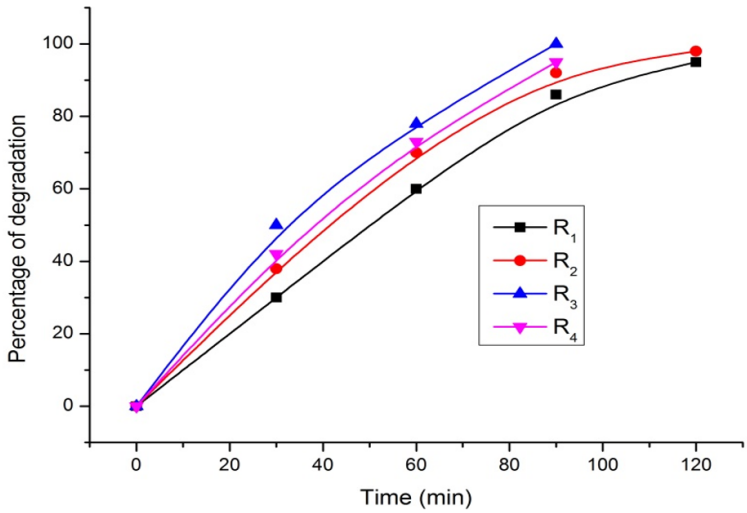

FIG. 7. Degradation Percentage of *hibiscus* leaf mediated ZnO NPs

The experiments prove that *hibiscus* leaf extract mediated ZnO improves the photocatalytic ability. In heterogeneous photocatalysis, when catalyst is irradiated with light with the photon energy greater than or equal to the band gap of catalyst, an electron from valence band jumps to the conduction band leaving a hole behind. Valence band hole reacts with water molecules to give $^{-}$OH radicals and conduction band electron combines with adsorbed oxygen to give superoxide radical anion which further results in the formation of $^{-}$OH radicals. The $^{-}$OH radical is a strong oxidizing agent. It oxidizes dye molecules. This leads to its complete mineralization.

Temperature is one of the major factors that significantly influence the shape, size, stability, and yield of the NPs synthesized via a green route. Reaction temperature increase improves the reaction rate and high-temperature lead to increase of the nucleation rate. At high temperature, the NPs size was decreased. The underlying mechanism for green synthesis of ZnO NPs has not been fully understood as yet. Free amino and carboxylic groups of proteins, alkaloids, phenolics or avonoids, presented in the plant extract, may bind to the surface of zinc (Zn^{2+}) and trigger the formation of ZnO NPs. In heterogeneous photocatalysis, when catalyst is irradiated with light of photon energy greater than or equal to the band gap of catalyst, an electron from valence band jumps to the conduction band leaving a hole behind. Valence band hole reacts with water molecules to give OH radicals and conduction band electron combines with adsorbed oxygen to give superoxide radical anion which further results in the formation of OH radicals. The OH radical is a strong oxidizing agent. It oxidizes dye molecules. This leads to its complete mineralization

4. Conclusions

Synthesis of nanoparticles by using different parts of plants has been encouraged the designing of simple, green, cost and time effective approaches by minimizing the use of chemicals and solvents. Present study result highlights the effective use of leaf extract of Hibiscus rosasinesis towards synthesis of zinc oxide nanoparticles and their characterisation through XRD, SEM, UV-vis and FTIR study. The spherical structure and size (< 50 nm) of the synthesized nano ZnO is confirmed by SEM study. Moreover, XRD studies suggest that nano ZnO is absolutely crystalline in nature. The synthesized ZnO NPs (R_3) can be effectively used as an adsorbent which can remove approximately 94 % of methylene blue (MB) from aqueous solution. Therefore, it can be suggested that green synthesis of nano ZnO could be an alternative adsorbent for removal of dye from aqueous medium. Various efforts are being made to explore new materials as well as increasing the efficiency of existing bio adsorbents and designing of hybrid technologies targeting multicomponent bio adsorption. In future, bio adsorbents are poised to witness extensive applications at domestic and industrial scale to minimize the menace of environmental pollution. Moreover, the present study needs further field of application in order to explore more concrete information about the efficacy of this particular bio adsorbent.

References

[1] Vacchi F.I., Vendemiatti J.A.d.S., et al. Quantifying the contribution of dyes to the mutagenicity of waters under the influence of textile activities. *Sci. Total Environ.*, 2017, **601–602**, P. 230–236.

[2] Ghaffar A., Zhang L., Zhu X., Chen B. Porous PVdF/GO Nanofibrous Membranes for Selective Separation and Recycling of Charged Organic Dyes from Water. *Environ. Sci. Technol.*, 2018, **52**, P. 24265–4274.

[3] Gaya U.I., Abdullah A.H. Heterogeneous photocatalytic degradation of organic contaminants over titanium dioxide: A review of fundamentals, progress and problems. *J. Photochem. Photobiol. C*, 2008, **9**, P. 21–12.

[4] Janoš P. Sorption of Basic Dyes onto Iron Humate. *Environ. Sci. Technol.*, 2003, **37**, P. 5792–5798.

[5] Pal B., Kaur R., Grover I.S. Superior adsorption and photodegradation of eriochrome black-T dye by Fe^{3+} and Pt^{4+} impregnated TiO_2 nanostructures of different shapes. *J. Ind. Eng. Chem. (Amsterdam, Neth.)*, 2016, **33**, P. 2178–184.

[6] Santhosh C., Velmurugan V., et al. Role of nanomaterials in water treatment applications: A review. *Chem. Eng. J.*, 2016, **306**, P. 21116–1137.

[7] Shaari N., Tan S., Mohamed A. Synthesis and characterization of CNT/Ce-TiO2 nanocomposite for phenol degradation. *J. Rare Earths*, 2012, **30**, P. 2651–658.

[8] Pardeshi S.K., Patil A.B. Effect of morphology and crystallite size on solar photocatalytic activity of zinc oxide synthesized by solution free mechanochemical method. *J. Mol. Catal. A: Chem.*, 2009, **308**, P. 232–240.

[9] Ahmad M., Ahmed E., et al. Enhanced photocatalytic activity of Ce-doped ZnO nanopowders synthesized by combustion method. *J. Rare Earths*, 2015, **33**, P. 2255–2262.

[10] Cerrato E., Gionco C., Paganini M.C., Giamello E. Photoactivity properties of ZnO doped with cerium ions: an EPR study. *J. Phys.: Condens. Matter*, 2017, **29**, 444001.

[11] Samadi M., Zirak M., et al. Recent progress on doped ZnO nanostructures for visible-light photocatalysis. *Thin Solid Films*, 2016, **605**, P. 2–19.

[12] Maryanti E., Damayanti D., Gustian I., Yudha S.S. Synthesis of ZnO nanoparticles by hydrothermal method in aqueous rinds extracts of Sapindus rarak DC. *Mater. Lett.*, 2014, **118**, P. 296–298.

[13] Zak A.K., Abrishami M.E., et al. Effects of annealing temperature on some structural and optical properties of ZnO nanoparticles prepared by a modified sol-gel combustion method. *Ceram. Int.*, 2011, **37**, P. 2393–2398.

[14] Jamal R.K., Hameed M.A., Adem K.A. Optical properties of nanostructured ZnO prepared by a pulsed laser deposition technique. *Mater. Lett.*, 2014, **132**, P. 231–233.

[15] Zak A.K., Majid W.H.A., et al. Sonochemical synthesis of hierarchical ZnO nanostructures. *Ultrason. Sonochem.*, 2013, **20**, P. 2395–2400.

[16] Ao W., Li J., et al. Mechanochemical synthesis of zinc oxide nanocrystalline. *Powder Technol.*, 2006, **168**, P. 2148–2151.

[17] Salavati-Niasari M., Davar F., Khansari A. Nanospherical and nanobundles of ZnO: Synthesis and characterization. *J. Alloys Compd.*, 2011, **509**, P. 261–265.

[18] Porkalai V., Sathya B., Benny Anburaj D., Nedunchezhian G. Effect of calcinations on the structural and morphological properties of Ag and In co doped ZnO nanoparticles. *J. Mater. Sci.: Mater.Electron.*, 2017, **28**, P. 22521–22528.

[19] Stone F.S. UV-Visible Diffuse Reflectance Spectroscopy Applied to Bulk and Surface Properties of Oxides and Related Solids. In Bonnelle, J.P., Delmon, B., Derouane, E. (eds) *Surface Properties and Catalysis by Non-Metals*, NATO ASI Series, Springer, Dordrecht, 1983, **105**, P. 2237–2272.

Submitted 17 June 2021; revised 29 December 2021; accepted 4 July 2022

Information about the authors:

S. Roselin Mariyal – P.G. and Research Department of Physics, D.G. Govt Arts College (Affiliated to Bharathidasan University), Mayiladuthurai, India

G. Nedunchezhian – P.G. and Research Department of Physics Thiru. Vi. Ka. Govt Arts College (Affiliated to Bharathidasan University), Thiruvarur, India

D. Benny Anburaj – P.G. and Research Department of Physics, D.G. Govt Arts College (Affiliated to Bharathidasan University), Mayiladuthurai, India

S. Joshua Gnanamuthu – P.G. and Research Department of Physics, TBML College (Affiliated to Bharathidasan University), Porayar, India; joshuagnanamuthu@gmail.com

Conflict of interest: the authors declare no conflict of interest.

NANOSYSTEMS:
PHYSICS, CHEMISTRY, MATHEMATICS

Original article

Kapuganti V. Divya Lakshmi, et al. *Nanosystems: Phys. Chem. Math.*, 2022, **13** (4), 438–444.
http://nanojournal.ifmo.ru
DOI 10.17586/2220-8054-2022-13-4-438-444

Enhancement of photocatalytic and antibacterial activity performance of Mn–S co-doped TiO_2 nanocatalyst under visible light

Kapuganti V. Divya Lakshmi[1,2], Tirukkovalluri Siva Rao[2], Gorli Divya[2]

[1]Sri Satya Sai University for Human Excellence, Kalaburagi, Karnataka, India

[2]Department of Inorganic and Analytical Chemistry, Andhra University, Visakhapatnam 530003, India

Corresponding author: Tirukkovalluri Siva Rao, sivaraotvalluri.16@gmail.com

ABSTRACT This paper aims to explore the photocatalytic and antibacterial activity of Mn and S co-doped TiO_2 nanomaterial synthesized by the sol-gel method. Various instrumental techniques, XRD, BET, UV-Vis-DRS, TEM, XPS, SEM, FT-IR, were used to classify the catalyst samples. The characterization results show that the surface area is large, the particle size is small, band gap energy is low, the crystallite size is small, and the surface morphology is smooth. The efficiency of photocatalytic and antibacterial activity was evaluated by the degradation of Eosin yellow (EOY) and *Bacillus subtilis* (MTCC-441), respectively. The complete degradation of EOY was achieved in 70 min.

KEYWORDS TiO_2, Mn and S, sol-gel method, Eosin yellow, photocatalytic activity, antibacterial activity

FOR CITATION Kapuganti V. Divya Lakshmi, Tirukkovalluri Siva Rao, Gorli Divya Enhancement of photocatalytic and antibacterial activity performance of Mn–S co-doped TiO_2 nanocatalyst under visible light. *Nanosystems: Phys. Chem. Math.*, 2022, **13** (4), 438–444.

1. Introduction

Water is the largest part of vital substances for all existence on earth. It is known as a universal solvent, and it easily dissolves other substances. The aquatic environment can contain a wide range of micro pollutants, including pesticides, pharmaceuticals, and industrial compounds due to waste water effluent and agricultural runoff [1], mainly with reference to drinking water, which tends to become a limiting factor for the quality of life on earth. 25 % of pollution is caused by industries. They discharge hazardous materials to contaminate surface water and ground water. Toxic compounds enter into the water and reduce the quality [2, 3]. Dyes are used in many industries like paper, leather, textiles, plastic, ceramic, cosmetics, ink, food processing, etc. Wastewater offers eminent resistance to their biodegradation due to the presence of these heat and light-stable dyes, thus upsetting aquatic life [4]. While Eosin yellow (EOY) is commonly used for staining, it is regarded as a carcinogen. The current research strives to remove textile dyes and conduct an antibacterial study against *Bacillus subtilis* (MTCC-441), a gram-positive bacteria which causes pneumonia and septicaemia [5, 6]. The latest research focuses on the decontamination of polluted water and the elimination of dyes and pathogenic bacteria. TiO_2 is a semiconductor material widely used in photocatalytic reactions due to its non-toxicity, photo stability, and reusability [7–9]. The main drawback of TiO_2 is its wide bandgap energy (3.2 eV) and high recombination rate of photogenerated charge carriers, resulting in low quantum performance [10, 11]. As a result, changes to titanium have received a lot of attention, and several methods for increasing visible light photoactivity by doping with different metal and non-metal elements have been investigated [12, 13]. When compared to single-doped TiO_2, previous studies show that co-doped TiO_2 with metal and non-metal elements can enhance photocatalytic efficiency. Manganese is desired over all other transition metals because the t2g orbital of d is very close to the valence band, which causes the absorption to migrate to the visible region [14]. The photocatalytic activity of TiO_2 under visible light has been improved using a variety of non-metal materials, and the benefit of non-metal doping is that it reduces recombination centres. Sulfur is preferred since it replaces certain Ti^{4+} ions in the TiO_2 lattice [15, 16]. As a result, we chose Mn and S as dopants for the sol-gel method of synthesis of co-doped TiO_2. The main advantage of this method for preparing catalytic material is that it allows one to ensure excellent control of the product's properties through a variety of parameters such as ageing, homogeneity, grain size control, drying, and heat treatment [17].

2. Experiment

2.1. Materials

All of the chemicals used in the synthesis process were reagent grade, and the solutions were made with double distilled water. N-Butyl tetra ortho titanate ($Ti(OBu)_4$), Manganese nitrate $[Mn(NO_3)_2]\cdot 6H_2O$ and Thiourea were obtained from E-Merck (Germany) and used as Titanium, Manganese, and Sulfur precursors for the preparation of undoped TiO_2 and co-doped TiO_2 catalysts.

2.2. Preparation of Mn and S co-doped TiO_2 nano materials

The sol-gel method was used to make Manganese and Sulfur co-doped (1.0 Wt% Mn – 0.25 Wt% S) nano Titania. In this procedure, 20 mL of n-Butyl ortho titanate was added to ethanol and acidified with 3.2 mL of nitric acid in a beaker (solution-I) and stirred for 15 min. Manganese Nitrate and Thiourea were prepared by dissolving precursors of Mn and S in ethanol and adding deionized water (7.2 mL) to another beaker. A colloidal suspension formed after the complete addition of solution (II) was stirred for 90 min and aged for 48 h. The gel was dried at 70 °C in an oven, then ground and calcined in a muffle furnace at 450 °C for about 5 h. Finally, it was allowed to cool before being ground into a uniform powder. The same technique was used to make undoped TiO_2 but without the addition of sulfur and Manganese precursor.

2.3. Characterization of catalyst

Powder X-ray diffraction (XRD) spectra were taken (model: Ultima IV Rigaku) using anode Cu–WL 1 ($= 1.5406$ nm) radiation with a nickel filter to determine the crystalline structure of the photocatalyst. The applied current and voltage were 40 mA and 40 kV, respectively. The average crystallite size of anatase was determined according to the Scherrer equation using (FWHM) data of the selected peak. The size and shape of the nanoparticles were recorded with TEM measurements using JEOL/JEM 2100, operated at 200 kV. The morphology and elemental composition of the catalyst were characterized using scanning electron microscope (SEM) (ZEISS-SUPRA 55 VP) equipped with an energy dispersive X-ray (EDS) spectrophotometer and operated at 20 kV. The surface area and porosity measurements were carried out with a micrometrics Gemini VII surface area analyzer. The Nitrogen adsorption/desorption isotherms were recorded 2 – 3 times to obtain reproducible results and reported by BJH surface/volume mesopore analysis. The micropore volume was calculated using the Frenkel–Halsey–Hill isotherm equation. Each sample was degassed at 300 °C for 2 h. FT-IR spectra of the samples were recorded on FT-IR spectrometer (Nicolet Avatar 360). The diffuse reflectance spectra (DRS) were recorded with Shimadzu 3600 UV-Visible-NIR Spectrophotometer equipped with an integrating sphere diffuse reflectance accessory, using $BaSO_4$ as reference scatter. Powder samples were loaded into a quartz cell and spectra were recorded in the range of 200 – 900 nm. The extent of EOY degradation was monitored using UV-Vis spectrophotometer (Shimadzu 1601).

2.4. Photocatalytic activity

The photocatalytic performance of the synthesized catalyst Mn–S co-doped (MNS-5) nano titania was evaluated using the degradation of EOY dye under visible light irradiation in a photocatalytic reactor. A high-pressure 400 W (35,000 lm) mercury vapour lamp with UV filter was used as a visible light source (Oriel, 51472). The degradation procedure was carried out in a 150 mL Pyrex glass vessel with vigorous stirring positioned about 20 cm away from the light source, using 100 mL of EOY dye solution of necessary concentration (1 – 10 mgL^{-1}) containing adequate amount of the catalyst. The running water was circulated around the sample container to filter IR radiation to maintain constant solution temperature in a pyrex glass reaction vessel. The solution was stirred in dark for 30 min to attain adsorption-desorption equilibrium of EOY dye on the catalyst surface. After visible light illumination, small aliquots of sample were collected from the reaction mixture using Millipore syringe (0.45 μm) at different intervals of time to observe the change in EOY dye concentration by measuring the absorbance at 516 nm using UV-Visible (Milton Roy Spectronic 1201) Spectrophotometer. For investigation of pH variation during the degradation process, Elico Digital pH metre model 111E, EI was used. Prior to irradiation, the dye solutions' pH was adgusted with 0.1 N NaOH / 0.1 N HCl to achieve the desired pH. The following equation was used to determine the percent of EOY dye degradation (α):

$$\alpha = \frac{A_0 - A_t}{A_0} \cdot 100\ \%,$$

where A_0 represents the initial absorbance of the dye solution prior to degradation and A_t represents the absorbance of the dye solution at time t.

The optimum reaction conditions are attained by varying the reaction parameters, such as dopant concentration, effect of pH, catalyst dosage, and initial dye concentration, and the results are discussed in Sections 4.1 – 4.4.

2.5. Antibacterial activity study

The Agar-well diffusion method was used to study the antibacterial activity of MNS-5 against the Gram-positive bacteria *Bacillus subtilis* (MTCC-441). In a 100 mL conical flask, nutrient agar (High media – India) was dissolved in water and sterilised in an autoclave at 121 °C 15 lbp for 15 min. The media was autoclaved before being poured onto sterilised petri dishes. A sterile cork-borer was used to make the wells. Different concentrations of TiO_2 co-doped (MNS-5) nanoparticles are injected into wells in petri plates (200, 300 and 400 μg/mL). The TiO_2 nanoparticles were dispersed in sterile water and used as a negative control, while the normal antibiotic Chloramphenicol (100 μg/mL) was used as a positive control.

3. Characterizations

The synthesized catalysts was characterized by X-ray diffraction (XRD), X-ray photo electron spectroscopy (XPS), Scanning electron microscopy (SEM), Energy dispersive X-ray Spectroscopy (EDX), Fourier transform infrared spectroscopy (FT-IR), UV-Visible Diffused Reflectance Spectroscopy (UV-Vis-DRS), Transmission electron Microscopy (TEM) and Brunauer–Emmett–Teller (BET). In XRD, all the diffraction peaks represented the anatase phase with a characteristic high intensity peak at $2\theta = 25.50$ and small peaks corresponding to 2θ values at 37.9, 48.4, 54.8, and 62.6 °, which can be indexed as (101), (004), (200), (105), (211) and (204) planes of anatase TiO_2 (JCPDS card no. 21-1272) respectively. The SEM results in agglomeration and particle size can be inferred from this because of the co-doping of Mn and S into TiO_2. The Mn and S contents in MnS-5 are greatly reduced. Their presence was confirmed by EDX analysis. The FT-IR study confirms that Mn and S are substitutionally doped in the TiO_2 lattice by replacing Ti^{4+} ions. The TEM images illustrated that the undoped and co-doped TiO_2 (MnS-5) nanocatalysts are small in size with a spherical shape. The diffused reflectance spectra (DRS) of undoped and co-doped TiO_2 samples are observed to show remarkable decreases in band gap and extension of the absorption edge towards longer wave lengths. The X-ray photo electron spectroscopy (XPS) analysis of MnS-5 revealed the dopant elements such as (Mn, S). This indicates that the dopant elements are incorporated into the TiO_2 lattice. The co-doped samples of MnS-5 have high surface areas of 155.878 m^2/g, pore volumes of 0.204 cm^3/g, and pore diameters of 4.8 nm. This could be because a catalyst with larger surface area stimulates the adsorption of more dye molecules.

The characterization results are reported in the previous article [18].

4. Evaluation of photocatalytic efficiency of catalyst (MNS-5) by degradation of Eosin yellow (EOY)

The effect of reaction parameters such as dopant concentration, pH, catalyst dose, and initial dye concentrations on the photocatalytic degradation of EOY was investigated by varying the desired parameter while keeping the other parameters constant.

4.1. Effect of dopant concentration

Figure 1 illustrates the photocatalytic degradation of the EOY dye (516 nm) by a synthesized catalyst. The co-doped samples showed increased photocatalytic activity compared to undoped TiO_2 under visible light irradiation. The possible reason is that the dopant concentration contributes to a reduced TiO_2 band gap, smaller particle size, and a larger surface area of the catalyst among the different co-doped catalysts. At this dopant concentration, photo generated electron/hole pairs can easily pass to the catalyst surface through Mn, resulting in oxidative species such as $OH\cdot$, $O_2\cdot$, and $HO_2\cdot$.

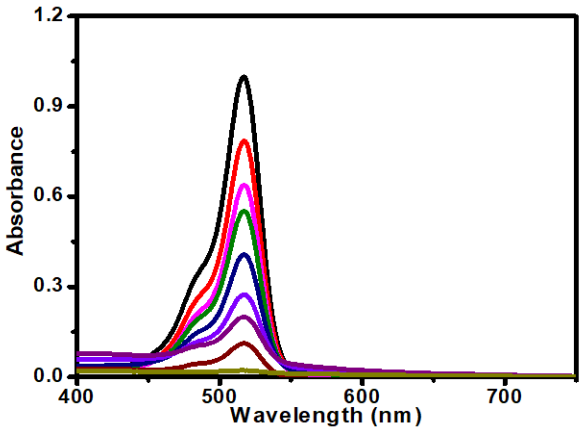

FIG. 1. Effect of dopant concentration on photocatalytic of co-doped Titania for rate of degradation of EOY dye. Here, catalyst dosage 100 mg/L, pH 4 and EOY = 10 mg/L

4.2. Effect of pH

The electrostatic interactions between the catalyst surface dye and charged radicals are dependent on the pH of the solution, pH is a significant variable parameter in the evaluation of photocatalytic dye degradation efficiency of the catalyst in aqueous medium [19]. Fig. 2 depicted the percentage degradation of EOY using the MNS-5 catalyst at various pH values (2, 4, 8 and 10) when exposed to visible light. The percentage of EOY degradation in acidic medium is higher than in basic medium, as shown in the figure. This may be due to a stronger electrostatic interaction between the catalyst's positively charged surface and the negatively charged dye molecules. As the pH is raised to a basic medium, the catalyst surface takes on a -Ve charge and repels the same charged dye molecules electrostatically. In acidic pH medium, the percentage of degradation of EOY was high at pH 4, at which the positive charge (H^+ ions) on TiO_2 surface increases and negatively charged EOY can easily adsorbed on the catalyst surface.

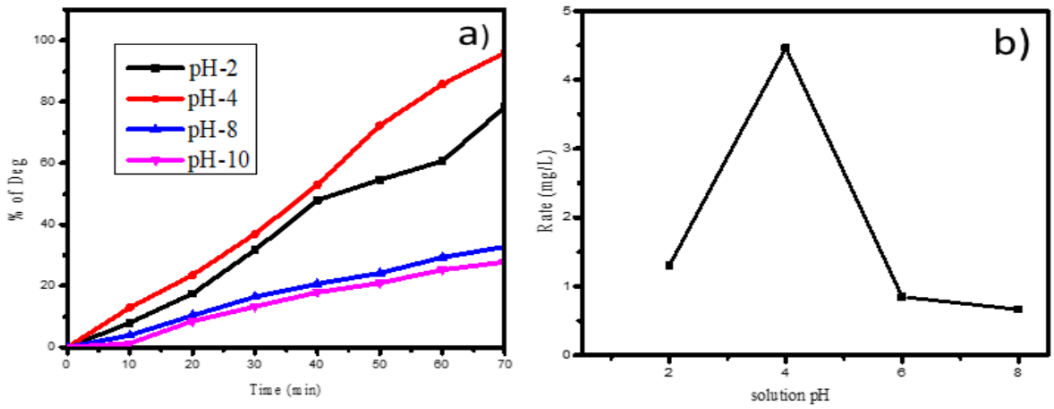

FIG. 2. The effect of pH on the rate of degradation of EOY dye by Mn 2p & S 2p co-doped TiO_2. Here, catalyst dosage 100 mg/L and EOY =10 mg/L

4.3. Effect of catalyst dosage

The effect of catalyst dosage on the degradation of EOY is shown in Fig. 3. The rate of degradation was carried out by varying the catalyst amounts of 0.05, 0.10, 0.15, and 0.20 g added to 100 mL of solution containing 10 mg/L of dye at pH 4. The rate of degradation increases linearly with the increase of catalyst loading up to 0.10 g. Degradation decreases as the catalyst dosage is increased. This may be due to increased turbidity and agglomeration of catalyst particles, which prevent light from penetrating to activate the catalyst particles [20], as well as collisions between active molecules and ground state molecules of co-doped TiO_2 result in catalyst particle deactivation [21]. Hence, the optimum catalyst dosage is 0.10 g.

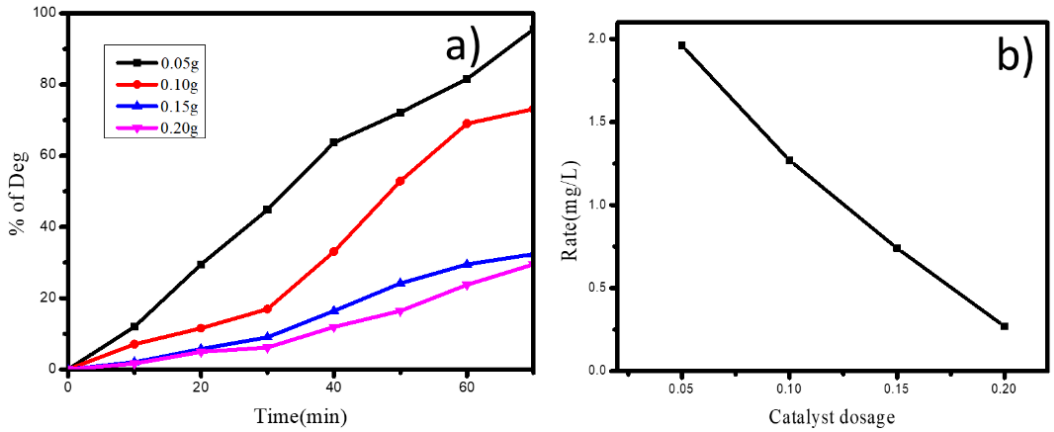

FIG. 3. Effect of catalyst dosage on the degradation of EOY by MNS-5 co-doped TiO_2 here pH = 4 and EOY =10 mg/L

4.4. Effect of initial concentration of dye (EOY)

Experiments were carried out with different concentrations of EOY dye from 5 to 30 mg/L to research the effect of initial dye concentration (EOY) at fixed weight of catalyst dose (10 mg/L) and pH 4, and the graphs were plotted in Fig. 4. These results show that the rate of EOY dye degradation increased by up to 10 mg/L. However, due to the blanket effect, raising the dye concentration causes the catalyst to deactivate, slowing the rate of degradation [22].

5. Antibacterial studies

The antibacterial activity of TiO_2 nano particles was investigated using the Agar-well diffusion method [23] against *Bacillus subtilis* (MTCC-441) and varying concentrations of co-doped TiO_2 (MNS-5) nanoparticles which were placed in different wells in a petri dish with concentrations ranging from 200, 300, 400 μg/mL, and chloromphenicol (control). The activity results (Fig. 5 and Table 1) showed that (400 μg/ml) is the best concentration for co-doped TiO_2 for the zone of inhibition of both bacteria and is also very nearer to the standard values. As a result, the co-doped TiO_2 nanoparticles have higher antibacterial activity. This inhibition could be caused by an e–/h+ that occurs in the valence band of TiO_2 when the catalyst is exposed to visible light. This e–/h+, +ve hole acts as a strong oxidising agent under visible light, destroying the bacterial protein coat and inhibiting the growth of the organism.

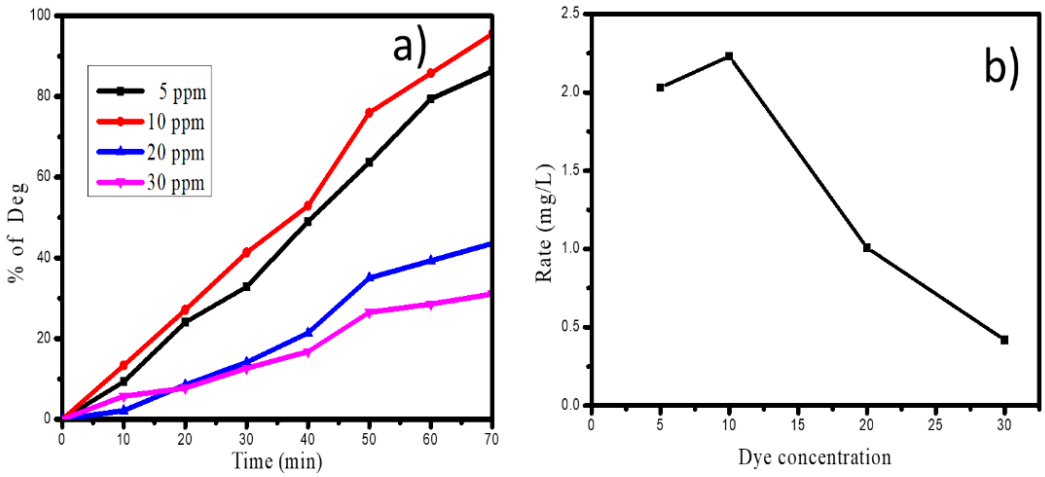

FIG. 4. Effect of initial concentration of the dye on the rate of degradation of EOY dye Here, pH = 4 and catalyst dosage – 100 mg/L

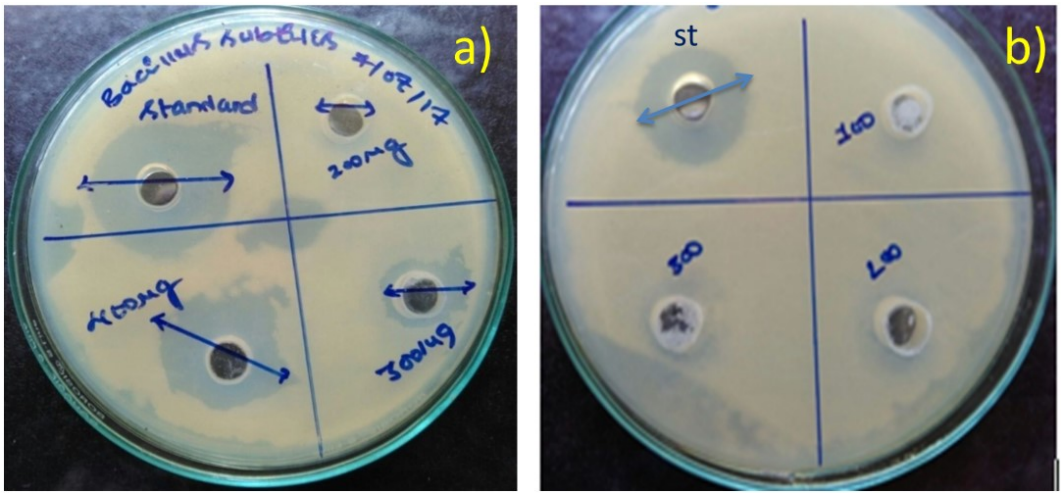

FIG. 5. Zone of inhibition of *Bacillus subtilis* (MTCC-441) (a); undoped TiO_2 (b)

TABLE 1. Agar-well diffusion of co-doped TiO_2 nanoparticles (MNS-5) *Bacillus subtilis* (MTCC-441) and undoped TiO_2

s. no	Catalyst	Organism	Zone of inhibition (mm)			
			200 μg/mL	300 μg/mL	400 μg/mL	Standard (Chloramphenicol) 100 μg/mL
1	MNS-5	*Bacillus subtilis* (MTCC-441)	9	11	**24**	25
2	Undoped TiO_2	*Bacillus subtilis* (MTCC-441)	—	—	—	24

6. Conclusion

The Mn and S co-doped anatase TiO_2 was effectively synthesized using the sol-gel method, and it was later characterized using different analytical methods. In Mn and S co-doped TiO_2, Sulfur causes the shift in the absorbance band of TiO_2 from the UV to visible region, whereas doping of Mn inhibits the electron/hole recombination and acts as a charge carrier during photocatalytic degradation under visible light irradiation. As compared to undoped TiO_2, co-doped TiO_2 with 1.00 wt % Mn and 0.25 wt % S had a small particle size and a high surface area. The resulting Eosin yellow (10 ppm) was successfully degraded by 0.10 g co-doped catalyst (MNS-5) at pH 4 in 70 min, as well as MNS-5 demonstrating good antibacterial activity against *Bacillus subtilis* (MTCC-441). It is possible to infer that Mn and S co-doped TiO_2 has increased photocatalytic activity and is an efficient antibacterial agent.

References

[1] Pirbazaria A.E., Monazzama P., Kisomi B.F. Co/TiO_2 Nanoparticles: preparation, characterization and its application for photocatalytic degradation of methylene blue. *Desalination and Water Treatment*, 2017, **63**, P. 283–292.

[2] Zhang H., Tang Q., et al. Enhanced photocatalytic properties of PET filament coated with Ag–N co-doped TiO_2 nanoparticles sensitized with Disperse blue dyes. *Nanomaterials*, 2020, **10**, 987.

[3] Basavarajappa P.S., Patil S.B., et al. Recent progress in metal-doped TiO_2, non-metal doped/co-doped TiO_2 and TiO_2 nanostructure hybrids for enhanced photocatalysis. *Int. J. of Hydration Energy*, 2020, **45**, P. 7764-7778.

[4] Manga Raju I., Siva Rao T., et al. Poly 3-Thenoic acid sensitized, Copper doped anatase/brookite TiO_2 nanohybrids for enhanced photocatalytic degradation of an organo phosphorus pesticide. *J. of Env. Chem. Eng.*, 2020, **7**, 103211.

[5] Anirudhan T.S., Rejeena S.R. Photocatalytic Degradation of Eosin yellow using poly (pyrrole-co-aniline)-coated TiO_2/nanocellulose composite under solar light irradiation. *J. of Materials*, 2015, 636409.

[6] Yuan Y., Ding J., et al. TiO_2 Nanoparticles co-doped with Silver and Nitrogen for antibacterial application. *J. of Nanoscience and Nanotech.*, 2010, **10**, P. 4868–4874.

[7] Alim S.A., Siva Rao T., et al. Fabrication of visible light driven nano structured Copper, Boron co-doped TiO_2 for photocatalytic removal of Lissamine Green B. *J. of Saudi Chem. Soc.*, 2018, **23**, P. 92–103.

[8] Vasilevskaia A.K., Popkov V.I., Valeeva A.A., Rempel A.A. Formation of Nonstoichiometric Titanium Oxides Nanoparticles Ti_nO_{2n-1} upon heat-treatments of Titanium hydroxide and anatase nanoparticles in a hydrogen flow. *Russ. J. of Appl. Chem.*, 2016, **89**, P. 961–970.

[9] Popkov V.I., Bachina A., et al. Synthesis, morphology and electrochemical properties of spherulite titania nanocrystals. *Ceramics Int.*, 2020, **46** (15), P. 24483–24487.

[10] Lee S.Y., Dooho K., et al. Photocatalytic degradation of Rhodamine B dye by TiO_2 and gold nanoparticles supported on a floating porous Polydimethylsiloxane sponge under ultraviolet and visible light irradiation. *ACS Omega*, 2020, **8**, P. 4233–4241.

[11] Audina Putri R., Safni S., et al. Degradation and mineralization of violet-3B dye using C–N co-doped TiO_2 photocatalyst. *Env. Eng. Research*, 2020, **25**, P. 529–535.

[12] Mancuso A., Sacco O., et al. Enhanced visible-light-driven photo degradation of Acid Orange 7 azo dye in aqueous solution using Fe–N co-doped TiO_2. *Arabian J. of Chem.*, 2020, **13**, P. 8347–8360.

[13] Sharotri N., Sharma D., Sud D. Experimental and theoretical investigations of Mn-N-Co-doped TiO_2 photocatalyst for visible light induced degradation of organic pollutants. *J. of Materials Research and Technology*, 2019, **8**, P. 3995–4009.

[14] Abderrahim E., Logvina M.V., et al. Synthesis of Fe- and Co-doped TiO_2 with improved photocatalytic activity under visible irradiation toward Carbamazepine degradation. *Materials*, 2019, **12**, 3874.

[15] Bayan E.M., Lupeiko T.M., et al. Zn–F co-doped TiO_2 nanomaterials: Synthesis, structure and photocatalytic activity. *J. of Alloys and Compounds*, 2020, **82**, 153662.

[16] Divya Lakshmi K.V., Siva Rao T., et al. Structure, photocatalytic and antibacterial activity study of meso porous Ni and S co-doped TiO_2 nanomaterial under visible light irradiation. *Chinese J. of Chem. Eng.*, 2019, **27**, P. 1630–1641.

[17] Singla P., Pandey O.P., Singh K. Study of photocatalytic degradation of environmentally harmful phthalate ester using Ni-doped TiO_2 nanoparticles. *Int. J. of Environmental Science and Technology*, 2016, **13**, P. 849–856.

[18] Divya Lakshmi K.V., Siva Rao T., et al. Visible light driven mesoporous Mn and S co-doped TiO_2 nano material: characterization and applications in photocatalytic degradation of Indigocarmine dye and antibacterial activity. *Enviromental Nanotechnology, Monitoring & Management*, 2018, **10**, P. 494–504.

[19] Manamon C., John O.C., et al. A facile route to synthesis of S-doped TiO_2 nanoparticles for photocatalytic activity. *J. of Molecular Catalalysis A: Chemical*, 2015, **406**, P. 51–57.

[20] Thanh Le T.T., Trinh Dinh T. Photocatalytic degradation of Rhodamine B by C and N codoped TiO_2 nanoparticles under visible-light irradiation. *J. of Chemistry*, 2020, 4310513.

[21] Alok Garg, Tejasvi Singhania, et al. Photocatalytic degradation of Bisphenol-A using N, Co co-doped TiO_2 catalyst under solar light. *Sci. Report*, 2019, **9**, 765.

[22] Mahlambi M.M., Mishra A.K., et al. Comparison of Rhodamine B degradation under UV irradiation by two phases of titania nano-photocatalyst. *J. of Thermal Analysis and Colorimetry*, 2012, **110**, P. 847–855.

[23] Ahmad T., Phul R., Khatoon N., Sardar M. Antibacterial efficacy of Ocimum Sanctum leaf extract-treated Iron oxide nanoparticles. *New J. Chem.*, 2017, **41** P. 2055–2061.

Submitted 5 January 2022; revised 9 July 2022; accepted 1 August 2022

Information about the authors:

Kapuganti V Divya Lakshmi – Sri Satya Sai University for Human Excellence, Kalaburagi, Karnataka, India; Department of Inorganic and Analytical Chemistry, Andhra University, Visakhapatnam 530003, India; kdivyalaxmi@gmail.com

Tirukkovalluri Siva Rao – Department of Inorganic and Analytical Chemistry, Andhra University, Visakhapatnam 530003, India; ORCID-0000-0002-6558-5762; Telephone: +91891-2844667; Mobile: +91 7702110459; sivaraotvalluri.16@gmail.com

Gorli Divya – Department of Inorganic and Analytical Chemistry, Andhra University, Visakhapatnam 530003, India; gorlidivya@gmail.com

Conflict of interest: the authors declare no conflict of interest.

NANOSYSTEMS:
PHYSICS, CHEMISTRY, MATHEMATICS

Ulyanova E.S., Shalaeva E.V., et al. *Nanosystems: Phys. Chem. Math.*, 2022, **13** (4), 445–455.
http://nanojournal.ifmo.ru
DOI 10.17586/2220-8054-2022-13-4-445-455

Original article

Near-IR photoluminescence and structural properties of TiO_2 powders with nanocrystalline anatase/brookite matrix

Ekaterina S. Ulyanova[1,a], Elizaveta V. Shalaeva[1,b], Yuriy S. Ponosov[2,c], Olga A. Lipina[1,d], Alexey A. Markov[1,e]

[1]Institute of Solid State Chemistry of Ural Branch of the Russian Academy of Sciences, Ekaterinburg, Russia
[2]M. N. Mikheev Institute of Metal Physics of Ural Branch of the Russian Academy of Sciences, Ekaterinburg, Russia

[a]tsivileva.yekaterina@yandex.ru, [b]shalaeva@ihim.uran.ru, [c]ponosov@imp.uran.ru, [d]LipinaOlgaA@yandex.ru, [e]aamarkov1@yandex.ru

Corresponding author: Ekaterina S. Ulyanova, tsivileva.yekaterina@yandex.ru

PACS 81.07.-b, 78.30.j, 78.55.-m, 73.20.Hb

ABSTRACT The properties are studied for near-IR photoluminescence (PL) observed at 865 – 870 nm for precipitated TiO_2 powders having nanocrystalline anatase/brookite structure: the dependence of NIR PL on annealing in oxygen, on content and crystallinity quality of brookite, and on excitation energy (E_{ex}). NIR PL in bi-phase powders was found to demonstrate a behavior characteristic of NIR PL in brookite. NIR emission intensity grows with increasing brookite content and at annealing in oxygen, when oxygen vacancies content decreases and crystallinity quality of brookite improves. The results indicate that in the bi-phase powders, brookite contains deep-level defect traps which are regarded responsible for NIR-PL in brookite and are favorable for photocatalytic reactions. NIR emission is observed for the band ($E_{ex} \approx E_b$) and below band-gap green ($E_{ex} < E_b$) excitation. A mechanism underlying NIR-PL in brookite with green excitation is suggested to be similar to that for the red PL known for anatase at below band-gap excitation.

KEYWORDS anatase/brookite TiO_2, nano-powders, NIR-photoluminescence, structural properties, defect states

ACKNOWLEDGEMENTS The authors are grateful to Dr. I. V. Baklanova for measurements of IR-spectra. The research was carried out in accordance with the state assignment for ISSC UB RAS and financial support from ISSC UB RAS (theme AAAA-A19-119031890025-9). Yu. S. P. acknowledges financial support from Ministry of Science and Higher Education of the Russian Federation (theme "Electron" No. 122021000039-4).

FOR CITATION Ulyanova E.S., Shalaeva E.V., Ponosov Yu.S., Lipina O.A., Markov A.A. Near-IR photoluminescence and structural properties of TiO_2 powders with nanocrystalline anatase/brookite matrix. *Nanosystems: Phys. Chem. Math.*, 2022, **13** (4), 445–455.

1. Introduction

Until recently, major research attention has been dedicated to the creation of photoactive materials to be based on anatase and rutile polymorphs of titanium dioxide and on their combinations [1–3]. It is only over the last years that intensive studies have been under way, reporting one more low-temperature, metastable polymorph of titanium dioxide, namely, brookite and its combinations with anatase [4–11]. Brookite has an advantage that is perceived to be in having structural defects/electron traps with the energy depth greater than that of anatase and smaller than that of rutile, which favors a more effective process of separation of photogenerated electron-hole pairs and provides for a longer life of charge carriers [10]. According to some researchers, it is exactly the reason why brookite nanoparticles and nanocrystals have excellent photocatalytic properties [5, 10, 11]. Similarly to single-phase brookite samples, mixed anatase/brookite nanocrystalline matrices also have good photocatalytic characteristics in some redox reactions [12–14]. Such good properties are found to be demonstrated by bi-crystalline hydrothermally synthesized TiO_2 with coherent interfaces between nanoparticles of brookite and anatase [12], mixed anatase and brookite nanoparticles [13], as well as aggregated nanocrystalline powders with anatase/brookite structure synthesized using the wet precipitation method [14]. Besides, binary anatase/brookite matrix is of additional research interest, which is caused by good photocatalytic properties of the composites containing sulfides and obtained in-situ by the wet precipitation method [15].

Improved photocatalytic properties of bi-crystalline anatase/brookite TiO_2 are related, firstly, to the fact that brookite has a more negative conduction band which may induce electron transfer from brookite to anatase via coherent interface thus enhancing charge separation, and, secondly, to the intrinsic defects in brookite, which act as deep traps enhancing the

electron trapping [13]. HRTEM study does not reveal coherent boundaries anatase/brookite in the aggregated nano powders, unlike the bi-crystalline TiO_2 [14, 16]. In this regard, to find out the causes for improved photocatalytic properties and to further clarify the separation mechanisms of photogenerated carriers in the mixed nano powders, it appears necessary to have information on the defects that play the role of electron traps and are presented in the brookite component of such mixed matrices. It is also deemed important to determine the energy range (UV only or visible light) within which these defect states get excited.

Photoluminescence (or else fluorescence) is one of the major methods for characterizing the energy of radiative recombination of photogenerated carriers (electrons and holes) [17]. A photoluminescence energy spectrum provides information on the basic energy level of structural defects that play the role of charge carrier traps at certain excitation energy, which is to be selected close or slightly lower than the energy gap width. For nano-sized objects, photoluminescence demonstrates high sensitivity to defects in the near-the-surface layer and thus turns out to be quite useful for photocatalytic applications [18]. By now, a considerable body of research has been carried out on the photoluminescence (PL) for nanostructured single-phase anatase and PL mechanisms have been suggested that are associated with defects in anatase [19–26]. Photoluminescence in anatase is known to be observed in a wide range of the visible light spectrum from 400 nm up to nearly 700 nm. Studies of PL as a function of atmosphere type (oxidative or reductive), annealing temperature, number of defects, size of crystallites and the excitation energy ($E_{ex} \geq E_b$ or $E_{ex} < E_b$) have allowed two bands to be distinguished in visible PL [27, 28]. "Green" band with the center at 530 – 510 nm is preferably attributed to radiative recombination at shallow electron-trapping sites such as $V_{O^{2-}}$ oxygen vacancies, while shallowly trapped electrons recombine with holes from the valent band (VB). "Red" band centered around 600 – 690 nm is attributed to recombination at deeper electron traps V_{O^-}/Ti^{3+}, V_O/Ti^{3+} [27, 28]. It has been established that "Red" band of photoluminescence (PL) is also observed at the excitation energies higher and lower than the band gap of TiO_2; and the PL mechanisms have been suggested for defect-containing anatase [27].

PL studies of brookite are scarce, addressing only single-phase brookite samples which were obtained by hydrothermal synthesis, and these studies were conducted for the excitation energies ranging close to the energy gap width [10, 11, 29]. An earlier study has provided data only on the visible PL recorded in the range of 400 to 650 nm for aggregated nanocrtystalline brookite powders [29]. Later on, PL spectra taken from the hydrothermally synthesized nanocrystallites of brookite, which have a good crystallinity quality and a low aggregation degree, showed not only a weak visible PL but also an intense photoluminescence in the near-IR (NIR) region in the vicinity of 860 nm similar to NIR PL in rutile [10, 11]. It has been established that in brookite it is NIR-PL that is caused by radiative recombination between deeply trapped electrons and valence band holes. The life time of such NIR PL in brookite (or the lifetime of deeply trapped electrons) is several times longer than the lifetime of the visible PL and shallowly trapped electrons in anatase [10, 11]. In turn, similarly to the visible PL in anatase, the visible PL in brookite is assigned to radiative recombination between shallowly (or slightly deeper) trapped electrons and holes. Poorer crystallinity quality and the aggregation of brookite nanocrystallites result in a decrease in the NIR-PL and in enhanced visible PL. Similarly to the NIR PL in rutile and visible PL in anatase, the NIR and visible PL in brookite react differently on the type of the environment, including oxygen atmosphere. No final conclusion has yet been made on the type of lattice intrinsic defects responsible for NIR PL in titanium dioxides, however, the majority of researchers do not assign NIR PL to radiative recombination at the defect sites like oxygen vacancies [25, 30].

Unlike the well-studied mixed anatase/rutile matrices, photoluminescence research of anatase/brookite titanium dioxide is close to non-existent; however, there are preliminary photoluminescence data available on aggregated nanocrystalline powder synthesized using the wet precipitation method [31]. In the visible PL part of the spectrum, a broad band characteristic of anatase and brookite is observed. NIR band was also observed, which is supposed to be attributed to radiative recombination at deep traps in brookite.

The purpose of this study is to elucidate the properties of NIR-PL for the precipitated powders having nanocrystalline anatase/brookite structure. To this end, the effect of annealing in oxygen atmosphere on NIR PL was studied, the crystallinity quality of brookite phase and its content in the powder were analyzed, and the NIR PL was also investigated as a function of excitation energy. The structural state and composition of anatase/brookite samples were characterized with XRD, Raman spectroscopy, IR-spectroscopy, scanning and transmission electron microscopy. The energies of band gap and absorption properties were estimated by diffuse reflectance. It was found that NIR-PL observed in anatase/brookite aggregated powders demonstrate the behavior typical of NIR PL in brookite. Unlike the visible luminescence, NIR luminescence centered at 865-870 nm did not decrease under annealing in oxygen, as the content of oxygen vacancies decreases and quality of crystallinity improves. On the contrary, NIR PL increases. NIR PL also grows with increasing brookite content in the powder up to 30 %, which is indicative of the absence of NIR PL quenching effect in bi-phase anatase/brookite matrices. NIR-PL is observed for the excitation energy equal or less than the band gap width and demonstrates sublinear growth with excitation power. Possible mechanism is discussed for NIR-PL emission in brookite at visible excitation.

The obtained results provide evidence that the bi-phase powders prepared by wet precipitation route have intrinsic defects in the brookite lattice, which act as deep electron traps that may favor photocatalytic redox reactions.

2. Experimental part

TiO_2 powders with anatase/brookite structure were prepared by wet precipitation technique, and details of TiO_2 preparation can be found in Ref. [14]. In brief, a certain amount of titanium (IV) n-butoxide was added into the pure deionized water. To fabricate brookite-rich nanocrystalline powders, the samples were heated up to the boiling point under continuous stirring and aged at this temperature for 4 h. To remove the remaining organic species, the powders were centrifuged, redispersed twice in ethanol or water, and then dried in air at 120 °C for 3 h. Brookite-poor powders were prepared by the same hydrolysis route but without aging stage at boiling point. All powders were further annealed in oxygen atmosphere at 400 and 550 °C for 2 hours in TG-92 chamber. Oxygen pressure was 1 atm. and oxygen flow rate was 15 ml/min. To avoid the formation of high-temperature rutile phase in the samples, the maximum annealing temperature was limited to no more than 550 °C.

X-ray diffraction (XRD), Raman micro-spectroscopy, high resolution transmission electron microscopy (HRTEM) and electron diffraction were employed to characterize structural properties, defects and crystallinity quality of TiO_2 nanopowders. The XRD patterns of samples were recorded by Shimadzu MAXima-X XRD-7000 (Shimadzu, Japan) automatic diffractometer with CuKα radiation ($\lambda = 1.5406$ Å) in 2θ angle range 10 – 80 ° with a step 0.03 ° and an exposure time of 10 sec at each step. The volume fractions and structural characteristics of constituent phases were calculated employing PCW 2.4 software (http://powdercell-forwindows.software.informer.com/2.4). High resolution TEM images and electron diffraction patterns were obtained with the help of JEM-2100 and JEM-200CX microscopes (JEOL, Japan). The specific surface area of the powder was determined with the Brunauer–Emmett–Teller model (BET method) using Gemini VII 2390 microcrystal analyzer. Raman and photoluminescence spectra were excited by a low-power (up to 3 mW) laser irradiation at wave length of 405 and 532 nm at room temperature, and they were recorded by a Renishaw inVia Reflex laser Raman spectrometer (Renishaw, UK), providing a focal spot on the samples of 1 – 2 μm diameter. Spectral resolution was about 0.5 cm^{-1}. The acquisition time was up to 10 s, and each spectrum was scanned 3 times. Several spectra were taken for each sample to test for homogeneity and reproducibility. Raman and photoluminescence spectra were analyzed with multi-peak Gaussian fitting method using the "Peakfit v 4.11" software package. Infrared spectroscopy was used to identify the remaining hydrocarbon species and hydroxyl groups on the surface of TiO_2 powder particles. The infrared spectra of samples were registered on Vertex 80 IR Fourier spectrometer (Bruker, Germany) using MVP-Pro ATR Accessory with diamond crystal (Harrick, USA) in the interval of 4000 – 400 cm^{-1}.

Optical absorption properties and band gap were evaluated with diffuse reflectance spectroscopy. The diffuse reflectance spectra of the powders were measured with a Shimadzu UV-3600 spectrophotometer (Japan) using $BaSO_4$ as a reference. The reflectance data was converted to the extinction coefficient $F(R_\infty)$ values according to the Kubelka–Munk equation:

$$F(R_\infty) = \frac{(1 - R_\infty)^2}{2R_\infty}, \tag{1}$$

where $F(R_\infty)$ is proportional to the extinction coefficient. The transformed Kubelka–Munk function was constructed by plotting $(F(R_\infty) \cdot h\nu)^{1/2}$ against the energy of excitation source to obtain the band gap of TiO_2 powder, which is considered to be an indirect band-gap semiconductor [32].

3. Results and discussion

3.1. Structural and photoluminescence properties of the precipitated TiO_2 powder with nanocrystalline anatase/brookite matrix

TiO_2 powders synthesized via the wet precipitation route with the thermal aging of hydrolysis products [14, 16] demoinstrate XRD and Raman spectra which show that the powder is bi-phase anatase/brookite with nanocrystalline structure (Fig. 1(a,b)). The indexing of XRD reflections and curve-fitting of XRD patterns were carried out using a bi-phase model: the orthorhombic structure of brookite (S. G. Pcab, JCPDS no. 029-1360) and the tetragonal structure of anatase (S. G. I4(1)/amd, JCPDS no. 21-1272). According to the profile-fitting of XRD spectra, the brookite phase content is up to 33 %, and the average crystallite size is 7.5 – 8 nm for both phases. Table 1 gives the structural characteristics determined using profile-fitting of the XRD spectra. HRTEM study of these powders reveals a minor amount of amorphous phase, no more than 5 % [16], and the average crystallite size of about 6.5 (± 0.5) nm (Fig. 1(c)). SEM images demonstrate a high aggregation in the powders (Fig. 1(d)).

Figure 2 displays a typical PL spectrum with excitation energy of 532 nm taken for the powder with the anatase/brookite matrix containing 33 % of brookite. The spectrum demonstrates a wide band of visible light and NIR PL emission. Visible PL emission can be described with three most intensive Gaussian sub-bands centered at 591 nm (2.1 nm), 638 nm (1.95 nm), and 693 nm (1.8 eV). The observed visible PL emission with below-bandgap excitation of 2.33 eV (green excitation) means that a great number of defects are presented in the anatase phase, which act as deep electron traps and as radiative recombination centers [28]. All the three bands of visible emission can be assigned to radiative recombination on the surface defects such as oxygen vacancies, Ti^{3+} defects and hydroxyl groups which all are the predominant trapping sites for low-temperature sol-gel nano-powders [20]. Decomposition of the spectrum shows the presence of sub-bands

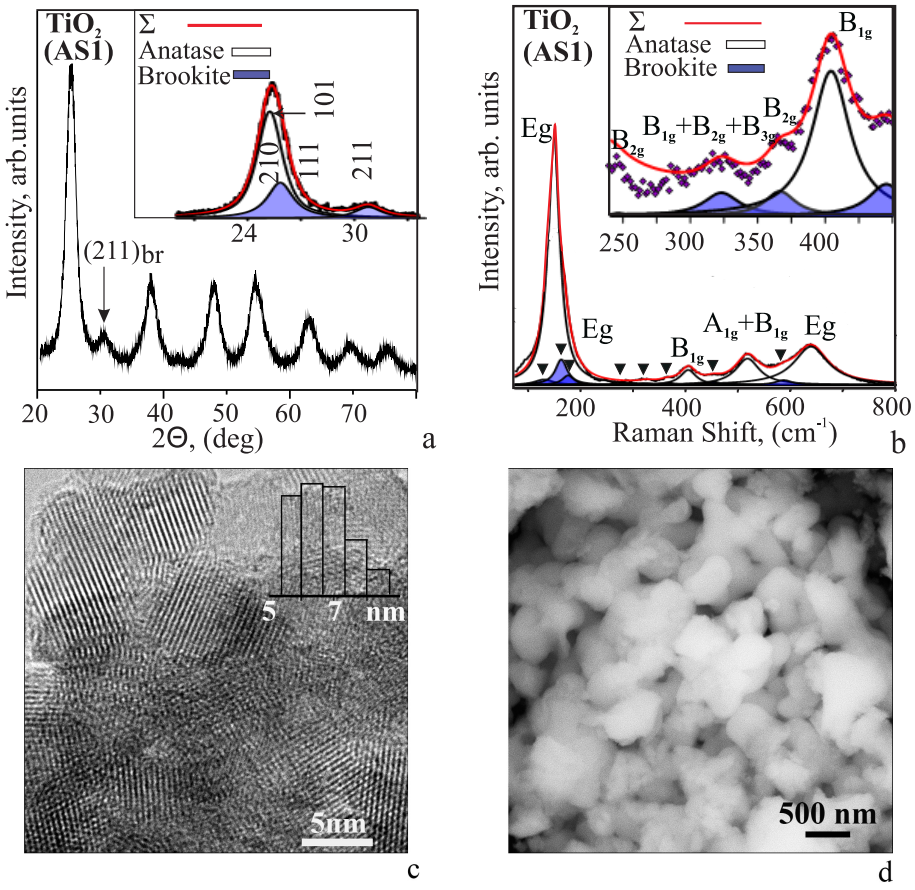

FIG. 1. Structure of precipitated TiO_2 powder (AS1) with nanocrystalline rich-brookite matrix: a – XRD pattern (XRD spectrum and profile calculated with a two-phase model are shown in the insert); b – Raman spectrum, brookite modes are marked by triangles, excitation is 532 nm; c,d – HRTEM and SEM images, respectively. Crystallite size distribution is shown in the insert.

characteristic of the visible PL observed in the conditions of green excitations for the anatase phase containing an appreciable number of oxygen vacancies [28]. Thus, visible emission at 1.95 and 1.8 eV can be attributed to the deexcitation from the deep levels of oxygen vacancies associated with Ti^{3+} in anatase lattice to the ground state [20, 21, 28]. In turn, the sub-band at 2.1 eV is due to the deexcitation from lower levels in Ti^{3+} 3d states of TiO_2 lattice to the deep levels created by OH^- group [20]. The presence of OH^- hydroxyl groups is supported with the observed wide band at 2500 – 3700 cm^{-1} and the vibrational mode at 1633 cm^{-1} in the IR-spectra of the powders. Besides, it should be considered that the surface oxygen vacancies of the aggregated brookite nanoparticles are also deemed responsible for the visible PL observed.

One Gaussian sub-band at 870 nm (1.42 eV) is located in the near-IR region of the spectrum. This NIR PL emission at 1.42 eV could be a signature of the brookite phase and could be associated with the deep traps at the brookite lattice defects. Further, in order to clarify the properties of the observed NIR PL and the defect states responsible for this PL, a comparative study was carried out for visible and NIR PL, and also for the light absorption and structural properties of bi-phase nano-powders depending on annealing in oxygen. NIR PL was estimated for the powders with different brookite contents. NIR PL was studied as a function of excitation energy.

3.2. Structural, photoluminescence and light absorption properties of TiO_2 powder with nanocrystalline anatase/brookite matrix: effect of annealing in oxygen atmosphere and brookite content

Under annealing in oxygen at temperatures of 400 and 550 °C, the bi-phase structure of brookite-rich powders (AS1) remains (Fig. 3(a)), however, according to the results of profile-fitting of XRD spectra, the brookite fraction falls from 33 down to 17 % at a temperature of 550 °C (Table 1). The electron diffraction study shows that there is no high-temperature rutile phase, with up to ten SAED (selected area electron diffraction) patterns obtained from various parts of the powder (Fig. 3(b)). For brookite-rich sample, with increasing annealing temperature, anatase and brookite crystallite size consequently grows, and amounts to 10 and 12.5 nm, respectively, at the annealing temperature of 400 °C, and 15 and 17 nm at the annealing temperature of 550 °C. Evaluated using the BET method, the specific surface area decreases from 245 m^2/g (AS1) down to 140 m^2/g (AS1 + 440 °C) and to 115 m^2/g (AS1 + 550 °C). Microstrains, which are indicative

TABLE 1. Structural characteristics determined using profile-fitting of XRD spectra for as-prepared (AS1) and annealed nanopowders

Structural properties *		TiO_2 bulk	TiO_2 (AS1)	TiO_2 (AS1) +400O_2 °C	TiO_2 (AS1) +550O_2 °C
Phase composition, brookite/anatase(%)			33 /67	31/ 69	17 / 83
	Anatase				
Crystalllite size, nm			7.5(±0.4)	10(±0.5)	15(±0.8)
Lattice parameters, nm	a	3.785	3.804(3)	3.796(3)	3.786(3)
	b	9.514	9.458(7)	9.481(7)	9.511(7)
Unit cell volume		136.3	136.8(3)	136.6(3)	136.3(3)
Microstrains, %			0.6	0.6	0.1
	Brookite				
Cristallite size, nm			8.0 (±0.4)	12(±0.5)	17(±0.8)
Lattice parameters, nm	a	5.135	5.207(4)	5.211(4)	5.151(4)
	b	9.166	9.066(7)	9.066(7)	9.127(7)
	c	5.436	5.355(4)	5.384(4)	5.443(4)
Unit cell volume		255.8	252.8(6)	254.4(6)	255.9(6)
Microstrains, %			0.6	0.4	0.2

*The typical values of R factors: $R_p = 7 \div 9$ and $R_{wp} = 9 \div 11$.

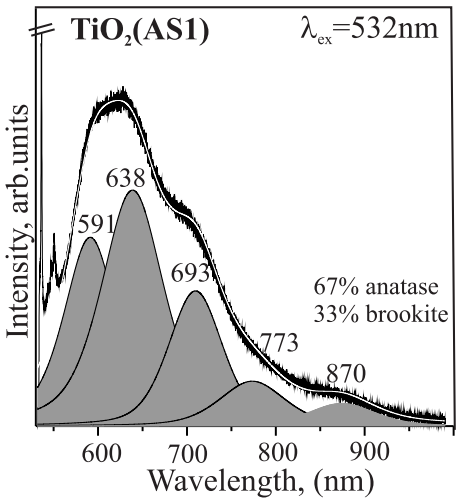

FIG. 2. PL spectrum for anatase/brookite nanopowder with high content of brookite phase

of defect concentration, decrease consistently from 0.63 down to 0.6 % (400 °C) and 0.1 % (550 °C) for anatase; and from 0.6 down to 0.4 % (400 °C) and 0.2 % (550 °C) for brookite. The unit cell volume decreases for anatase and grows for brookite, approaching the bulk values. For the annealed brookite, the deviation of the unit cell from the bulk value is insignificant: 0.5% at an annealing temperature of 400 °C and 0.2 % at 550 °C (Table 1).

Being sensitive to nanocrystallite size, to defect concentration and to crystallinity quality, the Raman spectra undergo substantial changes (Fig. 3(c)) as the annealing temperature grows.

Figures 3(c) (insert), 3(d) and Table 2 demonstrate the results of spectra decomposition, which was carried out using the Gaussian-Lorentzian profile of Raman bands. The spectra decomposition reveals all six Raman peaks of anatase ($3E_g$, A_{1g} and $2B_{1g}$) and the majority of vibrational modes of brookite having very strong, strong and medium intensities according to the notations reported by Iliev M. et al [33]. As the annealing temperature grows, all the anatase peaks demonstrate an increase in intensity and the peak narrowing (i.e., decreasing FWHM) and the red-shift of peak positions.

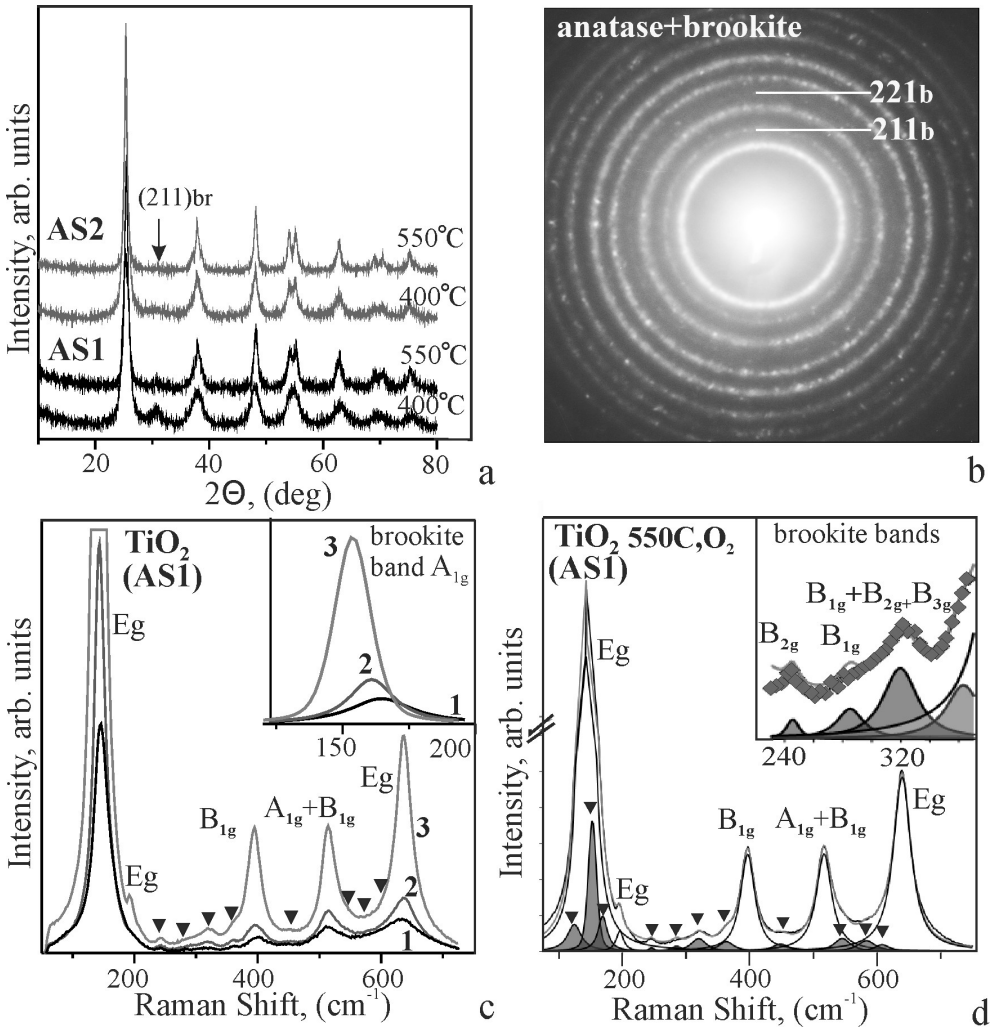

FIG. 3. XRD (a), electron diffraction (b) and Raman spectra (c,d) for anatase/brookite powders annealed in oxygen atmosphere, brookite modes are marked by triangles; excitation is 532 nm. AS1, AS2 – powders with rich- and poor-brookite composition, respectively. 1 – as-prepared powder; 2, 3 – powders annealed at 400 and 550 °C, respectively.

The same tendency is observed for all brookite peaks, including the spectra of powders annealed at 550 °C. As an example, Fig. 3(c) (insert) exhibits a brookite peak corresponding to the most intense vibrational mode A_{1g} for as-prepared and annealed powders. Despite the considerable decrease in brookite content at an annealing temperature of 550 °C, the intensity of Raman peak grows owing to the increased crystallinity quality and smaller number of defects in brookite structure. Besides, for powder annealed at 550 °C, Raman phonon wavenumbers (in cm^{-1}) for brookite and anatase components of the nanopowders are quite close to those for bulk crystalline brookite [33] and anatase [34], respectively (Table 2). For the powders annealed at 550 °C, the crystallite sizes of both phases are larger than 15 nm and, according to a number of research works [35–38], the Raman peak shifts due to the size-induced phonon confinement effect should not be observed. Then the shifts of the Raman peak position, which are related to the structural disorder and defects (including interstitial atoms, vacancies and Vo/Ti^{3+} centers), should be very insignificant for these samples. Therefore, the results of XRD and Raman spectroscopy imply that, in the samples annealed at 550 °C, brookite as well as anatase particles exhibit good crystallinity quality and have relatively low defect concentration.

Figure 4(a) exhibits the PL spectra of brookite-rich (AS1) nanocrystalline powders as-prepared and annealed in oxygen atmosphere. It can be seen that all sub-bands of visible red PL, including those associated with deexcitation of oxygen-vacancy states, decrease appreciably at an annealing temperature of 400 °C already, the intensity maximum of visible PL being shifted to the short-wave region. At an annealing temperature of 550 °C, the visible PL intensity is observed to be close or slightly lower than the visible PL intensity at 400 °C. That may be caused by the growing content of anatase component, which makes the major contribution into the visible PL. The observed annealing behavior of visible PL confirms once again that this PL is mostly associated with recombination at the defect states. No signs of size factor influence on PL was found, which appears because of the quantum confinement effect in semiconductor nm-sized system. In this case, as the crystallite size grows from 7.5 up to 15 nm, which occurs at annealing, the PL maximum

TABLE 2. Peaks position and FWHM of vibration modes in Raman spectra of brookite-rich nanopowders, as prepared and annealed in oxygen atmosphere

Raman mode	Peak position / FWHM (in cm^{-1})				
	as prepared	annealing at 400 ° C, oxygen atm.	annealing at 550 ° C, oxygen atm.	Anatase mode, [34]	Brookite mode, [33]
(A_{1g}) **B***	130.5 / 42.8	125.7 / 35.2	124.4 / 26.3		**125** (m)
(E_g) **A***	149.3 / 26.5	147.1 / 19.8	143.1 / 13.7	**144** (vs)	
(A_{1g}) **B**	163.4 / 27.4	159.7 / 19.5	152.8 / 15.5		**152** (vs)
$(B_{1g} + B_{2g})$ **B**	175.3 / 26.5	170.7 / 22.4	169.1 / 17.3		**169** (m), **160** (s)
(E_g) **A**	197.4 / 30.6	197.6 / 16.8	195.9 /13.7	**197** (w)	
(A_{1g}) **B**		247.1 / 8.1	245.6 / 11		**246** (s)
(B_{1g}) **B**		292.7 / 25.3	285.1 / 22.3		**283** (s)
$(B_{1g}+B_{2g}+B_{3g})$ **B**	323.7 / 33.1	321.2 / 30.7	319.6 / 28.4		**327** (m), **325** (m), **318** (s)
(B_{2g}) **B**	365.5 / 36.1	363.8 / 28.3	363.1 / 28.3		**366** (s)
(B_{1g}) **A**	404.9 / 35.7	400.7 / 32.9	396.5 / 26.8	**399** (m)	
(B_{1g}) **B**	452.3 / 31.9	449.8 / 42.9	448.5 / 32.8		**449** (m)
$(A_{1g} + B_{1g})$ **A**	517.7 / 54.6	519.1 / 42.9	516.3 / 29.2	**513, 519** (m)	
(A_{1g}) **B**			544.8 / 30.3		**545** (s)
(B_{2g}) **B**	586.5 / 38.6	586.5 / 34.1	583.0 / 32.9		**584** (m)
(E_g) **A**, (A_{1g}) **B**	641.3 / 79	640.9 / 52.7	638.9 / 33.4	**639** (m)	**640** (s)

* **B** – brookite, **A** – anatase

should be noticeably shifted to the long-wave region [35]. Annealing atmosphere plays a decisive role in decreasing the luminescence associated with oxygen vacancies. Annealing carried out in air at 400 °C leads even to some growth of the visible PL, which may be attributed to the improved crystallinity in the near-surface layers and to crystallization of the residual amorphous phase with annealing. HRTEM images confirm the lack of amorphous components in the powders.

In nanopowders of titanium dioxide under annealing in oxygen at 400 – 550 °C, the decrease in the content of oxygen vacancies agrees with the data available in literature [39]. For the studied nanocrystalline powders, this effect is confirmed with the comparative study of optical absorption properties of as-prepared and annealed powders, which was carried out using the diffuse reflectance method. Fig. 5 displays the transformed Kubelka–Munk function $(F(R) \cdot h\nu)^{1/2}$ vs. the energy of excitation for these samples, since TiO_2 would usually be considered as indirect band-gap semiconductor. In the range of 3 to 2 eV (from 415 to 620 nm), absorption falls for the powders annealed in oxygen as compared to the as-prepared powder. This fact definitely supports the decrease in the concentration of deeper trap states associated with the oxygen vacancies [30] and agrees well with the observed decrease in the PL in the red region over 500 nm. In the range greater than 3 eV, on the contrary, absorption is greater for the annealed powders, which can be mostly due to the self-trapped states and size quantization effect [40].

To estimate the bandgap width for indirect band-gap semiconductors, the following dependence of absorption coefficient (K) on radiation energy should be used:

$$K = \begin{cases} 0, & h\nu < E_G - E_P; \quad (2a) \\ A\left(h\nu - E_G + E_P\right)^2, & E_G + E_P > h\nu > E_G - E_P; \quad (2b) \\ A\left(h\nu - E_G + E_P\right)^2 + B(h\nu - E_G - E_P)^2, & h\nu > E_G + E_P, \quad (2c) \end{cases}$$

where $h\nu$ is the excitation energy, E_G is the band gap, E_P is the value of the phonon energy associated with the indirect transition, $\sqrt{K}$ is proportional to $\alpha \cdot h\nu$ (α is the extinction coefficient) [41] and, therefore, is also proportional to $(F(R_\infty) \cdot h\nu)$. Based on this equation, we would expect to observe two linear regions in the plot of the square root of the absorption coefficient: the first linear region (eq. (2b)) being associated with phonon absorption, and the second linear region (eq. (2c)) being associated with phonon emission. However, only one linear region is presented in the plot

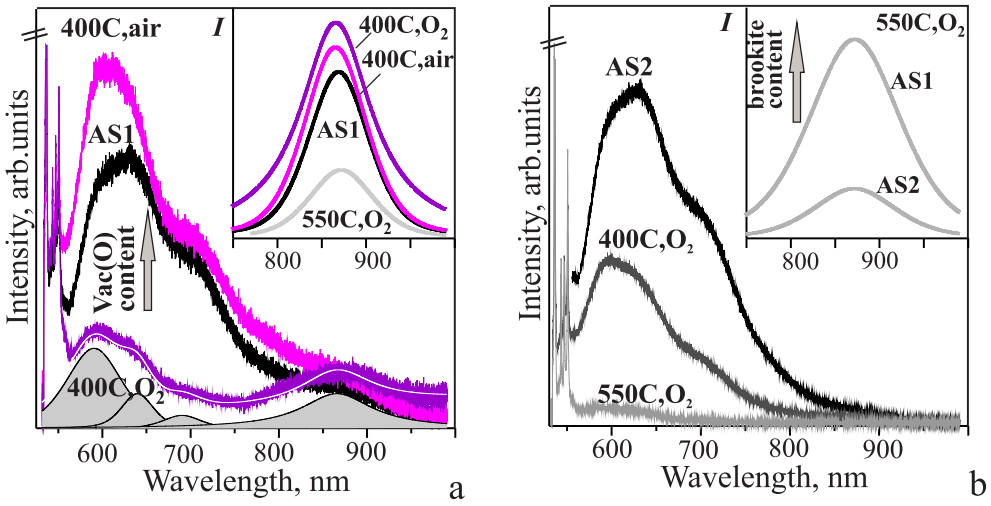

FIG. 4. PL spectra for brookite-rich (AS1) (a) and brookite-poor (AS2) nanopowders annealed at 400 and 550 °C in oxygen atmosphere and in air (the annealing parameters are given at the corresponding curves). In the inserts, intensity of NIR PL sub-band is given for different annealing temperatures (a) and brookite content (b). The laser excitation is 532 nm.

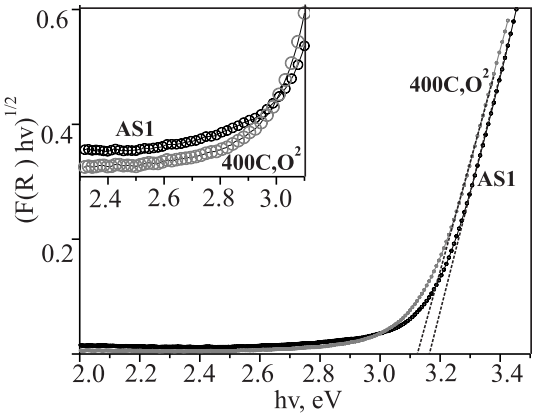

FIG. 5. Transformed Kubelka–Munk function $(F(R) \cdot h\nu)^{1/2}$ vs. excitation energy ($h\nu$) for brookite-rich nanopowders: as-prepared (AS1) and annealed in oxygen atmosphere at 400 °C

$(F(R) \cdot h\nu)^{1/2}$ vs. excitation energy (Fig. 5). In this case, because the phonon emission region is masked, only the value of $(E_G + E_P)$ can be determined [42]. Hence, the band gap of TiO_2 (AS1) and annealed TiO_2 (AS1) nanopowders are suggested to be slightly less than 3.18 and 3.16, respectively.

The decrease in the content of oxygen vacancies with annealing at 400 °C appears to be not that significant, as no widening of the band gap width is observed. A slight decrease of the band gap (or red-shift) from 3.18 to 3.16 takes place with annealing at 400 °C and with the growth of crystallite size in TiO_2 nanopowders, and hence, the quantum size effects are prevalent. As follows from the literature data [40], for anatase nanoparticles the widening of the band gap width with decreasing crystallite size due to the quantum size effect, should be observed exactly for the crystallite crystallite size less than 17 nm.

For brookite-rich nanopowder, annealing behavior of NIR PL demonstrates a fundamental difference from the behavior of visible PL. Fug. 4(a) (insert) exhibits the NIR PL sub-band resulted from decomposition of PL spectra. As can be seen, the annealing in oxygen at 400 °C and the decrease in the content of traps associated with oxygen vacancies in dioxide titanium phase results even in the growth of NIR PL rather than in a decrease. Besides, a somewhat lower growth in the intensity of NIR PL sub-band is also observed under annealing in air at 400 °C. For anatase/brookite matrix, the observed behavior of NIR PL sub-band allows one to assign the luminescence to the deep defect levels in brookite. As established earlier, NIR PL is enhanced in brookite as the crystallinity quality improves [11], and it is expected to be growing similarly to the case of rutile [25] in oxygen atmosphere as the content of oxygen vacancies decreases.

At the same time, annealing at 550 °C is accompanied with the decrease in the intensity of NIR PL sub-band, although according to the XRD and Raman spectroscopy data the brookite phase exhibits good crystallinity quality and has relatively low defect concentration (Fig. 4(a), insert). The nearly two-fold decrease in the content of brookite (from

33 to 17 %) may be the major reason for the decrease in NIR intensity, because no effect of quenching of NIR PL was observed in the mixed bi-phase anatase/brookite samples, although NIR PL quenching of rutile does occur in bi-phase anatase/rutile matrices [24]. The above discussed suggestion is confirmed with the comparative study carried out on photoluminescence of TiO_2 (AS2) samples containing no more than 3 % of brookite, which were obtained without the thermal aging stage (Fig. 3(a)). The as-prepared samples synthesized following this technique are found to be X-ray amorphous [16]; and the annealing at 400 and 550 °C in oxygen leads to the formation of nanocrystalline brookite-poor structure. For the brookite-poor powder annealed at 550 °C, the crystallite sizes and the Raman phonon wavenumbers (in cm^{-1}) for brookite and anatase components are practically the same as those for the brookite-rich powder annealed at 550 °C. For the brookite-poor samples, similarly to the brookite-rich nanopowders, annealing in oxygen also results in the considerable decrease in visible PL (Fig. 4(b)). In addition, intensity of NIR PL in these brookite-poor samples is significantly lower than that in brookite-rich samples (Fig. 4(b), insert). Therefore, it can be deduced that, quenching of NIR PL is not essential in mixed anatase/brookite nanopowders with brookite content up to 20 – 30 %.

As demonstrated by the experiments carried out with annealing in oxygen, NIR PL of anatase/brookite aggregated powders exhibit a behavior characteristic of NIR PL in brookite. However, it turns out quite significant that NIR PL is observed as well as the visible PL at excitation energy less than band-gap energy for these powders. Further, a discussion of possible PL mechanism is provided and the PL spectra are considered for the energy excitation close to the value of band gap energy.

3.3. NIR photoluminescence in anatase/brookite nanopowders at violet and green excitation

Figure 6 exhibits a PL spectrum recorded at the excitation energy of 405 nm ($E_{ex} \approx E_b$), for the brookite-rich nanopowder annealed at 400 °C in oxygen. In these samples, the maximum content of brookite and the crystallinity quality are greater than those of as-prepared nanopowders. The spectrum, along with the visible band, demonstrates an intense NIR PL, and the comparison with NIR PL recorded for the excitation energy of 532 nm ($E_{ex} < E_b$) does not reveal any appreciable shift of the maximum of luminescence band. It means that in the both cases the NIR PL is associated with radiative recombination at the same deep defect levels in brookite. Intensity of NIR band grows with the excitation power considerably more than that of visible PL but it follows the sublinear law $I \sim P^{\gamma}$ ($\gamma = 0.7$), indicating the saturation of these levels at high excitation energy [22].

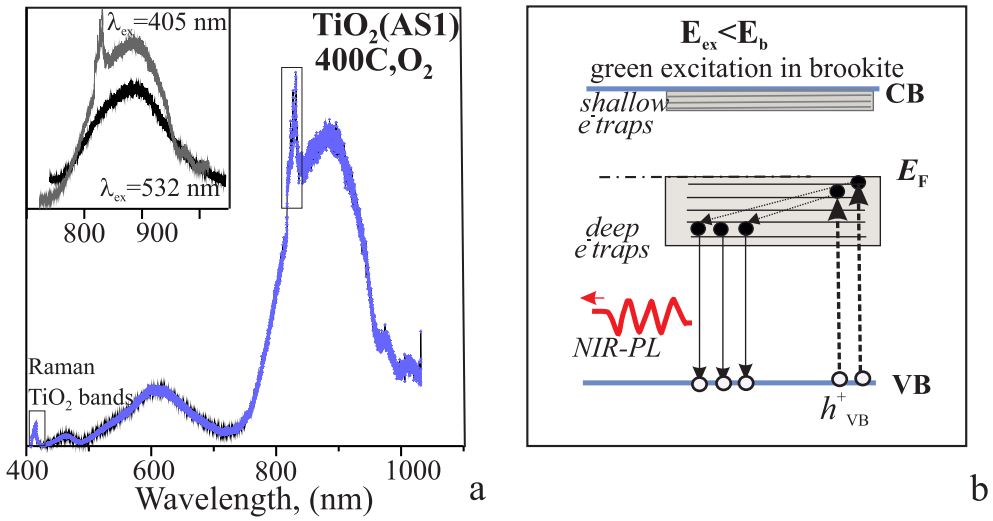

FIG. 6. a – PL spectrum of brookite-rich nanopowder at laser excitation of 405 nm. In insert, NIR band for different laser excitations, power $P = 0.3$ mW. Raman band are marked with rectangles. b – Scheme of possible NIR PL mechanism in brookite at sub-bandgap excitation.

According to the reports on the investigation of photoluminescent behavior in brookite [11], NIR emission observed at UV-excitation ($E_{ex} > E_b$ or $E_{ex} \approx E_b$) is assigned to radiative recombination between deeply trapped electrons and valence band holes, with intrinsic defects acting as deep traps of photogenerated electrons excited from the valence band. Then, NIR PL observed at green excitation with $E_{ex} < E_b$ can be caused by the sub-bandgap (below-bandgap) excitation of electrons from the valence band to reach some defect states, their migration into these deep traps and, finally, their radiative recombination with the valence band holes. Fig. 6(b) displays a schematic illustration of this NIR PL mechanism in brookite. A similar mechanism has earlier been suggested for the red PL in anatase at visible (blue, green and yellow) excitation [27, 28], and it is considered possible as for the red PL as for the NIR PL in brookite at visible excitation. The suggested NIR PL mechanism is supported with the data of transient absorption (TA) spectroscopy of TiO_2 brookite nanocrystals [10, 11]. Three groups of surviving electrons were found for brookite using TA spectroscopy.

Apart from the largest group of the deeply trapped electrons, there are also a number of groups of surviving electrons at excitation in brookite: these are small groups, where the first group includes free and shallow-trapped electrons and the second group includes trapped electrons. Both of the groups may be assigned to various oxygen vacancies. It is the electron traps associated with the second group that can act as intermediate states, and the sub-bandgap (green) excitation can promote electrons to these defect states from the VB. Within the framework of the suggested mechanism, the decrease in the concentration of oxygen vacancies of the second group, which is clearly observed at annealing in oxygen, may be the reason for the lower intensity of NIR PL emission at visible excitation in the annealed samples.

4. Conclusions

NIR-PL properties were studied for the precipitated TiO_2 nanopowders having anatase/brookite structure, i.e., the effect caused on photoluminescence by annealing at 550 °C in oxygen, by crystallinity quality and defect concentration and by the content of brookite phase. The dependence of NIR PL on excitation energy ($E_{ex} \approx E_b$ and $E_{ex} < E_b$) was also considered. The structural properties of the powders were characterized by XRD, HRTEM, SEM, electron diffraction and Raman spectroscopy. Optical absorption properties and band gap were evaluated using the diffuse reflectance method.

It was found that NIR PL in brookite-rich powders (up to 33 %) show the signs of NIR PL of brookite, which is associated with the lattice intrinsic defects of brookite, acting as deep electron traps. Unlike the visible PL, the intensity of NIR PL emission in bi-phase powders grows at annealing in oxygen, while the content of oxygen vacancies decreases and the structural disorder of brookite crystal lattice decreases (crystallinity quality of brookite improves). With the brookite content growth, NIR PL grows as well, which is indicative of the insignificant NIR PL quenching effect in bi-phase anatase/brookite nanopowders.

NIR PL is also observed for the band ($E_{ex} \approx E_b$) and below-bandgap ($E_{ex} < E_b$, green) excitation. The NIR PL mechanism at below-bandgap excitation is assumed to be similar to the mechanism for the red PL at sub-band excitation of nanocrystalline anatase, which has earlier been suggested by Pallotti et al. [27]. At below-bandgap excitation of brookite, the electrons excited from the valence band can get into some intermediate states associated with defects and then migrate to deep traps and escape these traps by way of NIR radiative recombination with the valence band holes.

The obtained results provide evidence that in the precipitated nanopowders with anatase/brookite structure, brookite contains deep defect traps, which are considered to be favorable for photocatalytic redox reactions, with the deep level lattice defects acting as electron traps for band ($E_{ex} \approx E_b$) as well as for sub-bandgap green ($E_{ex} < E_b$) excitation(s).

References

[1] Katal R., Masudy-Panah S., et al. A review on the synthesis of the various types of anatase TiO_2 facets and their applications for photocatalysis. *Chemical Engin. J.*, 2020, **384**, 123384.

[2] Verma R., Gangwar J., Srivastava A.K. Multiphase TiO_2 nanostructures: a review of efficient synthesis, growth mechanism, probing capability, and applications in bio-safety and health. *RSC Advances*, 2017, **7**, P. 44199–44224.

[3] Miyoshi A., Nishioka S., Maeda K. Water splitting on rutile TiO_2-based photocatalysts. *Chemistry: A European J.*, 2018, **24**, P. 1–17.

[4] Paolo A. Di, Bellardita M., Palmisano L. Brookite, the least known TiO_2 photocatalyst. *Catalysts*, 2013, **3**, P. 36–73.

[5] Monai M., Montini T., Fornasiero P. Brookite: nothing new under the sun. *Catalysts*, 2017, **7**, P. 304–323.

[6] Choi M., Yong K. A facile strategy to fabricate high-quality single crystalline brookite TiO_2 nanoarrays and their photoelectrochemical properties. *Nanoscale*, 2014, **6**, P. 3900–13909.

[7] Li Z., Cong S., Xu Y. Brookite vs anatase TiO_2 in the photocatalytic activity for organic degradation in water. *ACS Catalysis*, 2014, **4**, P. 3273–3280.

[8] Ohno T., Higo T., et al. Dependence of photocatalytic activity on aspect ratio of brookite TiO_2 nanorod and drastic improvement in visible light responsibility of a brookite TiO_2 nanorod by site-selective modification of Fe3+ on exposed faces. *J. of Molecular Catalysis A: Chemical*, 2015, **396**, P. 261–267.

[9] Mamakhel A., Yu J., et al. Facil synthesis of brookite TiO_2 nanoparticles. *Chem. Commun.*, 2020, **56**, P. 15084–15087.

[10] Vequizo J.M., Matsunaga H., et al. Trapping-induced enhancement of photocatalytic activity on brookite TiO_2 powders: comparison with anatase and rutile TiO_2 powders. *ACS Catalysis*, 2017, **7**, P. 2644–2651.

[11] Vequizo J.M., Kamimura S., Ohno T., Yamakata A. Oxygen induced enhancement of NIR emission in brookite TiO_2 powders: comparison with rutile and anatase powders. *Phys. Chem. Chem. Phys.*, 2018, **20**, P. 3241–3248.

[12] Zhao H., Liu L., Andino J.M., Li Y. Bicrystalline TiO_2 with controllable anatase-brookite phase content for enhanced CO_2 photoreduction to fuels. *J. of Materials Chemistry A*, 2013, **1**, P. 8209–8216.

[13] Fischer K., Gawel A., et al. Low-temperature synthesis of anatase/rutile/brookite TiO_2 nanoparticles on a polymer membrane for photocatalysis. *Catalysts*, 2017, **7**, P. 209–223.

[14] Kozhevnikova N.S., Ulyanova E.S., et al. Low-temperature sol-gel synthesis and photoactivity of nanocrystalline TiO_2 with the anatase/brookite structure and an amorphous component. *Kinetics and Catalysis*, 2019, **60**, P. 325–336.

[15] Vorokh A.S., Kozhevnikova N.S., et al. Facile, rapid and efficient doping of amorphous TiO_2 by pre-synthesized colloidal CdS quantum dots. *J. Alloys and Comp.*, 2017, **706**, P. 205–214.

[16] Ulyanova E.S., Zamyatin D.A., et al. Local environment of CdS nanoparticles incorporated into anatase/brookite matrix via sol-gel route: HRTEM, Raman spectroscopy and MD simulation. *Materials Today Communications*, 2020, **25**, 101465.

[17] Cong Y., Zhang J., Chen F., Anpo M. Synthesis and Characterization of nitrogen-doped TiO_2 nanophotocatalyst with high visible light activity. *J. Phys.Chem.*, 2007, **111**, P. 6976–6982.

[18] Yan J., Wu G., et al. Understanding the effect of surface/bulk defects on the photocatalytic activity of TiO_2: anatase versus ritule. *PCCP*, 2013, **15**, P. 10978–10988.

[19] Abazovic N.D., Comor M.I., et al. Photoluminescence of anatase and rutile TiO_2 particles. *J. Phys. Chem. B*, 2006, **110**, P. 25366–25370.

[20] Mathew S., Prasad A.K., et al. UV-Visible photoluminescence of TiO_2 nanoparticles prepared by hydrothermal method. *J. Pluoresc.*, 2012, **22**, P. 1593–1599.
[21] Chetibi L., Busko T., et al. Photoluminescence properties of TiO_2 nanofibers. *J. Nanopart. Res.*, 2017, **19**, 129.
[22] Zhang W.F., Zhang M.S., Yin Z., Chen Q. Photoluminescence in anatase titanium dioxide nanocrystals. *Appl. Phys. B*, 2000, **70**, P. 262–265.
[23] Preclikova J., Galar P., et al. Nanocrystalline titanium dioxide films: Influence of ambient conditions on surface- and volume-related photoluminescence. *J. of Appl. Phys.*, 2010, **108**, P. 113502.
[24] Knorr F.J., Mercado C.C., McHale J.L. Trap-state distributions and carrier transport in pure and mixed-phase TiO_2: influence of contacting solvent and interphasial electron transfer. *J. Phys. Chem. C*, 2008, **112**, P. 12786–12794.
[25] Shi J., Chen J., et al. Photoluminescence characteristics of TiO_2 and their relationship to the photoassisted reaction of water/methanol mixture. *J. Phys. Chem. C*, 2007, **111**, P. 693–699.
[26] Wang X., Feng Z., et al. Trap states and carrier dynamics of TiO_2 studied by photoluminescence spectroscopy under weak excitation conditio. *PCCP*, 2010, **12**, P. 7083–7090.
[27] Pallotti D.K., Passoni L., et al. Photoluminescence mechanisms in anatase and rutile TiO_2. *J. Phys. Chem. C*, 2017, **121**, P. 9011–9021.
[28] Mascaretti L., Russo V., et al. Excitation wavelength- and medium-dependent photoluminescence of reduced nanostructured TiO_2 films. *J. Phys. Chem. C*, 2019, **123**, P. 11292–11303.
[29] Bellardita M., Paolaa A., et al. Preparation and photoactivity of samarium loaded anatase, brookite and rutile catalysts. *Appl. Catalysis B: Environmental*, 2011, **104**, P. 291–299.
[30] Santara B., Giri P.K., Imakita K., Fujii M. Evidence for Ti interstitial induced extended visible absorption and near infrared photoluminescence from undoped TiO_2 nanoribbons: an in situ photoluminescence study. *J. Phys. Chem. C*, 2013, **117**, P. 23402–23411.
[31] Ulyanova E.S., Zamyatin D.A., Kolosov V.Yu., Shalaeva E.V. Visible light photoluminescence in TiO_2/CdS nanopowders synthesized by sol-gel route: effect of gel aging time. *Nanosystems: Phys. Chem. Math.*, 2020, **11**, P. 480–487.
[32] Lopez R., Gomez R. Band-gap energy estimation from diffuse reflectance measurements on sol-gel and commercial TiO_2: a comparative study. *J. Sol-gel Sci Technol.*, 2012, **61**, P. 1–7.
[33] Iliev M.N., Hadjiev V.G., Litvinchuk A.P. Raman and infrared spectra of brookite (TiO_2): Experiment and theory. *Vibrational spectroscopy*, 2013, **64**, P. 148–152.
[34] Ohsaka T., Izumi F., Fujiki Y. Raman Spectrum of Anatase, TiO. *J. of Raman Spectroscopy*, 1978, **7**, P. 321–324.
[35] Gupta S.K., Desai R., et al. Titanium dioxide synthesized using titanium chloride: size effect study using Raman spectroscopy and photoluminescence. *J. of Raman Spectroscopy*, 2010, **41**, P. 350–355.
[36] Sahoo S., Arora A.K., Sridharan V. Raman line shapes of optical phonons of different symmetries in anatase TiO_2 nanocrystals. *J. Phys. Chem. C*, 2009, **113**, P. 16927–16933.
[37] Georgescu D., Baia L., et al. Experimental assessment of the phonon confinement in TiO_2 anatase nanocrystallites by Raman spectroscopy. *J. of Raman Spectroscopy*, 2012, **43**, P. 876–883.
[38] Ceballos-Chuc M.C., Ramos-Castillo C.M., et al. The influence of brookite impurities on the Raman spectrum of TiO_2 anatase nanocrystals. *J. Phys. Chem. C*, 2018, **123**, P. 19921–19930.
[39] Ho Y.C., Hoque N.F., et al. Reduction of oxygen vacancy related traps in TiO_2 and the impacts on hybrid perovskite solar cells. *J. Phys. Chem. C*, 2017, **121**, P. 23939–23946.
[40] Lin H., Huang C.P., et al. Size dependency of nanocrystalline TiO_2 on its optical property and photocatalytic reactivity exemplified by 2-chlorophenol. *Appl. Catalysis B: Environmental*, 2006, **68**, P. 1–11.
[41] Moss T.S., Burrell G.J., Ellis B. *Semiconductor Opto-electronics*. Butterworths, London, 1973.
[42] Bost M.C. Mahan J.E. An investigation of the optical constants and band gap of chromium disilicide. *J. Appl. Phys.*, 1988, **63**, P. 839–844.

Submitted 31 January 2022; revised 23 June 2022; accepted 30 July 2022

Information about the authors:

Ekaterina S. Ulyanova – Institute of Solid State Chemistry of Ural Branch of the Russian Academy of Sciences, Pervomayskaya, 91, Ekaterinburg, 620990, Russia; ORCID 0000-0002-0922-3863; tsivileva.yekaterina@yandex.ru

Elizaveta V.Shalaeva – Institute of Solid State Chemistry of Ural Branch of the Russian Academy of Sciences, Pervomayskaya, 91, Ekaterinburg, 620990, Russia; ORCID 0000-0002-8617-3329; shalaeva@ihim.uran.ru

Yuriy S. Ponosov – M. N. Mikheev Institute of Metal Physics of Ural Branch of the Russian Academy of Sciences, S. Kovalevskaya, 18, Ekaterinburg, 620108, Russia; ORCID 0000-0001-5643-966X; ponosov@imp.uran.ru

Olga A. Lipina – Institute of Solid State Chemistry of Ural Branch of the Russian Academy of Sciences, Pervomayskaya, 91, Ekaterinburg, 620990, Russia; ORCID 0000-0003-3685-5337; LipinaOlgaA@yandex.ru

Alexey A. Markov – Institute of Solid State Chemistry of Ural Branch of the Russian Academy of Sciences, Pervomayskaya, 91, Ekaterinburg, 620990, Russia; ORCID 0000-0002-2454-8674; aamarkov1@yandex.ru

Conflict of interest: the authors declare no conflict of interest.

NANOSYSTEMS:
PHYSICS, CHEMISTRY, MATHEMATICS

Original article

Patil P.V., Chaudhari N.D., et al. *Nanosystems: Phys. Chem. Math.*, 2022, **13** (4), 456–463.
http://nanojournal.ifmo.ru
DOI 10.17586/2220-8054-2022-13-4-456-463

Synthesis, investigation, structural and elastic properties of $Mg_xZn_{1-x}Fe_2O_4$ nanoparticles

Pradip V. Patil[1,a], Nandkishor D. Chaudhari[2,b], Prabhakar R. Kute[2,c], Rajendra D. Kale[3,d]

[1]PG Department of Physics and Research Centre, VP's ASC College Baramati (Pune), 413133, India
[2]Department of Physics and Chemistry, Pratishthan Mahavidyalaya, Paithan (Aurangabad), 431107, India
[3]Department of Physics, Tuljaram Chaturchand College, Baramati (Pune), 413102, India

[a]vpasccphysics@gmail.com, [b]nk.dchaudhari@gmail.com, [c]kuteprabhakar@gmail.com,
[d]rajendra_kale@yahoo.com

Corresponding author: Rajendra D. Kale, rajendra_kale@yahoo.com

ABSTRACT Magnesium-Zinc Ferrite nanoparticles of different compositions are synthesized by using the sol-gel auto-combustion method with citric acid as a fuel. Structural characteristics were studied using X-ray diffraction technique and it confirms the formation of cubic spinel structure. The ferrite nanoparticle size of synthesized powder ranges from 22 – 24 nm. The effect of change in Mg^{2+} content results in a change of the lattice parameter of ferrite nanoparticles. In the present paper, the structural parameters such as cation-cation and cation-anion distances, tetrahedral, octahedral bond lengths and bond angles, hopping lengths, shared, unshared tetrahedral, and octahedral edge are reported. FTIR spectra show two prominent peaks around 524 – 532 cm^{-1} (tetrahedral site) and 409 – 432 cm^{-1} (octahedral site) and the force constants of the octahedral and tetrahedral site of Mg–Zn ferrite were calculated. The elastic moduli and other factors such as longitudinal, transverse and mean velocity, Poisson ratio, and Debye temperature were determined.

KEYWORDS Magnesium–Zinc ferrite nanoparticles, sol-gel auto-combustion method, cubic spinel structure, bond lengths and bond angles, hopping lengths, elastic moduli

FOR CITATION Patil P.V., Chaudhari N.D., Kute P.R., Kale R.D. Synthesis, investigation, structural and elastic properties of $Mg_xZn_{1-x}Fe_2O_4$ nanoparticles. *Nanosystems: Phys. Chem. Math.*, 2022, **13** (4), 456–463.

1. Introduction

Spinel ferrites are an important magnetic materials for application in different branches of biomedical, ferrofluid, microwave and data storage devices, magnetocaloric refrigeration, gas sensors, etc. due to its electronic, magnetic, and catalytic properties [1]. The promising and extensively used Mg–Zn ferrite nanoparticles are suitable for applications not only in the field of electronics [2], heterogeneous catalysis, sensors, magnetic technologies, but also in medicine for cancer treatment by hyperthermia [3] and other biomedicines [4]. Chemically and thermally stable zinc ferrite material are used for photocatalysis, magnetic resonance imaging (MRI), drug delivery, and pigments [5,6]. Rahaman and Ichiyanagi [7,8] reported that in Mg–Zn ferrite, Mg ferrite has an inverse spinel structure with Mg^{2+} cations mainly on octahedral site while Zn ferrite has a normal spinel structure in which Zn^{2+} occupies the tetrahedral site [7,9]. The cations distribution is mainly dependent on the synthesis technique and ambient conditions [10–12].

To tailor the desired properties of ferrite nanoparticles, various physical and chemical routes are used for synthesizing ferrite materials such as ceramic, co-precipitation, auto-combustion, hydrothermal, citrate precursor, etc. [13]. The preparation of Mg–Zn ferrite nanoparticles [14–16] through the Sol-Gel auto-combustion route has its importance in the area of research and development. Better control over particle size can be possible by combustion route which helps one to improve properties of the materials. Keeping in mind the importance of this synthesis route, the different compositions of Mg–Zn ferrites has been synthesized in the present work and its structural and elastic properties as a function of composition are reported.

2. Experimental

The Magnesium Nitrate $Mg(NO_3)_2 \cdot 6H_2O$, Zinc Nitrate $Zn(NO_3)_2 \cdot 6H_2O$, Ferric Nitrate $Fe(NO_3)_2 \cdot 6H_2O$, and citric acid ($C_6H_8O_7H_2O$) are used for preparing the composition of $Mg_xZn_{1-x}Fe_2O_4$ ferrite for $x = 0.0, 0.2, 0.6, 0.8,$ and 1.0. All the metal nitrates are dissolved in distilled water and are mixed with a 1:3 ratio of nitrate to citric acid. By keeping these solutions on the hot plate (90 °C) on the magnetic stirrer, the mixed solutions become viscous and finally formed into a viscous gel. This viscous gel began frothing after evaporating all water molecules' contents and the gel automatically ignited and burned with glowing flints and fully loosed powdered ash remained in the container of the gel. This powdered ash was then sintered (at 1000 °C) for four hours in an automatic temperature-controlled muffle furnace.

The structural characteristics of both of these sintered and non-sintered ferrite powder were studied by FTIR spectrometer (IRAffinity – 1S WL of Shimadzu Corporation, Japan) and powder X-ray diffractometer (BRUKER D8).

3. Results and discussion

3.1. X-ray diffraction(XRD)

Figures 1 and 2 show the X-ray diffraction patterns for $Mg_xZn_{1-x}Fe_2O_4$ ferrite compositions (both non-sintered and sintered) and confirm the formation of single-phase cubic spinel structure of ferrites. All the compositions also show the characteristics reflections of cubic spinel ferrites and confirm the formation of cubic spinel structure without any signs of the secondary phase. The peaks (222), (311), (222), (400), (422) were indexed using JCPDS. X-ray diffraction patterns clearly show the sintering temperature-dependent increase in peak intensity confirming the crystallinity increase with simultaneous decrease of full width at half maxima (FWHM).

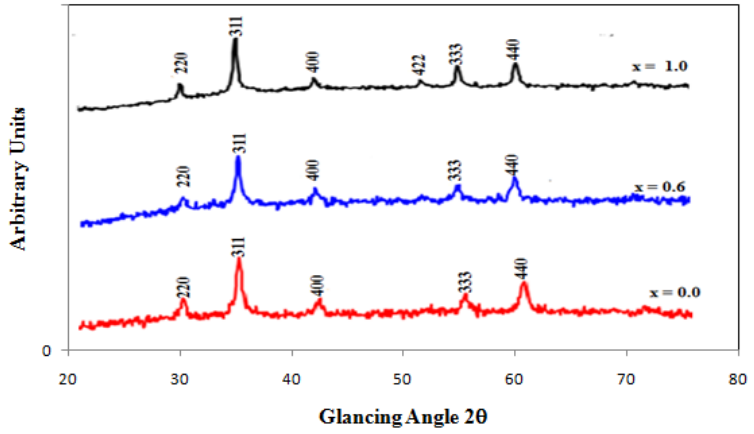

FIG. 1. XRD pattern of non-sintered (as synthesized) $Mg_xZn_{1-x}Fe_2O_4$ ferrite

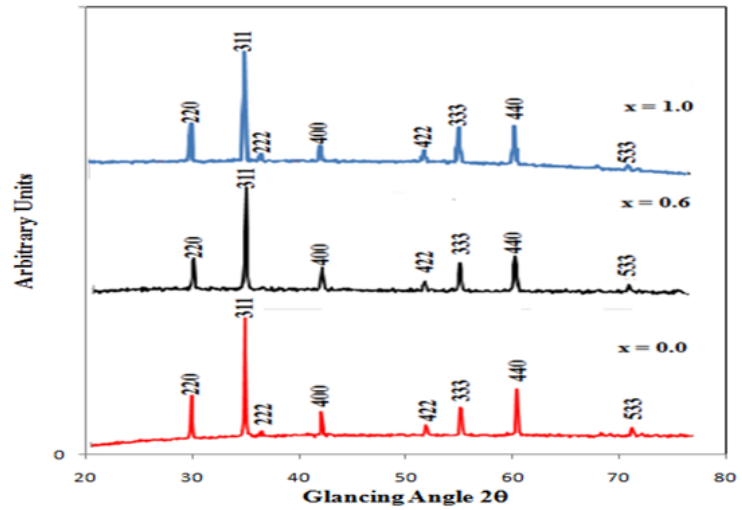

FIG. 2. XRD pattern of sintered $Mg_xZn_{1-x}Fe_2O_4$ ferrite

The broadening of the most prominent peaks (311) of synthesized powder of all compositions is used for the analysis of crystallite size. The Debye–Scherrer formula was used to calculate crystallite size of ferrite nanoparticles, $D_{311} = \dfrac{k\lambda}{\beta \cos\theta}$, where, $k = 0.9$ is a crystallite size constant, λ is the wavelength of radiation, θ is the diffraction angle and β is the full width at half maximum (FWHM) of intensity for (311) peak. Experimental lattice parameters were obtained using relation $a_{exp} = d_{hkl}[h^2 + k^2 + l^2]^{1/2}$ while the theoretical lattice parameter [17] was calculated by the following relation:

$$a_{th} = \frac{8}{3}\sqrt{3}\left[(r_A + R_0) + \sqrt{3}\,(r_B + R_0)\right]. \tag{1}$$

Here, $R_0 = 1.38$ Å is the oxygen ion radius, ionic radii of the tetrahedral [A] and the octahedral [B] sites are r_A, r_B, respectively.

Both these experimental and theoretical lattice parameters for the present ferrite composition are listed in Table 1. The decrease in both the theoretical and experimental values of lattice constant (a) confirms the increase in Mg^{2+} content from 8.441 to 8.349 Å, clearly obeying Vagard's Law [18]. The difference in the ionic radii of replaced and replacing ions causes this abetment, which depicts the linear change in the lattice constant with the substation of different ions. The ionic radii difference of Mg^{2+} (0.65 Å) and Zn^{2+} (0.83 Å) causes the diminution of the lattice constant. Manikandan et al. [1] and Rahman [7] also reported similar results. The X-ray density was calculated by relation $\rho_x = \dfrac{ZM}{Na^3}$ and the bulk density or actual density was obtained by making the pellet of synthesized material, using relation $\rho_a = \dfrac{m}{\pi r^2 h}$. Here m is the mass, r is the radius and h is the thickness of the pellet.

TABLE 1. Lattice Parameter (a_{exp} and a_{th}), Crystallite size (D), X-ray density (ρ_x), actual density (ρ_a) [± 0.006]

x	a_{exp} (Å)	a_{th} (Å)	D (nm)	ρ_x (gm/cc)	ρ_a (gm/cc)
0.00	8.349	8.441	22.6	5.325	4.635
0.20	8.331	8.423	23.4	5.176	4.759
0.40	8.310	8.402	23.4	5.030	4.568
0.60	8.302	8.394	22.8	4.860	4.237
0.80	8.276	8.368	23.5	4.719	4.108
1.00	8.349	8.441	23.8	4.565	4.059

The bond length (d_{AX}, d_{BX}) site radii (r_A, r_B), tetrahedral edge (d_{XX}), octahedral edges (shared and unshared) (d'_{XX}, d''_{XX}), hoping length radii (L_A, L_B) are calculated by the following relations. The corresponding values are presented in Table 2.

$$\begin{gathered} d_{AX} = a\sqrt{3}(u - \frac{1}{4}), \quad d_{BX} = a\sqrt{3u^2 - \frac{11}{4}u + \frac{43}{64}}, \quad d_{XX} = a\sqrt{2}(2u - \frac{1}{2}), \\ d'_{XX} = a\sqrt{2}(1 - 2u), \quad d''_{XX} = a\sqrt{4u^2 - 3u + \frac{11}{16}}, \quad L_A = a\frac{\sqrt{3}}{4}, \quad L_B = a\frac{\sqrt{2}}{4}. \end{gathered} \tag{2}$$

TABLE 2. Hopping lengths (L_A, L_B), bond length (d_{AX}, d_{BX}), site radii (r_A, r_B), tetrahedral edge (d_{XX}), shared and unshared octahedral edges (d'_{XX}, d''_{XX}) for present ferrite composition [± 0.0004]

x	L_A	L_B	d_{AX}	d_{BX}	r_A	r_B	d_{XX}	d'_{XX}	d''_{XX}
0.00	3.6551	2.9843	1.8275	2.1103	0.4475	0.7302	2.9844	2.9843	2.9843
0.20	3.6473	2.978	1.8236	2.1058	0.4436	0.7257	2.9779	2.978	2.978
0.40	3.6382	2.9706	1.8190	2.1005	0.4391	0.7205	2.9705	2.9706	2.9706
0.60	3.6347	2.9677	1.8173	2.0985	0.4374	0.7185	2.9677	2.9677	2.9677
0.80	3.6235	2.9585	1.8117	2.0920	0.4317	0.7120	2.9585	2.9585	2.9585
1.00	3.6152	2.9518	1.8076	2.0873	0.4276	0.7072	2.9518	2.9518	2.9518

The values of all these parameters clearly show the effect of an increase in Mg^{2+} content in the composition which is related to larger values of Zn^{2+} ions as compared to Mg^{2+} ions. This substitution dependent bond length change for tetrahedral and octahedral sites was reported by Vara Prasad et al. [19]. The hopping length behavior may be attributed to the ionic radii difference and causes the decrease in hopping length [20].

The lattice and oxygen parameter variation in terms of cation-cation [Me–Me] and cation-anion [Me–O] bond length and bond angles [21, 22] are obtained using relations. Particularly, cation-cation [Me–Me] bond lengths are as follows :

$$b = \sqrt{2}\frac{a}{4}, \quad c = \sqrt{11}\frac{a}{8}, \quad d = \sqrt{3}\frac{a}{4}, \quad e = \sqrt{3}\frac{3a}{8}, \quad f = \sqrt{6}\frac{a}{4}, \tag{3}$$

cation-anion [Me–O] bond lengths:

$$p = a\left(\frac{5}{8} - u\right), \quad q = a\left(u - \frac{\sqrt{3}}{4}\right), \quad r = a\left(u - \frac{\sqrt{11}}{4}\right), \quad s = a\left(\frac{u}{3} + \frac{1}{8}\right)\sqrt{3}. \tag{4}$$

Here $u = \dfrac{5\sqrt{3}l_A^T + 6l_A^o}{8\left[\sqrt{3}l_A^T + 3l_A^o\right]}$ for normal spinel and $u = \dfrac{5}{8} - \dfrac{9l_A^o}{8\left[\sqrt{3}l_B^T + 3\frac{Z_A l_A^o + Z_B l_B^o}{Z_A + Z_B}\right]}$ for inverse spinel structure [21].

The values of all these parameters in Table 3 show that both these [Me–Me] and [Me–O] bond lengths decreases due to an increase in ions of Mg^{2+} in the composition. The variation in the ionic radii of Mg^{2+} and Zn^{2+} ions and the lattice constant affects the changes in the bond length of all the compositions.

TABLE 3. Cation-cation [Me–Me] and cation-anion [Me–O] bond length for present ferrite composition [± 0.0004]

x	cation-cation					cation-anion			
	b	c	d	e	f	p	Q	r	s
0.00	2.9843	3.4995	3.6551	5.4825	5.1690	2.1102	1.8275	3.4994	3.6551
0.20	2.9779	3.4920	3.6473	5.4709	5.1580	2.1057	1.8236	3.4919	3.6473
0.40	2.9705	3.4833	3.6382	5.4572	5.1451	2.1005	1.8190	3.4832	3.6382
0.60	2.9677	3.4800	3.6347	5.4520	5.1402	2.0985	1.8173	3.4799	3.6347
0.80	2.9585	3.4692	3.6235	5.4352	5.1243	2.0920	1.8117	3.4691	3.6235
1.00	2.9518	3.4613	3.6152	5.4228	5.1127	2.0872	1.8076	3.4613	3.6152

The concentration-dependent bond angles (θ_1, θ_2 , θ_3, θ_4, θ_5) shown in Fig. 3 were calculated by trigonometric relations [21] and were found to be 125.25 close to ideal and reported values [23] for all compositions of Ni–Zn ferrite.

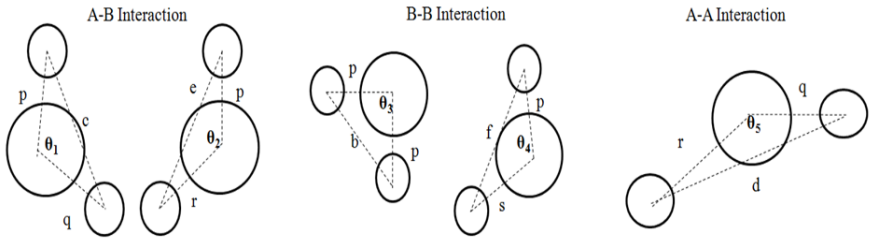

FIG. 3. Spinel structure with bond length and bond angles

$$\theta_1 = \cos^{-1}\left[\frac{(p^2+q^2-c^2)}{2pq}\right], \quad \theta_2 = \cos^{-1}\left[\frac{(p^2+r^2-c^2)}{2pr}\right], \quad \theta_3 = \cos^{-1}\left[\frac{(2p^2-b^2)}{2p^2}\right],$$
$$\theta_4 = \cos^{-1}\left[\frac{(p^2+s^2-f^2)}{2ps}\right], \quad \theta_5 = \cos^{-1}\left[\frac{(r^2+q^2-d^2)}{2rq}\right]. \tag{5}$$

3.2. FTIR study

The Fourier transforms IR spectroscopy is useful to determine the crystalline symmetry. It is used for the analysis of spinel structure formation in ferrites. Fig. 4 shows FTIR spectra of sintered ferrite nanoparticles of $Mg_xZn_{1-x}Fe_2O_4$ for $x = 0.0, 0.6, 1.0$ composition.

As shown in the Fig. 4, FTIR spectra for these compositions depict the spinel structure formation of ferrite by absorption dip corresponding to tetrahedral and octahedral vibrational complexes at around 528 – 465 and 409 – 432 cm^{-1} respectively. The increase in Mg^{2+} concentration results in the shifting of the wavenumber of band: υ_1 shifts towards higher values and υ_2 shifts towards lower values. The tetrahedral site is occupied by Zn^{2+} ions with a larger ionic radius which affects the band position. The stretching of tetrahedral ions and oxygen bonding causes absorption band ν_1 while the transverse vibrations of oxygen with tetrahedral sites cause band υ_2. Absorption band ν_1 with the intrinsic vibration

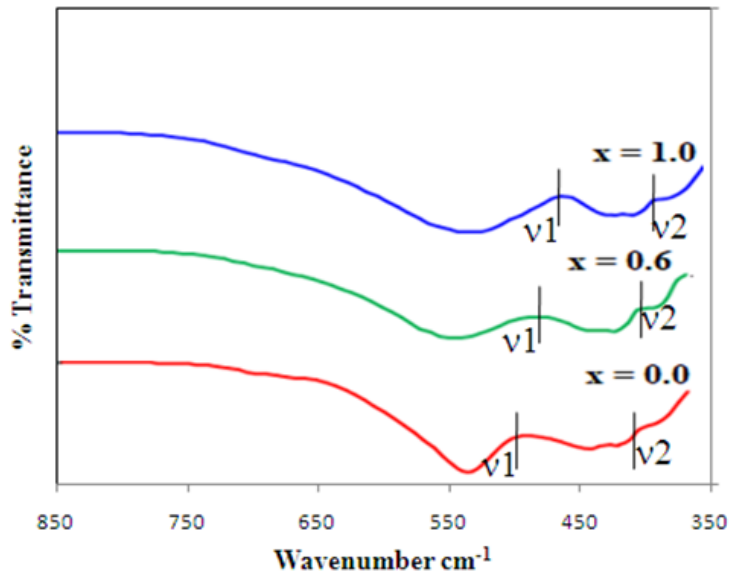

FIG. 4. FTIR spectra for sintered $Mg_xZn_{1-x}Fe_2O_4$ ferrite composition for $x = 0.0, 0.6, 1.0$

of tetrahedral groups corresponds to the restoring force and band ν_2 of octahedral groups corresponds to bond bending vibrations [24].

The difference in Fe^{3+}–O^{2-} distance of A and B site also reflects the dissent between the positions of both ν_1, ν_2 bands in FTIR spectra. In the present work, the absorption bands for the present ferrite composition (Mg–Zn) were found close to the reported values. Table 4 shows force constants for the tetrahedral and octahedral sites calculated in [25] using the following formulas, $K_t = 7.62 \times M_1 \times \upsilon_1^2 \times 10^{-7}$ N/m and $K_0 = 10.62 \times \frac{M_2}{2} \times \upsilon_2^2 \times 10^{-7}$ N/m, where, K_t, K_0 are the force constants, M_1, M_2 are the molecular weights and ν_1, ν_2 are the vibrational bands corresponding to tetrahedral and octahedral sites, respectively.

TABLE 4. Vibrational bands, force constants, longitudinal modulus (L), shear modulus (G), bulk modulus (B), Young modulus (E)

x	ν_1 (cm^{-1})	ν_2 (cm^{-1})	K_t (N/m)	K_0 (N/m)	L (GPa)	G (GPa)	B (GPa)	E (GPa)
0.00	490	415	136.79	110.68	146.59	48.86	81.44	122.16
0.20	526	426	133.82	101.55	139.70	46.57	77.62	116.42
0.40	526	428	129.8	96.37	134.58	44.86	74.77	112.15
0.60	492	402	128.66	82.4	125.71	41.90	69.84	104.76
0.80	528	412	122.68	77.93	119.85	39.95	66.59	99.88
1.00	465	392	120.44	71.19	114.76	38.25	63.76	95.63

The force constants values from Table 4 show decrement in force constant K_0 and K_t as a function of increasing Mg^{2+} content in all compositions, such that $K_t > K_0$.

The elastic parameter and Debye temperature [24, 26] are calculated here using frequency band relation $\theta_1 = 1.438\upsilon_{av}$, where $\upsilon_{av} = \left(\frac{\upsilon_1 + \upsilon_2}{2}\right)$. The Debye temperature variation from 676 to 687 K regulates the heat conduction mechanism in the ferrites. Based on specific heat theory and the heat conduction mechanism, a decrease in Debye temperature with an increase in Mn content in Li–Mn ferrites also was reported in [27].

Debye temperature (θ_D) was calculated using the density of the sample, the molecular weight and the mean wave velocity in accordance with the following relation:

$$\theta_D = \frac{h}{K_B}\left(\frac{3\rho q N_A}{4\pi M}\right)^{1/3} V_m, \tag{6}$$

where h is Planck's constant, K_B is Boltzmann's constant, N_A is Avogadro's number, M is the molecular weight, q is the number of atoms in unit formula, ρ is the density of the sample [28].

The product of the stiffness constant ($C_{11} = L$; Longitudinal modulus) and the lattice constant (a) was used to obtain elastic moduli [29] estimation by the force constant ($K = (K_t + K_0)/2$). The pore fraction ($p = 1 - \rho_a/\rho_x$) for each composition was obtained using the corresponding values of the X-ray density (ρ_x) and the bulk density (ρ_a).

The longitudinal wave velocity (V_L) and the transverse wave velocity (V_T) [30] were determined by, $V_L = \left(\frac{C_{11}}{\rho_x}\right)^{1/2}$ and $V_T = \frac{V_L}{\sqrt{3}}$. Similarly, the shear modulus (G), the bulk modulus (B), the Young modulus (E), Poisson's ratio (σ), the mean wave velocity (V_m) [31] are determined using the following relations,

$$G = \rho \times (V_T)^2, \quad B = L - \left(\frac{4}{3}\right) G, \quad E = (1+\sigma)\, 2G, \quad \sigma = \frac{3B - 2G}{6B + 2G}, \quad V_m = \left[\frac{1}{3}\left(\frac{1}{{V_L}^3} + \frac{2}{{V_T}^3}\right)\right]^{-1/3}. \quad (7)$$

The elastic moduli and the wave velocity values are listed in Table 5. This elastic moduli value depicts the dependence on the Mg^{2+} content due to weaken interatomic bonding. The effect of changes in the interatomic bonding strength on the elastic parameters with Zn^{2+} content in Zn–Co ferrites was reported in works [32, 33].

TABLE 5. The longitudinal wave velocity and the transverse wave velocity, the mean wave velocity (V_m), Poisson's ratio ($\sigma \pm 0.06$), the elastic moduli corrected to zero porosity (E_0, G_0, B_0, L_0, σ_0)

x	V_L (m/s)	V_T (m/s)	V_M (m/s)	E_0 (GPa)	G_0 (GPa)	B_0 (GPa)	L_0 (GPa)	σ	σ_0
0.00	5623.8	3246.9	3604.66	165.054	60.08	95.57	186.346	0.25	0.21
0.20	5418.2	3128.2	3472.89	138.84	55.28	94.79	168.49	0.25	0.25
0.40	5427.9	3133.8	3479.11	137.51	54.70	94.27	167.21	0.25	0.26
0.60	5447	3144.8	3491.35	141.01	55.93	98.15	172.73	0.25	0.26
0.80	5401.5	3118.6	3462.21	134.91	53.51	93.96	165.31	0.25	0.26
1.00	5317.3	3069.9	3408.2	122.98	48.85	84.95	150.09	0.25	0.26

The transverse propagation of energy keeps the particles in vibration mode that results in the collisions. Hence, more energy is needed during the transverse wave propagation than for the longitudinal wave [34].

The Debye temperature is used to determine the mode of vibrations and the rigidity of the ferrite material. From Table 6, it is observed that the Debye temperature obtained from the Waldron equation is greater than that obtained from the Anderson equation. Similar behavior was observed by Mazen and Elsaad [35] for Li–Mn ferrite. Both Debye temperatures show decreasing trend with increasing Mg^{2+} content. According to the theory of specific heat, part heat absorbed by electrons causes a decrease in the Debye temperature (θ_D) [35]. It is suggested that the conduction is due to electron in the synthesized ferrite material.

TABLE 6. Debye temperatures (θ_D, θ_1), B_0/G_0 ratio [± 0.08]

x	θ_D (K)	θ_1 (K)	B_0/G_0
0.00	460.84	687.36	1.70
0.20	456.79	684.48	1.71
0.40	456.84	685.92	1.72
0.60	452.68	676.57	1.75
0.80	450.07	675.86	1.75
1.00	447.28	676.58	1.87

These two temperature relations (θ_D, θ_1) reflect the dependence of Mg^{2+} content. The elastic moduli do not show any significant dependence on porous polycrystalline ferrites by nature [36]. The magnitudes of the elastic moduli corrected to zero porosity are higher than non-corrected to zero porosity.

The Pugh criteria [37], the ratio of the Bulk modulus and the Rigidity modulus B_0/G_0, is used to decide ductility and brittleness of synthesized material. The ratio greater than the critical value of 1.75 indicates the ductile nature and the ratio lower than 1.75 indicates the brittle nature. In the present case, the ratio B_0/G_0 for all the compositions presented in Table 6 varies between 1.70 and 1.87. It leads to the conclusion that the compositions with $x = 0.60$ and 0.80 are ductile and the remaining are brittle.

4. Conclusions

Compositions of $Mg_xZn_{1-x}Fe_2O_4$ with $x = 0.0, 0.2, 0.4, 0.6, 0.8$, and 1.0 were successfully synthesized using sol-gel auto-combustion process. Both the X-ray diffraction and FTIR spectra of non-sintered (as-synthesized) and sintered compositions confirm the formation of cubic spinel structure. The crystallite size lies within the 22 – 24 nm for all compositions. An increase in Mg^{2+} content shows a decrease in the lattice constant from 8.441 to 8.349 Å and verifies Vagard's law. There is a decrease in the structural parameters such as tetrahedral, octahedral bond lengths, cation-cation, cation-anion distances, bond angles, hopping length with the increase in Mg^{2+} content. Two absorption bands of FTIR spectra depict tetrahedral site 524 – 532 cm^{-1} and octahedral site at 409 – 432 cm^{-1}. Tetrahedral absorption band υ_1 shifts towards higher values and octahedral absorption band υ_2 shifts towards lower values when there is an increase of Mg^{2+} concentration. The force constants for tetrahedral and octahedral sites show Mg^{2+} content dependence. FTIR data also depict that the increase in Mg^{2+} content affects the changing of the wave velocity, the elastic constants, and the Debye temperature. All the elastic moduli are corrected to zero porosity. The bulk modulus to the rigidity modulus ratio found to vary between 1.70 and 1.87 which leads to the conclusion that the compositions with $x = 0.60$ and 0.80 are more ductile than their counterparts (brittleness).

References

[1] Manikandam A., Judith Vijaya J., et al. Optical and magnetic properties of Mg-doped $ZnFe_2O_4$ nanoparticles prepared by rapid microwave combustion method. *Superlattices and Microstructures*, 2013, **64**, P. 118–131.

[2] Kopaev A.V., Bushkova V.S. Application of the Electron Theory of Sintering to the Ferrite Systems. *Acta Phys. Pol., A*, 2010, **117**, P. 30–33.

[3] Pulisova P., Kovac J., Voigt A., Raschaman P. Structure and magnetic properties of Co and Ni nano-ferrites prepared by atwo step direct microemulsions synthesis. *J. Magn. Magn. Mat.*, 2013, **341**, P. 93–99.

[4] Rodriguez P.Y.R., Hernandez D.A.C., et al. Structural and magnetic properties of Mg–Zn ferrites prepared by sol-gel method. *J. Magn. Magn. Mat.*, 2017, **427**, P. 268–271.

[5] Koseoglu Y., Baykal A., et al. Synthesis and characterization of $ZnFe_2O_4$ magnetic nanoparticles via a PEG-assisted route. *J. Alloys and Comp.*, 2008, **462**, P. 209–213.

[6] Qiu J., Wang C., Gu M. Photocatalytic properties and optical absorption of zinc ferrite nanometer films. *Mater. Sci. Eng. B*, 2004, **112**, P. 1–4.

[7] Rahman S., Nadeem K., et al. Structural and magnetic properties of ZnMg-ferrite nanoparticles prepared using the co-precipitation method. *Ceram. Int.*, 2013, **39**, P. 5235–5239.

[8] Ichiyanagi Y., Kubota M., et al. Magnetic properties of Mg ferrite nanoparticles. *J. Magn. Magn. Mat.*, 2007, **310**, P. 2378–2380.

[9] Thummer K.P., Chhantbar M.C., et al. Localized canted spin behavior in $Zn_XMg_{1.5-X}Mn_{0.5}Fe_2O_4$ spinel ferrite system. *J. Magn. Magn. Mat.*, 2004, **28**, P. 23–30.

[10] Qunnunkad S., Winotal P., Phanichphant S. Cation distribution and magnetic behavior of $Mg_{1-X}Zn_XFe_2O_4$ ceramics monitored Mossbauer Spectroscopy. *J. Electroceram.*, 2006, **16**, P. 363–368.

[11] Gismelseed A.M., Mohammed K.A., et al. Structure and magnetic properties of $Zn_XMg_{1-X}Fe_2O_4$ ferrites. *J. Phys. Conf. Ser.*, 2010, **217**, 012138.

[12] Da Silva S.W., Nakagomi F., et al. Effect of Zn content in the structural and magnetic properties of $Zn_XMg_{1-X}Fe_2O_4$ mixed ferrites monitored by Raman and Mossbauer spectroscopies. *J. Appl. Phys.*, 2010, **107** (9), 09B503.

[13] Ajitanshu Vedrtnam, Kishor Kalauni, Sunil Dubey, Aman Kumar. A comprehensive study on structure, properties, synthesis and characterization of ferrites. *AIMS Materials Science*, 2020, **7** (6), P. 800–835.

[14] Md Atiqur Rahman, Mohammad Tariqul Islam, et al. Synthesis and characterization of Mg–Zn ferrite based flexible microwave composites and its application as SNG metamaterial. *Scientific Reprots*, 2021, **11**, 7654.

[15] Pankaj P. Khirade, Apparao R. Chavan, et al. Tuning of physical properties of multifunctional Mg–Zn spinel ferrite nanocrystals: a comparative investigations manufactured via conventional ceramic versus green approach sol-gel combustion route. *Mater. Res. Express*, 2020, **7**, P. 1–16.

[16] Thomas Dippong, Erika Andrea Levei, Oana Cadar. Recent advances in synthesis and applications of MFe_2O_4 (M = Co, Cu, Mn, Ni, Zn) Nanoparticles. *Nanomaterials (Basel)*, 2021, **11** (6), 1560.

[17] Kazi Haruum Maria, Choudhary Shamima, Hakim, M.A. Structural transformation and hysteresis behavior of Cu–Zn ferrites. *Inter. Nano. Letters*, 2013, **3**, 42.

[18] Pervaiz E., GulI. H. High frequency response, DC resistivity and magnetic studies of holomium substituted Ni-ferrite: A novel electromagnetic material. *J. Magn. Magn. Mat.*, 2014, **349**, P. 27–34.

[19] Prasad V.B.B.V.S. Cation distribution, structural and electric studies on cadmium substituted nickel zinc ferrites. *Mod. Phys. Lett. B*, 2014, **28** (19), 1450155.

[20] Talanov V.M.. Calculation of structural parameters of spinels. *Phys. Stat. Sol. B*, 1981, **106**, P. 99–106.

[21] Khot V.M., Salunkhe A.B., et al. Low temperature synthesis of $Mn_XMg_{1-X}Fe_2O_4$ ($x = 0$ –1) nanoparticles: Cation distribution, structural and magnetic properties. *J. Phys. D Appl. Phys.*, 2013, **46**, 055303

[22] Penchal Reddy M., Balkrishna G., et al. Structural, magnetic and electrical properties of NiCuZn ferrites prepared by microwave sintering method suitable for MLCI applications. *J. Physics Chem. Solids*, 2010, **71** (9), P. 1373–1380.

[23] Vara Prasad B.B.V.S., Rajesh Babu B., Siva Ram Prasad M. Structural and dielectric studies of Mg^{2+} substituted Ni–Zn ferrites. *Material Science – Poland*, 2015, **33** (4), P. 806–815.

[24] Waldron R.D. Infrared spectra of ferrites. *Physical Review*, 1955, **99** (6), P. 1727–1735.

[25] Pathak T.K., Buch J.J.U., et al. Infrared spectroscopy and elastic properties of nanocrystalline Mg–Mn ferrites prepared by co-precipitation technique. *J. Nanoscience and Nanotechnology*, 2008, **8**, P. 4181–4187.

[26] Mazen S.A., Zaki H.M., Mansour S.F. Infrared absorption and dielectric properties of Mg–Zn ferrite. *Int. J. Pure and Applied Physics*, 2007, **3** (1), P. 40–48.

[27] Kazi H.M., Choudhary S., Hakim M.A. Structural phase transformation and hysteresis behavior of Cu–Zn ferrites. *Int. Nano. Letters*, 2013, **3** (42), P. 1–10.

[28] Anderson O.L. *Physical Acoustics*, Vol. III, Part B, Academic Press, NY, 1965.

[29] Kakani S.L., Hemrajani C. *Text Book of Solid State Physics*, 3rd Edition, S. Chand and Sons, New Delhi, 1997.

[30] Wooster W.A. Physical properties and atomic arrangements in crystals. *Rep. Prog. Phys.*, 1953, **19**, P. 62–82.
[31] Baldev Raj, V., Rajendran P., Palanichamy. *Science and Technology of Ultrasonics*, Narosa Pub. House, New Delhi, 2004.
[32] Lakhani V.K., Modi K.B. Al^{3+} modified elastic properties of copper ferrite. *Solid State Sci.*, 2010, **12** (12), P. 2134–2143.
[33] Waldron R.D. Infrared spectra of ferrite. *Physical Review*, 1995, **99** (6), P. 1727–1735.
[34] Patil V.G., Shirsath S.E., et al. Effect of zinc substitution on structural and elastic properties of cobalt ferrite. *J. Alloys and Comp.*, 2009, **488**, P. 199–203.
[35] Mazen S.A., Abu-Elsaad N.I. IR spectra, elastic and dielectric properties of Li–Mn ferrite. *Hindawi Research Article*, 2012, 907257.
[36] Hasselmann D.P.N., Fulrath R.M. Effect of small fraction of spherical porosity on elastic moduli of glass. *J. Am. Ceram. Soc.*, 1964, **47**, P. 52–53.
[37] Pugh S.F. Relation between the elastic moduli and the plastic properties of polycrystalline pure metals. *Phil. Mag.*, 1954, **45**, P. 823–843.

Submitted 8 March 2022; revised 7 June 2022; accepted 5 July 2022

Information about the authors:

Pradip V. Patil – PG Department of Physics and Research Centre, VP's ASC College Baramati (Pune), 413133, India; vpasccphysics@gmail.com

Nandkishor D. Chaudhari – Department of Physics and Chemistry, Pratishthan Mahavidyalaya, Paithan (Aurangabad), 431107, India; nk.dchaudhari@gmail.com

Prabhakar R. Kute – Department of Physics and Chemistry, Pratishthan Mahavidyalaya, Paithan (Aurangabad), 431107, India; kuteprabhakar@gmail.com

Rajendra D. Kale – Department of Physics, Tuljaram Chaturchand College, Baramati (Pune), 413102, India; rajendra_kale@yahoo.com

Conflict of interest: the authors declare no conflict of interest.

NANOSYSTEMS:
PHYSICS, CHEMISTRY, MATHEMATICS

Dubey R.S., Venkatesh Yepuri. *Nanosystems: Phys. Chem. Math.*, 2022, **13** (4), 464–467.
http://nanojournal.ifmo.ru
DOI 10.17586/2220-8054-2022-13-4-464-467

Original article

Sol-gel spin coating of dielectric reflector for energy harvesting and heat shielding applications

Raghvendra S. Dubey[1], Venkatesh Yepuri[2]

[1]Department of Nanotechnology, Swarnandhra College of Engineering and Technology, Seetharampuram, Narsapur (A.P.), India

[2]Department of Electrical and Electronics Engineering, Swarnandhra College of Engineering and Technology, Seetharampuram, Narsapur (A.P.), India

Corresponding author: Venkatesh Yepuri, Venkatesh.yepuri555@gmail.com

ABSTRACT There are seasonal changes in the environment temperature which leads to additional usage of various devices like air-conditioners in the summer season and space heaters in the winter season. The usage of this equipment incurs increased consumption of electricity that can result in increased usage costs. High usage of air conditioners also releases large amounts of fluorocarbons that can contribute to global warming. Hence, to minimize the usage of air-conditioners and to protect from the seasonal temperature changes it is necessary to mold the light, which can be done by dielectric optical coatings. These coatings are derived from the thin films of varying refractive index that can be fabricated by many bottom-up techniques available in nanotechnology. Herein, we report one of the bottom-up technique i.e., sol-gel spin coating technique for the fabrication of a dielectric reflector that can serve as a window for the seasonal temperature changes by filtering the ultraviolet and near-infrared spectra. The fabricated reflector was investigated with FE-SEM for thickness and layer identification and UV-VIS-NIR spectroscopy analysis for the reflectance analysis.

KEYWORDS Ultraviolet and infrared radiation, sol-gel spin coating, dielectric reflector, smart window

FOR CITATION Dubey R.S., Venkatesh Yepuri Sol-gel spin coating of dielectric reflector for energy harvesting and heat shielding applications. *Nanosystems: Phys. Chem. Math.*, 2022, **13** (4), 464–467.

1. Introduction

Seasonally, the environment's temperature and meteorological conditions alter. The presence of UV and infrared radiations in the solar spectrum are principally responsible for the shift in temperatures and its repercussions, which can cause major harm to human organs [1, 2]. Due to their high exposure, skin, the most important organ of the human body, is prone to tanning and burning. UV radiation causes cataracts and retinal damage in the eyes, which can lead to blindness [3]. Humans are responding to the seasonal temperature variations by installing luxury items such as air-conditioners, space heaters, and air-coolers. Increased use of the aforesaid luxury equipment increases electrical consumption and emits chlorofluorocarbons (CFCs), which deplete the ozone layer by destroying hundreds of ozone molecules [4]. Protecting against these dangerous radiations can be accomplished by reflecting light back into the atmosphere through reflecting surfaces/reflectors. Reflectors are passive optical components that can be made from thin metal and dielectric sheets. Metal surfaces, on the other hand, are of little appeal because to their poor fading resistance and expensive maintenance costs [5]. Dielectric reflectors, which are made of dielectric materials with variable refractive index, are an alternative to metallic reflectors [6, 7], which can undergo constructive interference, resulting in a dazzling reflection pattern. TiO_2 with its refractive index 2.4 and SiO_2 with its refractive index 1.5 are the dielectric materials with a high refractive index contrast among dielectric materials which has the capability to result in a broad stop band for the desired wavelength spectrum [8].

Typically, dielectric reflectors are made via bottom-up nanotechnology processes, which include both expensive and inexpensive ways. It is necessary for the researcher to keep the reflector's fabrication costs low enough to cover the electrical costs associated with air conditioners and space heaters. Vapor based techniques such as chemical and physical vapor deposition are considered as the expensive techniques, whereas sol-gel dip-coating, spray pyrolysis and spin coating are considered as the inexpensive techniques. Out of the inexpensive bottom-up techniques, sol-gel spin coating technique is considered as the finest method due to its flexibility in tuning the process parameters (precursor, catalyst, spin speed and temperature) and its ease in operation [9]. The proper tuning of the process parameters can identify the reflectors in the mentioned spectral region with the minimal number of layers. Venkatesh et al. fabricated dielectric reflectors with TiO_2 and SiO_2 by varying the process parameters of sol-gel spin coating [10]. XRD, AFM and spectroscopic ellipsometry investigations on the fabricated thin films endorsed increase in precursor and catalyst concentration can increase the grain size and hence refractive index. This study identified a dielectric reflector for the near-infrared wavelength spectrum

with only five layers of TiO_2/SiO_2 and also proved as a smart window by evidencing 105 °C temperature difference between in and out temperatures when studied with infrared source. Furthermore, the research identified 80 % reflection in the ultraviolet region along with the near-infrared region with the mentioned five layers. Hu et al. fabricated dielectric reflector with dense and porous films of TiO_2 by adding different amounts of polystyrene using sol-gel spin coating technique [11]. Ellipsometry investigations endorsed refractive indices of dense and porous TiO_2 as 2.17 and 1.49 with thicknesses about 24 and 115 nm respectively. The study evidenced the effect of number of pairs from in increasing the reflectance from 60 to 90 % by tuning the multilayer structures from 2.5 to 6.5. Further increase in the number of layers of the structure identified 100 % reflectance in the ultraviolet region. Ma et al. prepared a reflector with poly methyl methacrylate (PMMA) and TiO_2 using sol-gel spin coating technique by increasing the number of pairs from 2 to 6 [12]. Ellipsometry investigations identified refractive indices of PMMA and TiO_2 as 1.395 and 1.780 with thicknesses about 55 and 112 nm respectively. The study suggested increased number of pairs for the enhanced reflectance and shifting the stop-band towards higher wavelengths. Venkatesh et al. presented ultraviolet and near-infrared reflector with TiO_2/SiO_2 using sol-gel spin coating technique [13]. The study presented the influence of precursor and catalyst in shifting the stop band towards higher wavelengths. The cross-sectional FE-SEM investigations evidenced that increased precursor and catalyst concentrations can result in increased thickness of the multilayer structures. Finally, the change in thickness of the multilayer structures evidenced shift in the stop band from ultraviolet to infrared region. Romanova et al. deposited thin films of TiO_2/SiO_2 using sol-gel spin coating technique with thicknesses about 90 and 60 nm respectively [14]. The multilayer structure was fabricated with 12 layers and studied its reflectance through UV-vis spectroscopy technique. The as-fabricated reflector endorsed 100 % reflectance in the near-infrared region. Furthermore, the theoretical studies exactly correlated and supported the experimental studies.

The primary purpose of this study is to offer a low-cost method for producing a dielectric reflector capable of reflecting both harmful ultraviolet and infrared radiations utilising a multilayer $TiO_2/SiO_2/TiO_2$ structure. Section 2 presented below reports the experimental fabrication of the three layers along with the molar ratios of the various chemicals and spin coating parameters involved and further the Section 3 demonstrates the analysis on the fabricated reflector using cross-sectional field emission scanning electron microscopy (FESEM) and ultraviolet visible near-infrared (UV-VIS-NIR) spectroscopy. These structures can be used in office buildings, school buildings, and automobiles to shield people from the above-mentioned hazardous radiation.

2. Materials and methods

For the synthesis of TiO_2 sol solvent ethanol: precursor TTIP (Titanium isopropoxide): catalysts: acetic acid, HCl and H_2O in the molar ratios of 2.5:0.75:0.75:0.01:1 respectively. Similarly, SiO_2 sol was synthesized by considering solvent ethanol: precursor TEOS (Tetra ethyl orthosilicate): catalysts: acetic acid, HCl, and H_2O in the molar ratios of 2.5:0.75:0.75:0.01:1 respectively. The precursors TTIP and TEOS were purchased from sigma Aldrich, solvent from Changshu Hongsheng, HCl from Fischer scientific and acetic acid from Sisco research laboratories. All the chemicals were of analytical grade which doesn't require any further purification.

Figure 1(a,b) represents the flowchart and experimental fabrication of sol-gel spin coating process. Initially, the solvent was taken in a freshly cleaned beaker and in the next step catalyst, HCl, and acetic acid were added to the solvent on a magnetic stirrer as shown in Fig. 1(a). Finally, the precursor is added to the mixed solution of catalyst and solvent in a magnetically stirred beaker. The sol will be ready within very few seconds of magnetic stirring and requires no further aging. The procured sols were spin-coated on a thoroughly cleaned glass substrate by maintaining the spin rate of 2000 RPM for 15 seconds as shown in Fig. 1(b). The spin-coated films were sintered in a muffle furnace at 500 °C for 60 minutes to achieve crystallinity in the fabricated films. Multilayer ($TiO_2/SiO_2/TiO_2$) structure was obtained by following the same specifications periodically on the glass substrate.

The as-fabricated multilayer structures were characterized with cross sectional filed emission scanning electron microscopy (FESEM) for film thickness and layer identification (MIRA3 TESCAN) and ultraviolet visible and near-infrared (UV-VIS-NIR) spectrophotometer with a specular reflectance attachment (UV1800 Shimadzu, Japan) for reflectance analysis.

3. Results and discussion

Figure 2(a,b) shows the cross-sectional analysis and top-view of the multilayer ($TiO_2/SiO_2/TiO_2$) structure using field emission scanning electron microscopy (FE-SEM).

The cross-sectional FE-SEM investigation shown in Fig. 2 confirms the existence of TiO_2 and SiO_2 with their bright and dark appearance respectively. The thickness of the individual layers in the multilayer structure ($TiO_2/SiO_2/TiO_2$) is estimated at about 94/267/189 nm respectively. The study conveys that the films derived were very thick, and these thick films can shift the reflectance peak towards higher wavelengths due to the accumulation of a greater number of atoms on the surface [15, 16]. The increase in the film thickness can enhance the reflectance of the fabricated structure by increasing the photon absorption states [17]. It was also noted from the Fig. 2(b) that the multilayer ($TiO_2/SiO_2/TiO_2$) structure fabricated is uniform and free from cracks.

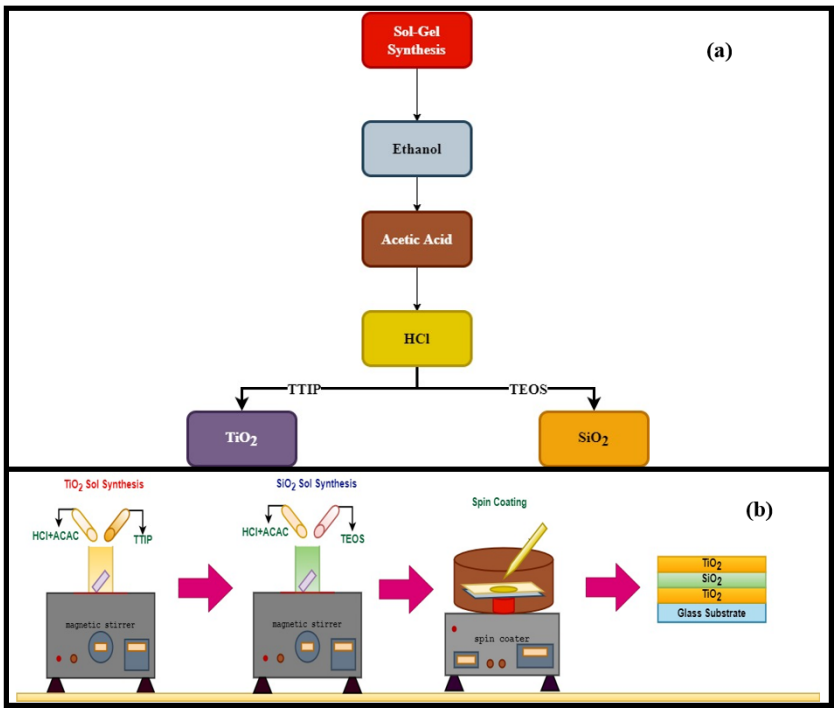

FIG. 1. Flow chart of sol-gel synthesis (a) and schematic of the experimental fabrication (b)

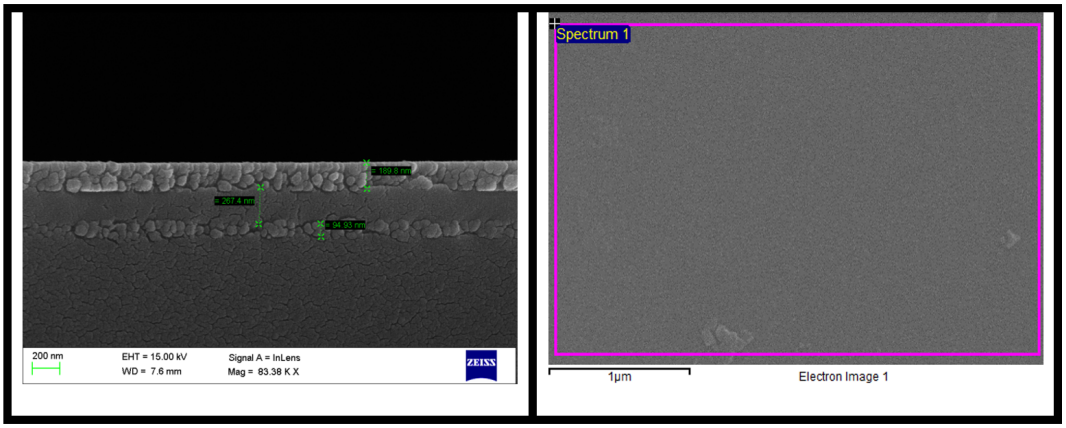

FIG. 2. Cross-sectional FE-SEM of the multilayer ($TiO_2/SiO_2/TiO_2$) structure (a) and top-view of the ($TiO_2/SiO_2/TiO_2$) structure (b)

The reflectance analysis on the multilayer ($TiO_2/SiO_2/TiO_2$) is performed using UV-vis spectrophotometer along with its digital image as inset and depicted in Fig. 3.

Figure 3 shows a multilayer ($TiO_2/SiO_2/TiO_2$) structure that clearly shows the presence of interfaces, which were interfered with to form a reflection pattern on the surface. The multilayer structure endorsed 60 % reflection in the infrared region with a central wavelength of 1000 nm and 72 % reflection in the ultraviolet zone, according to the reflectance analysis. This was a significant breakthrough in the field, reflecting both ultraviolet and infrared wavelengths in a single triple-layer construction. The as-reported structure can be applied in windows from protecting the seasonal temperature changes which reduce the usage of luxury equipment and also reduces the release of CFCs in the atmosphere.

4. Conclusions

An inexpensive method for the fabrication of ultraviolet and infrared reflector was proposed with only three layers of TiO_2 and SiO_2 by using sol-gel spin coating technique. The bright and dark bands shown in the cross-sectional FE-SEM analysis endorsed the presence of TiO_2, SiO_2, and TiO_2 films with their thicknesses about 94, 267, and 189 nm respectively. Furthermore, the reflectance analysis using UV-vis spectroscopy revealed that the thick films fabricated can undergo interference at the interfaces resulting 72 % reflectance in the ultraviolet region and 60 % reflectance in the infrared region. This kind of property made the multilayer promising for window application.

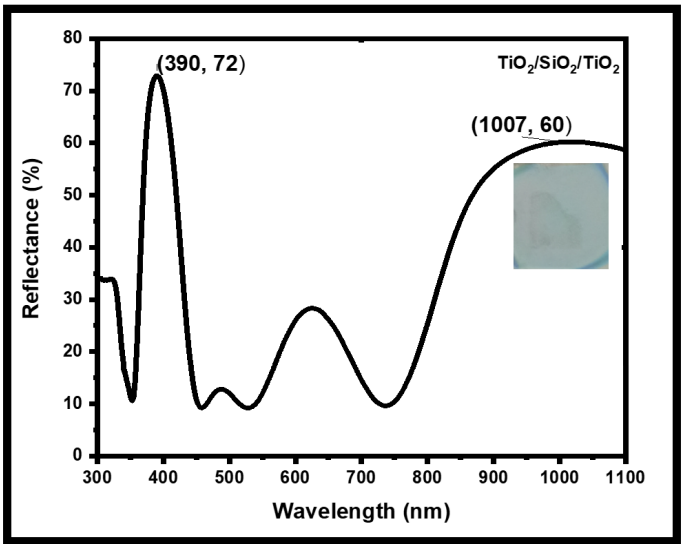

FIG. 3. Reflectance analysis of the multilayer ($TiO_2/SiO_2/TiO_2$) structure

References

[1] Hathaway J.A., Sliney D.H. Visible light and infrared radiation. In: *Physical and Biological Hazards of the Workplace*, Wiley online library, 2016, 203 p.
[2] Hoel D.G., Berwick M., de Gruijl F.R., Holick M.F. The risks and benefits of sun exposure 2016. *Dermatoendocrinology*, 2016, **8** (1), e1248325.
[3] Fleury N., Geldenhuys S., Gorman S. Sun Exposure and Its Effects on Human Health: Mechanisms through Which Sun Exposure Could Reduce the Risk of Developing Obesity and Cardiometabolic Dysfunction. *Int. J. of Env. Research*, 2016, **13** (10), P. 1–18.
[4] Calm J.M. Emissions and environmental impacts from air-conditioning and refrigeration systems. *Int. J. of Refrigeration*, 2002, **25** (3), P. 293–305.
[5] Hamzeh Jamali. Investigation and review of mirrors reflectance in parabolic trough solar collectors (PTSCs). *Energy Reports*, 2019, **5**, P. 145–158.
[6] Sparks M. Flannery M. Simplified description of multilayer dielectric reflectors. *J. of the Optical Society of America*, 1979, **69** (7), P. 993–1006.
[7] Kochergin V. Omnidirectional Dielectric Reflectors. In: *Omnidirectional optical Filters*, Springer Science & Business Media, Berlin, 2003, P. 105–123.
[8] Yue Y., Gong J.P. Tunable one-dimensional photonic crystals from soft materials. *J. of Photochemistry Photobiology C: Photochemistry Reviews*, 2015, **23**, P. 45–67.
[9] Nistico R., Scalarone D., Magnacca G. Sol-gel chemistry, templating and spin-coating deposition: A combined approach to control in a simple way the porosity of inorganic thin films/coatings. *Microporous Mesoporous Materials*, 2017, **248**, P. 18–29.
[10] Yepuri V., Dubey R.S., Kumar B. Rapid and economic fabrication approach of dielectric reflectors for energy harvesting applications. *Scientific Reports*, 2020, **10**, 15930.
[11] Hu X., Zhang X., Chen X., Luo M. Solution Route to Large Area All-TiO_2 One-Dimensional Photonic Crystals with High Reflectivity and Different Structural Colors. *Nanotechnology*, 2019, **31**, P. 1–9.
[12] Ma W., Kou Y., Zhao P., Zhang S. Bioinspired Structural Color Patterns Derived from 1D Photonic Crystals with High Saturation and Brightness for Double Anti-Counterfeiting Decoration. *ACS Applied Polymer Materials*, 2020, **2**, P. 1–9.
[13] Yepuri V., Dubey R.S., Kumar B. A Low-Cost Fabrication Approach of UV, VIS and NIR Dielectric Reflectors. *Advances in Materials Research. Springer Proceedings in Materials*, 2021, **5**, P. 355–362.
[14] Romanova V.A., Matyushkin L.B. Sol-gel fabrication of one-dimensional photonic crystals. *2017 IEEE Conference of Russian Young Researchers in Electrical and Electronic Engineering (EIConRus)*, 2017, 16839343.
[15] Taherniya A., Raoufi D. Thickness dependence of structural, optical and morphological properties of sol-gel derived TiO_2 thin film. *Materials Research Express*, 2018, **6**, P. 1–20.
[16] Bensouyad H., Sedrati H., et al. Structural, thermal and optical characterization of TiO_2:ZrO_2 thin films prepared by sol-gel method. *Thin Solid Films*, 2010, **519**, P. 96–100.
[17] Nadeem M.Y., Ahmed W. Optical properties of ZnS thin films. *Turkish J. of Physics*, 2000, **24** (5), P. 651–659.

Submitted 19 April 2022; revised 7 June 2022; accepted 6 July 2022

Information about the authors:

Raghvendra S. Dubey – Department of Nanotechnology, Swarnandhra College of Engineering and Technology, Seetharampuram, Narsapur (A.P.), India;

Venkatesh Yepuri – Department of Electrical and Electronics Engineering, Swarnandhra College of Engineering and Technology, Seetharampuram, Narsapur (A.P.), India; Venkatesh.yepuri555@gmail.com

Conflict of interest: the authors declare no conflict of interest.

NANOSYSTEMS:
PHYSICS, CHEMISTRY, MATHEMATICS

Original article

Chernova E.A., et al. *Nanosystems: Phys. Chem. Math.*, 2022, **13** (4), 468–474.
http://nanojournal.ifmo.ru
DOI 10.17586/2220-8054-2022-13-4-468-474

Ageing of graphene oxide thin films: the dynamics of gas and water vapors permeability in time

Ekaterina A. Chernova[1,a], Konstantin E. Gurianov[1,b], Mikhail V. Berekchiian[1,c], Victor A. Brotsman[2,d], Rishat G. Valeev[3,e], Olesya O. Kapitanova[2,f], Alina V. Kirianova[1,g], Alexey V. Lukashin[1,h]

[1]Lomonosov Moscow State University, Faculty of Materials Science, Moscow, Russia

[2]Lomonosov Moscow State University, Faculty of Chemistry, Moscow, Russia

[3]Udmurt Federal Research Center of the Ural Brunch of Russian Academy of Sciences, Izhevsk, Russia

[a]chernova.msu@gmail.com; [b]gurianovke@yandex.ru; [c]mikhail.berekchiyan@yandex.ru;
[d]brotsman_va@mail.ru; [e]rishatvaleev@mail.ru; [f]olesya.kapitanova@gmail.com,
[g]vov-lena2010@yandex.ru; [h]alexey.lukashin@gmail.com

Corresponding author: Ekaterina A. Chernova, chernova.msu@gmail.com

PACS 81.05.Rm, 47.56.+r

ABSTRACT Composite membranes are formed based on ultrathin 20 nm-thick selective layers of graphene oxide nanoflakes deposited on porous anodic alumina substrates. The long-term dynamics of permanent gases transport and water vapor permeability across the composite membranes is measured during 240 days (8 months). It is revealed that the permeability towards permanent gases remains nearly constant during a prolonged period of time. Contrary, water vapor flux decreases rapidly within the first 30 days from the membrane preparation moment and reaches about 80% of permeability loss during 8 months. The rapid decrease of membrane permeability during the first month could be attributed to a gradual packing of graphene oxide nanoflakes, particularly, locating in the surface sublayers, into more tight microstructure due to the evaporation of remaining solvent (membrane drying) under ambient conditions. Further decrease in permeability during more prolonged time could be caused additionally by deoxygenation of surface GO nanoflakes preventing water vapors diffusion into the GO film. This phenomenon, the so called "ageing" accompanies graphene oxide thin films similarly to some types of highly-permeable polymers. Holding the aged membrane under saturated water vapors, and even liquid water, didn't allow one to revitalize completely its permeability. The obtained results should be taken into account when designing membranes and other devices based on graphene oxide and its derivatives.

KEYWORDS graphene oxide nanoflakes, anodic alumina, membrane ageing, dehumidification, water vapor transport.

ACKNOWLEDGEMENTS The work is supported by the Russian Science Foundation (project 22-23-00662 "Membranes for molecular filtration and membrane electrocatalysis based on reduced graphene oxide").

FOR CITATION Chernova E.A., Gurianov K.E., Berekchiian M.V., Brotsman V.A., Valeev R.G., Kapitanova O.O., Kirianova A.V., Lukashin A.V. Ageing of graphene oxide thin films: the dynamics of gas and water vapors permeability in time. *Nanosystems: Phys. Chem. Math.*, 2022, **13** (4), 468–474.

1. Introduction

At present time, graphene oxide (GO) is considered as an advanced material both for the preparation of graphene, and as a building block for a variety of applications including the design of membrane materials [1], sensors [2], and catalytic platforms [3]. The lamellar microstructure of graphene oxide is represented by an assembly of stacked nanoflakes richly decorated with functional oxygen-containing groups endowing GO with an ability to separate water vapors from gas mixtures for a variety of industrial applications. For instance, GO-based composite membranes can achieve water vapor permeance of 10–60 $m^3 \cdot m^{-2} \cdot bar^{-1} \cdot h^{-1}$ in the relative humidity range of a feed stream from 40 to 90% and can be used for the dehumidification of gases with moderate-to-high concentrations of water vapor [4, 5]. Moreover, by adjusting oxygen-to-carbon ratio (C/O ratio), it is possible to tune the permeance-selectivity characteristics of GO-based membranes [6]. On the other hand, functional properties of GO composite membranes strongly depend on the packing architecture and ordering of GO nanoflakes, which are pre-determined by methods of GO thin films preparation including filtration, spin/spray-coating, solvent evaporation, etc [7].

All the parameters discussed above are usually reported for the freshly prepared graphene oxide membranes. However, as every material, GO can be prone to dynamical changing of its characteristics with time which can influence on its functional characteristics. This phenomenon, the so called "ageing", for instance, accompanies microporous polymers

and manifests itself in tight packing of macromolecules in a polymeric membrane and appears as a dramatic decrease in permeability [8]. Recently, ageing has been also reported for graphene oxide. To date, ageing of GO was reported for GO films [9], powders [10] and suspensions [11]. For instance, dynamics in swelling behavior was reported for 5–50 μm thick GO films prepared by Hummers' method (HGO) aged during 1–5 years under ambient conditions [9]. It was shown that even after 0.6–2 years of air storage, the swelling degree of HGO in ethanol and methanol became drastically smaller with time, and the swelling completely disappeared for larger alcohol molecules. Moreover, the 5 years-old samples did not show any signs of lattice expansion when immersed in alcohols but preserved a good swelling in liquid water [9]. The observed results were attributed to gradual deoxygenation of GO nanosheets covering the surface of graphene oxide films accompanied by drying caused by solvent evaporation from the GO film. In other work, the dynamics of structural and thermal characteristics with time for HGO powders stored during 2 years at ambient conditions was studied [10]. It was revealed that average d-spacing of the samples decreased from 0.660 to 0.567 nm, while the C/O ratio of graphene oxide increased from 1.96 to 2.76 which was attributed to the desorption of oxygen-containing groups from GO nanoflakes. Recently, a long-term studying of ageing of high-concentrated (10 mg/mL) aqueous GO suspensions has revealed that within the first year of storage both the viscosity and dynamic moduli of suspension increased with time [11]. The authors attributed this result to gradual time-dependent oxidation of GO nanoflakes in suspension, however, it is a matter of dispute and requires more detailed experiments.

The analysis of the literature data has shown that the phenomenon of ageing was considered for GO mainly in terms of its physico-chemical and rheological properties, while the dynamics of GO membranes permeability was not taken into account. In this work we report on the dynamics of water vapor and gas transport characteristics in graphene oxide-based membranes. The results are important not only for the design and storage of GO-based membranes, but also for the development of platforms for sensors, catalysis and other devices based on GO thin films.

2. Experimental part

Suspensions of graphene oxide nanosheets were prepared using the improved Hummers' method [12] by oxidizing medium flake graphite with graphite:KMnO4 ratio of 1:6; the detailed description of the method is presented in our previous paper [6]. The suspensions were purified from residual inorganic ions by dialysis during 30 days under constant stirring. The removal of sulfate-ions from the resulting GO suspensions was controlled by conductometry and XPS. The obtained suspension of graphene oxide was denoted as MFGO (medium-flake graphene oxide). The average size of MFGO nanosheets obtained by the described procedure is 750$\pm$100 nm [6].

The composite membranes were prepared in the form of thin MFGO films deposited onto porous anodic aluminum oxide (AAO) membranes with pore diameter of $\sim$80 nm and a thickness of 100 μm. The detailed description of the AAO films preparation and their gas permeance is given in [13, 14]. Briefly, the porous AAO supports were prepared by a standard anodic oxidation procedure of high purity aluminium foils (99,999%) in 0.3M $H_2C_2O_4$ at 120V followed by selective etching of aluminum and removing a barrier layer to obtain aluminum-reinforced AAO supports with the average N2 permeance of 90–100 $m^3 \cdot m^{-2} \cdot bar^{-1} \cdot h^{-1}$ [15]. To prepare composite membranes, the water-methanol (H_2O:CH_3OH vol. ratio of 1:1) suspension of MFGO with the concentration of 1.0 mg/mL was prepared. The thin films of MFGO were formed by successive deposition (3 times, aliquot of 40 ml) and spin-coating of the MFGO suspension onto porous AAO supports under slight vacuum suction ($\sim$30 kPa) at the rotation rate of 1500 rpm.

The X-ray photoelectron (XPS) spectra (overview and region C1*s* and O1*s)* of the composite membranes were registered on SPECS (Germany) instrument by employing MgK-α excitation (E_{ex}=1254 eV). The resulting spectra were calibrated to pure graphite C1*s* energy (284.6 eV) and were treated using CasaXPS software package. For spectra deconvolution, Shirley type background and mixed Gauss (70%)-Lorentz (30%) functions were used (the FWHM was kept fixed for all the spectral components). The C–C band subdivision into sp^2–C, sp^3–C components was neglected because of an insufficient spectral resolution [16]. Also, spectral component corresponding to O–C=O groups was not taken into consideration due to its low intensity.

Scanning electron microscopy (SEM) studies of a bottom part and cross-sections of the composite membranes were performed using Nvision 40 (Carl Zeiss) microscope. The obtained SEM micrographs were statistically treated using ImageJ software to extract the average thickness of the MFGO selective layer. To estimate the thickness of a single MFGO nanosheet, atomic-force microscopy (AFM) was employed. A diluted suspension of GO nanosheets was deposited on mica, dried carefully and subjected to AFM analysis using N-TEGRA NT-MDT instrument.

The transport characteristics of MFGO-based membranes were measured towards a set of permanent gases (H_2, N_2, O_2, CO_2, CH_4, C_4H_{10} and SF_6) and water vapors in dynamic and steady modes depending on the relative humidity (RH) of the feed streams [17]. A measurement cell consisting of a feed chamber and calibrated permeate chamber was employed. The permeate chamber was evacuated to a residual pressure of less than 0.1 mbar. Then, the stream of the measured gas was introduced into the feed chamber and a gradual pressure increase of the gas inflowing into the permeate chamber was registered in the form of a pressure-time curve. To study the transport of water vapors in a dynamic mode, wet nitrogen flow (relative humidity $\sim$100%) was used as a feed stream and a gradual pressure growth inside the permeate chamber was registered until the time when the pressure level exceeding the saturated H2O vapors pressure ($\sim$5 kPa, at

TABLE 1. XPS peak assignment for MFGO-based selective layer of the composite MFGO-based membrane

Sample	Spectral region	Band assignment	Initial GO		
			XPS component	Component content, %	C:O ratio
MFGO/AAO composite membrane	C1s	C–C	284.60	47.31	1.8:1
		C–O	286.96	42.78	
		C=O	288.30	9.91	
	O1s	C=O	532.74	26.59	
		C–O	531.01	73.41	

292K) was achieved. The fluxes of permanent gases as well as water vapors in a dynamic mode were calculated using a slope of the linear part of the pressure-time dependence.

Water vapor permeability under steady mode was measured under varied relative humidity of the feed stream. The detailed protocol was described earlier in our paper [18]. Briefly, a gas flux with a controlled humidity (feed stream pressure = 1 bar) was introduced into the feed side of the composite membrane, while the permeate side of the membrane was blown by He flux (pressure = 1 bar). The humidity and temperature of both gas fluxes were controlled using HIH-4000 sensors (Honeywell, USA). The experiments were performed at the temperatures of 23–25°C.

3. Results and discussion

According to SEM results (Fig. 1a,b), the selective layer of the MFGO-based composite membrane reveals its inherent wavy texture with large wrinkles more than 3 μm in length owing to corrugated shape of individual MFGO nanosheets composing the entire microstructure. According to the statistical analysis of the membrane cross-section, MFGO-based selective layer is uniform and ultrathin with the average thickness of 20 nm and is spreading uniformly on the porous AAO substrate. AFM results reveal that the average thickness of a single MFGO nanoflake is 0.925 nm which stays in the typical thickness range for single-layer GO nanosheets (0.8–1.2 nm depending on oxidation degree) [23] (Fig. 1c,d). Thus, the membranes in this work are prepared from high-quality single-layer graphene oxide. As has been shown by us earlier, the typical d-spacing for MFGO films is 0.83 nm under ambient conditions [18]. To estimate the number of MFGO nanosheets in the membrane, the thickness of MFGO film (20 nm) could be divided into a typical d-spacing [9], giving an average number of MFGO nanosheets equal to 24.

According to X-ray photoelectron analysis (Fig. 1e,f, Table 1), the MFGO-based selective layer of the composite membrane has the oxidation degree (C/O ratio) of 1.8 which is typical for the graphene oxide samples obtained by improved Hummers' method with graphite/$KMnO_4$ ratio of 1:6 and suggests the high quality of the prepared MFGO sample [18]. The oxygen-containing functional groups are dominated mainly by C–OH and –C–O–C– groups (single C–O bonds, see Table 1).

The composite MFGO-based membrane exhibits strong barrier properties towards permanent gases which favors its application in gas dehumidification processes (Fig. 2a). The permeability of the gases follows a tendency towards Knudsen diffusion. Typical permeability for the entire range of the studied gases does not exceed 0.0031 Barrer revealing the tight interlocking of graphene oxide nanosheets in the microstructure of MFGO ultrathin selective layer. It should be noted that the permeability of GO-based membranes strongly depends on the method of assembly of graphene oxide nanosheets. For instance, high H2-permeance was achieved in membranes obtained by spray-evaporation method resulting in GO membranes with high porosity [19]. However, common trend towards gas barrier properties is generally exhibited both by neat [20] and/or specially cross-linked/reduced graphene oxide [21], and our result stay in line with this trends.

It is remarkable, that the permeability of the composite membrane towards the studied gases has not changed with time: during 240 days, a little loss of about 2% is registered staying within the error range of gas flux measurement (Fig. 3a). The permeability of the composite membrane stands constant in time, probably, owing to small amounts of tiny packing defects inside the MFGO thin selective layer which constantly ensurre the transport of gas molecules across the membrane. It should be expected that graphene oxide nanosheets begin to shrivel due to gradual drying with time resulting in shrinkage and detachment of graphene oxide thin films from the support and should cause an increase in gas permeability. However, in our study, the employment of porous AAO supports favors the stability and constant gas permeability of MFGO-based thin film owing to cross-linking with aluminum ions and aluminol-groups on the surface of the AAO support. The structural stabilization of graphene oxide thin films with AAO supports was also evidenced in [22] and [23] for transport in liquid aqueous medium and water vapors, respectively. Therefore, the thin MFGO-based selective layer deposited on the AAO support is compact and stable in time providing constant gas barrier properties.

The game changes when we turn to the behavior of water vapors transport (Fig. 2b). The permeability of water vapors, measured in a dynamic mode, decreases rapidly within the first 30 days from membrane fresh state as the starting

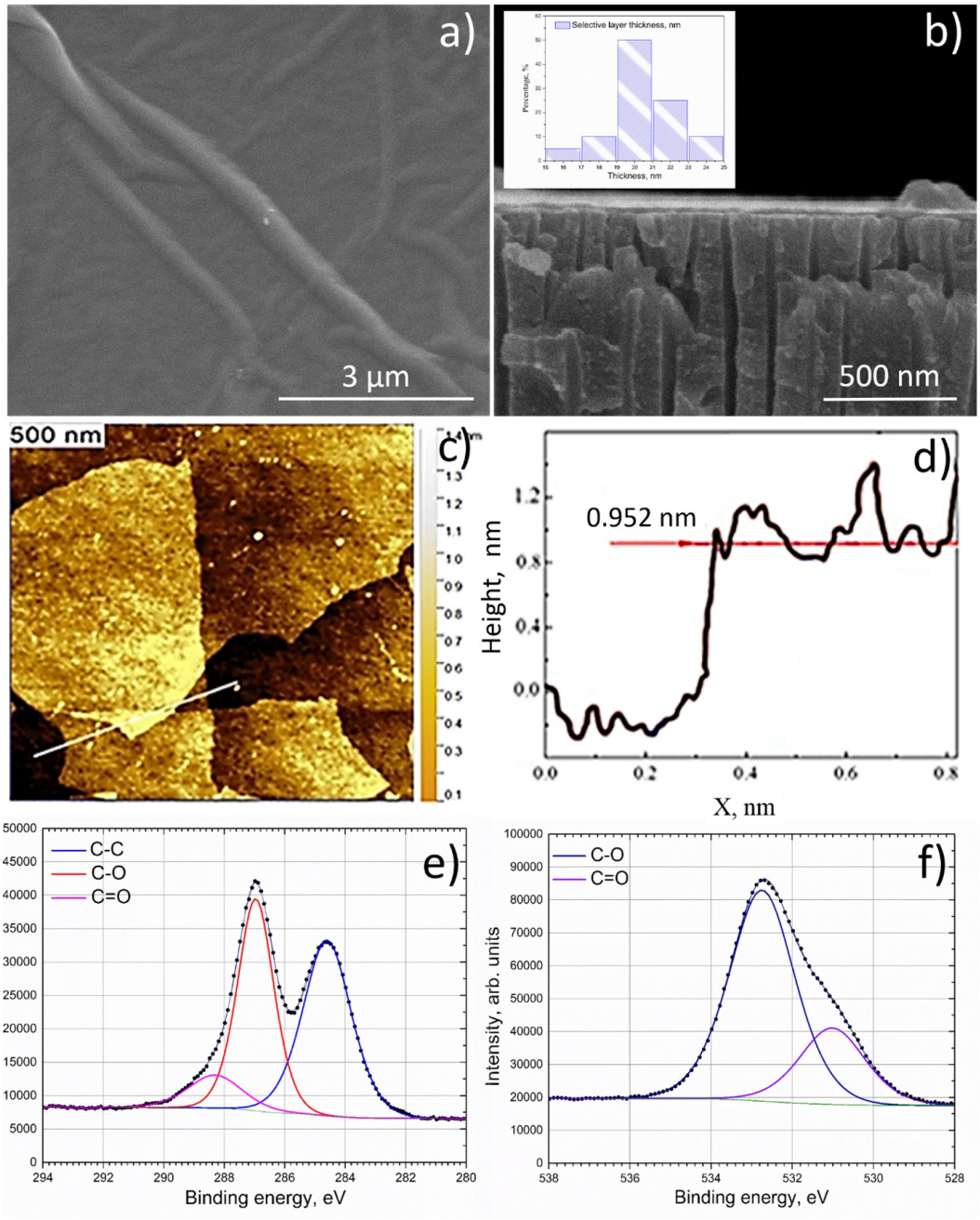

FIG. 1. a), b) SEM images of MFGO-based composite membrane: a) bottom site; b) cross-section The insert in b) shows the statistical distribution of the thickness of the MFGO-base selective layer; c), d) AFM image and height profile of MFGO nanosheets; e), f) XPS spectra fits for e) C1s and f) O1s regions for MFGO/AAO composite membrane

point. To characterize the dynamics of permeability, the coefficient of permeability loss (L_P, %) was calculated by the formula:

$$L_P = 100 \cdot \frac{P_0 - P_t}{P_0}$$

where P_0 and P_1 are permeability of the fresh membrane and the permeability of the membrane at a certain point in time (day of measurement).

According to the calculations, during the first 5 days, the membrane loses 15% of its original permeability reaching nearly 60% loss by the period of 30 days. The average daily permeability loss during the first 30 days is about 3.5% per day followed by a gradual stabilization at the level of about 0.75% per day within the remaining time up to 240 days. The rapid loss of permeability during the first month can be attributed to gradual evaporation of remaining solvent (water and methanol molecules) from interlayer galleries of the GO selective layer leading to the compaction and tightening of GO nanoflakes (particularly, the surface GO nanoflakes) until reaching some equilibrium and stable level of packing.

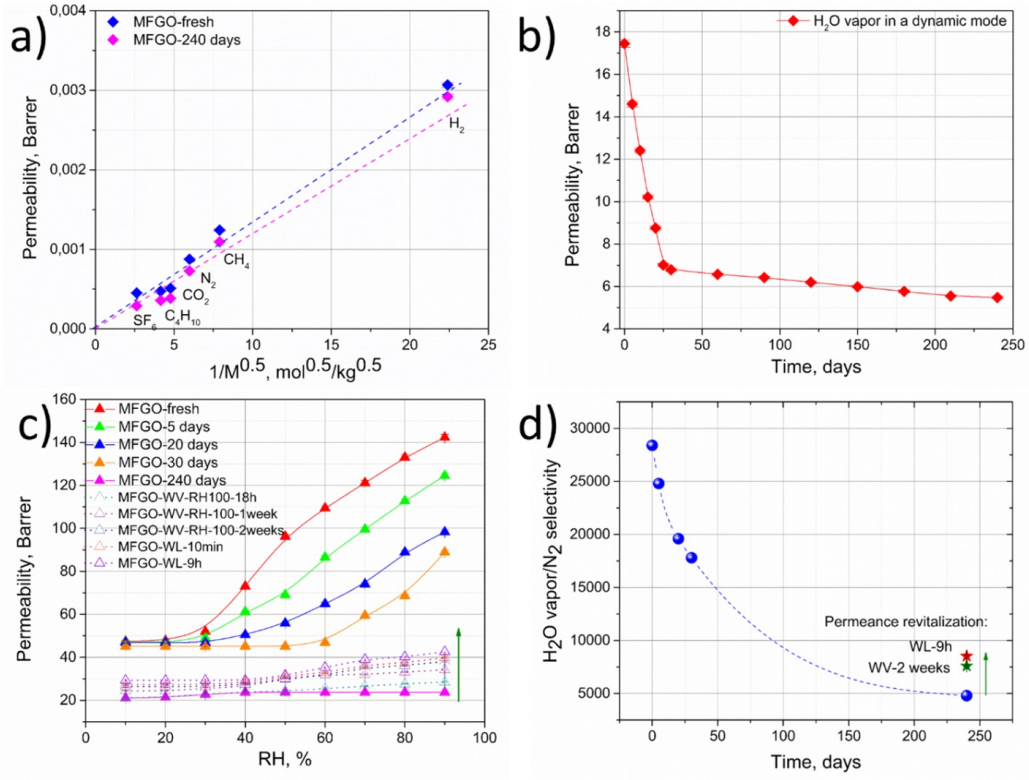

FIG. 2. Gas and vapor transport characteristics of the composite MFGO-based membrane: a) permeability towards permanent gases for MFGO freshly-prepared and aged during 240 days; b) permeability change of water vapors in a dynamic mode within 240 days; c) dynamics of RH-dependency of water vapors with time and during treatment under water vapors (WV, at RH = 100%) and liquid water (WL); d) change of water vapor-to-nitrogen selectivity with time. The restored selectivity registered under treatment with water vapors for 2 weeks (WV-2 weeks) and liquid water for 9 hours (WL-9h) is shown with green and red stars, respectively

To further understand the time-dependent water vapor transport evolution of the MFGO-based membranes, the dynamics of water vapor permeability in the entire range of relative humidity (RH) of the feed flux was measured during the 240 days. The membranes were stored in air between the measurements. According to the results (Fig. 2c), a gradual decrease in the water vapor permeability occurs in an entire range of relative humidity. It should be noted that at low relative humidity (10–30%), MFGO-based membrane reveals a relatively small permeability of about 40–50 Barrer and this range of RH of the feed stream is not valuable for practical dehumidification process. Meanwhile, a 2-fold decrease in permeability is registered even in the low-RH range after 240 days of ageing. In the middle (40–60%) and high (70–90%) RH range, an average decrease of 40% and 50% is registered, respectively, during the first 30 days reaching a 70–80% decrease within 240 days of ageing. The rapid loss of permeability during the first 30 days could be attributed to the gradual compaction of GO nanoflakes upon storage in air. In the a freshly-prepared MFGO membrane, the assembled GO nanoflakes are commonly hold in a metastable loosely-packed structure becoming compacted upon gradual evaporation of solvent molecules which are always remaining in the microstructure of as-prepared GO membranes. It is expectable that this process could mainly touch the surface sublayers of the membrane: once the solvent molecules have moved from the d-spacing of the sublayers, the entering of water molecules across the surface to the bulk of the membrane becomes restricted. The process may gradually propagate with time covering more and more GO layers of the membrane. Further decrease in water vapor permeability during more prolonged time could be caused by gradual deoxygenation of surface layers of the GO film. Obviously, the permeability of the aged GO film becomes close to that of the reduced GO [6]. The obtained results are complementary to the finding of Talyzin et al [9] who have studied the structural changes in GO during a prolonged period of time. It was shown that the GO ageing takes its origin in the process of drying and deoxygenation which starts on the surface GO nanosheets at the “GO film-air” interface and gradually penetrates deeper into the GO film.

The observed results are close to time-dependent physical ageing of some highly permeable polymers containing a large number of free diffusion volume [24, 25]. The ageing of the polymers is attributed to gradual relaxation of macromolecules from non-equilibrium conformations in freshly-prepared membranes towards stable equilibrium ones owing to a gradual evaporation of remaining solvent and thermal movement of the polymer chains. For instance, a

classical polymer with intrinsic microporosity (PIM-1) reveals rapid ageing towards water vapors exhibiting permeability loss of 3–5 times in the relative humidity range of 10–70% [26]. It is remarkable that the permeability of the polymers can be partially revitalized by treatment with low-molecular alcohols (particularly, methanol) [17,26], however, within several weeks after the treatment, the polymer again inevitably loses its permeability. To check the possibility of revitalizing the GO permeability after ageing, the membrane was subjected to water vapors treatment under RH =100% in a desiccator during 18 h, 1 and 2 weeks. It was revealed that the treatment of the membrane during 2 weeks allows one to restore water permeability by only 20 and 40% from the aged state in the low/middle and high RH range of the feed stream. Next, the membrane was soaked in liquid water for 10 min, 3 and 9 hours. However, even after treatment with liquid water, the maximum level of permeability restoration of 40% from the aged state for high RH-levels of feed stream was achieved (Fig. 3c). The observed results indirectly show that the decrease in water vapor permeability is caused not only by gradual drying of GO-thin film but also by partial deoxygenation of surface sublayers of the GO membrane which strongly restrict the diffusion of water molecules into the bulk of the membrane. A decrease in water vapor transport significantly affect the H2O/N2 selectivity: a nearly 6-fold decrease of this membrane characteristic is observed (Fig. 3d).

The obtained results show that GO-based thin films can dramatically lose their permeability towards water vapors and, moreover, the aged membranes cannot be revitalized by treatment with water neither in the form of vapors nor liquid. It should be noted, that these conclusions could be applied only towards thin GO films (20 nm), whereas for thicker films (in micrometer range), other ageing behavior could be registered and further experiments are required. Moreover, the use of water-methanol suspension and large size of GO nanoflakes (750$\pm$100 nm) also could favor the ageing process. Thus, to consider GO-based membranes, particularly, in the form of thin films, for industrial application, it is of high importance to develop standards for the conditions of the membrane storage and special modifications to prevent ageing effects.

Generally, whereas, the impact of ageing of polymers on the permeability of gas and vapors components is studied well enough [8], the long-term permeability dynamics of not only GO, but other 2D materials-based membranes in time suffers from the lack of attention. At present, the so called phenomenon of wetting ageing of 2D-materials is generally considered [27], and, coupled with long-term measurements of membrane transport characteristics it could give a complete information for a reliable design not only for membranes but also for membrane catalysts, sensors and elements for energy storage devices.

4. Conclusions

The ageing of thin GO-based membranes during storage under ambient conditions don't cause any significant changes in permanent gas transport, but induces a strong decrease in water vapors permeability. Gradual structural compaction caused by drying of GO at ambient conditions results in a decline of GO film permeability, particularly, during the first 30 days of storage (with the average permeability loss coefficient of 50–60%) and lost of 80% of initial permeability along the period 240 days. Treatment of the aged membrane under saturated water vapors for 2 weeks as well as soaking in liquid water for 9 h allowed one to achieve 40% restoration of the membrane permeability from the aged state at high RH of the feed stream. Thus, it is highly recommended to store freshly-prepared GO-based membranes under saturated water-vapor environment (for instance, in a desiccator with 100% RH of water vapors) to preserve the original permeability of the membranes.

Ageing of GO membranes can dramatically hinder their performance and should inevitably be taken into consideration for the design of GO-based membranes as well as other devices employing graphene oxide films as a working material. Further experiments are required concerning the influence of long-term ageing on the performance of GO-membranes with different thickness, C/O ratio and deposited from various solvents. Moreover, the rational search and design of different types of spacers and modifying agents preventing the GO nanoflakes compaction as well as deoxygenation during ageing is of high demand.

References

[1] Su P., Wang F., Li Z., Tang C.Y., Li W. Graphene oxide membranes: controlling their transport pathways. *J. Mater. Chem. A*, 2020. **8**(31), P. 15319–15340.

[2] Nag A., Mitra A., Mukhopadhyay S.C. Graphene and its sensor-based applications: A review. *Sensors and Actuators A: Physical*, 2018, **270**, P. 177–194.

[3] Butun S., Demirci S.,Yasar A.O.,Sagbas S.,Aktas N.,Sahiner N. Chapter 9 - 0D, 1D, 2D, and 3D Soft and Hard Templates for Catalysis. *Morphological, Compositional, and Shape Control of Materials for Catalysis*, 2017, **177**, P. 317–357.

[4] Petukhov D.I., Chernova E., Kapitanova O., Boytsova O., Valeev R., Chumakov A.P., Konovalov O., Eliseev A.A. Thin graphene oxide membranes for gas dehumidification. *Journal of Membrane Science*, 2019, **577**, P. 184–194.

[5] Chernova E., Petukhov D., Kapitanova O., Boytsova O., Lukashin A., Eliseev A. Nanoscale architecture of graphene oxide membranes for improving dehumidification performance. *Nanosystems: Physics, Chemistry, Mathematics*, 2018, **9**(5), P. 614–621.

[6] Chernova E.A., Petukhov D.I., Chumakov A.P., Kirianova A.V., Sadilov I.S., Kapitanova O.O., Boytsova O.V., Valeev R.G., Roth S.V., Eliseev A., Eliseev A. The role of oxidation level in mass-transport properties and dehumidification performance of graphene oxide membranes. *Carbon*, 2021, **183**, P. 404–414.

[7] Tsou C.-H., An Q.-F., Lo S.-C., De Guzman M., Hung W.-S., Hu C.-C., Lee K., Lai J.-Y. Effect of microstructure of graphene oxide fabricated through different self-assembly techniques on 1-butanol dehydration. *Journal of Membrane Science*, 2015, **477**, P. 93–100.

[8] Müller N., Handge U.A., Abetz V. Physical ageing and lifetime prediction of polymer membranes for gas separation processes. *Journal of Membrane Science*, 2016, **516**, P. 33–46.
[9] Iakunkov A., Sun J., Rebrikova A., Korobov M., Klechikov A., Vorobiev A., Boulanger N., Talyzin A.V. Swelling of graphene oxide membranes in alcohols: effects of molecule size and air ageing. *J. Mater. Chem. A*, 2019, **7**(18), P. 11331–11337.
[10] Li C., Lu Y., Yan J., Yu W., Zhao R., Du S., Niu K. Effect of long-term ageing on graphene oxide: structure and thermal decomposition. *Royal Society Open Science*, 2021, **8**(12), P. 202309.
[11] Gyarmati B., Farah S., Farkas A., Sáfrán G., Voelker-Pop L.M., László K. Long-Term Aging of Concentrated Aqueous Graphene Oxide Suspensions Seen by Rheology and Raman Spectroscopy. *Nanomaterials* (Basel, Switzerland), 2022, **12**(6).
[12] Marcano D.C., Kosynkin D.V., Berlin J.M., Sinitskii A., Sun Z., Slesarev A., Alemany L.B., Lu W., Tour J.M. Improved Synthesis of Graphene Oxide. *ACS Nano*, 2010, **4**(8), P. 4806–4814.
[13] Petukhov D.I., Buldakov D.A., Tishkin A.A., Lukashin A.V., Eliseev A.A. Liquid permeation and chemical stability of anodic alumina membranes. *Beilstein Journal of Nanotechnology*, 2017, **8**, P. 561–570.
[14] Petukhov D.I., Eliseev A.A. Gas permeation through nanoporous membranes in the transitional flow region. *Nanotechnology*, 2016, **27**(8), P. 085707.
[15] Petukhov D.I., Napolskii K.S., Eliseev A.A. Permeability of anodic alumina membranes with branched channels. *Nanotechnology*, 2012, **23**(33), P. 335601.
[16] Park S., An J., Jung I., Piner R.D., An S.J., Li X., Velamakanni A., Ruoff R.S. Colloidal Suspensions of Highly Reduced Graphene Oxide in a Wide Variety of Organic Solvents. *Nano Letters*, 2009, **9**(4), P. 1593–1597.
[17] Chernova E., Petukhov D., Boytsova O., Alentiev A., Budd P., Yampolskii Y., Eliseev A. Enhanced gas separation factors of microporous polymer constrained in the channels of anodic alumina membranes. *Scientific Reports*, 2016, **6**, P. 31183.
[18] Petukhov D.I., Chernova E.A., Kapitanova O.O., Boytsova O.V., Valeev R.G., Chumakov A.P., Konovalov O.V., Eliseev A.A. Thin graphene oxide membranes for gas dehumidification. *Journal of Membrane Science*, 2019, **577**, P. 184–194.
[19] Guan K., Shen J., Liu G., Zhao J., Zhou H., Jin W. Spray-evaporation assembled graphene oxide membranes for selective hydrogen transport. *Separation and Purification Technology*, 2017, **174**, P. 126–135.
[20] Nair R.R., Wu H.A., Jayaram P.N., Grigorieva I.V., Geim A.K. Unimpeded Permeation of Water Through Helium-Leak–Tight Graphene-Based Membranes. *Science*, 2012, **335**(6067), P. 442 LP – 444.
[21] Kim D.W., Kim H., Jin M.L., Ellison C.J. Impermeable gas barrier coating by facilitated diffusion of ethylenediamine through graphene oxide liquid crystals. *Carbon*, 2019, **148**, P. 28–35.
[22] Yeh C.-N., Raidongia K., Shao J., Yang Q.-H., Huang J. On the origin of the stability of graphene oxide membranes in water. *Nature Chemistry*, 2015, **7**(2), P. 166–170.
[23] Athanasekou C., Pedrosa M., Tsoufis T., Pastrana-Martínez L.M., Romanos G., Favvas E., Katsaros F., Mitropoulos A., Psycharis V., Silva A.M.T. Comparison of self-standing and supported graphene oxide membranes prepared by simple filtration: Gas and vapor separation, pore structure and stability. *Journal of Membrane Science*, 2017, **522**, P. 303–315.
[24] Swaidan R., Ghanem B., Litwiller E., Pinnau I. Physical Aging, Plasticization and Their Effects on Gas Permeation in "Rigid" Polymers of Intrinsic Microporosity. *Macromolecules*, 2015, **48**(18), P. 6553–6561.
[25] Harms S., Rätzke K., Faupel F., Chaukura N., Budd P.M., Egger W., Ravelli L. Aging and Free Volume in a Polymer of Intrinsic Microporosity (PIM-1). *The Journal of Adhesion*, 2012, **88**(7), P. 608–619.
[26] Chernova E.A., Roslyakov I.V., Dorofeev S.G., Lukashin A.V. Composite membranes based on geometrically constrained PIM-1 for dehumidification of gas mixtures. *Nanosystems: Physics, Chemistry, Mathematics*, 2019, **10**(3), P. 282–288.
[27] Chen X., Yang Z., Feng S., Golbek T.W., Xu W., Butt H.-J., Weidner T., Xu Z., Hao J., Wang Z. How Universal Is the Wetting Aging in 2D Materials. *Nano Letters*, 2020, **20**(8), P. 5670–5677.

Submitted 1 July 2022; revised 10 August 2022; accepted 11 August 2022

Information about the authors:

Ekaterina A. Chernova – Lomonosov Moscow State University, Faculty of Materials Science, 119991, Moscow, GSP-1, 1-73 Leninskiye Gory, Russia; chernova.msu@gmail.com

Konstantin E. Gurianov – Lomonosov Moscow State University, Faculty of Materials Science, 119991, Moscow, GSP-1, 1-73 Leninskiye Gory, Russia; gurianovke@yandex.ru

Mikhail V. Berekchiian – Lomonosov Moscow State University, Faculty of Materials Science, 119991, Moscow, GSP-1, 1-73 Leninskiye Gory, Russia; mikhail.berekchiyan@yandex.ru

Victor A. Brotsman – Lomonosov Moscow State University, Faculty of Chemistry, 119991, Moscow, GSP-1, 1-3 Leninskiye Gory, Russia; brotsman_va@mail.ru

Rishat G. Valeev – Udmurt Federal Research Center of the Ural Brunch of Russian Academy of Sciences (UdmFRC of UB RAS), Izhevsk, st. them. Tatiana Baramzina 34, 426067, Russia; rishatvaleev@mail.ru

Olesya O. Kapitanova – Lomonosov Moscow State University, Faculty of Chemistry, 119991, Moscow, GSP-1, 1-3 Leninskiye Gory, Russia; olesya.kapitanova@gmail.com

Alina V. Kirianova – Lomonosov Moscow State University, Faculty of Materials Science, 119991, Moscow, GSP-1, 1-73 Leninskiye Gory, Russia; vov-lena2010@yandex.ru

Alexey V. Lukashin – Lomonosov Moscow State University, Faculty of Materials Science, 119991, Moscow, GSP-1, 1-73 Leninskiye Gory, Russia; alexey.lukashin@gmail.com

Conflict of interest: the authors declare no conflict of interest.

NANO
ФИХМ

NANOSYSTEMS:

PHYSICS, CHEMISTRY, MATHEMATICS

INFORMATION FOR AUTHORS

The journal publishes research articles and reviews, and also short scientific papers (letters) which are unpublished and have not been accepted for publication in other magazines. Articles should be submitted in English. All articles are reviewed, then if necessary come back to the author to completion.

The journal is indexed in Web of Science Core Collection (Emerging Sources Citation Index), Chemical Abstract Service of the American Chemical Society, Zentralblatt MATH and in Russian Scientific Citation Index.

Author should submit the following materials:

1. Article file in English, containing article title, the initials and the surname of the authors, Institute (University), postal address, the electronic address, the summary, keywords, MSC or PACS index, article text, the list of references.
2. Files with illustrations, files with tables.
3. The covering letter in English containing the article information (article name, MSC or PACS index, keywords, the summary, the literature) and about all authors (the surname, names, the full name of places of work, the mailing address with the postal code, contact phone number with a city code, the electronic address).
4. The expert judgement on possibility of publication of the article in open press (for authors from Russia).

Authors can submit a paper and the corresponding files to the following addresses: nanojournal.ifmo@gmail.com, popov1955@gmail.com.

Text requirements

Articles should be prepared with using of text editors MS Word or LaTex (preferable). It is necessary to submit source file (LaTex) and a pdf copy. In the name of files the English alphabet is used. The recommended size of short communications (letters) is 4-6 pages, research articles– 6-15 pages, reviews – 30 pages.

Recommendations for text in MS Word:

Formulas should be written using Math Type. Figures and tables with captions should be inserted in the text. Additionally, authors present separate files for all figures and Word files of tables.

Recommendations for text in LaTex:

Please, use standard LaTex without macros and additional style files. The list of references should be included in the main LaTex file. Source LaTex file of the paper with the corresponding pdf file and files of figures should be submitted.

References in the article text are given in square brackets. The list of references should be prepared in accordance with the following samples:

[1] Surname N. *Book Title*. Nauka Publishing House, Saint Petersburg, 2000, 281 pp.
[2] Surname N., Surname N. Paper title. *Journal Name*, 2010, **1** (5), P. 17-23.
[3] Surname N., Surname N. Lecture title. In: Abstracts/Proceedings of the Conference, Place and Date, 2000, P. 17-23.
[4] Surname N., Surname N. Paper title, 2000, URL: http://books.ifmo.ru/ntv.
[5] Surname N., Surname N. Patent Name. Patent No. 11111, 2010, Bul. No. 33, 5 pp.
[6] Surname N., Surname N. Thesis Title. Thesis for full doctor degree in math. and physics, Saint Petersburg, 2000, 105 pp.

Requirements to illustrations

Illustrations should be submitted as separate black-and-white files. Formats of files – jpeg, eps, tiff.

NANOSYSTEMS:

PHYSICS, CHEMISTRY, MATHEMATICS

Журнал зарегистрирован
Федеральной службой по надзору в сфере связи, информационных технологий и массовых коммуникаций
(свидетельство ПИ № ФС 77 - 49048 от 22.03.2012 г.)
ISSN 2220-8054

Учредитель: федеральное государственное автономное образовательное учреждение высшего образования
«Санкт-Петербургский национальный исследовательский университет информационных технологий, механики и оптики»

Издатель: федеральное государственное автономное образовательное учреждение высшего образования
«Санкт-Петербургский национальный исследовательский университет информационных технологий, механики и оптики»

Отпечатано в Учреждении «Университетские телекоммуникации»
Адрес: 197101, Санкт-Петербург, Кронверкский пр., 49

Подписка на журнал НФХМ
На первое полугодие 2023 года подписка осуществляется через
ОАО «АРЗИ», подписной индекс Э57385